Bridging Macro- and Mesoscopic Methodologies for the Modeling of Nanoparticle Synthesis and Population Dynamics

Von der Fakultät für Ingenieurwissenschaften, Abteilung Maschinenbau und Verfahrenstechnik

der

Universität Duisburg-Essen

zur Erlangung des akademischen Grades

eines

Doktors der Ingenieurwissenschaften

Dr.-Ing.

genehmigte Dissertation

von

Patrick Wollny
aus
Dormagen

Gutachter: Univ.-Prof. Dr.-Ing. Andreas M. Kempf
Prof. Dr. Sotiris E. Pratsinis

Tag der mündlichen Prüfung: 13.03.2023

Abstract

The present work aims for the development of new classes of multiscale simulation models for gas-phase nanoparticle synthesis processes that are tailored for application with computational fluid dynamics (CFD). Directly coupled CFD approaches developed in the context of large-eddy simulation (LES) of turbulent flames, or for laminar synthesis processes in hot-wall and microwave-plasma reactors, are therefore presented. The particle dynamics models were designed to be independent of the synthesis application for suitable nucleation and growth mechanisms (i.e., nucleation from vapor phase, kinetically based growth, etc.). After explaining the basic theory of reactive and particle-laden flows and their numerical treatment, published and unpublished models that originated as parts of this work are presented.

The first of the three published papers presents a novel model for simulating heterogeneous particle systems. It is able to simulate the deposition of Pt-particles on Al_2O_3 carrier-particles formed by spray-flame synthesis. A multiclass model based on the extensively extended sectional approach has been developed to simulate the heterogeneous particle system. It includes size distributions for particles in the gas phase and on the surface of the carrier particles, which can grow by deposition, direct collision and collision on the surface. The tabulated chemistry approach used includes a new formulation for the nucleation process that allows the nucleated mass to be calculated at any location and time. This work involves the first simulation of spray flame synthesis of heterogeneous nanoparticles and provides promising results for further applications and extensions.

A novel CFD model using the sectional representation of the particle size distribution (PSD) is the subject of the second publication. It is designed for application in the context of synthesis processes of silicon nanoparticles in microwave-plasma reactors. The particle dynamics model presented involves a direct coupling with the gas phase through nucleation, condensation and evaporation. The simulations show a good agreement with the experimental data from the presented measurements and correctly describe unique process features, such as local particle zones and particle growth in the recirculation zone. In a further investigation, it was found that thermophoresis has a decisive effect on the trajectories of the particles in the present case: Thermophoresis causes nanoparticles to drift away from the hot zones where they would otherwise evaporate. This is a new finding showing that thermophoresis inhibits particle evaporation in the present case.

The third paper presents a bivariate approach for modeling particle dynamics developed for cases with complex nucleation and growth kinetics. The model was applied in simulations

of low-temperature synthesis processes from monosilane (SiH_4) in hot-wall reactors. The monodisperse formulation of the particle phase is linked to the gas phase by a series of of inception, condensation and surface reaction processes coupled with the gas phase. Due to the high volatile content that may be present in such particles, an additional conservation equation balances the volatile fraction in the particle phase, while an internal reaction describes the emission of these substances into the gas phase. The results of the model agree well with the measured values of a zero-dimensional validation case from the literature. The detailed simulations of a pilot-scale hot-wall reactor describe strong recirculation zones in the reactor that mix particles with different residence times, explaining the evolution of the complex particle morphology. The simulation results are again in good agreement with experimentally determined data and contribute significantly to the understanding of the process.

The first of the two unpublished models combines the monodisperse particle phase representation with nucleation, condensation, and evaporation formulations allowing full coupling to the gas phase. Due to the monodisperse assumption, the implementation of evaporation is critical, though, thus the new approach includes a transition function that prescribes the fractions of shrinkage and disappearance of the particles. The model has been shown to provide good accuracy compared to the sectional approach at a lower computational cost and also allows the prediction of particle morphology.

The second model, the "Digital Clone Probability Weighted Monte-Carlo Method" was developed to achieve detailed modeling of the particle system. The model is capable of simulating hundreds of thousands of individual particles in combination with gas-phase and surface kinetics in a stand-alone 0D simulation or in one-way coupling with CFD simulations. Very good agreement with established data from the literature is achieved for particle sizes and gas phase concentrations, confirming the good accuracy of the method. Images of artificially generated 3D models of the calculated aggregates are presented for visual comparison with TEM images from the experiments. For this study, the new simulation software "Another Nano-Tool" (ANT) was developed by the author, which now serves as a stochastic nanoparticle in-house code.

The results presented confirm the success of the novel classes of coupled multiscale simulation models, as all cases considered could be successfully reproduced by CFD simulations when the crucial interfaces between the gas and particle phases were included. This approach is now being discussed in other research groups and has led to collaborations and co-author publications. The latter are presented in the appendix of this work.

Zusammenfassung

Die vorliegende Arbeit zielt auf die Entwicklung neuer Klassen von Multiskalen-Simulationsmodellen für Gasphasen-Nanopartikelsyntheseprozesse, die für die Anwendung in der der numerischen Strömungssimulation (CFD) zugeschnitten sind. Vorgestellt werden daher direkt gekoppelte CFD-Ansätze, die im Rahmen der Large-Eddy-Simulation (LES) von turbulenten Flammen, oder für laminare Syntheseprozesse in Heißwand- und Mikrowellenplasmareaktoren entwickelt wurden. Die Partikeldynamikmodelle wurden so gestaltet, dass sie unabhängig von der Syntheseanwendung für passende Nukleations- und Wachstumsmechanismen anwendbar sind (d.h. Nukleation aus Dampfphase, kinetisch basiertes Wachstum, usw.). Nach der Erläuterung der grundlegenden Theorie der reaktiven und partikelbeladenen Strömungen sowie ihrer numerischen Behandlung, werden veröffentlichte und unveröffentlichte Modelle vorgestellt, die als Teile dieser Arbeit entstanden sind.
Die erste der drei publizierten Arbeitn stellt dabei ein neuartiges Modell für die Simulation eines heterogenen Partikelsystems vor. Es ist in der Lage, die Ablagerung von Pt-Partikeln auf Al_2O_3-Trägerpartikel zu simulieren, die durch Spray-Flammen-Synthese entstehen. Für die Simulation des heterogenen Partikelsystems ist ein Mehrklassenmodell auf der Grundlage des umfassend erweiterten sektionalen Ansatzes entwickelt worden. Es beinhaltet Größenverteilungen für Partikel in der Gasphase und auf der Oberfläche der Trägerpartikel, die durch Ablagerung, direkte Kollision und Kollision auf der Oberfläche wachsen. Der verwendete Ansatz der tabellierten Chemie beinhaltet eine neue Formulierung für den Nukleationsprozess, die es ermöglicht, die nukleierte Masse an jedem Ort und zu jeder Zeit zu bestimmen. Diese Arbeit beinhaltet die erste Simulation der Sprühflammensynthese von heterogenen Nanopartikeln und liefert vielversprechende Ergebnisse für weitere Anwendungen und Erweiterungen.
Ein neuartiges CFD-Modell, das sich der sektionalen Darstellung der Partikelgrößenverteilung (PSD) bedient und für die Anwendung im Rahmen von Mikrowellenplasma-Syntheseprozessen von Silizium-Nanopartikeln entwickelt wurde, ist Thema der zweiten Publikation. Das vorgestellte Partikeldynamikmodell beinhaltet eine direkte Kopplung mit der Gasphase durch Nukleation, Kondensation und Verdampfung. Die Simulationen zeigen eine gute Übereinstimmung mit den experimentellen Daten aus den vorgestellten Messungen und beschreiben einzigartige Prozessmerkmale, wie lokale Partikelzonen und das Partikelwachstum in der Rezirkulationszone, korrekt. In einer weiteren Untersuchung wurde festgestellt, dass Thermophorese im vorliegenden Fall einen entscheidenden Einfluss auf die Partikeltrajektorien hat: Aufgrund der Thermophorese driften die Nanopartikel von den heißen Zonen

weg, in denen sie sonst verdampfen würden. Im vorliegenden Fall ist dies ist eine neue Erkenntnis, die zeigt, dass Thermophorese die Partikelverdunstung hemmt.
In der dritten Veröffentlichung wird ein bivariater Ansatz für die Modellierung der Partikeldynamik vorgestellt, der für Fälle mit komplexer Keimbildung und Wachstumskinetik entwickelt wurde. Das Modell wurde in einer Simulation von Niedertemperatur-Syntheseprozessen aus Monosilan (SiH_4) in Heißwandreaktoren angewendet. Die monodisperse Formulierung der Partikelphase ist mit der Gasphase durch eine Reihe von von Inzeptions-, Kondensations- und Oberflächenreaktionsprozessen mit der Gasphase gekoppelt. Aufgrund des hohen Gehalts an flüchtigen Stoffen, die in derart gebildeten Partikeln enthalten sein können, bilanziert eine zusätzliche Erhaltungsgleichung den Anteil an flüchtigen Stoffen in der Partikelphase, während eine interne Reaktion die Emission dieser Stoffe in die Gasphase beschreibt. Die Ergebnisse des Modells stimmen gut mit den Messwerten eines null-dimensionalen Validierungsfalls aus der Literatur überein. Die detaillierten Simulationen eines Heißwandreaktors im Pilotmaßstab beschreiben starke Rezirkulationszonen im Reaktor, die Partikel mit unterschiedlichen Verweilzeiten mischen und damit die Entwicklung der komplexen Partikelmorphologie erklären. Die Simulationsergebnisse stimmen wiederum gut mit den experimentell ermittelten Daten überein und tragen wesentlich zum Prozessverständnis bei.
Das erste der beiden unveröffentlichten Modelle kombiniert die monodisperse Darstellung der Partikelphase mit Formulierungen für die Nukleation und Kondensation oder Verdampfung, die eine vollständig Kopplung mit der Gasphase erlauben. Aufgrund der monodispersen Annahme ist die Implementierung der Verdunstung jedoch kritisch, so dass der neue Ansatz eine Übergangsfunktion enthält, die die Anteile der Schrumpfen und Verschwinden der Partikel vorgibt. Das Modell hat bewiesen, dass es eine gute Genauigkeit im Vergleich zum sektionalen Ansatz bei geringeren Rechenkosten liefert und außerdem die Vorhersage der Partikelmorphologie ermöglicht.
Das zweite Modell, die „Digital Clone Probability Weighted Monte-Carlo Method“, wurde entwickelt, um eine detaillierte Modellierung des Partikelsystems zu erreichen. Das Modell ist in der Lage, hunderttausende von Einzelpartikeln in Verbindung mit Gasphasen- und Oberflächenkinetik in einer eigenständigen 0D-Simulation oder in Einwegekopplung mit CFD-Simulationen zu handhaben. Eine sehr gute Übereinstimmung mit etablierten Daten aus der Literatur wird für Partikelgrößen und Gasphasenkonzentrationen erreicht, was die gute Genauigkeit der Methode bestätigt. Bilder von künstlich erzeugten 3D-Modellen der berechneten Aggregate dienen zum visuellen Vergleich mit TEM Bildern aus den Experimenten. Für diese Studie wurde die neue Simulationssoftware "ant" vom Autor entwickelt, die nun als stochastischer Nanopartikel Inhouse-Code dient.
Die vorgestellten Ergebnisse bestätigen den Erfolg der neuartigen Klassen von gekoppel-

ten Multiskalen-Simulationsmodellen, da alle betrachteten Fälle erfolgreich durch CFD-Simulationen reproduziert werden konnten, wenn die Modellierung des entscheidenden Phasenübergangs einbezogen wurde. Dieses Vorgehen wird inzwischen auch in anderen Forschungsgruppen diskutiert und führten zu Kooperationen und zu Koautor-Publikationen. Letztere werden im Anhang dieser Arbeit vorgestellt.

Preface

This thesis was developed during my time as researcher at the Chair of Fluid Dynamics at the University of Duisburg-Essen under the supervision of Prof. Dr. Andreas Kempf. I would like to thank him for always being inspirational, motivational, supportive, and for giving me the chance to visit leading international conferences around the world.
Special thanks also go to Irenäus Wlokas, who always supported me with – too – detailed answers in case of urgent scientific questions. His mind is a never-ending fountain of terribly complicated ideas which he tends to share during one of his awesome BBQs. I am grateful to Prof. Dr. Christof Schulz and Prof. Dr. Hartmut Wiggers from the Institute for Energy and Materials Processes at University of Duisburg-Essen, as well as Prof. Dr. Igor Rahinov from the Department of Natural Sciences from the Open University of Israe for the valuable support in joint projects. Their advice has always been enlightening and a source of new inspiration.
Furthermore, I appreciate my examination committee: Prof. Dr. Kempf, Prof. Dr. Pratsinis, Prof. Dr. Kowalczyk, and Prof. Dr. el Moctar. Thank you for taking the time to study this tome, maintaining your interest, even though you have seen most of the theoretical part probably hundreds of times. I would like to extend my sincerest gratitude to my idol in science, Prof. Dr. Pratsinis, who traveled all the way from zenithal Zürich to dusty Duisburg to take on the role as examiner during my defense.
I am deeply grateful to all my colleagues at the Chair of Fluid Dynamics for cultivating a harmonious atmosphere and being receptive to all kinds of constructive discussions. A special mention goes to my colleagues and friends: Peter Janas, Andreas Rittler, Timo Lipkowicz, Johannes Sellmann, Linus Engelmann, Dominik Meller, Seung-Jin Baik, Monika Nanjaiah, and Andreas Unterberger for their collaboration and the enjoyable time shared during and after working hours.
Finally, I would like to thank my parents Karl and Edith for raising me to the man I am today and for always believing in me. I am grateful to my siblings Sebastian, Daniel, David, and Kerstin, who always support me and for moments full of joy and terrible jokes. I would like to express my gratitude to them for creating enough motivation to delve a little into the topic of my work without dozing off . . . well . . . most of the time. I am deeply grateful to my grandparents Hedwig, Helene, and Richard, who have always been a harbor of peace, security and love for me. I cannot express enough, how happy I am that they enriched my life for so long, making my memories colorful and warm. Therefore, I would like to say:

Thank you for the values that you have given me.
This work is your accomplishment.

There are many more people whom I would like to thank individually, but unfortunately, a page is very limited. To all those people: thank you so much – and I genuinely mean it!

The creative adult is the child who survived.
Ursula K. Le Guin

Dedicated to my wonderful family.

Table of contents

List of figures

List of tables

Nomenclature

Lower case latin symbols

a	surface area	m^2
$a_{d,i}$	components of the droplet acceleration vector	$\mathrm{m/s}^2$
a_m	surface area of monomer particles	m^2
c	molar concentration	$\mathrm{mol/m}^3$
c	normalized reaction progress variable	–
c	speed of sound	$\mathrm{m/s}$
c_p	heat capacity at constant pressure	$\mathrm{J/(kg \cdot K)}$
c_v	heat capacity at constant volume	$\mathrm{J/(kg \cdot K)}$
d	particle/droplet diameter	m
d_C	carrier particle diameter	m
d_c	collision particle diameter	m
d_p	primary particle diameter	m
d_v	volume averaged particle diameter	m
e_i	face normal vector	-
e_{ij}	displacement tensor	s^{-1}
f	mixture fraction	-
g_i	gravitational acceleration	$\mathrm{m/s}^2$
h	enthalpy	$\mathrm{J/kg}$
h_f^0	heat of formation	$\mathrm{J/kg}$
h_s	sensible enthalpy	$\mathrm{J/kg}$
k	turbulent kinetic energy	$\mathrm{m}^2/\mathrm{s}^2$
k	wave number	$1/\mathrm{m}$
k_{rb}	backward reaction rate	$\mathrm{mol/(m}^3 \cdot \mathrm{s)}$
k_{rf}	forward reaction rate	$\mathrm{mol/(m}^3 \cdot \mathrm{s)}$
m	mass	kg
n	particle number concentration in the PBE	-
n_s	number of sections	-
p	pressure	Pa
r	reaction rate	$\mathrm{mol/(m}^3 \cdot \mathrm{s)}$
s_l	laminar flame speed	$\mathrm{m/s}$

t	time	s
u_i	velocity vector	m/s
v_g	geometric mean particle volume	m^3
v_m	volume of monomer particles	m^3
x_i	spatial coordinate vector	m

Upper case latin symbols

A	particle surface concentration	m^2/m^3
A	pre exponential coefficient	-
A_1	surface concentration of monomers, bimodal model	m^2/m^3
A_2	surface concentration of main bin, bimodal model	m^2/m^3
B_h	Spalding number for heat transfer	-
B_m	Spalding number for mass transfer	-
C	molar concentration	$kmol/m^3$
C_S	constant in the Smagorinsky/Sigma turbulence model	-
D	diffusion coefficient	m^2/s
D_f	fractal dimension	–
E	activation energy in the Arrhenius equation	J/mol
E	energy	J
F_D	thickening factor in the ATF approach	-
I	identity matrix	-
I	monomer particles source term	$1/(m^3 s)$
J_i	diffusive flux vector	$m^2/(s \cdot m)$
L	length	m
L_t	turbulent length scale	m
L_{ij}	Germano identity/Leonard stress tensor	-
$M_{\phi\alpha}$	moment of ϕ of order α	ϕ^α/m^3
N	number concentration of particles	$1/m^3$
N	number	-
N_1	number concentration of monomer particles, bimodal model	$1/m^3$
N_2	number concentration of main bin, bimodal model	$1/m^3$
Q	volume source term in energy equation	J/kg
Q_k	number concentration of section k, sectional model	$1/m^3$
R	gas constant	$J/(kg \cdot K)$
S_{ij}	strain rate	1/s
T	temperature	K
T_0	reference temperature	K

V	volume concentration of particles	m^3/m^3
V_1	volume concentration of monomer particles, bimodal model	m^3/m^3
V_2	volume concentration of main bin, bimodal model	m^3/m^3
V_c	diffusion correction velocity	m/s
V_k	diffusion velocity	$m^3/m/s$
W	molecular weights	kg/kmol
X	molar fraction	-
Y_α	mass fraction of species alpha	-
Z	mixture fraction	-
Z_α	element mass fraction	-

Lower case greek symbols

α	free molecular collision pre-factor	-
α_c	on surface collision model constant	-
β	coagulation kernel / frequency	m^3/s
γ	ratio of specific heats	-
$\delta_\alpha(k)$	Dirac measure	-
δ_{ij}	Kronecker delta	-
δ_l^0	thermal flame thickness	m
ϵ	rate of dissipation	m^2/s^3
ζ	mixture fraction	-
η_K	Kolmogorov length scale	m
χ_{ijk}	interpolation term in the sectional particle model	-
λ	thermal conductivity	$W/(m \cdot K)$
η	dynamic viscosity	$Pa \cdot s$
η_m	carrier particle load	-
μ_{ij}	element mass fraction matrix	-
ν	kinematic viscosity	m/s^2
ξ_i	surface coverage of section i	-
ξ_t	total surface coverage	-
σ	standard deviation	-
σ_g	geometric standard deviation	-
ρ	density	kg/m^3
τ_{ij}	viscous stress tensor	N/m^2
τ_s	characteristic sintering time	s
ϕ	scalar quantity	-
χ	chemical species	-

$\dot{\omega}$	source term for species/progress variable	$\mathrm{kg}/(\mathrm{m}^3 \cdot \mathrm{s})$
$\dot{\omega}_\alpha$	chemical source term for species α	$\mathrm{kg}/(\mathrm{m}^3 \cdot \mathrm{s})$

Upper case greek symbols

$\dot{\Gamma}_\phi$	source term for ϕ in partial differential equations	$\phi/(\mathrm{m}^3 \cdot \mathrm{s})$
Δ	cell size	m
Δ	difference	$\star$
Ξ_Δ	sub-filter wrinkling factor	-
T	stress tensor	N/m^2
Ψ	flux limiter function in the TVD schemes	-
Ω	flame sensor	-

Subscripts to an arbitrary quantity ϕ

ϕ_0	initial
ϕ_α	species
ϕ_A	area
ϕ_{ij}	two dimensional tensor in index notation, $k = 1, 2, 3$
ϕ_i	vector in index notation, $i = 1, 2, 3$
ϕ_j	vector in index notation, $j = 1, 2, 3$
ϕ_k	vector in index notation, $k = 1, 2, 3$
ϕ_{max}	maximum of ϕ
ϕ_{min}	minimum of ϕ
ϕ_m	monomer
ϕ_p	at constant pressure
ϕ_s	sensible
ϕ_t	turbulent
ϕ_V	volume
ϕ_v	at constant volume

Superscripts to an arbitrary quantity ϕ

$\dot{\phi}$	time derivative
ϕ^0	initial value
ϕ'	fluctuation
ϕ^{sgs}	sub-grid scale
ϕ^S	surface

Operators to an arbitrary quantity ϕ

d	total derivative
$\overline{\phi}$	Filtered part of scalar quantity ϕ
∂	partial derivative
$\widetilde{\phi}$	Favre filtered part of scalar quantity ϕ
$\phi^{''}$	sub-filter part of fluctuating quantity ϕ

Dimensionsless numbers

B_h	Spalding number for heat transfer
B_m	Spalding number for mass transfer
CFL	Courant-Friedrichs-Lewy number: ratio of physical to numerical velocity
Kn	Knudsen number: ratio of mean free path of the gas phase to particle size
Le	Lewis number: ratio of thermal diffusivity to mass diffusivity
Ma	Mach number: ratio of velocity to speed of sound
Nu	Nusselt number: ratio of total to conductive heat transfer
Pr	Prandtl number: ratio of viscous to thermal diffusion
Re	Reynolds number: ratio of inertial to viscous forces
Re_d	Reynolds number of droplets/particles
Re_t	Reynolds number of turbulence
Sc	Schmidt number: ratio of momentum to mass diffusivity
Sh	Sherwood number: ratio convective mass transfer to diffusion rate

Physico-chemical constants

k_b	Boltzmann constant	$1.38065 \cdot 10^{-23}\,\mathrm{J/K}$
N_A	Avogadro constant	$6.022 \cdot 10^{26}\,1/\mathrm{kmol}$
R_m	ideal gas constant	$8.314459\,\mathrm{J/(molK)}$

Abbreviations

1D	one dimensional
3D	three dimensional
ATF	artificial thickened flame method
CCSS	Center for Computational Sciences and Simulation
CDS	central differencing scheme
CENIDE	Center for Nanointegration Duisburg-Essen
CFD	computational fluid dynamics
CMC	conditional moment closure

CV	control volume
DNS	direct numerical simulation
EDM	eddy dissipation combustion model
FGM	flamelet generated manifolds approach
FSP	flame spray pyrolysis
FVM	finite volume method
GDE	general dynamics equation for particle dynamics
GRI	gas research institute
HMDSO	hexamethyldisiloxane
IPC	iron-penthacarbonyl
LES	large eddy simulation
LHS	left hand side
MPI	message passing interface
PBE	population balance equation
PDE	partial differential equation
PDF	probability density function
PFGM	premixed flamelet generated manifolds approach
PIV	particle image velocimetry
PSD	partical size distribution
QUICK	quadratic upstream interpolation for convective kinematics
RANS	Reynolds averaged Navier-Stokes
RHS	right hand side
rms	root mean square
RST	Reynolds stress tensor
SD	size distribution
SGS	sub-grid scale
TVD	total variation diminishing
UDS	upwind differencing scheme
URANS	unsteady Reynolds averaged Navier-Stokes

1 Introduction

It began with a talk by physicist Richard Feynman ("There's Plenty of Room at the Bottom") in 1959 that the concepts and properties of nanoscience and -technology were discussed [82]. Owed to this young awareness of nanoscience as an individual research area, it might be surprising that mankind has been using artificially produced nanoparticles since ancient history [87]. In fact, the reinforcement of ceramic by including natural asbestos nanofibers was already exploited 4,500 years ago [76]. Ancient Egyptians were utilizing nanoparticles synthesized by a chemical process for hair dye more than 4,000 years ago [230], while "Egyptian blue", the first synthetic pigment, was produced around the 3^{rd} century BC using a mixture of sintered nanometer-sized glass and quartz [89]. The beginning of the metallic nanoparticle era dates back to the 14^{th} and 13^{th} century BC, when chemical methods where used to synthesize metallic nanoparticles for the glass production by Mesopotamian and Egyptians [191]. The Lyrcurgus Cup, a Roman glass workpiece from 4^{th}-century, is probably the most famous example of ancient metallic nanoparticle workmanship. It uses Ag-Au alloy nanoparticles to display different colors when light passes through the cup from different directions [44]. Ancient Chinese works from around 4_{th}-century BC like Mo Jing by Mozi consign a device for water harvesting from air called Fangzhu which was coated by a carbon nanoparticle layer [75]. The modern/scientific era of nanoscience has been initiated 1857, when Michael Faraday observed the difference between optical properties of ordinary metal and colloidal gold and did the first modern classification of nanoparticles. The reason behind this specific behavior of metal colloids where found later in 1908 by Mie [150], but the term of "nanotechnology" was first introduced 66 years later (1974) by Norio Taniguchi to describe processes involved in synthesizing and processing nano-materials [7].

In 1942, the German chemist Harry Kloepfer developed a groundbreaking process for manufacturing an exceptionally fine silica powder, later branded as AEROSIL. This innovative substance was used as a high-performance filler for automotive tires, revolutionizing the industry at that time. Subsequently, Kloepfer successfully patented the process for industrial-scale production in 1944 in collaboration with Degussa, a former German chemical company now known as Evonik Industries AG, and marked the beginning of an enduring success story for the German aerosol industry.

Since then, the global interest in nanotechnology increased and was again boosted in 2001, as the United States of America approved the "National Nanotechnology Initiative" (NNI) [82]. From 1999 to 2005 the funding of research in nanotechnology experienced a seven-fold

increase (USA, $1 billion, Western Europe $600 million, Japan $800 million in 2005) [11], while the budget by the US government allocated to the NNI alone was $ 1,740.9 million in 2018 [134]. In the period of 1999 to 2019, the number of released nanotechnology publications and applications increased from 1,581 (1999) to 81,303 (2019) [134], representing the growing interest and need of nanotechnology by the modern society. Nowadays, nanoparticles have a variety of applications in a broad field of different industries. In healthcare, metallic nanoparticles can be an option as alternative to antibiotics due to their antibacterial properties [71]. Nanoparticles can be used as drug delivery system to exert its effect at specific sides and avoid associated side effects [161]. This is especially promising for cancer treatment, where the enhanced permeability and retention (EPR) effect is used in order to place high drug concentrations specifically in tumor cells and very low concentrations in other tissues. This technology is in use, as approved therapies based on albumin nanoparticles already exist [201]. Nanoparticles are used in molecular diagnosis, for instance in highly visible indicator pregnancy tests [38], or to identify invading pathogens within the organism [27], genetic defects [34], cancer [160], and allergies [38]. Nanoparticles can create a barrier impervious to gases that could alter and reduce food stability. Together with their antibacterial properties, they play an important role in the food industry, especially in food preservation [182]. Titanium dioxide and zinc oxide nanoparticles are key components in sunscreens, as they effectively absorb ultraviolet light [130]. Further applications for nanoparticles are renewable energy sources [101], water purification [2], homeland security [6], sports equipment [101], and agriculture [211]. In fact, modern industry can not be imagined without nanotechnology for a good reason: it has the potential to counteract starvation, diseases, and pollution.
But applied nanotechnology and a booming market also come with environmental consequences that are not sufficiently investigated yet [11, 134]. For example, it is observed that titanium dioxide – used in sunscreen – causes microorganisms oxidation, as well as oxidation damage to other organisms [94]. It is also known that nanoparticles can enter the human body with direct consequences for its health [197]. Therefore, not only must the product be optimized for optimal functionality, but also in order to prevent unwanted environmental damage within their whole life cycle [134]. This faces science with the new challenge of creating novel classes of engineering tools for multiscale approaches which combine mesoscopic and macroscopic models in a joint framework including important condensation and reaction processes. Biswas and Wu [11] described this need as:

> *"For more effective implementation of such processes, a multiscale approach needs to be adopted. Such an approach includes developments at the molecular level, linking of these to fluid dynamics/transport, and reactor models at the micro- and macroscales."*

This work is dedicated to this goal and presents a set of new models which couple meso- and macroscales within a framework tailored for computational fluid dynamics (CFD) and focused on so called "bottom-up" processes (e.g., gas phase synthesis processes).
But modeling nanoparticle dynamics in synthesis reactors is a complex task, as the particle design is a result of a variety of intertwined thermochemical and transport phenomena. As such, the processes sensibly depend on the whole thermochemical history that a particle experienced. Gradients of the temperature for example can have a major impact on the nucleating particle characteristics, as faster cooling rates produce more and smaller nuclei in comparison to slower cooling rates [204, 159]. The effect of differences in such gradients is amplified within the particle phase, as particle number and size are changed, affecting particle evolution in a non-linear manner. High temperature spikes can cause particle evaporation [204], while the formed vapor can condense again on the surface of surviving particle or build new, smaller nuclei. Heterogeneous material systems can produce composite particles, which can – depending on the process – result in mixed aggregates, coatings, or carrier particles decorated with a secondary class of smaller particles [249]. Synthesis processes at low temperature tend to generate particles in a series of chemical reactions rather than through nucleation from vapor [156, 200]. The first metallic nuclei contain just a few metallic atoms, often in combination with impurities from the precursor substance. Nuclei are formed until the surface area provided by the dispersed phase becomes sufficiently large and most of the remaining silylens stick to or react with the particle surface [157, 79]. These observations show that the gas-to-particle transition is a complex and very dynamic process. State-of-the-art CFD models for particle dynamics as introduced in section 3.6 do not provide the necessary depth to describe such processes. The issue of those models is the absence of suitable gas to particle transition formulations, often assuming that pure metallic atoms (Si, Fe, ...), or oxide molecules (SiO_2, Fe_2O_3, ...) are forming single stable nuclei. This procedure allows a very simple model implementation as in an uncoupled fashion [52, 186]. The sectional model follows an univariate approach and assumes spherical particles, which can be understood as instant sintering of collision partners. This assumption does not hold, when gas temperatures become lower and aggregate structure are formed, but describes an appropriate simplification for cases that do not fall below that point [186]. Effort has been made to investigate the impact of additional surface growth [209] and nucleation mechanisms

[173] for zero-dimensional test cases and without phase coupling as shown by Shekar et al. [199, 200] and Menz and Kraft [146] for computationally more expensive stochastic models. Latter investigations show the importance of the described coupling for practically relevant processes. In case of a bivariate moment approaches like in the monodisperse model, over-simplified formation and growth modeling can result in major errors, as single particle mass conservation is violated when new seeded monomers split the mass of existing particles [88]. As shown in this work, appropriate closures for the particle formation and growth can solve this problem by predicting a realistic balance between particle inception and surface growth. It is therefore obvious that accurate predictions of the particle synthesis process require a correct description of the formation and growth processes as the interface for molecular fluxes between the phases. A joint framework with fluid dynamics is mandatory as transport processes must be accounted to capture the varying thermochemical conditions and important mixing processes within real synthesis reactors

Beginning with the fundamental physics behind reacting flows in chapter 2, this manuscript is organized in a sequential order. The chapter starts with an introduction of the important governing equations for gaseous flows, followed by the basic chemical kinetics theory. The basics of combustion modeling and tabulation techniques are presented concisely, as high-temperature combustion processes serve as the primary sources of industrially produced oxide nanoparticles [11]. The general theory of turbulence and the challenge of predicting turbulent flows is shown in the following together with a brief explanation of different turbulence models. The chapter is closed by an introduction into numerical methods used to discretize the underlying partial differential equations by applying the finite volume method and iterative procedures for solving the resulting non-linear system of equations.

In chapter 3, the population balance modeling of nanoparticles in a gas atmosphere is introduced and important phenomena of particle formation, growth, coagulation, and coalescence are explained. In the following, the general dynamic equation (GDE) of particles in convective fields is presented in chapter 3. Shown are different simplified approaches that make its' integration in the frame of CFD computationally affordable. Two new unpublished methods, which were developed by the author in the frame of this work, are introduced at the end of this chapter. The first model is the bivariate gas to liquid transition model (BGLT), which combines the monodisperse representation of the particle phase with extended nucleation and condensation/evaporation modeling for vapors condensing from the fully coupled gas phase. The Digital Clone Probability Weighted Monte Carlo method – the second unpublished model – is capable of simulating hundreds of thousands of digital particle representations in combination with chemical kinetics in the gas phase or at the particle surface. It can be either fully coupled in a stand-alone 0D simulation or one-way coupled with CFD. To ensure their

accuracy, both models have undergone either validation with literature data or benchmarking against existing, computationally more expensive models.
Further, three published manuscripts are presented which include novel approaches for particle synthesis in reactive flows that have been developed by the author. In chapter 4, a model is introduced for the simulation of a heterogeneous particle system of Al_2O_3 carrier-particles decorated by Pt-particles which are synthesized in a spray flame process. The shown simulations represent an attempt to predict heterogeneous spray flame synthesized nanoparticles. The results are promising for further applications and extensions. Another model was developed for the application in the frame of microwave plasma synthesis processes of silicon nanoparticles from monosilane (SiH_4) as precursor. The particle model is introduced in chapter 5 and features a direct coupling with the gas phase by nucleation, condensation, and evaporation with a curvature correction for the effect of different particle sizes and predicts the process in a detail that have not been reached before. The last publication – shown in chapter 6 – introduces a model that was developed for cases, in which amorphous particle structures are synthesized. It was applied in a simulation of a low temperature synthesis processes of silicon nanoparticles from monosilane (SiH_4) in semi-industrial hot wall reactor. The simulation data are in close agreement with the experiments and show spatially and time resolved results of the process for the first time. The conclusions section gives an overview over the key achievements of this work and briefly discuss an outlook of how existing models could be improved and which approach might be promising from the authors' perspective. In addition, an overview over other first and co-author publications is given in the appendix.

2 Mathematical Description of Reacting Flows

2.1 Conservation Equations

Resolution of the reacting flow field using numerical schemes is one of the fundamental topics of this work. Hence, the fluid is – with some exceptions – generally treated as a continuum in an Eulerian framework. The resulting equations, known as Navier-Stokes Equations, are shown and extended for reactive cases in this section. Since conservation of mass is fundamental in continuum theory, the conservation equation of mass must hold in any case. Following, also the first law of thermodynamics holds, i.e., energy is preserved within the control volume (CV). The latter can be defined by a flow device or a theoretical volume within the flow field (Fig. 2.1). The balance within the observed control volumes are derived

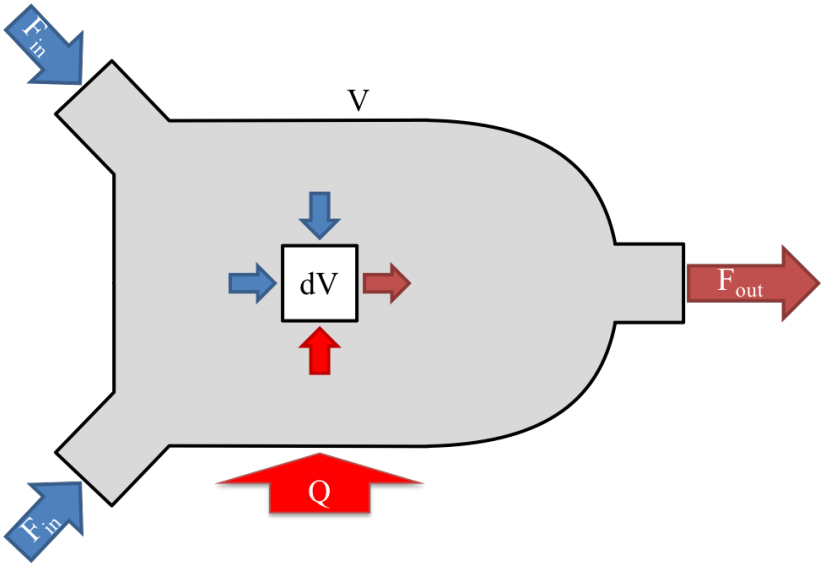

Fig.: 2.1 Control volume defined by a physical flow device and by a theoretical volume within the inner flow field. The flow inlets have the same diameter as the outlet, hence the out streaming flow is accelerated. Since the device is heated from the bottom, the outgoing flow shows a higher temperature.

by volume integrals with respect to temporal and convective changes. As shown in the figure above, the convective part can be replaced by surface integrals. Mathematically, this is done

by applying the Gauss theorem and leads to the following definition of the fundamental conservation equation of an intensive property ϕ and its source term Γ_ϕ:

$$\underbrace{\frac{\partial}{\partial t}\int_V \phi dV}_{\text{temporal change}} + \underbrace{\int_V \nabla\cdot(\boldsymbol{u}\phi)dV}_{\text{change due to convection}} = \frac{\partial}{\partial t}\int_V \phi dV + \oint_S (\boldsymbol{u}\phi)\cdot\boldsymbol{n}dS = \underbrace{\int_V \Gamma_\phi dV}_{\text{external source}} \tag{2.1}$$

The so-called divergence form is derived by a triple derivative of equation 2.1 (LHS) with respect to the volume $dV = dxdydz$:

$$\frac{\partial\phi}{\partial t} + \nabla\cdot(\boldsymbol{u}\phi) = \Gamma_\phi \tag{2.2}$$

Note that the diffusion term is omitted in the above equations in order to highlight and simplify the principle of conservation. It will be added to the respective conservation equations in the next steps, though.

2.1.1 Conservation of Mass and Species

According to equation 2.2, the mass conservation equation can be given by substituting the density ρ for the general property ϕ:

$$\frac{\partial\rho}{\partial t} + \nabla\cdot(\rho\boldsymbol{u}) = \Gamma_\rho \tag{2.3}$$

The mass conservation is also the basis for the conservation equations for species, as it denotes the sum of all mass fractions Y_k:

$$\sum_{k=1}^{N} Y_k = 1 \tag{2.4}$$

Defining the partial mass for species k as $Y_k\rho$, while accounting for the diffusive drift velocity V_k, a set of species conservation equations can be derived:

$$\boxed{\frac{\partial\rho Y_k}{\partial t} + \nabla\cdot(\rho(\boldsymbol{u}+\boldsymbol{V}_k)Y_k) = \dot{\omega}_k + \Gamma_{Y_k}} \tag{2.5}$$

Whereby $\dot{\omega}_k$ and Γ_{Y_k} are the chemical and the general source terms for species k, respectively. While $\dot{\omega}_k$ changes the composition due to chemical reactions such as combustion and thermal decay. The general source term Γ_{Y_k} combines sources due to phase transition such as nucleation and condensation processes – those processes will be explained later in this work.

According to Eq. 2.4, the sum of all diffusing species masses must be zero in order to fulfill the mass conservation.

$$\sum_{k=1}^{N} Y_k V_{k,i} = 0 \tag{2.6}$$

The diffusion gradient ∇X_i for each species i by detailed molar is obtained by solving a system of equations (Eq. (2.7)), which defines the diffusion of species k into all other species of a local mixture [245].

$$\nabla X_i = \sum_{k=1}^{N} \frac{X_i X_k}{D_{ik}} (V_k - V_i) + (Y_i - X_i) \frac{\nabla P}{P} + \frac{\rho}{p} \sum_{k=1}^{N} Y_i Y_k (f_i - f_k) \tag{2.7}$$

The binary diffusion coefficient D_{ik} denotes the mobility of two diffusing species and is given by the kinetic theory following the Chapman-Enskog theorem [31, 78]:

$$D_{ik} = \frac{1.863 \cdot 10^{-3} \sqrt{T^3 (W_i^{-1} W_k^{-1})}}{p \sigma_{ik}^2 \Omega_{ik}} \tag{2.8}$$

Here, σ_{ik} and Ω_{ik} are the averaged collision diameter $(\sigma_i + \sigma_k)/2$ and the collision integral. Other quantities are the pressure p, the molecular weight W_k of species k and the temperature T. Since solving for the detailed diffusion demands high computational effort, it is common practice to apply simplifications. Two popular forms are Fick's law and the Hirschfelder and Curtis approximation. The former is given by equation (2.9).

$$\nabla X_1 = \frac{X_1 X_2}{D_{12}} (V_2 - V_1) \tag{2.9}$$

Solving the equation analytically gives:

$$V_1 = -D_{12} \nabla ln(Y_1). \tag{2.10}$$

This equation is valid in cases with a mixture of just two species, or for more species, if all binary diffusion coefficients are equal ($D_{ik} = D$). Because those cases are rarely given, and the mixtures are generally more complex in combustion cases, the more sophisticated Hirschfelder and Curtis approximation [78] is used:

$$V_k X_k = -D_k \nabla X_k \tag{2.11}$$

The diffusion coefficient D_k is a mixture averaged form of the binary diffusion coefficient. It is averaged by applying equation (2.12):

$$D_k = \frac{1 - Y_k}{\sum_{j \neq k} X_j / D_{ij}} \tag{2.12}$$

The diffusion velocity given by equation (2.11) is inaccurate with respect to the total mass conservation, as condition (2.6) is not automatically fulfilled. One way to overcome this problem is transporting $N-1$ species, while the last species N is calculated by $Y_N = 1 - \sum_{k=1}^{N-1} Y_k$. Another, more accurate way of correcting the diffusive fluxes is introducing a correction velocity V_c to ensure mass conservation. Hence, the diffusion velocity becomes:

$$\boldsymbol{V}_k = -D_k \frac{W_k}{W} \frac{\nabla X_k}{X_k} + \boldsymbol{V}_c. \tag{2.13}$$

Where the correction velocity V_c is defined as:

$$\boldsymbol{V}_c = \frac{1}{W} \sum_{k=1}^{N} D_k W_k \nabla X_k. \tag{2.14}$$

Substituting the result into (2.5) delivers the species conservation equation for the Hirschfelder and Curtis theorem, which satisfies the total mass conservation:

$$\boxed{\frac{\partial \rho Y_k}{\partial t} + \nabla \cdot (\rho(\boldsymbol{u} + \boldsymbol{V}_c) Y_k) = \nabla \cdot \left(\rho D_k \frac{W_k}{W} \nabla X_k \right) + \dot{\omega}_k + \Gamma_{Y_k}} \tag{2.15}$$

2.1.2 Conservation of Momentum

As a vector, the momentum $\boldsymbol{u}\rho$ consists of one component for every physical direction. Hence, it is conserved by a set of three equations of type (2.2), which are additionally affected by frictional and body forces.

$$\frac{\partial \rho \boldsymbol{u}}{\partial t} + \nabla \cdot (\rho \boldsymbol{u}\boldsymbol{u} - \boldsymbol{T}) = \Gamma_{\boldsymbol{u}} \tag{2.16}$$

The external body force $\Gamma_{\boldsymbol{u}}$ includes gravity forces, magnetic fields or momentum losses due to particle formation, while $\boldsymbol{T}$ includes the pressure p and viscous stresses given by:

$$\boldsymbol{T} = -(p + \lambda^* \nabla \cdot \boldsymbol{u})\boldsymbol{I} + 2\eta \boldsymbol{E}. \tag{2.17}$$

Here, I, η and λ^* denote the identity matrix, the dynamic viscosity, and the coefficient of the deviatoric stress, given by $\lambda^* = 2/3\eta$. The variable $\boldsymbol{E}$ indicates the strain, which is the symmetric part of the displacement tensor and shown by the following equation.

$$\boldsymbol{E} = e_{ij} = \frac{1}{2}\left[\frac{u_i}{x_j} + \frac{u_j}{x_i}\right] \tag{2.18}$$

2.1.3 Conservation of Energy

A variety of different formulations for the energy conservation is discussed in the literature [171]. In this work, the formulation for the sensible energy as well as the sum of sensible and chemical enthalpy are of interest, which are defined by equations (2.19) and (2.20) for species i:

$$e_{s,i} = \int_{T_0}^{T} c_{p,i} dT - p/\rho \tag{2.19}$$

$$h_i = \int_{T_0}^{T} c_{p,i} dT + \Delta h^0_{f,i} \tag{2.20}$$

The variables $c_{p,i}$, p_i, $\Delta h^0_{f,i}$ indicate the heat capacity, the partial pressure and the enthalpy of formation of species i, respectively. The pure specie enthalpy $h_i = \int_{T_0}^{T} c_{p,i} dT$ is obtained by temperature depending NASA polynomials [96, 135], whereas only the mass averaged energy/enthalpy (2.19 or 2.20) of the mixture (represented by ϕ) is necessary for the conservation of energy:

$$\phi = \sum_{i=1}^{N} \phi_i Y_i \tag{2.21}$$

Hence, in regard to the definition of the sensible energy 2.19, the conservation equation is defined as:

$$\frac{\partial \rho e_s}{\partial t} + \nabla \cdot (\rho \boldsymbol{u} e_s) = \underbrace{-\sum_{k=1}^{N} \dot{\omega}_k \Delta h^0_{f,k}}_{\text{heat release}} \underbrace{+ \nabla \cdot (\lambda \nabla T)}_{\text{heat conduction}} \underbrace{- \nabla \cdot \left(\rho \sum_{k=1}^{N} h_{s,k} Y_k \boldsymbol{V_k} \right)}_{\text{species diffusion}} \underbrace{+ \boldsymbol{T} : \nabla \boldsymbol{u}}_{\text{frictional heating}} + \dot{Q}. \tag{2.22}$$

Here, $\dot{Q}$ denotes the volume source term, such as from radiation or gas excitation due to microwaves. As the sensible energy excludes the enthalpy of formation, the change due to chemical heat release must be taken into account by using the Hess theorem. For heat conduction, Fourier's law is applied, where λ is the heat conductivity of the mixture. The pressure and viscous stresses are included in the frictional heating term – see Eq. (2.17) For the sum of sensible and chemical enthalpy, the conservation equations must be modified

according to its definition (2.20), leading to the following expression:

$$\frac{\partial \rho h}{\partial t} + \nabla \cdot (\rho \boldsymbol{u} h) = \underbrace{\frac{Dp}{Dt}}_{\text{volume work}} \underbrace{+ \nabla \cdot (\lambda \nabla T)}_{\text{heat conduction}} \underbrace{- \nabla \cdot \left(\rho \sum_{k=1}^{N} h_k Y_k \boldsymbol{V_k} \right)}_{\text{species diffusion}} \underbrace{+ \boldsymbol{\tau} : \nabla \boldsymbol{u}}_{\text{frictional heating}} + \dot{Q}. \tag{2.23}$$

The viscous stress tensor $\boldsymbol{\tau}$ is defined as $\boldsymbol{\tau} = 2\eta \boldsymbol{E}$ and $\boldsymbol{E}$ indicates the strain (2.18). The pressure is now considered additionally with its material derivative. In this work, only the species diffusion, the heat release, as well as the heat conduction are of importance. The remaining terms play a negligible role in the considered low Mach number regime.

2.2 Equations of State

The aforementioned set of conservation equations can not be solved, as the number of unknowns is higher than the number of given equations. Quantities like the pressure p, the viscosity η and the thermal conductivity λ are therefore given as relation of the gas composition, the temperature and the material properties. The assumption of an ideal gas, i.e., molecules with negligible volume and inter-molecular forces, is used in this work and thus for the calculation of the equation of state for the pressure:

$$p = \rho R T \tag{2.24}$$

with ρ and R being the density and the gas constant of the mixture. The gas constant of the mixture is mass weighted and averaged and depends on the universal gas constant R_u, as well as on the species molecular weights W_k and mass fractions Y_k:

$$R = R_u \sum_{k=1}^{N} \frac{Y_k}{W_k} \tag{2.25}$$

The gas mixture viscosity must be averaged with respect to non-monotonical and nonlinear gas mixture behavior following Wilke [244] and Bird et al. [9]:

$$\eta = \sum_{k=1}^{N} \frac{X_k \eta_k}{\sum_{j=1}^{M} X_j \Phi_{kj}} \tag{2.26}$$

$$\Phi_{kj} = \frac{1}{\sqrt{8}} + \left(1 + \frac{W_k}{W_j}\right)^{\frac{1}{2}} \left(1 + \left(\frac{\eta_k}{\eta_j}\right)^{\frac{1}{2}} \left(\frac{W_j}{W_k}\right)^{\frac{1}{2}}\right) \tag{2.27}$$

Due to the computational effort of determining the pure species gas viscosity using detailed kinetic theory equations [78], applying a simpler model is common practice. A popular approach is to make use of the Sutherland law [212], which is a fitting function tailored to follow the natural temperature dependency of the viscosity:

$$\eta = \eta_0 \frac{T_0 + S}{T + S} \left(\frac{T}{T_0} \right)^{\frac{2}{3}} \tag{2.28}$$

Here, η_0 is the reference viscosity at reference temperature T_0, while S denotes the Sutherland fitting constant.
The isobaric heat capacity c_p and the heat conductivity λ of the mixture, are averaged using equations (2.29) and (2.30).

$$c_p = \sum_{k=0}^{N} c_{pk} Y_k \tag{2.29}$$

$$\lambda = \frac{1}{2} \left(\sum_{k=1}^{N} \lambda_k X_k + \left(\sum_{k=1}^{N} \frac{X_k}{\lambda_k} \right)^{-1} \right) \tag{2.30}$$

The pure species isobaric heat capacity c_{pk} is obtained by NASA polynomials [96, 135], whereas the heat conductivity for each species is calculated using kinetic theory expressions [235]. For a given case, gas molecules move with the convection velocity $\boldsymbol{u}$, while pressure propagates with the speed of sound $\boldsymbol{c}$. If the gas velocity is subsonic ($\boldsymbol{u} < \boldsymbol{c}$), pressure changes can propagate with and against the flow, and we talk of an elliptic problem. In the case of a supersonic ($\boldsymbol{u} > \boldsymbol{c}$) flow, pressure changes travel with the velocity and the set of conservation equations become mathematically hyperbolic. The Mach number Ma is defined as the ratio of velocity and speed of sound. The latter depends on the temperature T, the gas constant R and the isentropic exponent $\kappa = c_p / c_v$.

$$Ma = \frac{\boldsymbol{u}}{\boldsymbol{c}} \tag{2.31}$$

$$\boldsymbol{c} = \sqrt{\kappa R T} \tag{2.32}$$

A supersonic flow is characterized by a Mach number greater than unity, while a subsonic flow shows a Mach number below unity. For low Mach number cases, the mentioned set of differential equations become stiff, leading to higher computational costs for solution. To overcome this problem, the solution procedure is changed by applying a pressure correction method (see section 2.5.5).

2.3 Chemistry and Combustion Modeling

At atomic scale, chemical reactions are random collision processes between several reactive molecules resulting in a rearrangement of those in other species towards chemical equilibrium. While molecules are rearranged during that process, atoms (C, H, Si, Fe) are always conserved. Reactions can release or consume energy depending on the difference of enthalpy of formation Δh_k^0 of the reactants and the products (Hess theorem) [236]. A distinction is made between endothermic and exothermic reactions. Combustion is a special case of chemical processes characterized by the dominance of strong exothermic reactions. Combustion processes are complex, as they consist of hundreds of possible reaction steps with many different possible reaction routes and species at various chemical time scales τ_c. Due to the enormous demand of computational resources necessary for solving the resulting set of equations, detailed chemical investigations can only be made for laminar 1D or 2D cases. For turbulent real world cases, applying simplifications like reduced mechanisms or tabulated chemistry are unavoidable. In combustion science, it is common practice to distinguish between premixed and diffusion flames, as the process limiting phenomena are different in both cases.

2.3.1 Non-Premixed Flames

Non-premixed, or diffusion flames represent one fundamental type of combustion. The essential feature of this type of flame is that the oxidizer and fuel enter the combustion chamber separately, and combustion and mixing occur simultaneously. The combustion process is maintained only within a thin mixing zone between oxidizer and fuel, where the flame is fed by diffusive processes. The reaction process itself provides the high gradients necessary to drive the process, as the reactants are consumed within the flame. The process is therefore limited by the time scales of the mixing process. A relatively simple case of a non-premixed flame is the laminar counter-flow-flame configuration shown by figure 2.2.

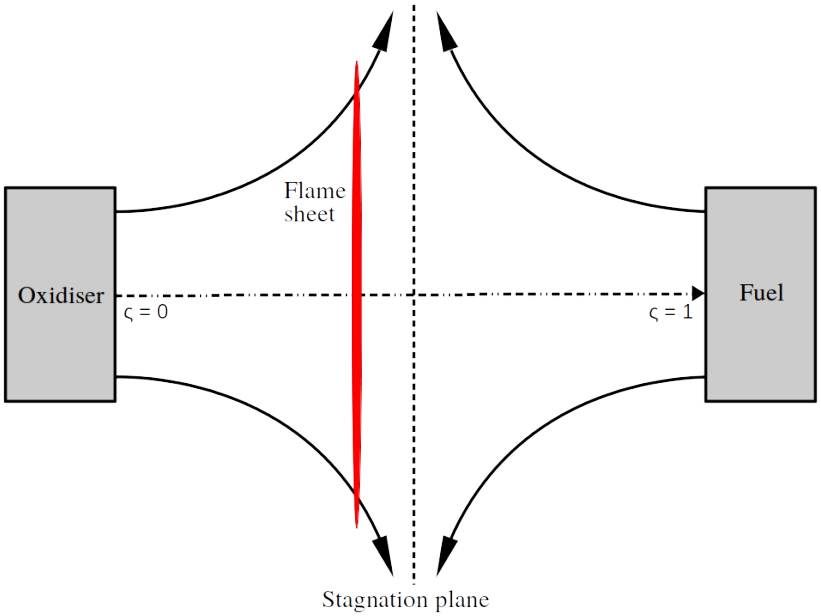

Fig.: 2.2 Sketch of a non-premixed counter flow flame with oxidizer and fuel entering the domain from the left and right, respectively. Equations (2.33) to (2.35) represent the solution along the axis (stagnation streamline). Typically, the flame sheet is shifted towards the oxidizer side in physical space.

Applying some simplifications given by Kee [96], the spatial dependencies can be reduced to one dimension, which represents the solution along the stagnation streamlines. The resulting set of equations are given depending on the axial coordinate z:

$$\frac{d(\rho u)}{dz} + 2\rho V = 0 \tag{2.33}$$

$$\rho u \frac{dV}{dz} + \rho V^2 = \frac{d}{dz}\left(\mu \frac{dV}{dz}\right) - \Lambda \tag{2.34}$$

Where u is the axial velocity, $\Lambda = (1/\rho)\,(\partial p/\partial r) = const.$, and $\rho V = \rho\, v/r = -dU(z)/dz$.

$$\rho u c_p \frac{dT}{dz} = \frac{d}{dz}\left(\lambda \frac{dT}{dz}\right) - \sum_{k=1}^{K} \rho Y_k V_k c_{pk} \frac{dT}{dz} - \sum_{k=1}^{K} h_k W_k \dot{\omega}_k \tag{2.35}$$

$$\rho u \frac{dY_k}{dz} = -\frac{d}{dz}(\rho Y_k V_k) + W_k \dot{\omega}_k \tag{2.36}$$

This simplified flame configuration can be solved for quite large reaction mechanisms in one-dimensional space and is implemented in standard chemical kinetic packages such

as "Cantera" [61]. Since the number of species can become very large and therefore detailed species transport and diffusion can become computationally demanding, a further simplification is commonly used: the assumption of a unity Lewis number.

$$Le = \frac{\lambda}{\rho D c_p} = 1 \tag{2.37}$$

According to this assumption, the diffusivity of all species is equal to the thermal diffusivity and the mixture fraction ζ_i (Eq. 2.38) can be employed to replace the whole set of species transport equations.

$$\zeta_i = \frac{Z_i - Z_i^O}{Z_i^O - Z_i^F} \tag{2.38}$$

$$Z_i = \sum_{j=1}^{N} \mu_{ij} Y_j \qquad i = 1, ..., M \tag{2.39}$$

The element mass fraction Z_i is calculated for any point in physical space, while the superscripts O and F mark the oxidizer and fuel stream composition, which are constant. Further, the matrix μ_{ij} contains the information about the mass fraction of element i in molecule j. As elements do not change during chemical conversion, mixture fractions are conserved scalars and can be reduced to one single quantity ζ ($\zeta_{co} = \zeta_{H_2O} = \zeta$) at $Le = 1$. The simplified set of equations (2.35 to 2.36) are therefore reduced to:

$$T = T(\zeta), \tag{2.40}$$

$$\rho u \frac{d\zeta}{dz} = -\frac{d}{dz}\left(D \frac{d\zeta}{dz}\right). \tag{2.41}$$

It is obvious that the replacement of the gas composition by the mixture fraction only results in the loss of information about the reaction progress. This approach is therefore used, if mixing is the limiting factor of the combustion process, or together with a progress variable C, which will be explained within the following subsection.

2.3.2 Premixed Flames

In premixed combustion, fuel and air are mixed before entering the combustion chamber. Because the fuel and oxidizer molecules are already distributed, this method generally provides a better combustion environment than the non-premixed case. Nevertheless, when gas mixtures become highly reactive (like oxygen-fuel mixtures), premixed combustion processes can be prone to flashback and the aforementioned premixed process is preferred.

In most industrial processes, however, the risk of flashback is relatively low, and premixed flames are therefore the most relevant flame type for industrial gas combustion. When a reactive gas mixture is ignited at a particular point within a volume, a flame propagates from the point of ignition towards the unburned gas mixture. The chemical process takes place within the flame front, converting the reactants to products as the flame front propagates driven by thermal conduction and diffusion. The laminar flame propagation speed s_L is an essential quantity in premixed flame modeling, as it is used for tracking the flame front in mathematical methods like the level-set model [39, 152, 170, 168], or to fix the flame location in one dimensional numerical experiments. The steady planar laminar premixed flame represents the simplest case of premixed flame configurations (Fig. 2.3) and is given by the following set of equations:

$$\rho u = const, \tag{2.42}$$

$$\rho u \frac{dY_k}{dz} = -\frac{d}{dz}(\rho Y_k V_k) + W_k \dot{\omega}_k, \tag{2.43}$$

$$\rho u c_p \frac{dT}{dz} = \frac{d}{dz}\left(\lambda \frac{dT}{dz}\right) - \sum_{k=1}^{K} \rho Y_k V_k c_{pk} \frac{dT}{dz} - \sum_{k=1}^{K} h_k W_k \dot{\omega}_k. \tag{2.44}$$

As the mixture fraction (see subsection 2.3.1) is constant, it is not the limiting factor for the combustion progress of premixed flames and can therefore not be used for tracking the flame progress. In order to overcome this issue, the normalized progress variable c was introduced by Boger et al. [13]:

$$c = \frac{\phi - \phi^u}{\phi^b - \phi^u} \tag{2.45}$$

The variable ϕ given in equation (2.45) represents a quantity of the gas mixture that is crucial for the reaction progress. The quantity is normalized by the valid range between the burned ϕ^b and the unburned ϕ^u state, while variable ϕ can be any species, species combination, or quantity that monotonically in- or decreases as the reaction develops. With the assumption of the mixture fraction being equal at every point, equations (2.43) and (2.44) can be replaced by:

$$\rho u \frac{dc}{dz} = -\frac{d}{dz} \rho^u s_L \left|\frac{dc}{dz}\right|, \tag{2.46}$$

$$T = T(c). \tag{2.47}$$

The temperature becomes a parameter depending on the progress variable only and can be tabulated or fitted by detailed kinetic investigations. Von Oijen, among others, applied this approach as an extension of the basic flamelet model [224, 225] to account for the combustion process in premixed flames.

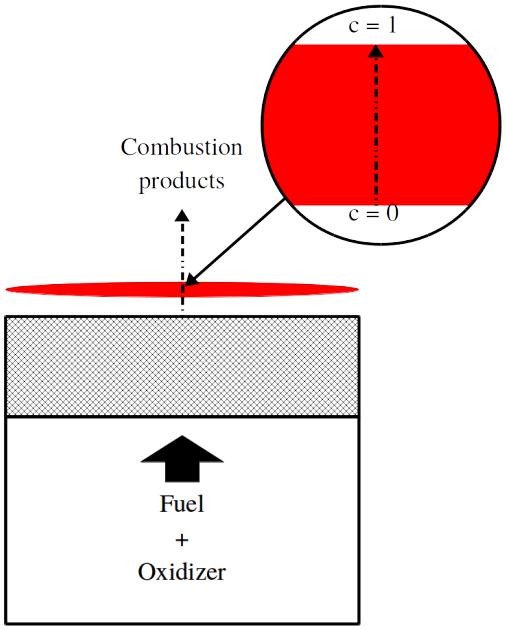

Fig.: 2.3 Sketch of a burner stabilized premixed flat flame, where the flow profile is straightened by a porous matrix (hashed zone). Equations (2.42) to (2.44) represent the mathematical description of the center line. The progress variable increases from a value of 0 (fresh gas) to 1 (exhaust gas) within the flame.

2.3.3 Partially Premixed Flames

In some cases, the flame can not be classified as diffusion or premixed flame due to the variety of conditions occurring during the combustion process. Examples for those kind of flames are spray flames, coal combustion and poorly premixed flames. In those flames, zones of ignitable mixtures exist as well as zones of almost pure oxidizer and fuel. In such cases, applying the simplification shown for pure non-premixed flames (Eq. 2.41) or premixed flames (2.46) is not sufficient, and the assumption that the flame is either mixing or chemically limited does not hold. One solution is extending the flame tracking methods by transporting the mixture fraction and calculating the flame speed based on the local mixture [133]. Another option is to combine the mixture fraction and progress variable approaches and define the dependent quantities as a function of both $\phi(\zeta, c)$, as done by Proch at al. [177–179] by modifying the flamelet generated manifolds model originally developed for premixed combustion.

2.3.4 Gas Phase Reaction Kinetics

Combustion can be described as global one step irreversible reaction. With given species and temperature conditions on the reactant side, the product composition and temperature can be estimated. A complete combustion of methane can therefore be described as:

$$CH_4 + 2\,O_2 \longrightarrow CO_2 + 2\,H_2O. \tag{2.48}$$

This global balance may be sufficient for estimating the released chemical energy and the fuel consumption of a process, but in reality, combustion processes consist of a large series of elementary reactions forming and rearranging intermediate species and radicals. A detailed reaction model for the combustion process of methane, given by the global reaction (2.48) contains more than 1000 reactions and around 100 intermediate species [16]. Other mechanism of more complex fuels can have more than hundreds of thousands of reactions and ten thousands of species [35]. Those complex mechanisms are not practical for any real flame investigation, but are able to predict the chemistry for almost the whole spectrum of conditions, whereas more convenient reduced mechanisms are only valid for a particular – in comparison – small field of conditions and applications. A good example is the 4-Step mechanism for methane combustion proposed by Jones and Linstedt [91], which predicts the exhaust temperature for air combustion close to stoichiometry sufficiently, but fails, as the conditions move further away from that point. For pure methane oxygen combustion, for example, the adiabatic temperature predicted by this mechanism is almost 2000 Kelvin above the true value.

A set of N_r chemical reactions can be expressed in a general form:

$$\sum_{k=1}^{N} \nu'_{rk} \chi_k \rightleftharpoons \sum_{k=1}^{N} \nu''_{rk} \chi_k \qquad r \in \{1...N_r\} \tag{2.49}$$

The variables r, χ_k, ν'_{rk}, and ν''_{rk} denote the index of reaction, the chemical symbol of species k, and the molar stoichiometric coefficient for the reactants and products, respectively. The bidirectional arrow $\rightleftharpoons$ indicates a reversible reaction, accounting for reaction progress in both directions. Further, the rate of reaction r is calculated by the following expression:

$$q_r = k_r^f \prod_{k=1}^{N} [X_k]^{\nu'_{rk}} - k_r^b \prod_{k=1}^{N} [X_k]^{\nu''_{rk}}. \tag{2.50}$$

The molar concentration $[X_k]$ of species k can be calculated from:

$$[X_k] = \rho \frac{Y_k}{W}. \tag{2.51}$$

The forward rate constant k_r^f is obtained by different expressions for three-body reactions, or pressure dependent fall off reactions. The simplest expression is probably the Arrhenius form (Eq. (2.52)), which depends only on the temperature. All other constants, namely the pre-exponential factor A_r, the temperature exponent β_r, as well as the activation energy E_r, are constants given for each reaction r, respectively.

$$k_r^f = A_r T^{\beta_r} \mathrm{e}^{\left(-\frac{E}{RT}\right)} \tag{2.52}$$

The backward reaction constant k_r^b is calculated as the ratio of the forward reaction constant k_r^f and the equilibrium constant K_r^c of reaction r:

$$k_r^b = \frac{k_r^f}{K_r^c} \tag{2.53}$$

An indicator for the direction, in which a reversible reaction r proceeds at a certain temperature and pressure, is the Gibbs-Energy ΔG_r. It is defined as a function of the Gibbs-Energy at standard conditions ΔG_r^0 [96], the universal gas constant R, the temperature T and the reaction quotient Q_r.

$$\Delta G_r = \Delta G_r^0 + RT \ln(Q_r) \tag{2.54}$$

If a reaction is assumed to be in equilibrium, i.e., the forward and backward reactions are equally fast, the Gibbs-Energy ΔG_r becomes 0 and the reaction quotient Q_r represents the pressure equilibrium constant K_r^p:

$$\Delta G_r^0 = -RT \ln(K_r^p) \tag{2.55}$$

The molar and pressure equilibrium constants K_r^c and K_r^p can be related by applying the ideal gas law, where $\Delta\nu = \sum_{k=1}^{N} \nu''_{rk} - \nu'_{rk}$ represents the sum of stoichiometric coefficient differences for products and reactants of species k in reaction r.

$$K_r^p = K_r^c (RT)^{\Delta\nu} \tag{2.56}$$

Substitution of equation (2.56) into equation (2.55) delivers a direct expression for K_r^c:

$$K_r^c = \exp\left(-\frac{\Delta G_r^0}{RT}\right)(RT)^{-\Delta\nu} \tag{2.57}$$

The standard Gibbs-Energy ΔG_r^0 is defined as a function of the standard reaction enthalpy ΔH_r^0 and standard reaction entropy ΔS_r^0, which again, can be calculated as the difference of the species standard enthalpy and entropy given by NASA polynomials:

$$\Delta G_r^0 = \Delta H_r^0 - T\Delta S_r^0 \tag{2.58}$$

The chemical source therm $\dot{\omega}_k$ in molar concentration per time can now be computed as the total molar conversion of species k of all reactions.

$$\dot{\omega}_k = \sum_{r=1}^{N_r}(\nu''_{rk} - \nu'_{rk})q_r \tag{2.59}$$

As explained at the beginning of this section, reaction mechanisms for combustion are usually large and complex, leading to a very large system of equations for calculating q_r. The fact that the involved reactions are acting on strongly different chemical time scales (known as stiff ODE problem), makes the ODE-system difficult to solve. It also leads to the development and application of reduced mechanisms, which are generally less stiff and therefore less problematic to solve. If the combustion chemistry for an application is in general fast in comparison to the mixing time scale, fast chemistry approaches like the basic flamelet model (see section 2.3.5) can be applied, which assume combustion to be limited by mixing phenomena and turbulence. The ratio of physical time scale to chemical time scale, the Damköhler number (Eq. 2.60), is an indicator for such cases: high values reveal that the chemistry is much faster than the mixing, which makes the latter the limiting factor.

$$Da = \frac{\tau_f}{\tau_c} \tag{2.60}$$

For premixed turbulent flames, τ_f is approximated by the ratio of integral length scale l_0 and fluctuation velocity v' (definition in section 2.4), while τ_c is the ratio of laminar flame speed s_L and flame front thickness δ_f, respectively:

$$Da = \frac{l_0 s_L}{\delta_f v'} \tag{2.61}$$

2.3.5 Flamelet Approach

The steady laminar flamelet approach assumes the three dimensional, turbulent flame to consist of infinitesimal thin one dimensional flame structures, which are wrinkled and stretched or squeezed in physical space. According to this theory, complex, real flames can be approximated by a series of one dimensional model flames, when an appropriate coordinate for transformation is given. As discussed before, the mixture fraction is a convenient variable for identification of the reaction location, when a high *Da* number is given – i.e., chemistry is fast. While the flame may be curved and wrinkled in physical space, it is one dimensional in mixture fraction space. The reaction zone can therefore be pre-claculated in a simple counter flow configuration, given by equations (2.34 to 2.36). The location of the flame in mass fraction space can then be computed by (2.38). The relation is shown in figure 2.4.

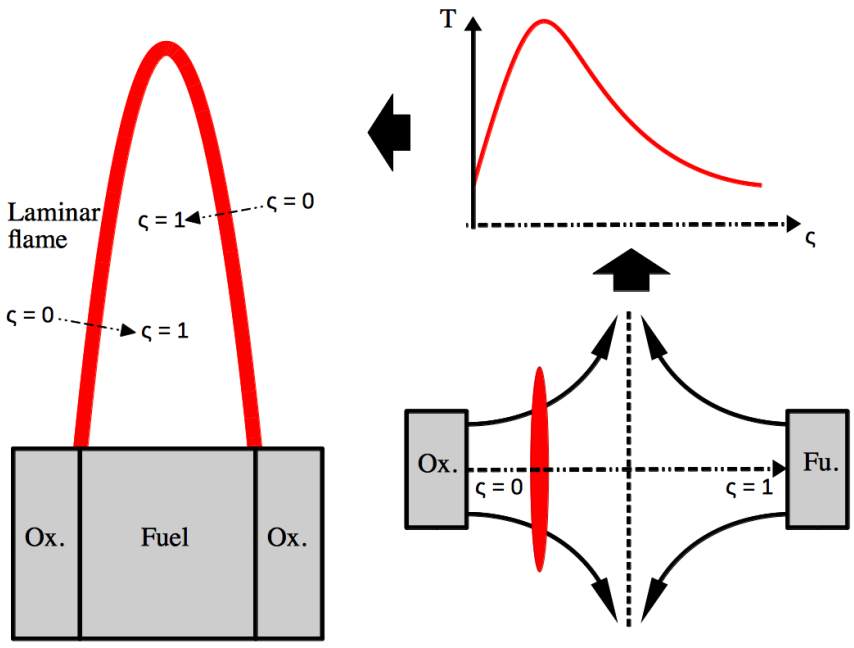

Fig.: 2.4 Concept of the steady laminar flamelet approach for laminar non-premixed flames. The flamelets are precalculated using counter flow model flames in mixture fraction space ζ, which is used to generate thermochemical profiles. The mixture fraction space is then used to map the profiles on the real flame.

The thermochemical data (e.g., species mass fraction, density, temperature, viscosity) can then be tabulated over the mixture fraction and other control variables. This can be the strain rate, the heat loss, and other affecting variables. When turbulence effects are involved,

statistical analysis must be applied and therefore at least one additional control variable is required to account for the probability density function (PDF): the mixture fraction variance ζ''^2. Equations (2.34) to (2.36) are transformed to mixture fraction space according to Peters [166, 167], leading to expressions (2.62) and (2.63) for describing the flamelet:

$$\rho\frac{\chi}{2}\frac{\partial^2 T}{\partial\zeta^2}+\sum_{k=1}^{K}\frac{h_k}{c_p}\dot{\omega}_k=0 \tag{2.62}$$

$$\rho\frac{\chi}{2}\frac{\partial^2 Y_k}{\partial\zeta^2}+\dot{\omega}_k=0 \tag{2.63}$$

The scalar dissipation in the mixture fraction space can be approximated by [168]:

$$\chi=\chi_{st}\frac{f(\zeta)}{f(\zeta_{st})} \tag{2.64}$$

Where χ_{st} and ζ_{st} are the scalar dissipation rate (which replaces the strain rate for tabulation) and the mixture fraction at stoichiometric conditions. A modified version of this method, where reaction progress is accounted by radiative heat loss, is applied by Wollny et al. [248].

2.4 Turbulence Modeling

In laminar flows, viscous forces are capable of damping the flow motion in such a way that the flow field looks smooth, directed and in many cases even steady. When the momentum of a flow field becomes strong enough to overcome the viscous damping, the flow field begins to fluctuate in a pseudo-random manner, forming eddies of different sizes (length scales). Within the size spectrum, the biggest eddies are geometry dependent, whereas the smaller eddies are isotropic. The Reynolds number *Re* describes the ratio of inertia to viscous forces and as such, it is a measure for the level of turbulence for a particular geometry. Many experiments have been performed in order to quantify the Reynolds numbers for the transition from laminar to turbulent flow regime for different geometries. The probably most acquainted example by Reynolds is the flow within a straight tube, where the transition region begins at a Reynolds number of about 2300. The Reynolds number is written as:

$$Re=\frac{\overline{u}L\rho}{\eta}, \tag{2.65}$$

where $\bar{u}$ is the mean flow velocity and L a characteristic length of the geometry. The latter differs from case to case: for the aforementioned straight tube, it is defined as the diameter, whereas in other cases, it may be the width of a plate or the gap distance between two plates.

Generally, turbulence is defined as pseudo-random fluctuation (here pseudo stating that turbulence is theoretically fully predictable but the required resolution being hard to achieve) of the flow field and all transported quantities, of which decomposition to their mean $\bar{\phi}$ and fluctuating value ϕ' has been suggested by Reynolds.

$$\phi = \overline{\phi} + \phi' \tag{2.66}$$

The intensity of turbulence I can then be defined as the ratio of root-mean-square (RMS) of the fluctuating part and its mean value of the velocity u:

$$I = \frac{\sqrt{\overline{u'^2}}}{\overline{u}} \tag{2.67}$$

A value of 0 means that the velocity is equal to its mean part and hence laminar, whereas values up to 5% denote a turbulent flow and higher values characterize a highly turbulent flow. As mentioned before, turbulence can be described as a spectrum of differently sized eddies, the so-called turbulent cascade [107, 183].Depending on the wave number k, it can be represented by the turbulent energy function $E(k)$ [172], as shown in Fig. 2.5. According to the theory, the largest, just produced eddies of integral scale l_0 contribute the most energy to the spectrum, while the energy contained by smaller eddies decreases with a logarithmic slope of $-5/3$ within the inertial subrange. As larger eddies break into smaller eddies, energy is transferred from the large to the small scales in the turbulent spectrum. This trend is continued, until the Kolmogorov scale η_K is reached, and the small eddies are not strong enough to resist the viscous forces. Hence, within the viscous subrange, the smallest eddies are rapidly dissipated to thermal energy. To clarify this relation, a Reynolds number for the turbulent scales, as shown in Eq. (2.68), can be used.

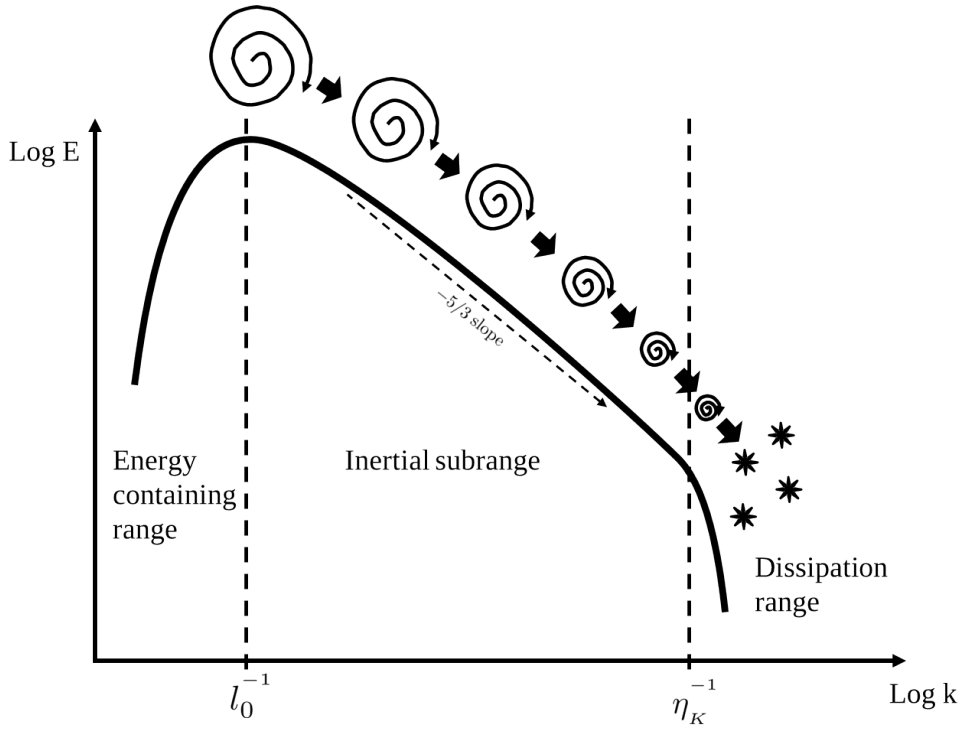

Fig.: 2.5 Sketch of the turbulent spectrum as energy function $E(k)$ over the wave number k. The energy containing eddies are born near the integral length scale l_0 and decay to smaller eddies within the inertial subrange. This process continues with an exponential slope of $-5/3$ until the energy of the smallest eddies dissipate to thermal energy when the Kolmogorov scale η_K is reached.

$$Re(l) = \frac{u'(l)l}{\nu} \tag{2.68}$$

Here, $u'(l)$ denotes the characteristic velocity of the turbulent structure with size l and ν is the kinematic viscosity. One can estimate that lager eddies have higher values of $Re(l)$ and are therefore mainly affected by inertia, while small eddies are damped and dissipated by viscous effects. The Reynolds number can also be defined as a function of the integral length l_0 scale and integral scale fluctuation u', which by definition is the turbulent Reynolds number:

$$Re_t = \frac{u'l_0}{\nu} \tag{2.69}$$

The Kolmogorov scale η_K, is defined as:

$$\eta_K = \left(\frac{\nu^3}{\epsilon}\right)^{1/4}. \tag{2.70}$$

Here ϵ is the dissipation rate, which is defined as the energy flux from one scale to the next smaller scale and is constant within the inertial subrange:

$$\epsilon = \frac{u'(l)^3}{l} = \frac{u'^3}{l_0} \tag{2.71}$$

The Kolmogorov length scale η_K is located at the transition point, where viscous forces start outweighing inertia. At this point, viscous forces are equal to inertia and hence, the Reynolds number for the Kolmogorov length scale $Re(\eta_K)$ must be unity:

$$Re_K = \frac{u'_K \eta_K}{\nu} = 1 \tag{2.72}$$

Due to the constant decreasing slope within the inertial subrange of the energy spectrum (Eq. 2.71), the ratio of the integral and Kolmogorov length scales can be expressed in terms of the turbulent Reynolds number:

$$\frac{l_t}{\eta_K} = \frac{u'/\epsilon}{(\nu^3/\epsilon)^{1/4}} = Re_t^{3/4} \tag{2.73}$$

As mentioned above, turbulence increases the width of the mixing layer and therefore has a mixing character, which can be understood as increased diffusion. Moreover, the flame surface expands through wrinkling caused by turbulent instabilities, resulting in faster and shorter combustion. Experiments conducted by Gülder [70] on premixed flames revealed a relationship indicating that under highly turbulent conditions – or low s_L, the turbulent flame speed s_t becomes nearly independent of the laminar propagation speed s_L.

$$s_t \approx s_L + u' \tag{2.74}$$

Hottel and Hawthorne [80] compared the flame lengths of premixed flames with different turbulence levels and observed an equal flame length for all turbulent flames, which were shorter as the flames within the laminar and transition region. Since turbulence was increased together with the mass flow rate, increasing the level of turbulence must go hand in hand with an acceleration of the turbulent flame speed s_t. Hottel and Hawthorne also observed that with further increasing turbulence, the flame lifts off from the nozzle, until it completely blows off, when the flow speed is too high for the flame to stabilize. It can be therefore concluded that the turbulence is a crucial factor for combustion scenarios and therefore must be modeled carefully.

Another important quantity for turbulent, reactive cases is the Schmidt number Sc, which

determines how the transported scalars and the velocity field are related in terms of diffusion:

$$Sc = \frac{\nu}{D} \tag{2.75}$$

A Schmidt number smaller than unity $Sc < 1$ for example indicates that scalar gradients are faster smoothed than velocity fluctuations. The Schmidt number for gas flows is usually around one $Sc_g \approx 1$, while high Schmidt numbers are common for liquid flows ($Sc_l \approx 1000$). The scale, at which molecular diffusion starts compensating the gradients of the scalar field is given by the Batchelor scale λ_B. Analogues to the Kolmogorov length scale, it determines the transition to the small scales, which rapidly decay due to scalar (mass) diffusion. For gas flows with $Sc \approx 1$, the Batchelor scale is similar to the Kolmogorov scale $\eta_K \approx \lambda_B$. The Bachelor scale is defined as follows:

$$\lambda_B = \frac{\eta_K}{\sqrt{Sc}} \tag{2.76}$$

For the modeling of turbulent combustion processes in the frame of CFD many levels of modeling – measured by the resolution of the turbulent spectrum – have been established within the last decades. A popular classification is to distinguish between three approaches: Reynolds Averaged Navier-Stokes Simulation (RANS), Large Eddy Simulation (LES), Direct Numerical Simulation (DNS). The approaches are briefly introduced in table 2.1 and will be explained in the following subsections. Figure 2.6 clarifies resolution of the mentioned models within the turbulent energy spectrum, which has been discussed before. The models will be briefly discussed in the following subsections. For further details about turbulence and turbulence chemistry interaction, the reader is referred to Hinze [77], Pope [172], and Lesieur [123].

Reynolds Averaged Navier-Stokes Simulation (RANS)	Completely modeled turbulent spectrum and computation of the temporal averaged flow field
Large Eddy Simulation (LES)	Resolves large and energy rich fluctuations, whereas the small scales are modeled
Direct Numerical Simulation (DNS)	Resolves entire turbulent spectrum above the Kolmogorov length scale

Table 2.1 Different levels of turbulence modeling in CFD simulations.

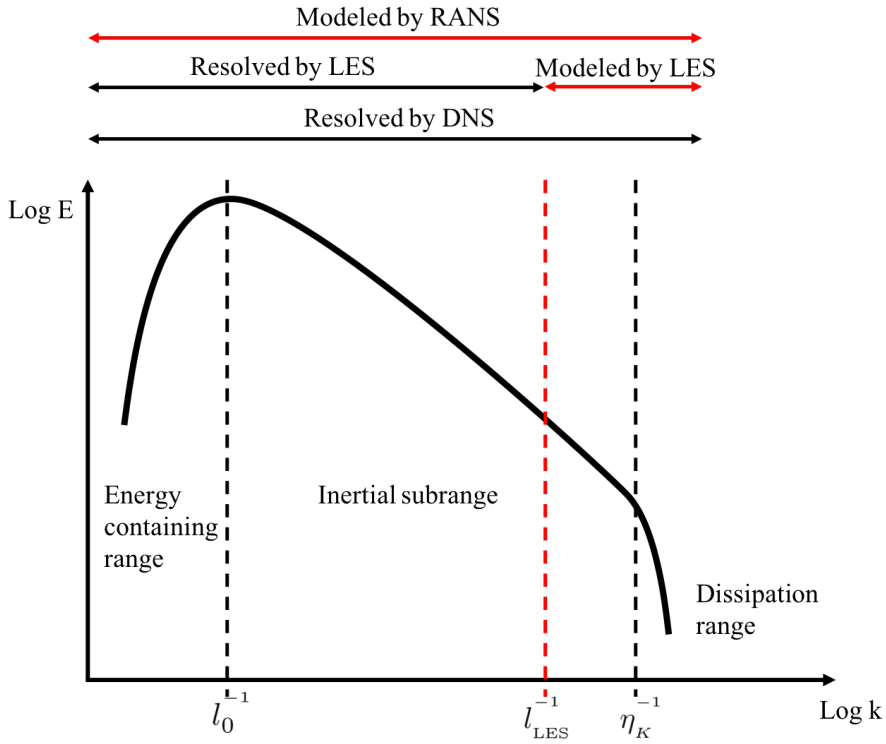

Fig.: 2.6 Areas of the turbulent spectrum modeled by the different approaches. The cut off length scale of the LES approach is denoted by l_{LES}^{-1}, it illustrates the border between the resolved "large scales" and the modeled "small scales" in a LES.

2.4.1 Reynolds Averaged Navier-Stokes (RANS)

Typical RANS simulations solve the balance equations for the time averaged transported quantities. In constant density flows Reynolds averaging is applied, where any fluctuating quantity is split into a mean and fluctuation part (i.e. $\phi = \overline{\phi} + \phi'$). In flows with variable density, however, this leads to unclosed and difficult to handle correlations like $\overline{\rho'\phi'}$. To overcome this problematic, the density weighted Favre average is usually applied in reactive flows [42]:

$$\widetilde{\phi} = \frac{\overline{\rho\phi}}{\overline{\rho}} \tag{2.77}$$

Like in the Reynolds averaging (Eq. (2.66)), any variable can be split into its Favre average and fluctuation:

$$\phi = \widetilde{\phi} + \phi'' \tag{2.78}$$

where also in this case, the fluctuation average is zero $\widetilde{\phi''} = 0$. Substituting the Favre averaged variables into the conservation equations mentioned in section 2.1 (neglecting extra source terms) leads to the following set of balance equations for the mass (2.79), species (2.80),

momentum (2.81) and sensible (2.82) inner energy:

$$\frac{\partial \overline{\rho}}{\partial t} + \nabla \cdot (\overline{\rho}\widetilde{\boldsymbol{u}}) = 0 \tag{2.79}$$

$$\frac{\partial \overline{\rho}\widetilde{Y}_k}{\partial t} + \nabla \cdot (\overline{\rho}\widetilde{\boldsymbol{u}}\widetilde{Y}_k + \overline{\boldsymbol{V}_k Y_k} + \overline{\rho}\widetilde{\boldsymbol{u}''Y_k''}) = \overline{\dot{\omega}}_k \qquad k \in \{1, ..., N\};\ k, N \in \mathbb{Z} \tag{2.80}$$

$$\frac{\partial \overline{\rho}\widetilde{\boldsymbol{u}}}{\partial t} + \nabla \cdot (\overline{\rho}\widetilde{\boldsymbol{u}}\widetilde{\boldsymbol{u}} - \overline{\boldsymbol{T}} + \overline{\rho}\widetilde{\boldsymbol{u}''\boldsymbol{u}''}) = 0 \tag{2.81}$$

$$\frac{\partial \overline{\rho}\widetilde{e}_s}{\partial t} + \nabla \cdot \left(\overline{\rho}\widetilde{\boldsymbol{u}}\widetilde{e}_s - \overline{(\lambda \nabla T)} + \overline{\rho \sum_{k=1}^{N} h_{s,k} Y_k \boldsymbol{V_k}} + \overline{\rho}\widetilde{\boldsymbol{u}'' e_s''} \right) = -\sum_{k=1}^{N} \overline{\dot{\omega}}_k \Delta h_{f,k}^0 + \overline{\boldsymbol{T} : \nabla \boldsymbol{u}} \tag{2.82}$$

Obviously, this set of equations ((2.79) to (2.82)) also contain unclosed fluctuation terms, which require the knowledge, or an assumption of the turbulent field. In RANS, the modeling of Reynolds stresses $\widetilde{\boldsymbol{u}''\boldsymbol{u}''}$ is of main importance. The basic assumption for their modeling was proposed by Boussinesq [77, 123, 172, 217], interpreting their influence as a viscous damping of the local velocity fluctuations, similar to the viscous tensor τ, but scaled by the turbulent dynamic viscosity η_t. It reads:

$$\overline{\rho}\widetilde{u_i'' u_j''} = -\eta_t \left(\frac{\widetilde{u}_i}{x_j} + \frac{\widetilde{u}_j}{x_i} - \frac{2}{3}\delta_{i,j} \frac{\partial \widetilde{u}_k}{x_k} \right) + \frac{2}{3}\overline{\rho} k, \tag{2.83}$$

with the turbulent kinetic energy k defined as:

$$k = \frac{1}{2} \sum_{k=1}^{3} \widetilde{u_k'' u_k''}. \tag{2.84}$$

The estimation of the turbulent viscosity η_t is task of the so called eddy viscosity turbulence models, which act as a closure and can roughly be categorized in three types, depending on the number of equations used by the model (table 2.2). The turbulent scalar fluxes $\widetilde{\boldsymbol{u}''\phi''}$ are generally modeled using the gradient assumption:

$$\overline{\rho}\widetilde{u_i'' \phi''} = -\frac{\eta_t}{Sc_k^t} \frac{\partial \widetilde{\phi}}{\partial x_i} \tag{2.85}$$

The variable Sc^t is the turbulent Schmidt number of scalar ϕ. The laminar diffusion and heat conduction are in general neglected due to their minor influence in turbulent gas flows. Nevertheless, those terms can be modeled using the averaged mean diffusion coefficient $\overline{D_k}$ and averaged thermal diffusivity $\overline{\lambda}$.

$$\overline{V_{k,i}Y_k} = \overline{-\rho D_k \frac{\partial Y_k}{\partial x_i}} \approx -\overline{\rho}\overline{D}_k \frac{\partial \widetilde{Y}_k}{\partial x_i} \tag{2.86}$$

$$\overline{\lambda \frac{\partial T}{\partial x_i}} = \overline{\lambda} \frac{\partial \widetilde{T}}{\partial x_i} \tag{2.87}$$

Zero equation (algebraic) models	Prandtl mixing length model [174]
One equation models	Prandtl-Kolmogorov model [171], Spalart-Allmaras model [208]
Two equation models	k-ϵ model [90, 91], k-ω model [242, 243], k-ω SST model [143–145]

Table 2.2 Examples for different categories of RANS closures.

The closures mentioned in table 2.2 assume isotropy of all eddies in the turbulent spectrum, which is not accurate, but in many cases an acceptable model error and computationally more stable and affordable compared to anisotropic closures like the Reynolds stress model (RSM) [117]. Probably the most popular RANS turbulence model is the k-ϵ model, a two-equation model developed by Jones and Lauder [90], which approximates the turbulent viscosity in dependency of the model constant C_η as:

$$\eta_t = \overline{\rho} C_\eta \frac{k^2}{\epsilon}. \tag{2.88}$$

The turbulent kinetic energy k and the dissipation rate ϵ are conserved by two balance equations:

$$\frac{\partial \overline{\rho} k}{\partial t} + \nabla \cdot \left(\overline{\rho} \widetilde{\boldsymbol{u}} k - \left(\eta + \frac{\eta_t}{\sigma_k} \right) \frac{\partial k}{\partial \boldsymbol{x}} \right) = P_k - \overline{\rho}\epsilon \tag{2.89}$$

$$\frac{\partial \overline{\rho} \epsilon}{\partial t} + \nabla \cdot \left(\overline{\rho} \widetilde{\boldsymbol{u}} \epsilon - \left(\eta + \frac{\eta_t}{\sigma_\epsilon} \right) \frac{\partial \epsilon}{\partial \boldsymbol{x}} \right) = C_{\epsilon 1} \frac{\epsilon}{k} P_k - C_{\epsilon 2}, \overline{\rho} \frac{\epsilon^2}{k} \tag{2.90}$$

The first terms on the RHS of the equations are responsible for the production and the second terms for the destruction of k and ϵ, respectively. The part P_k is given by:

$$P_k = -\overline{\rho}\widetilde{u_i'' u_j''}\frac{\partial \widetilde{u}_i}{\partial x_j}. \tag{2.91}$$

Here, $\overline{\rho}\widetilde{u_i'' u_j''}$ is modeled by equation 2.83, whereas the model constants, suitable for the most flow situation, are:

C_η	σ_k	σ_ϵ	$C_{\epsilon 1}$	$C_{\epsilon 2}$
0.09	1.0	1.3	1.44	1.92

Table 2.3 Model constants for the k-ϵ model.

Important variables like the integral and Kolmogorov length scales l_0 and η_K can be calculated by substituting the model quantities into their general definitions (2.71) and (2.70):

$$l_0 = \frac{k^{3/2}}{\epsilon} \tag{2.92}$$

$$\eta_K = C_\eta^{3/4}\frac{k^{3/2}}{\epsilon} \tag{2.93}$$

The k-ϵ model and many other two equation models mentioned in table 2.1 have been proven to perform very well in many highly turbulent flows, which are relevant for the industry. However, the simplicity and assumption of isotropic turbulence let them fail in cases with large and complex extra strain, as found in swirling flows or non-circular ducts. Further, the temporal averaged information about flow quantities are not sufficient for the prediction of some source terms, which highly depend on mixing conditions. In reactive flows, the averaged reaction source term $\overline{\dot{\omega}}$ strongly depends on the so called local unmixedness of the reacting species. Its' modeling therefore requires case dependent assumptions, which are not universal and should therefore be applied with caution.

2.4.2 Large Eddy Simulation (LES)

According to the discussed issues regarding RANS simulations and the reaction source term $\overline{\dot{\omega}}$, it can be concluded that reliable predictions of the reactive flow field require at least temporal resolution of the major fluctuations. LES is an option to achieve this goal without the computational cost of resolving all scales within a DNS. For this purpose, the transported quantities are low-pass filtered in the case of explicit filtering (either in spectral or physical

space), while the effect of smaller scales (or higher wave numbers) is approximated by sub scale models. A Favre filtered variable $\widetilde{\phi}$ is defined as:

$$\overline{\rho}\widetilde{\phi}(\boldsymbol{x}) = \int \rho\phi(\boldsymbol{x}')G(\boldsymbol{x}-\boldsymbol{x}',\Delta)d\boldsymbol{x}'. \tag{2.94}$$

Here, $\widetilde{\phi}(\boldsymbol{x})$ and $\phi(\boldsymbol{x}')$ indicate the filtered and unfiltered quantities, whereas $G(\boldsymbol{x}-\boldsymbol{x}',\Delta)$ denotes the filter function depending on the filter cutoff width Δ. The filtering is either done explicitly with a given shape of a filter function, or implicitly by damping the small scales using a subgrid scale viscosity ν_t, which depends on the filter width Δ and is defined by the subgrid model. In the context of implicit filtering, examples of filters that can be used for $G(\boldsymbol{x}-\boldsymbol{x}',\Delta)$ are the cutoff filter (Equation 2.95), box filter (Equation 2.96), and Gaussian filter (Equation 2.97). However, it's important to note that for the application of explicit filtering in LES, there are more suitable filters that are widely discussed in the literature.

$$G(\boldsymbol{x}-\boldsymbol{x}',\Delta) = \prod_{i=1}^{3} \frac{\sin[x_i - x_i'/\Delta]}{(x_i - x_i')} \tag{2.95}$$

$$G(\boldsymbol{x}-\boldsymbol{x}',\Delta) = \begin{cases} 1/\Delta^3 & |\boldsymbol{x}-\boldsymbol{x}'| \leq \Delta/2 \\ 0 & |\boldsymbol{x}-\boldsymbol{x}'| > \Delta/2 \end{cases} \tag{2.96}$$

$$G(\boldsymbol{x}-\boldsymbol{x}',\Delta) = \left(\frac{6}{\pi\Delta^2}\right)\exp\left(-6\frac{|\boldsymbol{x}-\boldsymbol{x}'|^2}{\Delta^2}\right) \tag{2.97}$$

However, explicit filters are rarely used in LES, which is why implicit filters play a predominant role.

Similar to the equations for RANS, the governing equations have to be filtered with respect to the density, leading to the following set of equations for the Favre filtered mass (2.98), species (2.101), momentum (2.99) and energy (2.100):

$$\frac{\partial\overline{\rho}}{\partial t} + \nabla\cdot(\overline{\rho}\widetilde{\boldsymbol{u}}) = 0 \tag{2.98}$$

$$\frac{\partial\overline{\rho}\widetilde{\boldsymbol{u}}}{\partial t} + \nabla\cdot\left(\overline{\rho}\widetilde{\boldsymbol{u}}\widetilde{\boldsymbol{u}} - \overline{\boldsymbol{T}} + \overline{\rho}(\widetilde{\boldsymbol{u}\boldsymbol{u}} - \widetilde{\boldsymbol{u}}\widetilde{\boldsymbol{u}})\right) = 0 \tag{2.99}$$

$$\frac{\partial \overline{\rho}\widetilde{e_s}}{\partial t} + \nabla \cdot \left(\overline{\rho}\widetilde{\boldsymbol{u}}\widetilde{e_s} - \overline{(\lambda \nabla T)} + \overline{\rho \sum_{k=1}^{N} h_{s,k} Y_k \boldsymbol{V_k}} + \overline{\rho}(\widetilde{\boldsymbol{u}e_s} - \widetilde{\boldsymbol{u}}\widetilde{e_s}) \right) = -\sum_{k=1}^{N} \overline{\dot{\omega}}_k \Delta h^0_{f,k} + \overline{\boldsymbol{T} : \nabla \boldsymbol{u}} \tag{2.100}$$

$$\frac{\partial \overline{\rho}\widetilde{Y_k}}{\partial t} + \nabla \cdot \left(\overline{\rho}\widetilde{\boldsymbol{u}}\widetilde{Y_k} + \overline{\boldsymbol{V}_k Y_k} + \overline{\rho}\left(\widetilde{\boldsymbol{u}Y_k} - \widetilde{\boldsymbol{u}}\widetilde{Y_k} \right) \right) = \overline{\dot{\omega}}_k \qquad k \in \{1, ..., N\};\ k, N \in \mathbb{Z} \tag{2.101}$$

Here, the unresolved filtered diffusive fluxes are modeled applying Fick's law:

$$\overline{V_{k,i} Y_k} = \overline{-\rho D_k \frac{\partial Y_k}{\partial x_i}} \approx -\overline{\rho}\overline{D}_k \frac{\partial \widetilde{Y}_k}{\partial x_i} \tag{2.102}$$

$$\overline{\lambda \frac{\partial T}{\partial x_i}} = \overline{\lambda} \frac{\partial \widetilde{T}}{\partial x_i} \tag{2.103}$$

The same approach is applied for the filtered scalar fluxes for species $(\widetilde{\boldsymbol{u}Y_k} - \widetilde{\boldsymbol{u}}\widetilde{Y_k})$ and internal energy $(\widetilde{\boldsymbol{u}e_s} - \widetilde{\boldsymbol{u}}\widetilde{e_s})$, which are generalized as $(\widetilde{\boldsymbol{u}\phi} - \widetilde{\boldsymbol{u}}\widetilde{\phi})$ here:

$$\widetilde{\boldsymbol{u}\phi} - \widetilde{\boldsymbol{u}}\widetilde{\phi} = -\frac{\nu_t}{Sc_k^t} \frac{\partial \widetilde{\phi}}{\partial x_i} \tag{2.104}$$

Similar as the Reynolds stress closure for RANS, a number of Reynolds stress sub filter models exist in order to approximate the $(\widetilde{\boldsymbol{u}\boldsymbol{u}} - \widetilde{\boldsymbol{u}}\widetilde{\boldsymbol{u}})$ term and calculate the sub filter viscosity for implicit filtering. The most commonly used model is the Smagorinsky subgrid model [206] due to its robustness and efficiency. It models the unresolved fluxes according the Boussinesq assumption. For variable density fluxes, the subgrid stresses are closed in the Smagorinsky model by means of an eddy viscosity approach:

$$\overline{\rho}(\widetilde{u_i u_j} - \widetilde{u}_i \widetilde{u}_j) = \frac{1}{3}\delta_{ij}\mathcal{T}_{kk} - 2\eta_t \left(\widetilde{S}_{ij} - \frac{1}{3}\delta_{ij}\widetilde{S}_{kk} \right) \tag{2.105}$$

The Favre filtered strain $\widetilde{S}_{ij}$ is calculated as:

$$\widetilde{S}_{ij} = \frac{1}{2}\left(\frac{\partial \widetilde{u}_i}{\partial x_j} + \frac{\partial \widetilde{u}_j}{\partial x_i} \right) \tag{2.106}$$

The subgrid scale viscosity η_t is given by:

$$\eta_t = \overline{\rho}(C_S \Delta)^2 \left(2\widetilde{S}_{ij}\widetilde{S}_{ij} \right)^{1/2} \tag{2.107}$$

The isotropic subgrid Reynolds stress contribution $\mathcal{T}_{kk}$ corresponds to a normal stress and is therefore solved implicitly together with the pressure for incompressible flows. For compressible cases it is generally modeled following Yoshizawa [254]:

$$\mathcal{T}_{kk} = 2\overline{\rho} C_I \Delta^2 \left(2\widetilde{S}_{ij}\widetilde{S}_{ij}\right)^{1/2} \tag{2.108}$$

The equations (2.107) and (2.108) are similar approaches, differing in the definition of the model constants C_S and C_I. Germano et al. [55] developed a more universal definition of C_S, introducing a test filter (larger than Δ) procedure, in order to optimize C_S depending on the resolved inertial subrange of the turbulent spectrum. The Smagorinsky model is known to overpredict the turbulent subgrid fluxes. As a result, it dampens the turbulence fluctuations too much in high strain rate regions. This weakness of the Smagorinsky model motivated the development of model variants, such as Vreman [229] and Nicoud et al.'s [154], which have similar weaknesses because they are based on the Boussinesq hypothesis.A modeling approach featuring a less dissipative nature but higher a-posteriori instability are the scale-similarity models, which project the energy transfer from the resolved onto the unresolved scales. Since they are usually formulated as a deconvolution of the LES filter operation, they provide a mathematically founded description of the subgrid stresses. Stabilization approaches for these models exist and manage to overcome the instability problems while maintaining the high accuracy [102, 84, 138].

2.4.3 Direct Numerical Simulation (DNS)

According to the previous subsections, turbulence modeling is applied to reduce the computational effort, i.e. the grid resolution to resolve the fine turbulent structures, while the effect of the unresolved turbulent structures is added to the resolved flow field. In order to verify those models, detailed direct simulations are mandatory. DNS do not apply any modeling and therefore allow the comparison with turbulence models used in less resolved simulations. The computational effort depends on the flow conditions and can be estimated assuming the smallest structure to be resolved within the grid in the order of the Kolmogorow length scale, whereas the domain must at least enclose one integral length scale to prevent the solution from numerical artifacts. Substituting the necessary grid size $\Delta \leq \eta_K$ into equation (2.73) allows the estimation of numerical grid points in one dimension:

$$\frac{l_0}{\Delta} \geq \frac{l_0 u'}{\nu} = Re_t^{3/4} \tag{2.109}$$

Consequently, for an equidistant grid the total number of grid points in time and space is $N_p \approx (Re_t^{3/4})^4 = Re_t^3$. This requirement of a DNS with respect to the turbulent Reynolds number is a clear indication that this type of simulation is only affordable for small-scale numerical studies. Turbulence modeling, as it is used in RANS and LES, will continue to be necessary in the future for industrial applications.
For DNS including combustion, an additional requirement is to sufficiently resolve the flame front within the simulation domain. Poinsot et al. [171] suggest a resolution of $Q = 20$ points for the flame thickness δ_L^0 as requirement to resolve the inner structure of the flame. This means, that the total domain size for a given number of grid points (in one direction) is restricted to $L \approx (N/Q)\delta_L^0$. This requirement extends the non reactive one (2.109) to:

$$\frac{l_0}{\delta_L^0} < \frac{L}{\delta_L^0} < \frac{N_p}{Q}. \tag{2.110}$$

A good example for the massive computational effort which is necessary to satisfy the requirements is the DNS of a hydrocarbon flame with an assumed flame thickness of $\delta_L^0 = 0.5$ mm. Even a simulation with a grid of 1024^3 points (1.07 billion), which is currently only possible on super computers, the requirement (Eq. 2.110) for the resolution only allows for a domain size of around 25 mm. Nevertheless, motivated by the variety of information which can be obtained by 3D DNS simulations – especially if they include complex chemistry turbulence interaction – numerically extensive DNS have been performed and published, for example by Thévenin [218], Chen et al. [23, 22], or Bisetti et al. [10].

2.5 Numerical Methods

2.5.1 Finite Volume Method

A broad band of discretization procedures for partial differential equation are established in science and industry for different applications. While the finite element method (FEM) is a popular tool in structural mechanics, the finite volume method is the by far most utilized method for spatial discretization in the field of fluid mechanics. The transport equation for any intensive (volume based) quantity ϕ can be described as:

$$\frac{\partial}{\partial t}\int_V \phi dV + \int_V \nabla\cdot(\boldsymbol{u}\phi)dV = \int_V \nabla\cdot\boldsymbol{j}_\phi dV + \int_V \dot{\omega}_\phi dV + \int_V \Gamma_\phi dV. \tag{2.111}$$

The diffusive flux $\boldsymbol{j}_\phi$ is given by $\boldsymbol{j}_\phi = \rho D_\phi \nabla\phi$. The divergence terms $(\nabla\cdot)$ within the covering equations of the form mentioned above can be converted to surface integrals of a control

volume (CV) using the Gauss theorem:

$$\int_V \nabla \cdot \boldsymbol{f}\, dV = \oint_S \boldsymbol{f} \cdot \boldsymbol{n} dS \tag{2.112}$$

The vector $\boldsymbol{n}$ is the surface normal of the respective surface, which is directed outwards the CV and parallel to one of the orientation vectors $(\boldsymbol{i}, \boldsymbol{j}, \boldsymbol{k})$ in the case of orthogonal grids. Substituting the divergence containing terms in equation (2.111) by surface integrals, we obtain:

$$\frac{\partial}{\partial t}\int_V \phi dV + \oint_S (\boldsymbol{u}\phi)\cdot \boldsymbol{n} dS = \oint_S \boldsymbol{j}_\phi \cdot \boldsymbol{n} dS + \int_V \dot{\omega}_\phi dV + \int_V \Gamma_\phi dV. \tag{2.113}$$

In the frame of the finite volume method, the control volumes have plane surfaces, whereas the number of surfaces and the control volume shape is not limited to any form. Nevertheless, the most common CV shape is hexahedral or tetrahedral, while the mathematically simplest form is the cubic CV. For this reason, the numerical schemes are explained for this type of CV here. When Δ denotes the constant grid width, the calculation of surface area and volume is trivial and given by $S_\sigma = S = \Delta^2$ and $V = \Delta^3$. Figure 2.7 shows the alignment of such a grid

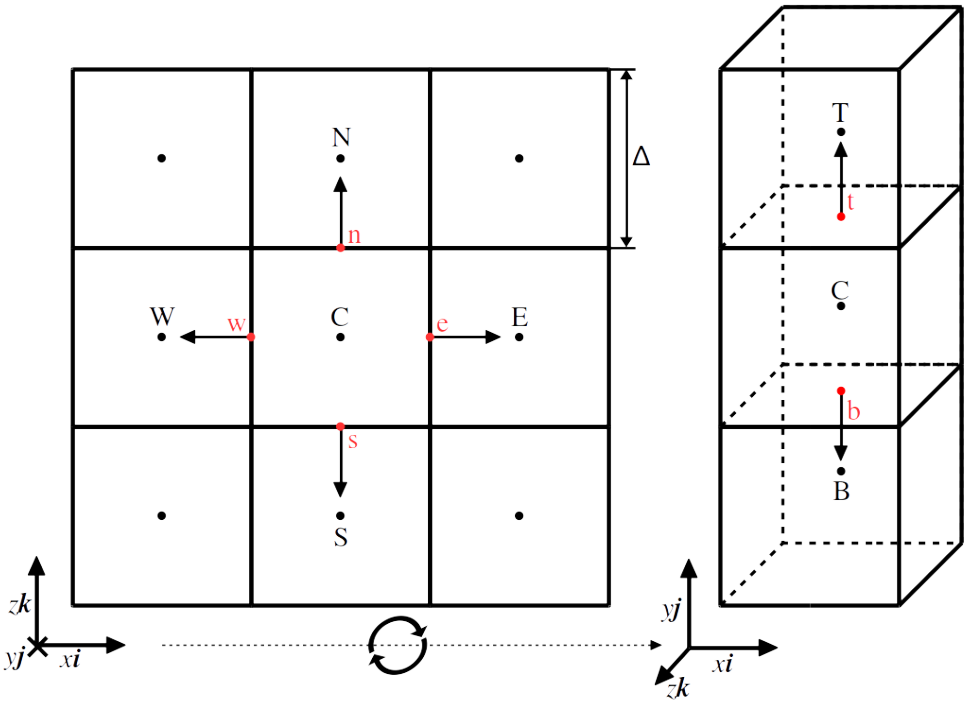

Fig.: 2.7 Sketch of the cubic grid used for illustration of the discretization of a fluid volume.

within a canonical coordinate system, where the coordinates x, y, z run along the orientation vectors $\boldsymbol{i}, \boldsymbol{j}, \boldsymbol{k}$, respectively. The terminology applied for the spatial arrangement in figure 2.7 (north, east, south, west, top, bottom) will be continuously used in this chapter to explain the numerical schemes for interpolation and spatial derivatives. Capitalized characters (N, E, S, W, T, B) indicate the neighbor cells, while their lowercase equivalents (n, e, s, w, t, b) determine the surfaces between the neighboring cells. The center of the observed cell is marked with a capital "C". Using the predefined x, y, z coordinate system, the conservation equation 2.113 can be discretized by the summation of the surface values:

$$\underbrace{\frac{\partial}{\partial t}\phi V}_{\text{Time derivative}} = \underbrace{-\sum_{\sigma=1}^{N_s}((\boldsymbol{u}\phi)\cdot\boldsymbol{n}S)_\sigma - \sum_{\sigma=1}^{N_s}(\boldsymbol{j}_\phi\cdot\boldsymbol{n}S)_\sigma + \dot{\omega}_\phi V + \Gamma_\phi V}_{\text{Right hand side (RHS)}} \tag{2.114}$$

The equation above is further simplified, as the surface and volume values are replaced by their center point values. This simplification is called the mid-point rule [43], which is second order accurate. Higher than second order interpolation and time integration schemes should use higher order surface and volume approximation methods like the Simpson's rule and the bi-quadratic shape function, which are fourth order accurate [43]. However, in this work only first to second order schemes are used for spatial derivatives and therefore the mid-point rule is applied in all cases. It is defined as:

$$\int_V f\,dV \approx f_{vc}V \quad ; \quad \int_S f\,dV \approx f_{fc}S. \tag{2.115}$$

2.5.2 Time Integration

In unsteady problems, the time derivative has to be solved as contribution for the temporal progression of the partial differential equations, which is solved numerically. The simplest temporal discretization scheme is the Euler scheme, which approximates the time derivative with:

$$\frac{\partial}{\partial t}\phi V = \frac{\phi^n - \phi^{n-1}}{\Delta t} \tag{2.116}$$

The superscripts n and $n-1$ denote the current time level, which will be solved and the previous time level, which is available. The Euler scheme is of first order ($\mathcal{O}(h^1)$) accuracy and computationally very cheap in its explicit formulation. Explicitly formulated means that it is based on the RHS data of the previous time level:

$$\phi^n = \phi^{n-1} + \mathrm{RHS}^{n-1}\Delta t \tag{2.117}$$

An explicit formulation of the temporal derivative is stable only as long as the solution propagates not more than one cell width per time step, i.e. the Courant–Friedrichs–Lewy (CFL) number does not exceed a value of unity:

$$\mathrm{CFL} = \frac{|\boldsymbol{u}|\Delta t}{\sqrt[3]{\prod_3^{i=1} \Delta x_i}} \leq 1. \tag{2.118}$$

In the implicit formulation, the solution of the new time step depends on the RHS data of the current time level n.

$$\phi^n = \phi^{n-1} + \mathrm{RHS}^n \Delta t \tag{2.119}$$

The implicit formulation of the Euler scheme is of the same order of accuracy as the explicit variant ($O(h^1)$), but is unconditionally stable and theoretically allows arbitrary large time steps. This can be beneficially, for example when a steady state of the solution is desired, or partially developed initial conditions are generated for more accurate simulations. However, when solving time-dependent solutions, large time steps are not applicable due to the low accuracy. A drawback is that the terms included in the RHS depend on the solved variable $\mathrm{RHS}^n = f(\phi^n)$ and a system of equations must therefore be solved within every time step. This is computationally expensive in comparison to the explicit formulation and only advantageous when time accuracy is not of importance.

A method which uses both the old and the new time level for the evaluation of the solution is known as a hybrid method. The time-level data are combined using the trapezoidal integration rule, while the contribution of the time-levels is weighted. If both time levels are weighted equally, the scheme is of second order accuracy and known as Crank-Nicolson method:

$$\phi^n = \phi^{n-1} + \frac{1}{2}(\mathrm{RHS}^n + \mathrm{RHS}^{n-1})\Delta t \tag{2.120}$$

This scheme is a combination of the Euler explicit and implicit method and requires therefore the computational expenses of both schemes at one time step.

For LES calculations performed with the in-house code PsiPhi, a third order low-storage Runge-Kutta time integration scheme is used as introduced by Williamson [246]. The solution is calculated using the coefficients a_k, b_k and w_k for three successive calculated sub time steps denoted by the subscript $k = 1, 2, 3$.

$$\begin{aligned} \phi^n &= \phi^{n-1} + b_k q_k \\ q_k &= a_l q_{k-1} + RHS^{n-1}\Delta t \\ t_k &= t_{k-1} + w_k \Delta t \end{aligned} \tag{2.121}$$

A variety of Runge-Kutta coefficients can be found in the literature, which impact the numerical behavior of the scheme. In this work, the coefficients are chosen as proposed by Williamson [246] as a good compromise between stability and precision.

$$\begin{aligned} a_k &= 0, -5/9, -153/128 \\ b_k &= 1/3, 15/16, 8/15 \\ w_k &= 1/3, 5/12, 1/4 \end{aligned} \tag{2.122}$$

2.5.3 Spatial Derivatives

In the discretized form of the conservation equation (eqn. 2.114) all divergence operators have vanished because the Gauss theorem has been applied priorly. However, this does not mean that the equation is free of spatial derivatives. A look at the definition of the diffusive flux $\boldsymbol{j}_\phi = \rho D_\phi \nabla \phi$ reveals the gradient within this term. Since fluxes are balanced at the cell faces, this derivative needs to be evaluated at the cell face center, when the mid-point rule is applied:

$$\left(\frac{\partial \phi}{\partial \boldsymbol{x}}\right)_e \approx \frac{\phi_E - \phi_C}{\Delta} \tag{2.123}$$

Here, a second order approximation of a Taylor series has been applied on the cubic grid in order to approximate the gradient of ϕ on the eastern cell center denoted by the subscript e.

2.5.4 Spatial Interpolation

Since the values for ϕ are calculated and stored at the cell centers, they have to be interpolated on the face centers for the calculation of the respective fluxes. The accuracy of these interpolation schemes are measured by the rate of convergence to the real solution in relation to the grid size. In other words: a scheme of first order accuracy ($O(h^1)$) converges linearly with a refined grid, whereas a scheme of second order ($O(h^2)$) converges quadratically. First order schemes have the advantage of being very simple mathematical expressions and are known for their stability. The most popular first order scheme in computational fluid mechanics (CFD) is the upwind differencing scheme, which detects the direction of the flow and maps the value of the upwind neighboring cell without any adjustment to the surface center.

$$\phi_e = \phi_U = \begin{cases} \phi_C & \text{if } \boldsymbol{u} \cdot \boldsymbol{n}_e \geq 0 \\ \phi_E & \text{if } \boldsymbol{u} \cdot \boldsymbol{n}_e < 0 \end{cases} \tag{2.124}$$

Although first order schemes are very stable, they are very inaccurate and hence add a high amount of numerical – nonphysical – diffusion to the solution (see figure 2.8). Another

simple but second order accurate scheme is the central differencing scheme (CDS), which interpolates linearly between the neighboring cell values. For the eastern face (subscripted by e) of a cell in our cubic grid (see fig. 2.1), it is written:

$$\phi_e = \frac{1}{2}(\phi_C + \phi_E). \tag{2.125}$$

The CDS is a simple way to achieve a second order interpolation, but it is not unconditionally stable and is known to oscillate and diverge from the real solution when a particular cell Péclet number is exceeded ($Pe_{c,i} = \Delta\rho u_i / D_\phi > 2$). This sensitivity to higher Péclet numbers is the result of the lack of adaptation to the transitivity of the problem. Another interpolation scheme that is also of second order accuracy, but takes the flux direction into account, is the quadratic upstream interpolation for convective kinetics (QUICK) scheme of Leonard [120]. As a quadratic interpolation, it needs three base points, which are directed and weighted by the direction of the flux:

$$\phi_e = \begin{cases} \phi_C + \frac{1}{8}(3\phi_E - 2\phi_C - \phi_W) & \text{if } \boldsymbol{u} \cdot \boldsymbol{n}_e \geq 0 \\ \phi_E + \frac{1}{8}(3\phi_C - 2\phi_E - \phi_{EE}) & \text{if } \boldsymbol{u} \cdot \boldsymbol{n}_e < 0 \end{cases} \tag{2.126}$$

Here, the subscript EE denotes the second neighbor cell in the eastern direction of cell C. QUICK is not as sensitive to the convective/diffusive flux ratio as CDS, but is also only stable within a certain range of conditions. A popular way for detecting and eliminating the unstable regions of higher order schemes is to artificially force them to operate inside the total variation diminishing (TVD) zone. These schemes are called TVD schemes, which basically increase the weight of the upstream contribution or increase the numerical diffusion in order to stabilize the solution. The interpolation schemes are generalized using the following formulation:

$$\phi_f = \phi_U + \Psi(r)\frac{1}{2}(\phi_D - \phi_U), \tag{2.127}$$

where ϕ_f denotes the face value, which has to be approximated. The limiter function $\Psi(r)$ is different for every TVD scheme variant, while all TVD schemes are equal to CDS for $\Psi(r) = 1$. The limiter function depends on the variable r, which is the local ratio of the upstream to the downstream gradient:

$$r = \frac{\phi_U - \phi_{UU}}{\phi_D - \phi_U} \tag{2.128}$$

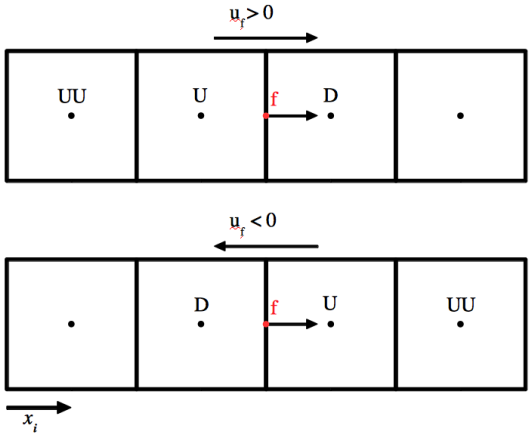

Fig.: 2.8 Sketch of the flux dependent order of downwind (D), upwind (U) and the second upwind neighbor (UU) for determination of the interpolation scheme base points within equations (2.127) and (2.128).

The subscript notation is based on the upstream formulation and clarified in figure 2.8. For the sake of completeness, table 2.4 shows a number of popular numerical schemes. Most TVD schemes are characterized by unconditional stability and second-order accuracy with respect to r ($1 \leq \lim_{r\to\infty} \Psi(r) \leq 2$), while others like the CHARM are only second order accurate within a certain range of r ($\lim_{r\to\infty}^{\text{CHARM}} \Psi(r) = 3$). Figure 2.9 visualizes the behavior of the limiter function $\Psi(r)$ within the TVD region for the mentioned schemes, while figure 2.10 gives an impression of the differences of some schemes applied on different types of transported profiles.

Name	$\Psi(r)$	TVD range
UDS	0	$0 < r < \infty$
CDS	1	$r > 0.5$
QUICK [120]	$(3+r)/4$	$0.0325 < r < 5$
Van Leer [222]	$(r+\|r\|)/(1+r)$	$0 < r < \infty$
Van Albada [221]	$(r+r^2)/(1+r^2)$	$0 < r < \infty$
CHARM [255]	$\max(0,r)(3\max(0,r)+1)/(\max(0,r)+1)^2$	$r < 5.562$
Min-Mod [188]	$\max[0,\min(r,1)]$	$0 < r < \infty$
SUPERBEE [188]	$\max[0,\min(2r,1),\min(r,2)]$	$0 < r < \infty$
Sweby [213]	$\max[0,\min(2\beta,1),\min(r,\beta)]$	$1 \leq \beta \leq 2 \Rightarrow \infty$
Exp	$2[1-\exp(\ln(0.5)\max(r,0))]$	$0 < r < \infty$
QUICK (limited) [121]	$\max[0,\min(2r,(3+r)/4,2)]$	$0 < r < \infty$

Table 2.4 List of numerical interpolation schemes, their functional $\Psi(r)$ and their stability criteria in terms of TVD.

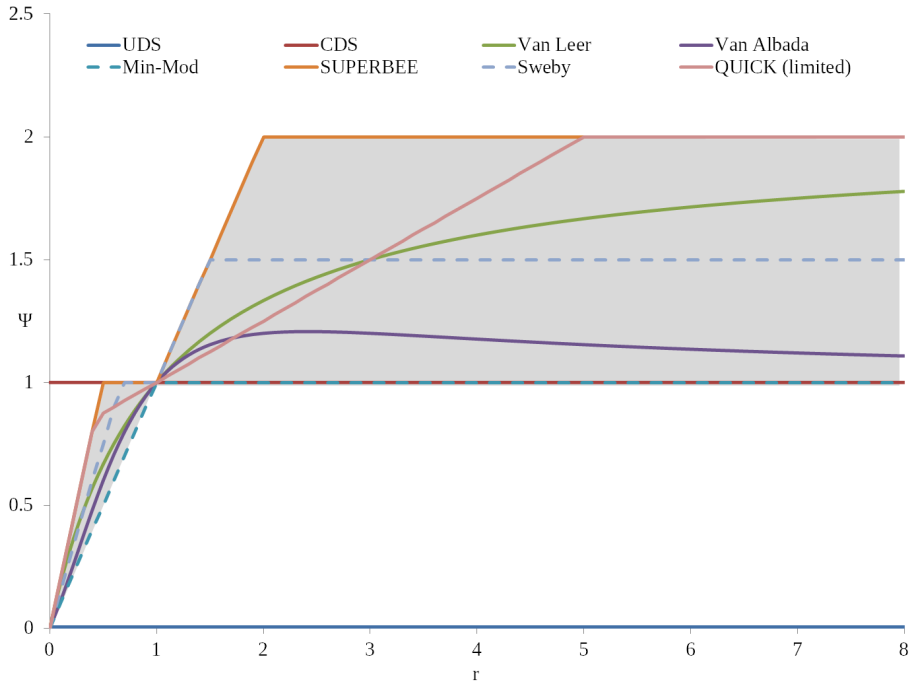

Fig.: 2.9 Visualization of schemes mentioned in table 2.4. Grey marked area determines the second order accuracy region defined by Sweby [213]. CDS leaves the general TVD area for values $r < 0.5$, whereas the UDS scheme is always stable, but below the 2nd order accuracy.

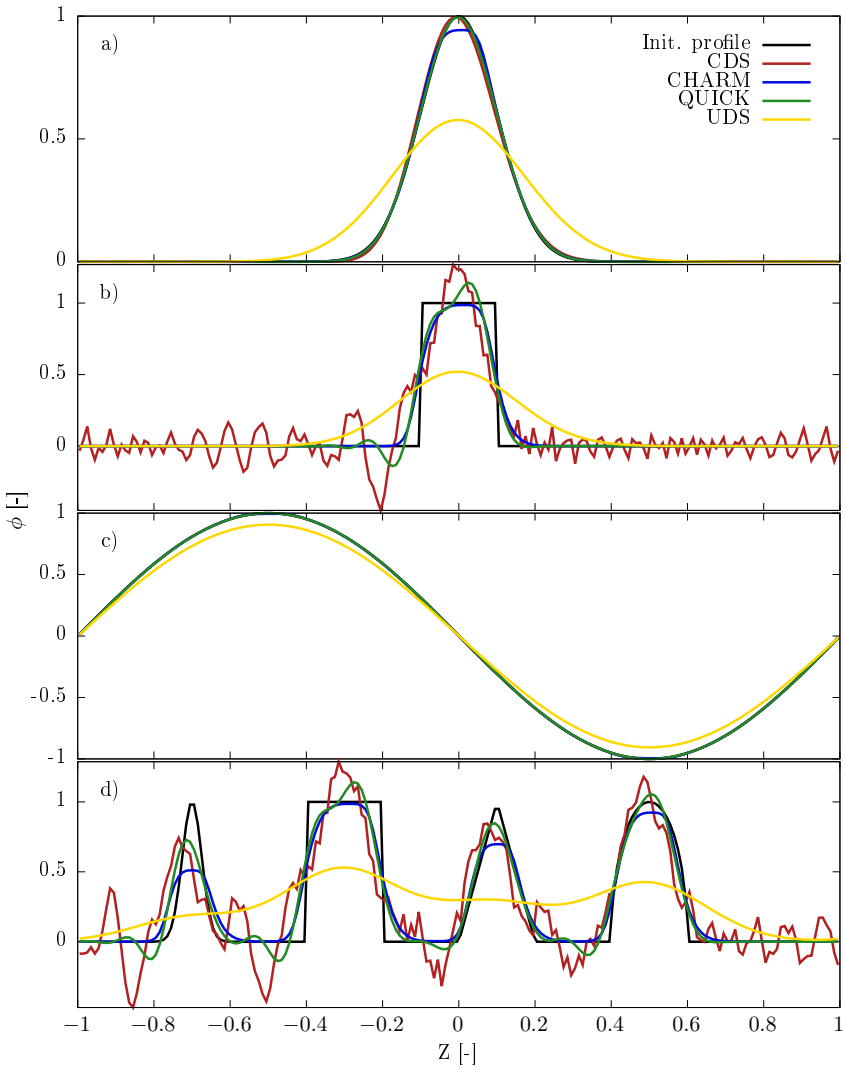

Fig.: 2.10 Comparison of different interpolation schemes (with and without limiter) for convective transport of various initial profiles (a) Gauss profile, b) step profile, c) sinus profile, d) mixed profiles). Grid resolution is 200 points in Z, resulting profiles correspond to a solution after 500 time steps with a CFL number of 0.4 (representing one cycle within the periodic domain).

2.5.5 Solution of Discrete Conservation Equations

When temporal, diffusive and interpolation schemes are applied to equation (2.114), an equation for the unknown variable in point P can be given in the form:

$$A_P \phi_P + \sum_l A_l \phi_l = Q_P. \tag{2.129}$$

Where A represents the coefficients of the variable ϕ, which is solved, whereas Q represents the source terms including the pressure gradient for the moment equations. It is obvious that the solution at point P depends on the solution of the neighboring cells l, what is unproblematic for explicit temporal integrations schemes, since all values are available from the previous time level. For implicit schemes, the equation system for the whole domain has to be defined by constructing a sparse coefficient matrix A_{ij}

$$A_{ij}\phi_j = Q_i \tag{2.130}$$

The coefficient matrix is sparse, whereby values exist around the main band (diagonal) of the matrix and a variety of solution procedures have been developed for such equation systems. In CFD, iterative methods, which locally apply the incomplete lower upper decomposition, the conjugate- and biconjugate gradients methods as well as multi grid methods have been proven to offer the best trade-off between accuracy and efficiency. For the theoretical description of those methods, the reader is referred to Ferziger and Perić [43] for deeper insight into this topic.

Pressure-Velocity Coupling

While in compressible flows of higher mach numbers, the continuity equation is used to obtain the density and the pressure is calculated by the equation of state, the continuity equation does not offer a variable that links mass conservation with the momentum equation for incompressible formulations. The result is that continuity is not ensured as the pressure gradient is not predicted. One way to overcome this issue is to construct a mathematical relation to calculate the pressure gradient in order to satisfy the continuity equation. This procedure is referred to as pressure-velocity coupling and will be explained here by means of an implicit method for orthogonal, equidistant grids. When the pressure gradient is excluded from the source term, the discretized, non-linear momentum equation at point P is written as:

$$A_P^{u_i} u_{P,i}^n + \sum_l A_l^{u_l} u_{l,i}^n = Q_{u_i}^n - \left(\frac{\partial p^n}{\partial x_i}\right)_P . \tag{2.131}$$

The variable $Q_{u_i}^n$ contains all explicitly calculated source terms calculated for the new time level n except the pressure gradient, which is written in symbolic form to stress that it is the variable we are solving for. Because of the non-linear character of the equation system, it can not be solved directly and an iterative procedure has to be applied. Hence, in order to distinguish between the time step and the outer iterations within one time step the new superscript m is introduced. It represents the current iteration of solution, in which the

coefficient and source matrices are updated. The velocity of the linearized momentum equation for the current outer iteration is then expressed as:

$$u_{P,i}^{m*} = \frac{Q_{u_i}^{m-1} - \sum_l A_l^{u_i} u_{l,i}^{m*}}{A_P^{u_i}} - \frac{1}{A_P^{u_i}} \left(\frac{\partial p^{m-1}}{\partial x_i} \right)_P . \tag{2.132}$$

The velocity obtained above represents the initial value of the velocity, which does not satisfy the continuity equation and is therefore marked by an asterisk. The correct velocity, which satisfies the continuity can be obtained after corrections with an updated pressure gradient:

$$u_{P,i}^{m} = \widetilde{u}_{P,i}^{m*} - \frac{1}{A_P^{u_i}} \left(\frac{\partial p^{m}}{\partial x_i} \right)_P \tag{2.133}$$

Where $\widetilde{u}_{P,i}^{m*}$ substitutes the velocity contribution without pressure term:

$$\widetilde{u}_{P,i}^{m*} = \frac{Q_{u_i}^{m-1} - \sum_l A_l^{u_i} u_{l,i}^{m*}}{A_P^{u_i}} \tag{2.134}$$

In order to solve for the correcting pressure and velocity parts, the variables are split according to their definition:

$$u_i^m = u_i^{m*} + u_i' \quad \text{and} \quad p^m = p^{m-1} + p' \tag{2.135}$$

By analogy of equation (2.134), we obtain the relation of correction velocity u_i' and pressure p':

$$u_{P,i}' = \widetilde{u}_{P,i}' - \frac{1}{A_P^{u_i}} \left(\frac{\partial p'}{\partial x_i} \right)_P \tag{2.136}$$

Where $\widetilde{u}_{P,i}'$ does not only exclude the pressure gradient, but also the source term and is therefore defined as:

$$\widetilde{u}_{P,i}' = -\frac{\sum_l A_l^{u_i} u_{l,i}'}{A_P^{u_i}}. \tag{2.137}$$

The velocity is substituted into the continuity equation in order to enforce mass conservation:

$$\frac{\partial (\rho u_i^m)}{\partial x_i} = 0 \tag{2.138}$$

It leads to the following pressure correction in the form of a Poisson equation:

$$\frac{\partial}{\partial x_i} \left[\frac{\rho}{A_P^{u_i}} \left(\frac{\partial p'}{\partial x_i} \right) \right]_P = \left[\frac{\partial (\rho \widetilde{u}_i^{m*})}{\partial x_i} \right]_P + \cancel{\left[\frac{\partial (\rho \widetilde{u}_i')}{\partial x_i} \right]_P} \tag{2.139}$$

The velocities $\widetilde{u}'_{P,i}$ are unknown at this point and are therefore neglected for the iterative process, as the correction quantities disappear when the solution converges. However, this simplification makes it difficult for the method to converge, which means that it is mainly used for steady-state problems where it is not necessary to ensure the accuracy of the intermediate time steps. The procedure is known as SIMPLE method [19] and it has been proven that under-relaxation of the correction pressure can drastically improve the convergence behavior:

$$p^m = p^{m-1} + \alpha_p p' \quad \text{with} \quad 0 \leq \alpha_p \leq 1 \tag{2.140}$$

For the PISO method, Issa [85] added a second correction step, in which the previously neglected velocity term is treated explicitly in order to obtain the second correction to the velocity $u''_{P,i}$:

$$u''_{P,i} = \widetilde{u}'_{P,i} - \frac{1}{A_P^{u_i}} \left(\frac{\partial p''}{\partial x_i} \right)_P \tag{2.141}$$

This relation is then used to calculate the second pressure-correction equation:

$$\frac{\partial}{\partial x_i} \left[\frac{\rho}{A_P^{u_i}} \left(\frac{\partial p''}{\partial x_i} \right) \right]_P = \left[\frac{\partial (\rho \widetilde{u}'_i)}{\partial x_i} \right]_P \tag{2.142}$$

By updating the velocity $\widetilde{u}'_{P,i}$, and solving the second correction in an iterative manner, the accuracy within a time step can be improved. This procedure is used for transient flow problems, as it offers a higher accuracy and better convergence behavior in comparison to the SIMPLE method.

2.5.6 The OpenFOAM Finite Volume Toolbox

The OpenFOAM (Open source Field Operation And Manipulation) toolbox is an open source software package written in C++ and originally built for numerical continuum mechanics discretized applying the finite volume method (FVM) on unstructured grids. Released in 2004 by H. Weller and H. Jasak, OpenFOAM profited from a growing community and their contribution to the code development. The modern OpenFOAM package is an enormous collection of numerical libraries and solvers, which support the finite element method (FEM), the discrete particle method and many other discretization methods besides the originally implemented FVM in order to model physical problems in aerodynamics, structure mechanics, heat conduction, electromagnetism and combustion. It supports the Message Passing Interface (MPI) for parallel computing and offers meshing software as well as high compatibility to the free post-processing software Paraview. OpenFOAM is designed to be highly configurable with respect to the choice of numerical methods, categorized

according to the physical problem to be addressed and managed by a sophisticated but complex "run-time selection" algorithm. Further, OpenFOAM uses a variety of wrapped and customized classes from the C++ standard and third party libraries, which leads to a meta language like code design with nested dependencies. As a result, code development is not straightforward, resulting in easy application but complicated customization at deeper code levels. Nevertheless, for the investigations carried out in this work, extensions on solver and library levels had to be done in order to add new combustion and coupled nanoparticle dynamic methods, as well as linking approaches for the data transfer to the statistical particle dynamics software described in chapter 3.8.
As OpenFOAM discretizes the investigated domain with non-orthogonal, unstructured grids, numerical methods for spatial interpolation and differentiation are mathematically more complex than with hexahedral grids, as mentioned in the last subsection. For example, the simple calculation to obtain the volume of a cell has to be performed by using the gradient of a coordinate $\nabla \cdot x\boldsymbol{i} = 1$, where $\boldsymbol{i}$ is the orientation vector of the x-axis. The gradient can then be used further to apply the Gauss theorem, giving the following relation:

$$\Delta V = \int_V \nabla \cdot (x\boldsymbol{i}) dV = \int_S x\boldsymbol{i} \cdot \boldsymbol{n} dS \approx \sum_\sigma x_\sigma S_\sigma^x. \tag{2.143}$$

Furthermore, the surface area vector $\boldsymbol{S}_\sigma$ can be obtained by the sum of the cross product of the triangulated surface:

$$\boldsymbol{S}_\sigma = \frac{1}{2} \sum_{i=3}^{N_{v,c}} [(\boldsymbol{r}_{i-1} - \boldsymbol{r}_1) \times (\boldsymbol{r}_i - \boldsymbol{r}_1)] \tag{2.144}$$

Where $\boldsymbol{r_i}$ is the coordinate of the i-th vertex of the cell and $N_{v,c}$ indicates the number of vertices of cell c. The superscript x in S_σ^x denotes it is the x-component of the full surface vector. The latter is perpendicularly aligned to the surface, pointing outwards the cell volume. Equation (2.143) uses the x-coordinate to define the volume, but one may also use any other canonical coordinate together with its orientation vector. In OpenFOAM, vertices of a respective surface are aligned according to a right hand rotation around the face normal. Further information can be found in the thesis of Jasak [86], as well as in the OpenFOAM programmers guide [65].

Pressure-Velocity-Density Coupling

The pressure-correction procedure used in OpenFOAM for compressible cases differs from the previously discussed general pressure correction for incompressible formulations. Since

it is not explained in detail in the standard OpenFOAM literature, it is included here for the sake of completeness. Adopting the notation from the basic projection method (2.132), an initial guess of the velocity is given by solving the discretized momentum equation for point P:

$$u_{P,i}^{m*} = \frac{Q_{u_i}^{m-1} - \sum_l A_l^{u_i} u_{l,i}^{m*}}{A_P^{u_i}} - \frac{\Delta V}{A_P^{u_i}} \left(\frac{\partial p^{m-1}}{\partial x_i} \right)_P \tag{2.145}$$

In arbitrarily unstructured grids, the coefficient matrix A^{u_i} and the pressure gradient excluding source term $Q_{u_i}^{m-1}$ contains the cell volume ΔV. Using the simplest implicit Euler discretization for demonstration purpose, the discretized continuity equation calculated using the initial velocities is given by:

$$\frac{\rho^{m-1} + \rho^{n-1}}{\Delta t} \Delta V + \sum_{\sigma=1}^{N_\sigma} \dot{m}_\sigma^* = Q_m^*. \tag{2.146}$$

The variable $\dot{m}_\sigma^*$ denotes the initial mass flow through surface S_σ, which together do not satisfy the continuity equation and therefore lead to a mass imbalance Q_m^*, which needs to be eliminated. Since in compressible flows, velocity is not proportional to the pressure correction gradient, the correction term must be derived from the mass fluxes, which again depend on the surface normal velocity component $u_n = \boldsymbol{u} \cdot \boldsymbol{n}$ and the density ρ that varies in compressible cases. The corrected velocity $\dot{m}_\sigma$ therefore reads:

$$\dot{m}_\sigma^m = (\rho^{m-1} + \rho')_\sigma (u_n^{m*} + u_n')_\sigma S_\sigma. \tag{2.147}$$

With ρ' and u_σ' being the correction density and velocity, respectively. By merging the resulting correction terms of equation 2.147, we obtain a relation for the correction flux:

$$\dot{m}_\sigma' = (\rho^{m-1} S u_n')_\sigma + (u_n^{m*} S \rho')_\sigma + \underline{(\cancel{\rho' u_n' S})_\sigma} \tag{2.148}$$

The underlined term is normally neglected because of his second order nature, which makes it small as the solution converges. When interpolated velocities are used for pressure correction on collocated grids, spatial oscillations, known as checker-boarding, may occur. In order to avoid those oscillations, the interpolated velocities are modified by using an approach developed by Rhie and Chow [181]:

$$u_{n,\sigma}^{m*} = \overline{(u_n^{m*})}_\sigma - \Delta V \overline{\left(\frac{1}{A_P^{u_n}} \right)}_\sigma \left[\left(\frac{\partial p}{\partial n} \right)_\sigma - \overline{\left(\frac{\partial p}{\partial n} \right)}_\sigma \right]^{m-1} \tag{2.149}$$

The terms with an overline are the interpolated values, whereas the pressure gradient without overline is directly calculated on the cell surface σ. Ferziger and Perić [43] describe a method to calculate this term with corrections for grid non-orthogonality. Using the same simplification as described for the incompressible correction velocity and applying equation (2.149), the first term of the mass flow correction (Eqn. (2.148)) delivers a term similar to the incompressible case:

$$(\rho^{m-1} S u_n')_\sigma = -(\rho^{m-1} S \Delta V)_\sigma \overline{\left(\frac{1}{A_P^{u_n}}\right)}_\sigma \left(\frac{\partial p'}{\partial n}\right)_\sigma \tag{2.150}$$

The second term on the right hand side (RHS) of the mass flow correction (Eq. (2.147)) represents the compressibility effect and involves the correction density in terms of pressure correction. It can be approximated at fixed temperature within one outer iteration:

$$\rho' \approx \left(\frac{\partial \rho}{\partial p}\right)_T p' = \psi_\rho p' \tag{2.151}$$

Where ψ_ρ is obtained by the equation of state for a perfect gas assumption:

$$\psi_\rho = \left(\frac{\partial \rho}{\partial p}\right)_T = \frac{1}{RT} \tag{2.152}$$

The final solutions are independent of the mentioned corrections, as those develop towards zero as the procedure converges. Nevertheless, it is important to find a correct relation between the pressure and density correction, since it strongly influences the convergence rate. The complete second mass flow correction term of equation (2.147) can be calculated by:

$$(u_{n,i}^{m*} S \rho')_\sigma = \left(\frac{\psi_\rho \dot{m}^*}{\rho^{m-1}}\right)_\sigma p'_\sigma. \tag{2.153}$$

The correction mass flux at face σ is then be rewritten as:

$$\dot{m}'_\sigma = -(\rho^{m-1} S \Delta V)_\sigma \overline{\left(\frac{1}{A_P^{u_n}}\right)}_\sigma \left(\frac{\partial p'}{\partial n}\right)_\sigma + \left(\frac{\psi_\rho \dot{m}^*}{\rho^{m-1}}\right)_\sigma p'_\sigma. \tag{2.154}$$

A continuity equation, which must satisfy the correction terms can then be constructed using the mass imbalance Q_m^*:

$$\frac{\rho'_P}{\Delta t} \Delta V + \sum_{\sigma=1}^{N_\sigma} \dot{m}'_\sigma + Q_m^* = 0 \tag{2.155}$$

For the correction pressure and density p'_P and $\rho'_P(p'_P)$ in point P, we then derive the algebraic system of equations for the pressure correction:

$$A_P p'_P + \sum_l A_l p'_l = -Q^*_m \tag{2.156}$$

It can be seen that the pressure correction equation in the compressible case shows major differences in comparison to the incompressible version. While the latter represents a Poisson equation, the compressible pressure correction includes both convective and unsteady terms, which can be considered as transport equation for pressure waves. The strength of the contribution of the two different terms within the mass flow correction depends on the flow conditions, the contribution of the pressure gradient correction together with the local pressure correction. Domination of the first contribution recovers the Poisson equation, while domination of the second contribution yields a continuity like convection equation, which shows a hyperbolic character at high Mach numbers. For simplification of the solution procedure for non-orthogonal grids, OpenFOAM uses a "deferred correction" method, which iteratively adds corrections for non-orthogonality [43]. The knowledge of how the pressure correction works is crucial, if new solvers are added or existing solvers are modified. The methods developed in the present work add phase transition from the gas to the disperse phase, which is interpreted as mass imbalance (see Eq. (2.146)) if the pressure correction is not adjusted. It is out of question that no- or wrong modification leads to bad convergence behavior in case of steady flows and to major instabilities and errors in case of transient flows.

3 Population Balance Modeling of Nanoparticles

A number of processes are responsible for the change in particle number and morphology in an observed volume. The most prominent ones are nucleation, surface growth, coagulation, diffusion, forced convection, and sedimentation. These processes are taking place at the same time, while their rates depend on the interaction of the particle ensemble and the gas phase. Due to this behavior, some processes become more dominant while the particle ensemble evolves, and others lose their impact or become even negligible, i.e., this evolution strongly depends on the time scale of competing processes. For example, the systems studied in the present work are subject to forced convection (e.g., gas phase and thermophoretic velocity), which is orders of magnitude faster than the sedimentation velocity, and which is therefore neglected. On the other hand, the influence of the competing processes of nucleation and condensation changes drastically towards condensation once enough nuclei are present.
In this chapter, the modeling of the mentioned processes is discussed in detail. Subsequently, the processes are applied together within a balance equation, known as General Dynamic Equation (GDE).

3.1 Particle Formation

Particle formation means the transition of material clusters from gas to bulk or liquid phase. In contrast to condensation – where molecules deposit on the particle surface – mass is added to the particle phase by seeding new nuclei. In further steps, those will grow or evaporate depending on the saturation rate of the gas and the particle properties.
Particle formation can arise due to two different mechanisms, depending on the gas phase and material conditions: homogeneous nucleation and molecular coagulation [48]. In order to determine which mechanism is dominating, Ulrich [219, 48] introduced a criterion based on the Kelvin relation (Eq. 3.1). He assumed the critical diameter d_K to be of the size of the condensable specie molecule $d_m = d_K$ (Eq. 3.2) and used the resulting partial pressure p_m as an indicator: if the partial pressure $p_{m,real}$ is assumed to be higher than the one given by equation (3.3), particle formation is likely to be driven by coagulation on molecular level, or

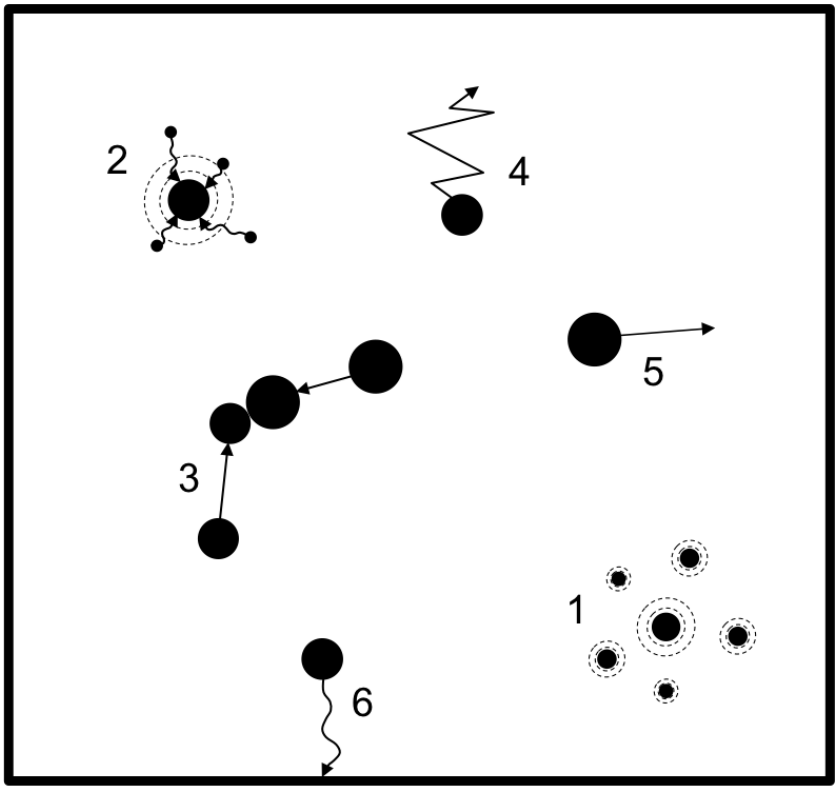

Fig.: 3.1 Processes affecting nanoparticle evolution on meso- and macroscopic level within an observed volume. 1: nucleation, 2: surface growth, 3: coagulation, 4: diffusion, 5: forced convection, 6: sedimentation

by condensation in the opposite case.

$$d_K = \frac{4\sigma v_m}{kT\, ln(p_m/p_s)} \tag{3.1}$$

$$d_m = \left(\frac{6v_m}{\pi}\right)^{\frac{1}{3}} \tag{3.2}$$

Inserting Eq. (3.2) into (3.1) (assuming $d_m = d_K$) delivers the particle formation criterion (Eq. (3.3)). Here, σ and v_m determine the investigated cluster molecule's surface tension and molecular volume.

$$p_m = p_s \exp\left[\left(\frac{\pi}{6}\right)^{\frac{1}{3}} \frac{4\sigma v_m^{(2/3)}}{kT}\right] \tag{3.3}$$

For cases, where the gas phase is non-saturated ($p_{m,real} < p_m$), clusters with the number of molecules g grow and shrink with the same overall rate and therefore remain in an equilibrium

state within the gas phase [48]:

$$\beta s_{g-1} n_{g-1} = \alpha_g s_g n_g \tag{3.4}$$

The variables s_g, n_g, and α_g are the area of evaporation, the concentration, and the evaporation rate of clusters of size g, respectively. The flux of condensing monomers on clusters of the size $g-1$ is given by β and can be calculated by:

$$\beta = \frac{p_1}{(2\pi mkT)^{\frac{1}{2}}} \tag{3.5}$$

Here, p_1 is the partial pressure of monomers, while m and k are the monomer mass and the Boltzmann constant. Applying the Kelvin relation (3.1), the evaporation flux can be approximated by:

$$\alpha_g = \frac{p_s}{(2\pi mkT)^{\frac{1}{2}}} \exp\left[\frac{4\sigma v_m}{d_g kT}\right] \tag{3.6}$$

The variable d_g is the diameter of the cluster and can be substituted using equation (3.2).
The process of condensation and evaporation continues until the gas is supersaturated ($p > p_s$), and the equilibrium assumption does not hold anymore. In that case, homogeneous nucleation occurs and the cluster distribution equation (3.4) becomes:

$$I_g = \beta s_{g-1} n_{g-1} - \alpha_g s_g n_g \tag{3.7}$$

The expression I_g is the drop current, which is the excess of clusters of size g produced per time. Integration of the non equilibrium cluster distribution equation (3.7) with respect to g and some further modifications (see [48]) delivers the nucleation rate given by:

$$I = 2\left[\frac{p_1}{(2\pi mkt)^{1/2}}\right](n_1 v_m^{2/3})\left[\frac{\sigma v_m^{2/3}}{kT}\right]^{(1/2)} \exp\left[-\frac{16\pi\sigma^3 v_m^2}{3(kT)^3(ln(S))^2}\right] \tag{3.8}$$

Here, S is the saturation ratio $S = p_1/p_s$. The interested reader is referred to the book of Friedlander [48] for further details about the derivation and background about the homogeneous nucleation theory.
As aforementioned, another nucleation mechanism than homogeneous nucleation applies, if $p_{m,real} > p_m$ in Eq. (3.3). In that case, molecular collisions of monomers are assumed to initiate nuclei (see 3.3), which grow further by collision and condensation. This phenomenon is not limited to a collective of pure substances, but also between reactive, intermediate species like silylene, which occur during the chemical decomposition of the precursor [79].

3.2 Particle Growth

Besides nucleation, the deposition of gaseous matter on particle surfaces is another phenomenon, which leads to a phase transition of gaseous molecules towards the particle phase. As heterogeneous condensation means the deposition of molecules onto the surface of existing particles, no further particles are generated, but particles grow in volume. Condensation occurs when the particle concentration is sufficiently high for the condensation rate to become dominant after nucleation, i.e. when a sufficient number of nuclei are present and the provided particle surface is large.
Particle growth can be divided into two categories: transport-limited growth and reaction-limited growth. The transport-limited rate per particle R_j^{co}, for a species j can be approximated by diffusion-driven particle-molecule collision [146]:

$$R_j^{co} = a_c C_j \sqrt{\frac{\pi k_b T}{2m_j}} (d_j + d_c)^2 \tag{3.9}$$

Where a_c is the sticking coefficient – a measure for the collision partner to stick permanently – and C is the concentration of the condensing species j. The variables m and d are the mass and diameter of species j, while d_c is the collision diameter of the respective particle. It is calculated by using the following equation [198, 199]:

$$d_c = \bar{d}_p \left[\frac{a^3}{36\pi v^2} \right]^{\frac{1}{D_f}} \tag{3.10}$$

Here, $\overline{d}_p$ and D_f are the primary particle diameter and the fractal dimension (see next section), while a and v are the surface and volume of the entire particle, respectively.
If the particle growth is limited by the chemical reaction, the growth rate per particle R_{ij}^r can be calculated by assuming a surface reaction:

$$R_{ij}^r = A_s \exp\left(-\frac{E_a}{RT}\right) \eta_i N_A C_j \tag{3.11}$$

The variables A_s, E_a, and N_A are the pre-exponential factor, the activation energy, and the Avogadro constant. The term η_i denotes the molecule number of surface active chemical components (i.e., Si, OH, H, ...). An example of such a reaction can be found in the work of Shekar et al. [200], where a silicic acid molecule reacts with the active OH component on

the particle surface:

$$Si(OH)_4(g) + OH(s) \rightarrow SiO(b) + 3OH(s) + H_2O(g) \tag{3.12}$$

The extensions g, b, and s denote that a chemical component/species is gaseous, or belongs to the particle bulk, or particle surface.

3.3 Particle Coagulation

Particles coagulate after getting into contact by collision with other particles, which results in a decrease in the particle number, but an increase in aggregate size. If particles do not coalesce (see section 3.4) after the collision, they coagulate to structures of different morphologies depending on the material system. The morphology is the structural attribute of a particle cluster and the fractal dimension D_f is a measure for this attribute. Studies conducted by Goudeli et al. [62, 63] have revealed that the fractal dimension D_f transitions from a value of 3 (indicating a spherical shape) to its asymptotic value, which varies depending on the material system. For a system consisting of monodisperse primary particles, an aggregate with approximately 10-30 primary particles n_p is required to reach the asymptotic value of D_f [62]. As the polydispersity of the primary particles increases – as indicated by the geometrical standard deviation $\sigma_{g,pp}$, a greater number of primary particles per aggregate is necessary to achieve the asymptotic value of D_f (approximately $n_p \approx 315$ for $\sigma_{g,pp} = 3.0$) [63]. Although the accuracy of assuming a constant fractal dimension D_f may be debatable, current state-of-the-art computational fluid dynamics (CFD) models generally treat D_f as a fixed value. For the purposes of this work, the approach of a constant fractal dimension is adopted due to the assumption of monodispersity or spherical particle shapes.
If coagulation is acting on a discrete particle distribution n_k with the spherical particle sizes v_k, the collision process can be described as [48]:

$$\frac{dn_k}{dt} = \frac{1}{2} \sum_{i+j=k} \beta_{ij} n_i n_j - n_k \sum_{i=1}^{\infty} \beta_{ik} n_i \tag{3.13}$$

Here, β_{ij} is the particle collision frequency and n_i is the number of particles of size v_i with $i, j, k \in \mathbb{N}$.
Smoluchowski [207] derived an expression for the collision frequency as a function of the particle diffusion D_{ij} and the particle radius r of a colliding pair i and j:

$$\beta_{ij} = 4\pi D_{ij}(r_i + r_j) \tag{3.14}$$

The diffusion coefficient can be described in terms of ensemble averaged relative particle displacement per time [48]. Considering the mean squared displacement in x-direction $\overline{(x_i - x_j)^2}$, it can be shown that due to the uncorrelated mean drifts ($\overline{x_i x_j} = 0$), the binary diffusion coefficient D_{ij} can be transformed into two single diffusion coefficients D_i and D_j:

$$D_{ij} = \frac{\overline{(x_i - x_j)^2}}{2t} = \frac{\overline{x_i^2}}{2t} - \frac{\overline{2x_i x_j}}{2t} + \frac{\overline{x_j^2}}{2t} = D_i + D_j \tag{3.15}$$

By substituting (3.15) into equation (3.14), a collision frequency equation with independent diffusion coefficients can be obtained:

$$\beta_{ij} = 4\pi(D_i + D_j)(r_i + r_j) \tag{3.16}$$

The Stokes-Einstein relation can be used for calculating the independent diffusion terms within the continuum regime:

$$D = \frac{k_B T}{3\pi\eta d} \tag{3.17}$$

The variable denotes η the dynamic viscosity, and d is the particle diameter. Substituting Eq. (3.17) into Eq. (3.16) and assuming a round sphere ($D_\mathrm{f} = 3.0$) for the particle volume delivers the collision frequency for the continuum range:

$$\beta_{ij}^{c} = \frac{2k_b T}{3\eta}\left[\frac{1}{v_i^{1/3}} + \frac{1}{v_j^{1/3}}\right]\left(v_i^{1/3} + v_j^{1/3}.\right) \tag{3.18}$$

This equation is valid in the scope of the continuum regime only and does not hold for the free molecular regime. Therefore, for the free molecular regime, another formulation for the collision frequency is derived from the kinetic theory. For this formulation, the molecules are assumed to be rigid, and collisions are fully elastic [48]:

$$\beta_{i,j}^{f} = \left(\frac{3}{4\pi}\right)^{1/6}\left(\frac{6k_b T}{\rho_b}\right)^{1/2}\left[\frac{1}{v_i} + \frac{1}{v_j}\right]^{1/2}\left(v_i^{1/3} + v_j^{1/3}\right)^2 \tag{3.19}$$

A good estimation for the frame in which the investigated system can be expected is the Knudsen number Kn. It is defined as the relation of mean free path length λ and the particle radius r:

$$\mathrm{Kn} = \frac{\lambda}{r} = \frac{2\lambda}{d} \tag{3.20}$$

The mean free path λ can be expressed as shown in Eq. (3.21).

$$\lambda = \frac{\eta}{p}\left(\frac{\pi k_b T}{2m}\right)^{\frac{1}{2}} \tag{3.21}$$

The variable p is the gas pressure and m is the molecular mass. Typically, the free molecular and the continuum regimes are characterized by $\mathrm{Kn} \gg 1$ and $\mathrm{Kn} \ll 1$. Both definitions do not cover the intermediate state, known as the transition regime, and specific interpolation expressions have to be used for predicting collision frequencies in that range. Probably the most important interpolation expression to mention is shown by Eq. (3.22) and was introduced by Fuchs et al. [51].

$$\zeta = \left[\frac{d_i + d_j}{d_i + d_j + 2\sqrt{g_i^2 + g_j^2}} + \frac{8(D_i + D_j)}{(d_i + d_j)(c_i^2 + c_j^2)^{1/2}}\right]^{-1} \tag{3.22}$$

The parameters g and c of particle i symbolize the transition parameter and the particle velocity, respectively, which are determined by Eqs. (3.23) and (3.24).

$$g_i = \left[(d_i + \lambda_i)^3 - (d_i^2 + \lambda_i^2)^{3/2}\right][3\lambda_i d_i]^{-1} - d_i \tag{3.23}$$

$$c_i = \left(\frac{8k_b T}{\pi m_i}\right)^{\frac{1}{2}} \tag{3.24}$$

Extending Eq. (3.16) by the Fuchs interpolation expression (3.22) ($\beta_{ij}^* = \beta_{ij}\zeta$) delivers Eq. (3.25), a collision equation that covers the whole range of possible Knudsen numbers $0 < \mathrm{Kn} < \infty$.

$$\beta_{ij}^* = 2\pi(D_i + D_j)(d_i + d_j)\left[\frac{d_i + d_j}{d_i + d_j + 2(g_i^2 + g_j^2)^{1/2}} + \frac{8(D_i + D_j)}{(d_i + d_j)(c_i^2 + c_j^2)^{1/2}}\right]^{-1} \tag{3.25}$$

Due to its mathematical complexity, it is computationally expensive and therefore not used in numerical simulations within this work. Instead, a less complex expression is used, which was found by Pratsinis [175]. It approximates Eq. (3.25) by calculating the harmonic mean of the continuum and free molecular collision expressions β^c and β^f (Eqs. 3.18 and 3.19). It deviates at worst by about 14% from the formulation given by Fuchs (Eq. 3.25), while being computationally cheaper compared to the expression given by Fuchs. Figure (3.2) shows a comparison of both definitions of β^* for a wide range of Knudsen numbers for an artificial

test case.

$$\beta_{ij}^{*} = \frac{\beta_{ij}^{c}\beta_{ij}^{f}}{\beta_{ij}^{c} + \beta_{ij}^{f}} \tag{3.26}$$

In practical cases, where the morphology of the particles is assumed to be of complex nature ($1 \leq \mathrm{Df} \leq 3$), the collision diameter d_c is used in the definition of β. Further, it has been shown that for smaller particles in the continuum regime ($\mathrm{Kn} < 1$) molecules tend to slip over the particle surface rather than collide. Therefore, the Stokes-Einstein relation (Eq. 3.17) overestimates the relative particle motion (Eq. 3.15) in that region. This behavior is corrected by extending the Stokes-Einstein relation by applying the Cunningham slip correction factor $C = 1 + 1.257\mathrm{Kn}$ [232]:

$$D = \frac{k_B T}{3\pi\eta d} C \tag{3.27}$$

Applying the aforementioned changes to the continuum collision frequency β_{ij}^{c} (Eq. (3.18)), a corrected expression based on the collision diameter is obtained:

$$\beta_{ij}^{c} = \frac{2k_b T}{3\eta}\left[\frac{C_i}{d_{c,i}} + \frac{C_j}{d_{c,j}}\right]\left(d_{c,i} + d_{c,j}\right) \tag{3.28}$$

The free molecular collision frequency is not affected by molecular slipping, but due to van der Waals forces acting on the molecular level, Eq. (3.19), it tends to underpredict the collision frequency in some cases – especially for very small particles. This is corrected by multiplying β_{ij}^{f} with the factor α, which is often set to the van der Waals enhancement factor $\alpha = 2.2$ [74]. The final expression for the free molecular collision frequency as a function of the collision diameter d_c is then derived as:

$$\beta_{ij}^{f} = \alpha\left(\frac{\pi k_b T}{2}\right)^{1/2}\left[\frac{1}{m_i} + \frac{1}{m_j}\right]^{1/2}\left(d_{c,i} + d_{c,j}\right)^2 \tag{3.29}$$

Coagulation processes typically reach a state of self-preservation after a certain time lag, resulting in a size distribution that follows a log-normal shape [49, 227, 231]. Population balance models often utilize this phenomenon to make assumptions about the shape of the particle size distribution. One such example is the classical method of moments, which is discussed in section 3.6.2.

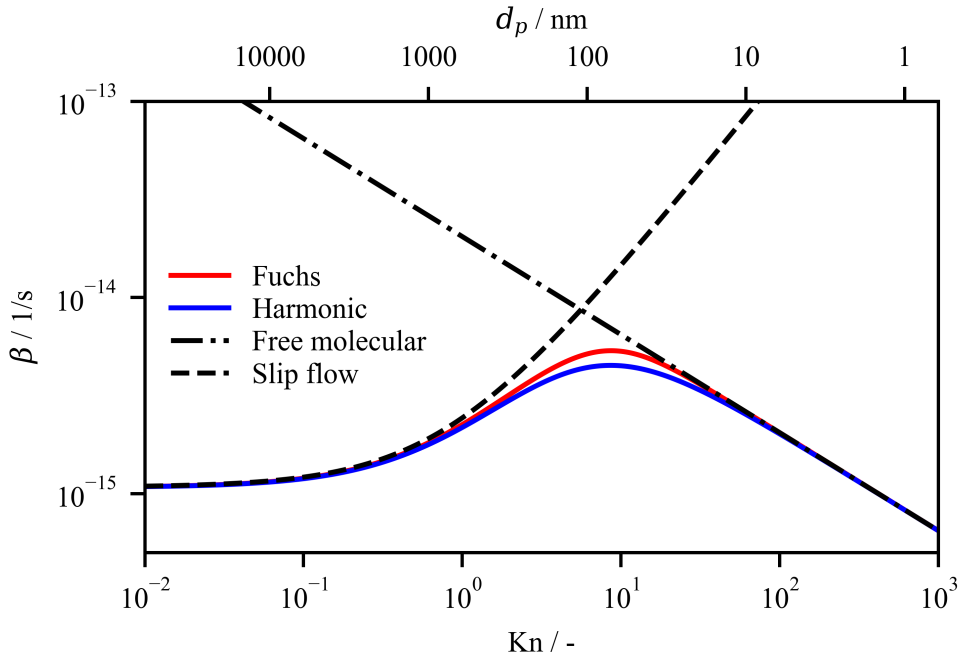

Fig.: 3.2 Comparison of the Fuchs (red) and harmonic mean (blue) formulation (Eqs. 3.22 and 5.28) for silicon particles in nitrogen at T = 1200 K and p = 1 bar. The factor α of Eq. (5.29) is set to 1.0.

3.4 Coalescence

As the process temperature increases, the collision rate is enhanced according to equations (3.18) and (3.19), and as a consequence, larger dendritic aggregates are expected to form. Contrarily, it is observed that with increased temperature, primary particles within an aggregate start fusing, leading to bulkier aggregates with decreased surface area. This phenomenon is known as coalescence, or sintering, and occurs – depending on the particle size – even way below the melting point of the bulk material [48]. Hence, the particle morphology depends on the ratio of coagulation and coalescence time scales. As figure 3.3 shows, if the sintering process is slow compared to coagulation, complex fractal-shaped particles are formed. The opposite happens, if sintering is the faster process: particles coalesce as they collide and tend to form a spherical unit.

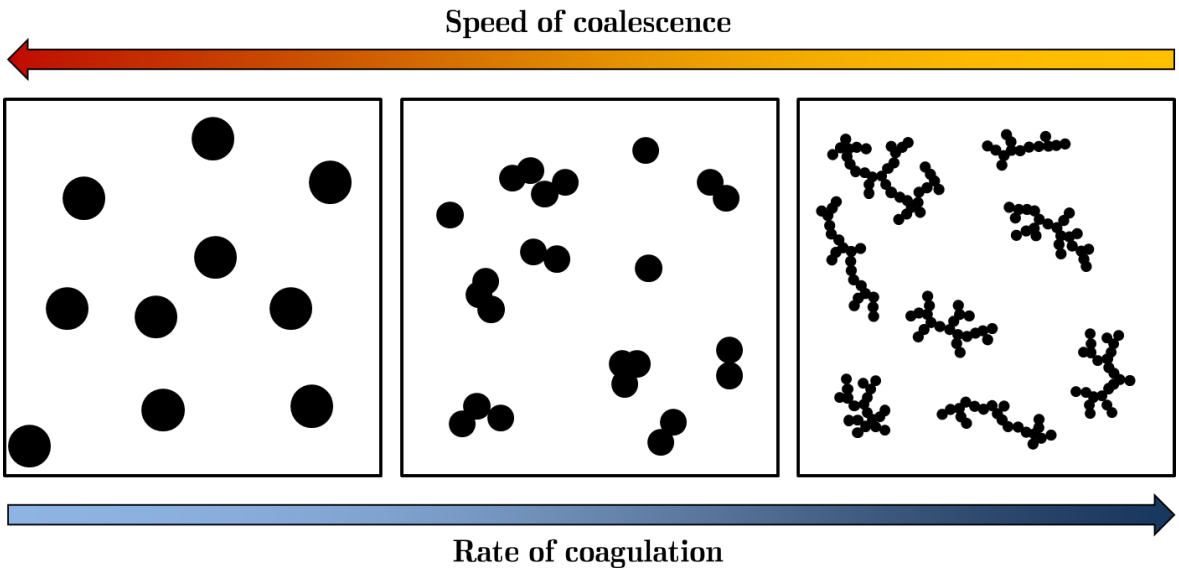

Fig.: 3.3 Correlation of particle morphology for different rates of coagulation and coalescence. If coalescence is fast compared to coagulation, particles tend to fuse to bigger spherical units. In the other case, if coagulation is faster, particles build more dendritic structures of partially sintered agglomerates.

Generally, the sinter process is described in terms of a characteristic sintering time τ and the difference of particle surface area a_i to the surface of a spherical shaped particle $a_{rnd,i}$ (stage of minimum surface energy) containing the same volume. The linear model (Eq. 3.30) is consistent with experimental and numerical investigations [45, 50] and is valid for the main sintering period after the short, non-linear initialization time [48].

$$\frac{da_i}{dt} = -\frac{1}{\tau_i}(a_i - a_{rnd,i}) \tag{3.30}$$

The characteristic sintering time τ is defined differently for liquid (droplets) and crystalline particles. In former case, τ is determined in dependency of viscosity η, surface tension σ and primary particle diameter d_p [45]:

$$\tau = \frac{\pi \eta d_p}{\sigma} \tag{3.31}$$

For crystalline particles, τ is derived as [50]:

$$\tau = \frac{3}{64\pi} \frac{kTv}{D\sigma v_m} \tag{3.32}$$

The variables v_m and v are the molecular- and the particle volume, while D determines the diffusion coefficient of the solid state. The latter takes the Arrhenius like form (3.33) for the solid state:

$$D = D_0 \exp(-E/RT) \tag{3.33}$$

In the equation above, E and D_0 represent the activation energy and an offset parameter for the diffusion coefficient, while R is the universal gas constant. The parameters D_0 and E are material specific and approximated for most materials.
There are other definitions and fits for the primary particle sintering time [25, 26, 105, 233]. Particle morphology is fundamentally affected by the rate of coalescence and coagulation: only when sintering rates are lower than coagulation rates complex particle structures are formed. An example discussed by Friedlander [48] illustrates the expected particle morphology for two different sintering rates compared to a fixed slope for the coagulation rate. The two cases (a and b) are visualized in Figure 3.4. In case (a), particles remain in point contact (soft agglomerates) when the sintering rate strongly decreases compared to the coagulation rate. Case (b) demonstrates the partially sintered state of primary particles, where sintering becomes less dominant, but still affects the particle structure, leading to the formation of stronger bonds with sintering necks.

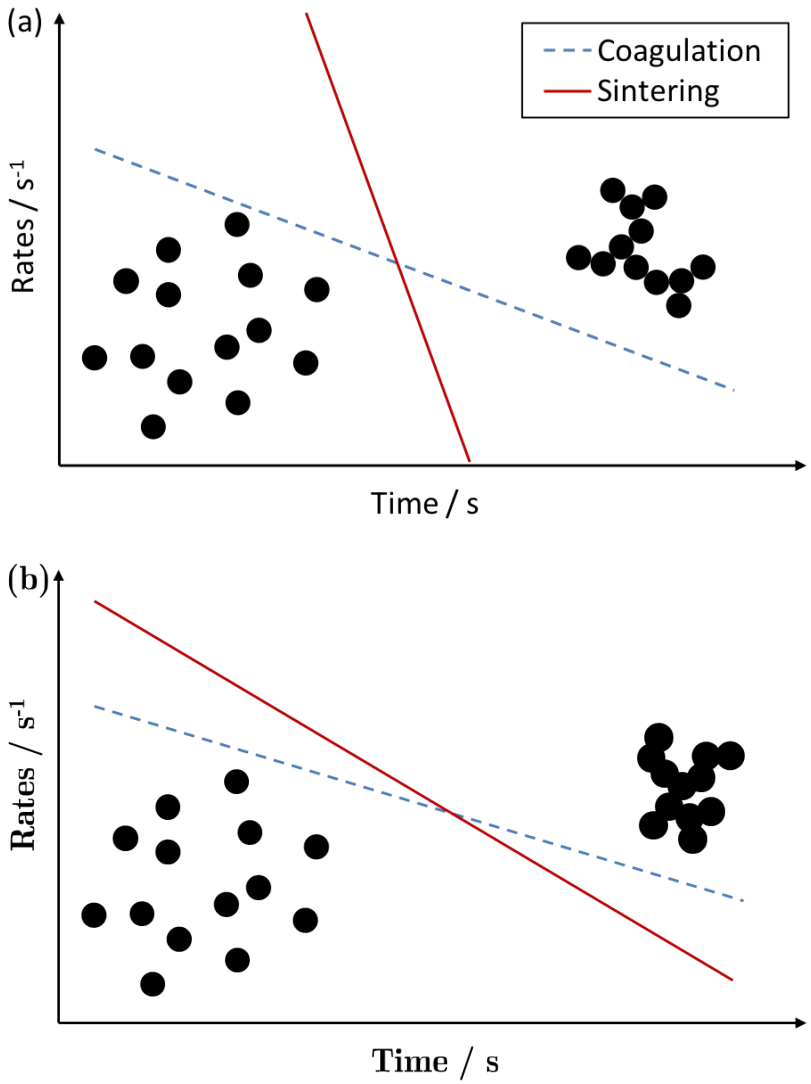

Fig.: 3.4 Particle evolution for different time histories of coagulation and coalescence rates. (a) The sintering rate drops rapidly, while the coagulation rate decreases moderately. Weakly point-connected aggregates are formed. (b) The sintering rate decreases slightly faster than the coagulation rate (but slower than in (a)). Primary particles are connected via strong sintering necks (partially sintered).

3.5 The General Dynamic Equation for Nanoparticle Evolution

In previous sections, all relevant phenomena for particle inception and growth, have been discussed. In this section, an equation is derived, which takes all those processes into account in order to capture the dynamics of a particle size distribution in time and space $n_i(\mathbf{x}, v, t)$. This equation is known as the general dynamic equation (GDE) and is of key importance for this work. Balance equations of several moments are derived from the continuous form of the GDE, which is discussed in this section. As already shown in previous sections, the processes described by the GDE directly depend on the gas state and properties, thus, the set of equations have to be solved in a coupled manner or the gas state has to be approximated when the GDE is solved. As a nonlinear partial differential equation, the GDE can be solved analytically only for simplified cases and requires otherwise iterative numerical methods for a solution.

3.5.1 The Generalised Smoluchowski Equation

The Smoluchowski coagulation equation (Eq. 3.13) can be extended by particle formation and growth in order to derive a discrete general dynamics equation:

$$\frac{\partial n_i}{\partial t} = \frac{1}{2} \sum_{\substack{j+k=i \\ i,j\neq 1}}^{i-2} \beta(j,k) n_j n_k - \sum_{j=2}^{\infty} \beta(i,j) n_i n_j + I_i - I_{i+1} \tag{3.34}$$

The number concentration n_i gives the count of particles of size i. The indices $i, j, k \in \mathbb{N}$ determine the particle size, i.e. the number of molecules contained in the particle. The first two terms on the right-hand side are the rates of change by coagulation, and the homogeneous nucleation rate I_i, which is defined by Eq. 3.7 for particle size i. It represents the rate of change in the distribution by monomers nucleating on or evaporating from the surface of particles. The monomer equation ($i = 1$) is generally used for particle initialization, where particles are seeded by chemical reaction sources $I_1 = \omega_1 N_A$ from the gas phase, or by an initial concentration.

$$\frac{\partial n_1}{\partial t} = -\sum_{j=2}^{\infty} \beta(1,j) n_1 n_j + \alpha_{k+1} S_{k+1} n_{k+1} + I_1 \tag{3.35}$$

By applying the transport theorems for diffusive and convective flow (see chapter 2.1) on the generalized Smoluchowski equation (3.34), a conservation equation, which accounts for

physical space and time can be derived as:

$$\frac{\partial n_i}{\partial t} + \nabla \cdot (n_i \mathbf{u}) = \nabla \cdot (D_i \nabla n_i) + \frac{1}{2} \sum_{\substack{j+k=i \\ i,j \neq 1}}^{i-2} \beta(j,k) n_j n_k - \sum_{j=2}^{\infty} \beta(i,j) n_i n_j + I_i - I_{i+1} - \nabla \cdot (\mathbf{c} n_i). \quad (3.36)$$

The vectors **u** and **c** represent the gas phase velocity and external drift velocities acting on the particle ensemble. Thus, the last terms on the right hand and left hand side of Eq. (3.36) account for convective fluxes. Typical examples for **c** are particle drift velocities forced by thermophoresis or magnetic fields [48]. The first term on the left hand side represents the diffusive flux with the diffusion coefficient D_i for particles of size i.

3.5.2 The GDE in Continuous Distribution Form

As particle sizes increase, the number of molecules within a particle can reach very high values, and Eq. (3.36) becomes inconvenient, and transforming the GDE into a continuous particle distribution space is convenient. Therefore, in the following, this transformation will be shown for particle sizes bigger than the monomer size ($v > v_1$).
The Smoluchowski equation for coagulation (Eq. 3.13) is integrated over the particle volume space $\tilde{v}$ of the collision partner, yielding an equation (3.37) for the particle number concentration as a function of the particle volume v.

$$\frac{\partial n}{\partial t}_{coag} = \frac{1}{2} \int_0^v \beta(v, v-\tilde{v}) n(\tilde{v}) n(v-\tilde{v}) d\tilde{v} - \int_0^{\infty} \beta(v,\tilde{v}) n(v) n(\tilde{v}) d\tilde{v} \quad (3.37)$$

The source of the particle current, which acts on different particle sizes v in v-space is responsible for growth and becomes:

$$\frac{\partial n}{\partial t}_{growth} = -\frac{\partial I}{\partial v} \quad (3.38)$$

The particle current I can be determined in terms of a diffusion drift velocity in v space [48].

$$I = -D_v \frac{\partial n}{\partial v} + nq \quad (3.39)$$

The variable q is the velocity at which particles migrate through the v space. Similar to the procedure for Eq. 3.36, the conservation equation for n is derived as:

$$\begin{aligned}\frac{\partial n}{\partial t} + \nabla \cdot (n\vec{u}) =& \nabla \cdot (D\nabla n) \frac{1}{2}\int_0^v \beta(v, v-\tilde{v}) n(\tilde{v}) n(v-\tilde{v}) d\tilde{v} \\ &- \int_0^\infty \beta(v, \tilde{v}) n(v) n(\tilde{v}) d\tilde{v} - \frac{\partial I}{\partial v} - \nabla \cdot (\vec{c} n).\end{aligned} \tag{3.40}$$

Starting with the first term on the left hand side, this equation covers changes for n in time, caused by convection, diffusion, coagulation, growth, and drift.

3.6 Simplified GDE solution Methods for Application in CFD

3.6.1 Method of Moments

In the method of moments, the distribution function is transformed into the moment space, where each moment M_r is defined as:

$$M_r = \int_0^\infty n(v) v^r dv. \tag{3.41}$$

Where $n(v)$ and v are the particle size distribution per particle volume unit and the respective particle volume. The size distribution function $n(v)$ itself can only be completely recovered by the knowledge of all moments ($r = 0, 1, 2, ..., \infty$). If the shape of $n(v)$ is not of interest itself, but can be assumed, a setup of three moments ($r = 0, 1, 2$) is a popular choice. In general, the size distribution function is not available when the moment method is used to approximate the GDE. Therefore, a functional $P(v,t)$ is chosen for estimation of the size distribution [37, 118, 169, 175, 240]. Hence, the moment equation is reformulated:

$$M_r = N \int_0^\infty v^r P dv \tag{3.42}$$

The variable N represents the absolute particle number concentration, and is equal to the first moment $N = M_0$. Once Brownian coagulation processes have reached the time to self-preservation, the resulting size spectra tend to follow a log-normal distribution, which is commonly used as the presumed size distribution (as shown in Eq. 3.43) [49, 227, 231].

$$P = \frac{1}{v\sqrt{2\pi}\sigma_v} \exp\left[-\frac{1}{2}\left(\frac{\ln\left(v/v_g\right)}{\sigma_v}\right)^2\right] \tag{3.43}$$

Here, σ_v and v_g are the standard deviation and the geometric mean particle volume [37]. The temporal derivatives of the moments are determined by the homogeneous nucleation rate R_r, the coagulation rate G_r and the particle growth (heterogeneous nucleation) rate W_r.

$$\frac{dM_0}{dt} = R_0 - G_0 \tag{3.44}$$

$$\frac{dM_1}{dt} = R_1 + W_1 \tag{3.45}$$

$$\frac{dM_2}{dt} = R_2 + G_2 + W_2 \tag{3.46}$$

$$\frac{dM_r}{dt} = R_r + G_r + W_r \tag{3.47}$$

The coagulation rate of the continuous particle size distribution is obtained by integration over the whole range of possible collisions. Applying the aforementioned log-normal distribution, Dobbins et al. [37] derived the following expressions for the coagulation rates for the zero and second moment:

$$G_0 = K_{fm} * 2\sqrt{2}N^2 v_g^{1/6} \exp(3/16\sigma_v^2) \tag{3.48}$$

$$G_2 = -K_{fm} * 4\sqrt{2}N^2 v_g^{13/6} \exp(65/48\sigma_v^2). \tag{3.49}$$

Using the monomer nucleation rate I and the surface growth S, the equivalent values for higher moments are calculated by:

$$R_r = I v_0^r \tag{3.50}$$

$$W_r = S v_0^r. \tag{3.51}$$

Here, $v_0^r = M_r/N = M_r/M_0$ are the volumetric moments and the higher moments M_r are scaled by the first moment M_0, which represents the particle number concentration N. The sources T and S can be calculated using the approaches aforementioned in this chapter. The time-dependent values σ_v and v_g of the log-normal distribution can be calculated by the knowledge of the first three moments:

$$v_g = \frac{V^2}{N^{3/2} M_2^{1/2}}, \tag{3.52}$$

$$\sigma_v = \ln\left(\frac{M_2 N}{V^2}\right) \tag{3.53}$$

Moreover, a variety of classes of the method of moments (MOM) exist, modified for different conditions. A more general description of the presumed size distribution can be achieved by using a complex iterative closure (MOMIC) [5, 46], or by the adaptive quadrature method of moments (QMOM) [136].

3.6.2 Monodisperse Model

The monodisperse model (MM) introduced by Kruis et al. [113] uses the simplest presumed distribution function, the delta distribution $\delta(x)$, which is ∞ for $x = 0$, otherwise 0 and has an integral of 1. It is equivalent to an ensemble consisting of particles of the same size, known as a monodisperse ensemble. The simplicity of this definition allows the introduction of a bivariate moment approach for the particle volume and surface, which contains information about the particle morphology:

$$M_1^v = N \int_0^\infty \delta(v_0 - v) dv = V \tag{3.54}$$

$$M_1^a = N \int_0^\infty \delta(s_0 - s) ds = A \tag{3.55}$$

The moments M_1^v and M_1^a represent the average particle volume concentration A and the average particle surface concentration V. Since the zeroth moment is represented by the number concentration $N = M_0$, the GDE can be described by the evolution of these three coupled quantities:

$$\frac{\partial N}{\partial t} + \nabla \cdot \boldsymbol{u} N = \nabla \cdot (D_N \nabla N) + I_N - \frac{1}{2} \beta N^2 \tag{3.56}$$

$$\frac{\partial A}{\partial t} + \nabla \cdot \boldsymbol{u} A = \nabla \cdot (\boldsymbol{j}_A) + I_A - \frac{1}{\tau} (A - A_S) \tag{3.57}$$

$$\frac{\partial V}{\partial t} + \nabla \cdot \boldsymbol{u} V = \nabla \cdot (\boldsymbol{j}_V) + I_V \tag{3.58}$$

The first term on the RHS describes the particle diffusion, which is defined using Fick's law. Since higher moments ($r > 0$) are attributes, which depend on the zeroth moment, calculating the terms $\boldsymbol{j}_A$ and $\boldsymbol{j}_V$ applying Fick's law is problematic, as the transported quantities may diffuse independent from each other. Because of low diffusivity of the particle phase, the error is assumed to be small and Fick's law is therefore applied as simple diffusion closure $j_\phi = D \nabla \phi$. The second term on the RHS of equations (3.56) to (3.58) denotes the inception rate source terms, where I_N is described in section 3.1, while I_A and I_V can be calculated – according to their definition – similar to Eq. (3.50) [159]. The last terms on the RHS

of equation (3.56) and equation (3.57) account for coagulation and sintering, where the definition of the collision kernel β and the characteristic sintering time τ can be found in sections 3.3 and 3.4, respectively. The completely fused particle surface concentration is given by:

$$A_S = \pi d_a^2 N \tag{3.59}$$

The volumetric particle diameter d_a calculated by:

$$d_a = \left(\frac{6V}{\pi N}\right)^{\frac{1}{3}} \tag{3.60}$$

By the relation of the particle volume and surface area, an expression for the primary particle diameter can be found assuming all primary particles being in point contact [113]:

$$d_p = \left(\frac{6V}{A}\right) \tag{3.61}$$

Moreover, the knowledge of the primary particle size yields the number of primaries contained within one aggregate:

$$n_p = \frac{6V}{\pi N d_p^3} \tag{3.62}$$

Both quantities d_p and n_p are necessary for calculating the collision diameter, a mathematical value, which accounts for the more complex morphology of particles by converting it to the collision based spherical equivalent.

$$d_c = d_p n_p^{\frac{1}{D_f}} \tag{3.63}$$

The fractal dimension D_f is considered a model constant in this approach [113]. It is represented by the asymptotic value for D_f attained, when an aggregate reaches a certain amount of primary particles ($n_p \approx 10-30$) [62, 63]. However, the actual value of D_f depends on the material system being studied [48].

The monodisperse method represents a simple and effective model for investigations of particle characteristics including the morphology. It delivers the accuracy to produce quantitative predictions and trends in many cases, while its efficiency makes it a valuable tool for CFD calculations. The main advantage of this method is also its disadvantage: the inclusion of particle morphology in the model requires the implementation of sophisticated formulations for particle nucleation and growth in many industrially relevant processes. Models like the basic MOM or the sectional model assume the particles to be spherical, which is equivalent to instant coalescence. For these models, homogeneous and heterogeneous nucleation means

the same since the univariate particle representation smears any differences. This is not the case, if multivariate models are applied. If, for example, only nucleation of monomers from a chemical source is accounted for particle inception, the surface increases drastically, leading to shrinking primary particle sizes, which violates the single particle mass conservation. This behavior may lead to a false prediction of long chained clusters of tiny particles and is also discussed by Jeong and Choi [88]. One potential solution is to adjust the sintering model parameters, which could correct some of the predicted particle values. However, this approach only provides a temporary fix and does not address the underlying model limitations, but rather masks them. Therefore, if multivariate models are applied, multiscale modeling in terms of molecular surface interaction (condensation, reaction) and homogeneous nucleation is mandatory. This might not be obvious in some academic synthesis cases, where very low precursor concentrations are used. Though, if the amount of precursor is enhanced or/and lower process temperatures are encountered, it is likely that significant errors in the mass conservation of existing particles essentially increase the uncertainties.

3.6.3 Bimodal Moment Method

When nucleation is modeled by adding numerous small monomers to the moments, the average primary particle size decreases as a result of the strong source with a high N to V ratio. This leads to errors especially, if a uniform size distribution is presumed, like it is the case in the monodisperse model. The model then instantly predicts a decreasing average particle size leading to a growing error in every depending quantity like β, τ, d_p, ... Jeong and Choi [88] therefore extended the monodisperse model by a further mode, which separates the mode of incepted monomer particles N_1 from the main mode N_2. Because all monomer particles within the inception node are assumed to be spherical and uniform in size, it is fully described by the number concentration N_1. The interaction between the two modes is realized by multi modal and inter modal coagulation. With this extensions, the continuous GDE is approximated by the following four conservation equations:

$$\frac{\partial \widetilde{N}_1}{\partial t} + \nabla \cdot \widetilde{\boldsymbol{u}} \widetilde{N}_1 = \nabla \cdot \left(D_{N_1} \nabla \widetilde{N}_1 \right) + I_{N_1} - \frac{1}{2} \beta_{11} \widetilde{N}_1^2 \left(\frac{r}{r-1} \right) - \beta_{12} \widetilde{N}_1 \widetilde{N}_2 \tag{3.64}$$

$$\frac{\partial \widetilde{N}_2}{\partial t} + \nabla \cdot \widetilde{\boldsymbol{u}} \widetilde{N}_2 = \nabla \cdot \left(D_{N_2} \nabla \widetilde{N}_2 \right) + \frac{1}{2} \beta_{11} \widetilde{N}_1^2 \left(\frac{1}{r-1} \right) - \frac{1}{2} \beta_{22} \widetilde{N}_2^2 \tag{3.65}$$

$$\frac{\partial \widetilde{A}_2}{\partial t} + \nabla \cdot \widetilde{\boldsymbol{u}} \widetilde{A}_2 = \nabla \cdot \left(\boldsymbol{j}_{A_2} \right) - \frac{1}{\tau} \left(\widetilde{A}_2 - \widetilde{A}_{S,2} \right) + \frac{1}{2} \beta_{11} \widetilde{N}_1^2 \left(\frac{r}{r-1} \right) a_m + \beta_{12} \widetilde{N}_1 \widetilde{N}_2 a_m \tag{3.66}$$

$$\frac{\partial \widetilde{V}_2}{\partial t} + \nabla \cdot \widetilde{\boldsymbol{u}} \widetilde{V}_2 = \nabla \cdot \left(\boldsymbol{j}_{V_2} \right) + \frac{1}{2} \beta_{11} \widetilde{N}_1^2 \left(\frac{r}{r-1} \right) v_m + \beta_{12} \widetilde{N}_1 \widetilde{N}_2 v_m \tag{3.67}$$

The inception mode N_1 includes the nucleation source term I_N and buffers the monomer particle contribution of the particle size distribution, while it interacts with the monodisperse aggregation mode determined by N_2, A_2 and V_2. The interaction of inception and aggregation mode is controlled by β_{11} and β_{12}, the intra-modal coagulation and the coagulation between inception and aggregation modes. Both processes result in a flux from mode 1 to mode 2, where β_{12} does not increase the number but the volume and surface of the aggregation mode, resulting in a condensation like behavior for the main mode. The process β_{11} on the other hand, reduces the particle size of the aggregation mode, but with particle sizes being increased by the factor r (see [88]). With a total volume concentration $V_t = V_1 + V_2$ and a total number concentration $N_t = N_1 + N_2$, the total average particle diameter is calculated by:

$$d_{t,av} = \left(\frac{6 V_t}{\pi N_t} \right)^{1/3} \tag{3.68}$$

The bimodal model improves the monodisperse model, especially, if the transition from gas to particle phase is simplified by nucleating monomers. The buffered monomer phase considerably decreases the error made by the monodisperse model, if similar simplifications are applied regarding the nucleation and condensation. Nevertheless, the model suffers from oversimplification of the nucleation model, which only depends on the factor r and by definition underpredicts the nucleation, if the volume of particles within the main mode v_2 is very large in comparison to those of the nucleation mode $v_2 \gg v_1$. An idea to avoid this problem could be applying the models mentioned in the sub-sections 3.2 and 3.3 to split condensation and nucleation contributions for the main mode.

3.6.4 Sectional Model

The sectional model can be understood as a discretization that describes a distribution at predefined grid points within the particle-size spectrum. In fact, the mathematical formulation supports various grid spacing, as long the mandatory interpolation function (3.73) holds. The discretization can be described as:

$$Q_k = \int_0^\infty n_k(v) dv = N_k \int_0^\infty \sigma(v_k - v) dv \tag{3.69}$$

Where Q_k is the number concentration of section k, containing a uniform particle size v_k. Since only spherically shaped particles are assumed, the sections are sufficiently described

by just one moment. A simplified GDE can then be recovered by a set of equations:

$$\frac{\partial Q_k}{\partial t} + \nabla \cdot \boldsymbol{u} Q_k = \nabla \cdot \left(D_{Q_k} \nabla Q_k \right) + \overline{I}_{Q_1} + \overline{\dot{\omega}}^{Q} \tag{3.70}$$

Here, D_{Q_k} represents the diffusion coefficient of particles within section k (see Eq. 3.17), while $\overline{\dot{\omega}}^{Q}$ covers the impact of coagulation. The first section usually represents the monomer $v_1 = v_m$ for simple nucleation models, which make the inception source I_{Q1} only affect the nucleation mode:

$$\overline{I}_{Q_1} = \int_{k=1}^{\infty} \overline{I} \delta(1-k) dk \tag{3.71}$$

The nucleation term $\overline{\dot{\omega}}^{Q}$ is calculated by equation (3.72), which is differently defined for the inception mode and for the remaining modes.

$$\overline{\dot{\omega}}^{Q} = \begin{cases} -\sum_{i=1}^{N_s} \beta_{i1} Q_i Q_1 & k = 1 \\ +\frac{1}{2} \sum_{i=1}^{N_s} \sum_{j=1}^{N_s} \chi_{ijk} \beta_{ij} Q_i Q_j - \sum_{i=1}^{N_s} \beta_{ik} Q_i Q_k & k \neq 1 \end{cases} \tag{3.72}$$

Here, β is the collision frequency, which was discussed in section 3.3, whereas χ_{ijk} is an interpolation function. The latter is necessary, as the particle sizes resulting from coagulation do not necessarily match the average diameter of a specific section. The interpolation formulation (3.73) therefore helps to ensure mass conservation by splitting the particle source between two neighboring sections.

$$\chi_{ijk} = \begin{cases} \frac{v_{k+1} - (v_i + v_j)}{v_{k+1} - v_k} & v_k \leq (v_i + v_j) < v_{k+1} \\ \frac{v_i + v_j - v_{k-1}}{v_k - v_{k-1}} & v_{k-1} \leq (v_i + v_j) < v_k \\ 0 & \text{else} \end{cases} \tag{3.73}$$

The volume average particle diameter d_{va} is then calculated by:

$$d_{va} = \left(\frac{6 v_{na}}{\pi} \right) \tag{3.74}$$

It depends on the average particle volume v_{na}, which is defined as:

$$v_{na} = \frac{\sum_{k=1}^{N_s} Q_k v_k}{\sum_{k=1}^{N_s} Q_k} \tag{3.75}$$

Equivalently, the number averaged particle diameter d_{na} can be determined using the following expression:

$$d_{na} = \frac{\sum_{k=1}^{N_s} Q_k d(v_k)}{\sum_{k=1}^{N_s} Q_k} \tag{3.76}$$

If heterogeneous condensation rates are low and sintering rates are significantly higher than collision rates, the sectional model can be a powerful tool for processes that are supposed to generate narrow to intermediate wide particle size spectra. This is the case in high temperature synthesis processes with very low precursor loading and short residence times. However, it is not straight forward to calculate the inception source I using the general nucleation theory (homogeneous or heterogeneous) discussed in sections 3.1 and 3.2, since the nucleation procedure described in equation (3.71) is limited to one size class. It is therefore common to treat monomers directly as instantly nucleated. This procedure leads to a very high number of small particles within the inception mode, which results in very small time step limits for the coagulation process and therefore stiffens the resulting ODE. Since wider spacing between section cause higher numerical diffusion in the particle size distribution space, higher accuracy claims a higher resolution and therefore higher computational effort. If we consider the volume increasing equally with the number of molecules within one particle, logarithmic sizing of section should be done with care: applying an exponential growth with a base of 2 already leads to a difference of 1024 times v_1 in between of section 11 and 12, between sections 15 and 16, the difference is already 16,384 times the monomer size v_1. This can result in particle flows getting stuck in – comparatively – very large sections that would normally move together in particle size space. Also, if big particles are large in number, round off errors may play a role within the interaction of small and large bins. Nevertheless, Prakash et al. applied nucleation modeling to the sectional model and showed that more appropriate nucleation models can be implemented by using an interpolation model in the region of smaller sections. Though, detailed surface reactions can not be realized without artificial widening of the distribution: the growth of sections is modeled as particle flux into neighboring bins. A drifting bin size could be a possible solution, but the formulation is challenging, since every bin experiences a different drift due to different surface grow rates leading to shifting spaces between sections. Moreover, the restrictions in number of sections and the exponentially growing complexity with increasing PSD dimensionality limit the

usability to univariate cases. Within this work, GDE models have been developed, which feature the sectional approximation of the particle size-distribution embedded in a framework that allows the simulation of more sophisticated synthesis processes. In chapter 4, a model is presented that was developed to predict complex heterogeneous particle systems. The model is applied in the context of spray flame synthesis, where a mass conserving tabulation method for the nucleation source is introduced together with a tabulated chemistry approach [224, 225]. Chapter 5 shows a novel model that couples the gas- with the particle phase by nucleation, condensation and evaporation modeling. Among others, a model for nucleation which was introduced by Girshick and Chiu [59] is combined with expressions for silicon vapor pressure and surface tension. The model is successfully applied in the simulation of a microwave plasma synthesis process.

3.7 Unpublished Models

Two new and unpublished methods which were developed by the author and follow the methodology of physically connected gas and particle phases by phase transition are introduced in this subsection. The first model is the "bivariate gas to liquid transition model" (BGLT), which combines the monodisperse representation of the particle phase with extended nucleation and condensation/evaporation modeling for vapors condensing from the fully coupled gas phase.
The "digital clone probability weighted Monte-Carlo method" – the second method – is a stochastic model capable of simulating hundreds of thousands of digital particle representations in combination with chemical kinetics in the gas phase or at the particle surface, while being either fully coupled in a stand alone 0D simulation, or one-way coupled with time histories sampled by CFD.

3.7.1 Bivariate Gas to Liquid Transition Model (BGLT)

This model combines the bivariate moment method with extended nucleation and condensation/evaporation modeling for metal vapors condensing from the gas phase. As such, it can also be not only understood as a bivariate, but also as a bimodal model with a hidden mode represented by the condensing species in the gas phase. This hidden mode interacts with the particle dynamics model through nucleation and condensation/evaporation. The monodisperse implementation used for the particle dynamics model is limited to the first moments of the volume V and surface A, as explained in chapter 3.6.2 and allows therefor the computation of the mean values of the particle size spectrum only. This limitation is accepted in exchange for the bivariate particle formulation, the model simplicity, and less

computational effort. Since particles shrink due to evaporation until they are completely absorbed by the gas phase, an implementation in a moment method is not straight forward. Especially the assumption of monodispersity makes the use of a threshold diameter impossible, as the spontaneous disappearance of all particles makes the model physically incorrect and numerically unstable. Therefore, a novel approach was developed which features a fitted complementary error function as transition, splitting the evaporation contributions into parts which decrease the particle diameter and remove existing particles in dependency of the metal atoms contained by the primary particles.

Introducing extensions for the contributions of nucleation, condensation/evaporation, coagulation, and sintering (suberscripted by $I, c/e, co, s$), the conservation equations for N, A, and V are defined as:

$$\frac{\partial N}{\partial t} + \nabla \cdot \boldsymbol{u}_t N = \nabla \cdot (j_N) + \Gamma^I + \Gamma_n^{c/e} + \Gamma^{co}, \tag{3.77}$$

$$\frac{\partial A}{\partial t} + \nabla \cdot \boldsymbol{u}_t A = \nabla \cdot (\boldsymbol{j}_A) + \Gamma^I a_K + \Gamma_a^{c/e} + \Gamma^s, \tag{3.78}$$

$$\frac{\partial V}{\partial t} + \nabla \cdot \boldsymbol{u}_t V = \nabla \cdot \left(\boldsymbol{j}_V\right) + \Gamma^I v_K + \Gamma_v^{c/e}. \tag{3.79}$$

The first three terms of all equations have already been discussed (see 3.6.2), while the nucleation source term Γ_I is calculated as suggested by Girshick and Chiu [59]:

$$\Gamma^I = v_{\mathrm{m}} \left(\frac{2\sigma}{\pi m_{\mathrm{m}}}\right)^{1/2} n_{\mathrm{s}}^2 S \exp\left(\Theta - \frac{4\Theta^3}{27(\ln S)^2}\right) \tag{3.80}$$

In above equation, v_m, m_m are the volume and molecular mass of a monomer of the condensing species, while the surface tension and the monomer number concentration at saturation are denoted by σ, and n_s. The saturation ratio is given by S, while Θ is the dimensionless surface tension, which is given by:

$$\Theta = \frac{\sigma s_m}{k_{\mathrm{B}} T}. \tag{3.81}$$

The variable s_m denotes the surface area of a monomer. The surface area and the volume of the condensing droplets a_K and v_K – used in Eqs. (3.78) and (3.79) – can be calculated by the knowledge of the critical droplet diameter:

$$d_K = \frac{\sigma v_m}{kT \ln(S)} \tag{3.82}$$

The condensation/evaporation source term as volume flux onto the particles surface $\Gamma_v^{c/e}$ is obtained by following equation:

$$\Gamma_v^{c/e} = N d_c^2 (n_n - n_s) v_m \left(\frac{\pi R_u T}{2 W_I} \right)^{\frac{1}{2}} \zeta(\mathrm{Kn}). \tag{3.83}$$

Here, W_I is the molar weight of the nucleating species, while $\zeta(Kn)$ is the free molecular to continuum transition correction function [237].
In case of evaporation (negative $\Gamma_v^{c/e}$ values), the sink must be split in parts for decreasing the particle sizes and removing complete particles in order to avoid nonphysical behavior as the primary particle size d_p decreases. Thus, a volume flux term for particle removal is calculated from the negative part of $\Gamma_v^{c/e}$:

$$R_d = \mathrm{neg}\left(\left[\frac{dV}{dt} \right]_{c/e} \right) \Xi \tag{3.84}$$

The complementary error function Ξ is defined in dependency of the upper and lower limits of atoms contained by the primary particle (γ_u and γ_l) within a primary particle d_p:

$$\Xi = \frac{1}{2} \mathrm{erfc}\left(4 \frac{v_p / v_m - 0.5(\gamma_u + \gamma_l)}{\gamma_u - \gamma_l} \right) \tag{3.85}$$

Applying R_d for the derivation of the condensation/evaporation source terms for the surface and number concentrations, the following expressions are obtained:

$$\Gamma_a^{c/e} = R_d \frac{a_p}{v_p} + \left(\Gamma_v^{c/e} - R_d \right) \frac{4}{d_p}, \tag{3.86}$$

$$\Gamma_n^{c/e} = \frac{R_d}{v_p}. \tag{3.87}$$

The sintering source term Γ^s applied in Eq. 3.78 is given by the last term in Eq. 3.57.
The novel method was verified by a generic 0D test case that features consecutive nucleation, condensation and evaporation as the temperature is changed from 2000 K to 500 K within a time frame of t_c. The same time frame is then used for heating the system from 500 K to 3000 K, resulting in the simulation time $t_{tot} = 2t_c$. Three simulations were performed with different operating times $t_{tot} = 2t_c = 20, 200, 2000$ ms and benchmarked by the comparison with the sectional approach introduced in chapter 5. In order to avoid the influence of particle morphology – the sectional model does not take particle morphology into account – the particles in this benchmark are assumed to be spherical. The vapor pressure p_s is given by an

Antoine-fit calculated by Kömer et al. [109]:

$$p_s = 10^{(7.5341-23399/T)} 101325 \text{ [Pa]} \tag{3.88}$$

The surface tension used in the comparison was fitted by linear regression to match the experimental data from Mezey and Giber [149]:

$$\sigma = 1152.0 \left[\frac{\text{kN}}{\text{m}}\right] - 0.1574/T \left[\frac{\text{kNK}}{\text{m}}\right] \tag{3.89}$$

The model constants, γ_u and γ_l for the upper and lower number of atoms per primary particle in Eq. 3.85 are chosen as 100 and 20, respectively.

Figure 3.5 shows the mass transition of the condensing matter for the three different heating and cooling rates as comparison between the extended sectional approach (left) and the monodisperse approach with transition function (right). It is obvious that both models deliver very similar results and only small differences can be identified during the transition period from gas to particle phase. The total particle number concentrations N_t ($N = N_t$ in the monodisperse case) and the volume averaged particle size d_p of both models are compared in Fig. 3.6 and plotted over the normalized time $\theta = t/t_{tot}$. It can be seen that the discrepancy to the sectional approach increases with decreasing cooling rate (larger t_{tot}), while an overall good agreement in all cases is achieved. The same applies to the prediction of the volume averaged diameter d_p: increasing deviations between both models can be observed for longer cooling/heating time frames.

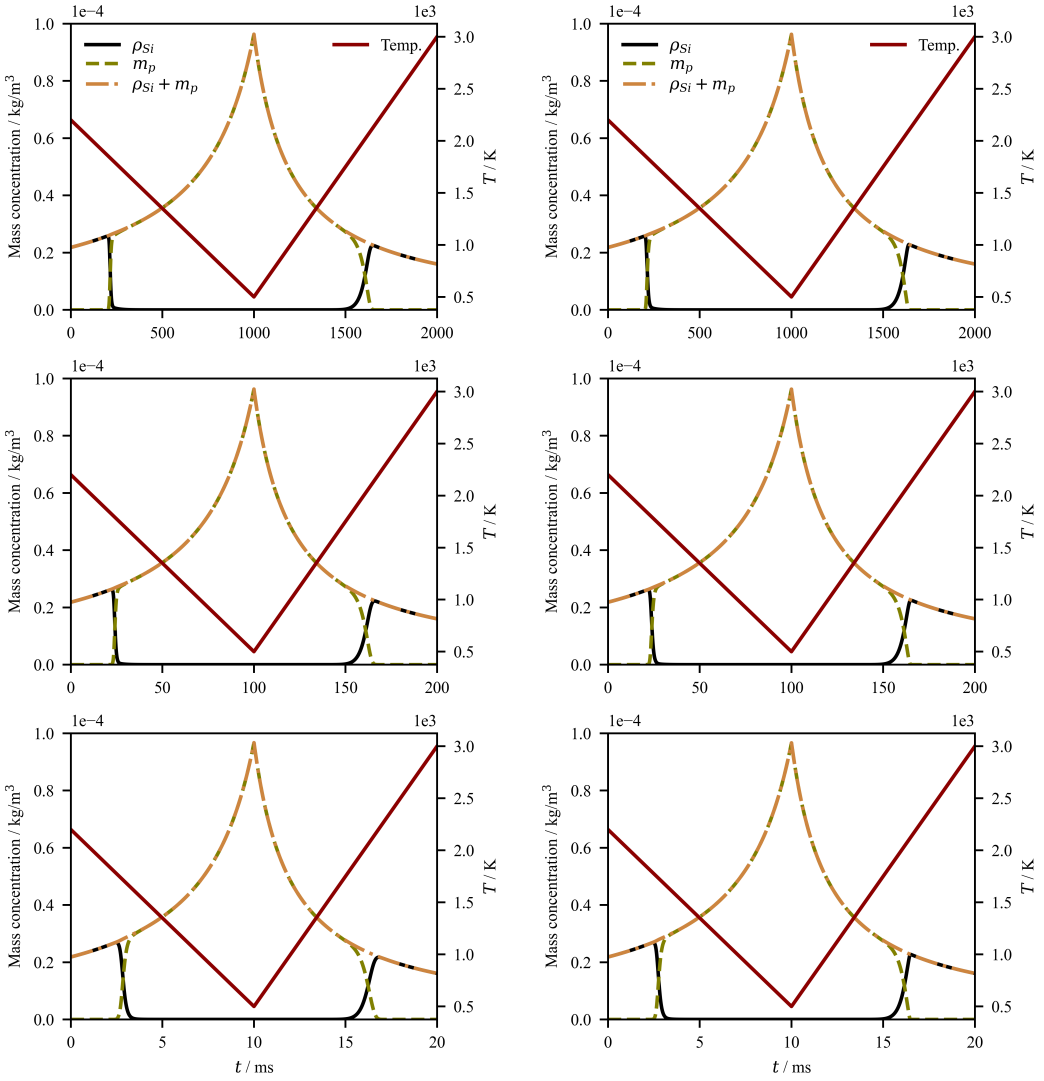

Fig.: 3.5 Mass concentrations of gaseous and dispersed silicon matter ρ_{Si} and m_p of the sectional (left) and the new monodisperse (right) approach for different total simulation timest_{tot} of (from top to bottom) 2000, 200, and 20 ms.

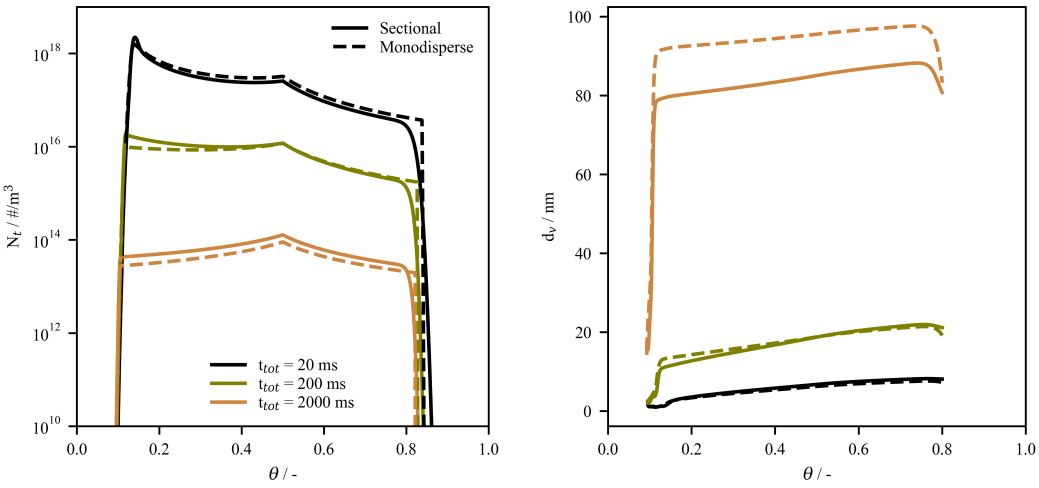

Fig.: 3.6 Total number concentrations N_t (left) and volume averaged particle diameters (right) for all cases (t_{tot} = 20, 200, 2000 ms) plotted over the normalized time θ. Results of the sectional (solid line) and the new monodisperse (dashed line) approach are shown in comparison.

Reasons for those differences are the strong dependencies of the condensation and evaporation rates regarding the particle size distribution. This is more relevant for longer and lower cooling, as condensation becomes more dominant in comparison to nucleation and takes place over a longer period. Figure 3.7 illustrates a comparison of the condensation (left) and evaporation (right) rates $\Gamma^{c/e}$. The rates are scaled by the simulation time t_{tot} in order to allow a better comparison of all cases. The maxima of the scaled condensation rates $\Gamma^{c/e} t_{tot}$ show an increasing discrepancy between the models with decreasing cooling rate, whereby the rates of the monodisperse model variant are generally lower, but start increasing earlier in all cases. Since condensation is a competitive process for nucleation, fewer nuclei and earlier growing particles are the consequence of the early condensation. The opposite happens in case of evaporation: the sectional model variant shows earlier evaporation, but with generally lower peak values.

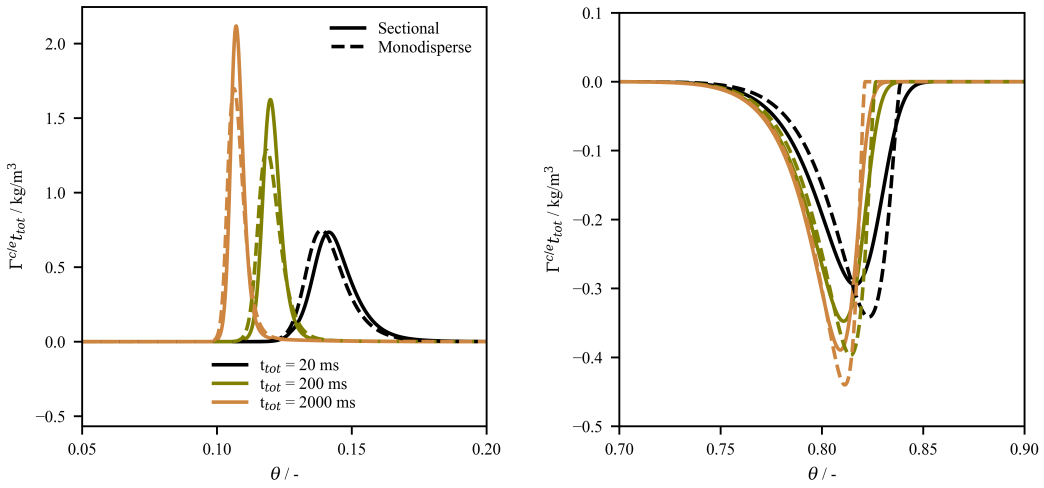

Fig.: 3.7 Scaled condensation/evaporation source term $\Gamma^{c/e}t_h$ for all cases ($t_{tot} = 20, 200, 2000$ ms) plotted over the normalized time θ during the condensation/nucleation (left) and evaporation (right) period. Results of the sectional (solid line) and the new monodisperse (dashed line) approach are shown in comparison.

The BGLT method offers a new approach for simulating nanoparticle dynamics that originate from the vapor phase, which is often present in hot environments like plasma or combustion synthesis processes. It is a monodisperse implementation that is fully coupled with the gas phase and features the phase transition in both directions by condensation/nucleation and evaporation. The model has proven to deliver good accuracy, as it performs well in comparison with a computationally more expensive sectional approach (see chapter 5) and allows predictions of the particle morphology due to its' bivariate definition.
Although the BGLT method has demonstrated good performance in comparison to the sectional approach, further validation using experimental data is necessary. The synthesis of silicon nanoparticles in a microwave plasma reactor, as discussed in chapter 5, is an appropriate validation case for such a study.

3.8 Digital Clone Probability Weighted Monte-Carlo Method

Since Hulburt and Katz [81] introduced a statistical solution method for the population balance modeling to investigate particle dynamics, statistical approaches gained attention in the field of aerosol modeling. Many techniques for solving the population balance equations have been reviewed in detail by Kraft [112], and it has been shown that statistical approaches provide the highest versatility. This is because the level of complexity can be adjusted with a wide range of different models that can be added, swapped, or combined. A good example is

the description of the aggregate: a simple formulation would be a spherical object, which grows by coagulation and additional surface fluxes. The particle type space $P_i(d_p, m)$ would be simply defined by the particle diameter d_p and mass m. Basically, the abstraction of an aggregate to model types, which participate in the simulation, is up to the model developer and depends on the level of detailed needed to reproduce the dynamic particle system. For this work, a statistical simulation software has been developed by the author from scratch, where aggregates are represented by digital clones employing graph theory. The driving simulation methodology is based on the direct simulation Monte Carlo algorithm introduced by Eibeck and Wagner [40] for coagulation, extended by additional procedures for nucleation, surface condensation/reaction and sintering. The theory is briefly explained after the definition of single particle types as digital clones has been clarified.

Figure 3.8 sketches how a real agglomerate (left) is represented by the abstract particle representation (right) by graph theory. Primary particles are defined as single spherical types $p_i(d_p, v_p, s_p, e1, \ldots, e_m)$, which are characterized by their diameter d_p, volume v_p, surface s_p, and virtual edges e_i. The virtual edges $e_i(S_s, C_s, I_s, s, p_l, p_r)$ are only present between

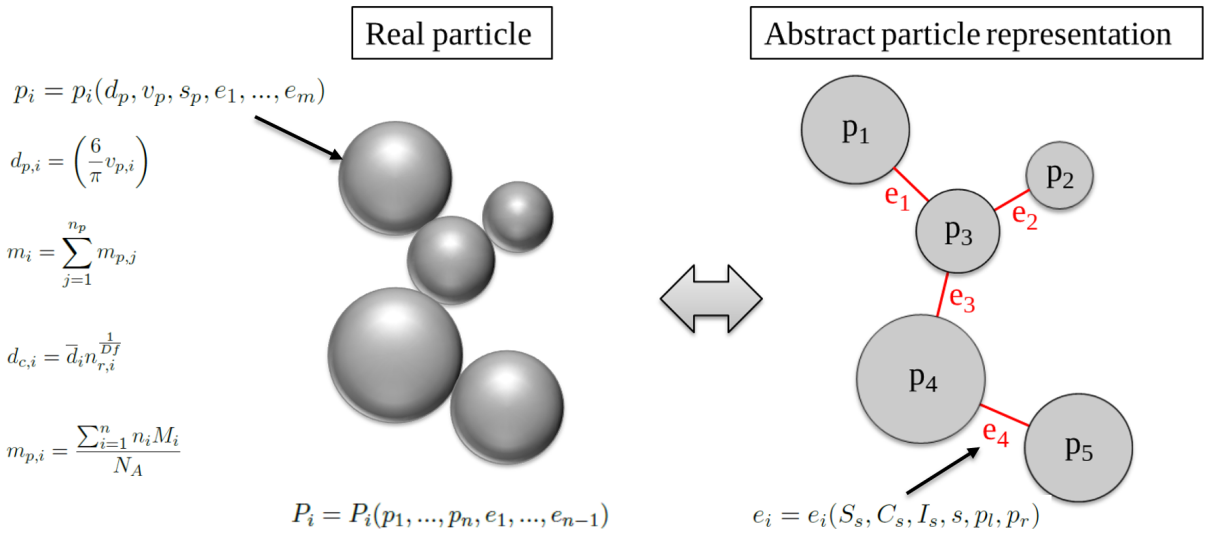

Fig.: 3.8 Sketch of real particle (left) represented by using graph theory (right). Primary particles are defined as single spherical types $p_i(d_p, v_p, s_p, e1, \ldots, e_m)$, edges $e_i(S_s, C_s, I_s, s, p_l, p_r)$ define the sinter state of connected particles. *Note that the angle between primary particles is not featured by the model. The similar arrangement between the real and the abstract aggregate serves as visual support only.*

particles, which are in point contact or partially sintered (p_l and p_r). They define sinter state of the connection by their common spherical (fused) surface S_s, their common surface C_s, their initial (non-sintered) common surface I_s, as well as their sintering progress s (0:

non-sintered, 1: fused; The interested reader is refereed to Sander et al. [190] for the detailed). The aggregate $P_i(p_1,\ldots,p_n,e_1,\ldots,e_{n-1})$ combines all primary particles and edges to a closed system of interconnected spheres. The aggregate mass and the collision diameter are calculated as a function of all primary particles d_{pi}. For the latter, the fractal dimension of the material system must be known (see Fig. 3.8).

Figure 3.9 visualizes the digital clone coagulation process by means of graph theory. One primary particle of each aggregate (P_1 and P_2) is picked (here p_5 of P_1 and p_1 of P_2) and connected by an edge. Subsequently, the smaller aggregate structure is inherited and united to one extended graph. Despite the addition of one edge, the primary particle characteristics do not change during this process. The aggregate mass and collision diameter m and d_c are updated within the aggregation process, as they depend on all enclosed primary particles p_i. It was mentioned that edges carry the information about the sintering status between primary

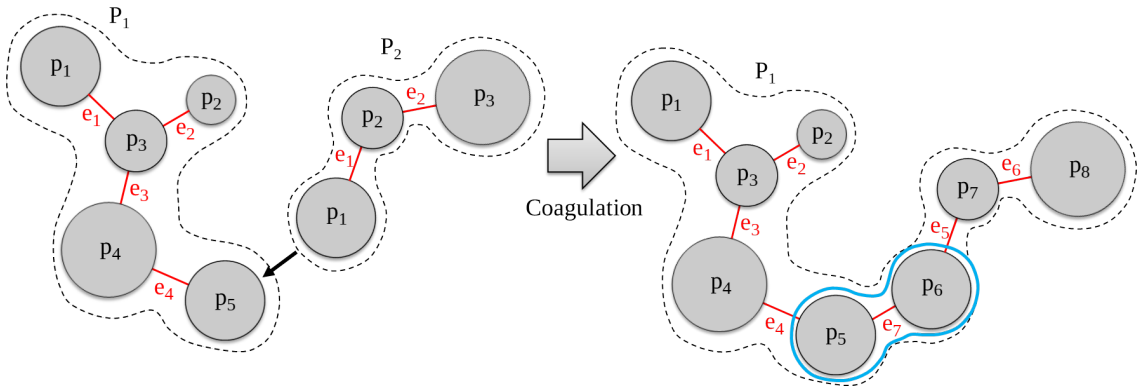

Fig.: 3.9 Sketch of digital clone coagulation by means of graph theory. One primary particle of each aggregate (P_1 and P_2) are picked (p_5 of P_1 and p_1 of P_2) and connected by an edge.

particles p_i of an aggregate P_j. The process of fusing (i.e., $s > 0.99$) is shown by Fig. 3.10, which illustrates the union of two primary particles (p_1 and p_2). For efficiency, the primary particle p_i with the least connecting edges is removed, while the joint particle volume is conserved by increasing the volume of the remaining particle.

Surface reactions with gas phase molecules are realized by increasing the primary particle volume v_p by the reaction products that deposit on the particle surface, while released volatiles remain in the gas phase (Fig. 3.11). The same mechanism is used for surface condensation, whereby the molecules deposit completely on the particle surface. In both cases, the deposited material layer will cause a certain degree of surface rounding (depending on the deposition rate) between connected particles, which increases the sintering level as the primary particle volume v_p grows. The effect of surface rounding is considered by the model proposed by Menz and Kraft [146]. Intra-particle reactions can cause the primary particles

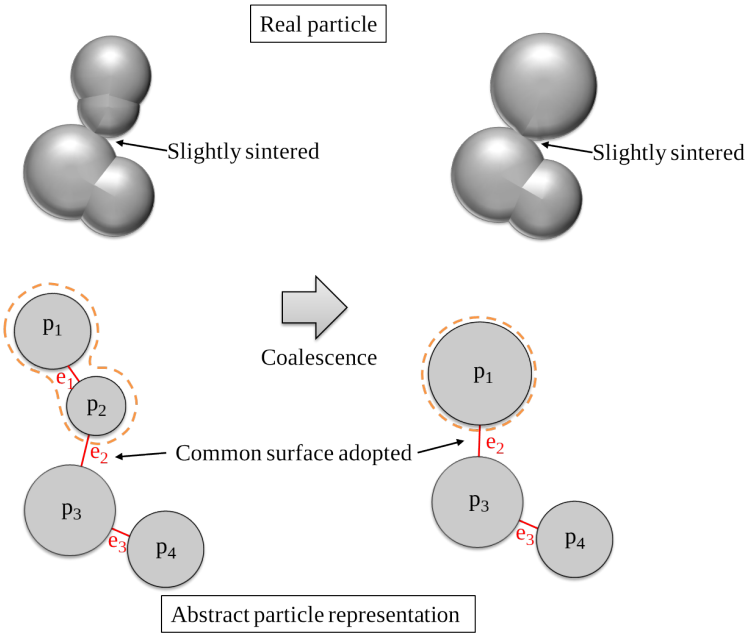

Fig.: 3.10 Illustration of the union of two primary particles (p_1 and p_2) by sintering. The primary particle p_i with the least connecting edges is removed, while the joint particle volume is conserved by increasing the remaining primary particles volume.

to shrink in size as enclosed volatiles are released. This process does simply decrease the primary particle volume v_p and release the diffusing molecules without changing the sintering state. As already mentioned, the simulation methodology is based on the direct simulation Monte Carlo algorithm introduced by Eibeck and Wagner [40], who developed this model for studying coagulation/gelation phenomena by introducing a fictitious jump Markov process. The fictitious jump process takes place in the space of discrete measures $\mathcal{S}^N$, which is defined by:

$$\mathcal{S}^N = \left\{ p = \frac{1}{N} \sum_{i=1}^{n} \delta_{x_i},\ x_i > 0,\ n \in \mathbb{N} \right\}. \tag{3.90}$$

Here, n is the number of particles, x_i is the size of particle i, and δ is the Dirac measure ($\delta_{x_i} = 1$ if $x_i \in \mathcal{S}^N$, otherwise 0). The process itself is calculated by a particle system:

$$U^N = \frac{1}{N} \sum_{i=1}^{n(t)} \delta_{x_i(t)} dx \tag{3.91}$$

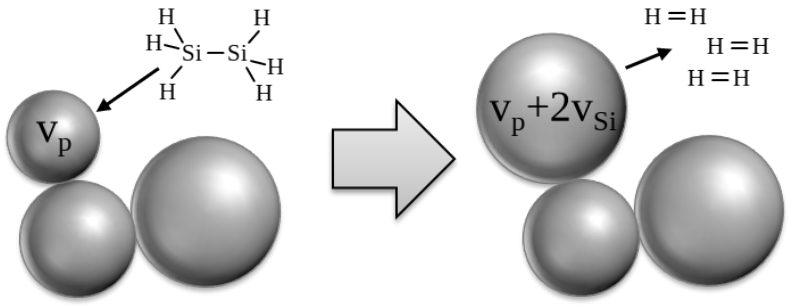

Fig.: 3.11 Sketch of surface reaction represented by the digital clone method. The primary particle volume v_p is increased by the reaction products that join the particle phase while released volatiles remain in the gas phase.

The infinitesimal generator in its' usual form for the given Markov jump processes (see [18] for more information) is defined as:

$$\mathcal{K}^N \Phi(p) = \int_{\mathcal{S}^N} [\Phi(q) - \Phi(p)] Q(p, dq). \tag{3.92}$$

The jump rates from state p into other state J are calculated by the sum of all possible states:

$$Q(p, dq) = \frac{1}{2N} \sum_{1 \le i \ne j \le n} \left\{ K(x_i, x_j) \delta_{J(p,i,j)}(dq) + \left[\hat{K}(x_i, x_j) - K(x_i, x_j) \right] \delta_p(dq) \right\}. \tag{3.93}$$

The change by a possible jump in the discrete space is given as:

$$J(p, i, j) = p + \frac{1}{N} (\delta_{x_i + x_j} - \delta_{x_i} - \delta_{x_j}). \tag{3.94}$$

To speed up the probability-based random process and avoid recomputing all integral values for each jump process, a linearized majorant $\hat{K}$ kernel was introduced. This linearized kernel replaces the quadratic dependency used to determine the entire spectrum of collision pairs. To ensure accuracy, an acceptance/discard procedure was implemented, which applies the original collision kernel to correct the overall probability of the collision processes. For more detailed information, refer to the works of Eibeck and Wagner [40] and Patterson et al. [162]. To accelerate the algorithm, the majorant kernel is introduced to linearize the dependencies of the coagulation kernel. It must satisfy the condition:

$$K(m, n) \le \hat{K}(m, n) \qquad \forall m, n > 0. \tag{3.95}$$

The jump process is timed by an exponential distributed waiting time $\tau(p)$. Reaching the state $p \in \mathcal{S}^N$, the process holds the state for the waiting time, which is calculated as:

$$\text{Prob}\{\tau(p) \geq s\} = \exp(-\rho_K(p)s), \qquad s \geq 0. \tag{3.96}$$

The parameter $\rho_K(p)$ reads:

$$\rho_K(p) = Q(p, \mathcal{S}^N) = \frac{1}{2N} \sum_{1 \leq i \neq j \leq j} \hat{K}(x_i, x_j). \tag{3.97}$$

The probability distribution of the process to jump to state $q \in \mathcal{S}^N$ is a superposition of simple distributions and is described as:

$$\rho(p)^{-1} Q(p, dq) = \sum_{1 \leq i \neq j \leq n} \frac{\hat{K}(x_i, x_j)}{2N\rho(p)} \left\{ \frac{K(x_i, x_j)}{\hat{K}(x_i, x_j)} \delta_{J(p,i,j)}(dq) + \left[1 - \frac{K(x_i, x_j)}{\hat{K}(x_i, x_j)} \right] \delta_p(dq) \right\}. \tag{3.98}$$

Following equation 3.98, the index distribution for a pair i, j is calculated by:

$$\frac{\hat{K}(x_i, x_j)}{2N\rho_K(p)} \tag{3.99}$$

The fictitious jump is then accepted with the probability:

$$1 - \frac{K(x_i, x_j)}{\hat{K}(x_i, x_j)} \tag{3.100}$$

If the jump is not discarded, the state is changed from p to $J(p, i, j)$ i.e. the coagulation step is performed (see Fig. 3.9). With the choice of the maximum number of simulated aggregates N at the starting concentration c_0, the initial number of particles can be determined by:

$$n(0) \backsim N \int_0^\infty c_0(x) dx. \tag{3.101}$$

Since the algorithm is used for higher precursor concentrations up to ambient pressures, a collision kernel must be used that covers both the free molecular and the continuous regime. This is not trivial, as majorant kernels have to be used whenever non-linear dependencies are present. Patterson et al. [162] describe a method to enable the use of the harmonic mean collision kernel for the applied fictitious jump Markov process. The idea is that the minimum

collision rate defines the dominant kernel and thus the transition rate:

$$\sum_{i\neq j} K^{tr}(x_i, x_j) \leq \min\left(\sum_{i\neq j} K^{sf}(x_i, x_j), \sum_{i\neq j} \hat{K}^{fm}(x_i, x_j)\right) = \min(R^{sf}, \hat{R}^{fm}) \tag{3.102}$$

$$\hat{R}^{tr} = \min(R^{sf}, \hat{R}^{fm}) \tag{3.103}$$

The collision pair of indices i, j is then chosen following Eq. (3.99) using the dominant kernel of Eq. (3.102). The jump is then accepted with the given probability:

$$\begin{cases} \dfrac{K^{tr}(x_i, x_j)}{K^{sf}(x_i, x_j)} & \text{if} \quad \hat{R}^{tr} = R^{sf} \\ \dfrac{K^{tr}(x_i, x_j)}{\hat{K}^{fm}(x_i, x_j)} & \text{else} \end{cases} \tag{3.104}$$

The majorant kernel used in Eqs. (3.102) to (3.104) must be close to the maximum of the free molecular kernel K^{fm} to minimize the number of discarded jumps during the acceptance procedure for performance reasons. Therefore, a majorant kernel introduced by Goodson and Kraft [60] is applied, which is most efficient in the range of fractional dimension of $1.7 < D_F < 2.5$.

$$\left(\frac{1}{x} + \frac{1}{y}\right)^{\frac{1}{2}} \left(x^{\frac{1}{Df}} + y^{\frac{1}{Df}}\right)^2 \leq \sqrt{2}\left(x^{-\frac{1}{2}} + y^{-\frac{1}{2}}\right)\left(x^{\frac{2}{Df}} + y^{\frac{2}{Df}}\right) \tag{3.105}$$

Due to the application for complex gas to particle processes of the algorithm developed in this work, more processes like inception, surface growth/reactions and sintering have to be considered. Describing all of those processes would exceed the scope of this chapter and for this reason, the reader is referred to the work of Menz et al. [146], Shekar et al. [199], and Sander et al. [190]. The software makes use of the chemical kinetics library Cantera [61] to account for all kind of chemical processes (combustion, precursor decay, ...) in a two way coupled manner and is capable of processing tracer particle histories from 3D simulations.

The model was tested on several stages of the development process on different levels of complexity using data of the work cited in this chapter. A validation of higher complexity has been performed using the experimental data provided by Seto et al. [198] for the synthesis of silica from 250 ppm tetraethyl-orthosilicate (TEOS) within a hot wall reactor experiment at ambient pressure. The temperatures of the reactor are configured to offer a zone for precursor decomposition and coagulation for a flow through time of 1 second at 900°C, followed by a sintering zone of 1750°C for a flow through time of 0.8 seconds. The reaction mechanism (27 species, 58 reactions) and sintering model constants were chosen as suggested by Shekar

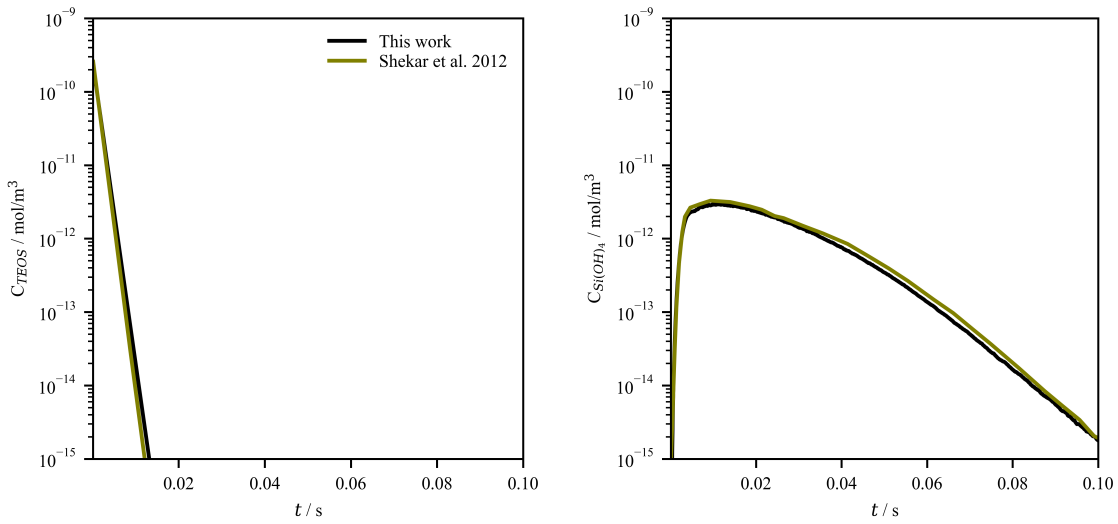

Fig.: 3.12 Gas phase conditions during the synthesis process in the coupled simulation. The calculated TEOS (left) and $Si(OH)_4$ (right) molar concentrations of this work are compared with the simulation results from Shekar et al. [200].

et al. [200]. Figure 3.12 shows the gas phase conditions over time for the mentioned setup. The TEOS and $Si(OH)_4$ molar concentrations are compared with the simulation results from Shekar et al. [200]. The particle size distributions of the collision diameter d_c and the primary particle diameter d_p in comparison with the experimental data by Seto et al. [198] are shown by Fig. 3.13. It can be seen that an excellent agreement for the size distributions for both the collision diameter d_c and the primary particle diameter d_p is achieved, proving that the developed framework is capable of predicting complex systems with coupled gas- and particle-phase.

A further validation has been performed by comparison of the simulation results of the model with the experiment presented by Onischuk et al. [156]. The experiment features the synthesis of silicon nanoparticles from a high concentration of monosilane precursor (x_{SiH4} = 5.0 %) in an argon atmosphere at the moderate temperature of T = 853 K. As this validation is part of the published work shown in chapter 6, all detailed information about the numerical and experimental setup of the hot wall experiment are given there. At this point, only the results of the introduced model are shown in comparison with the experimentally obtained data given by Onischuk et al. [156]. As shown in Fig. 3.14, the primary particle diameter d_p, the aggregate number concentration N, and the monosilane concentration normalized by the initial value $[SiH_4]/[SiH_4^0]$ are in excellent agreement with the experimental data for all shown quantities. A comparison with the results of the stochastic simulation as given by Menz and Kraft [146] for the primary particle diameter d_p proofs that the introduced model

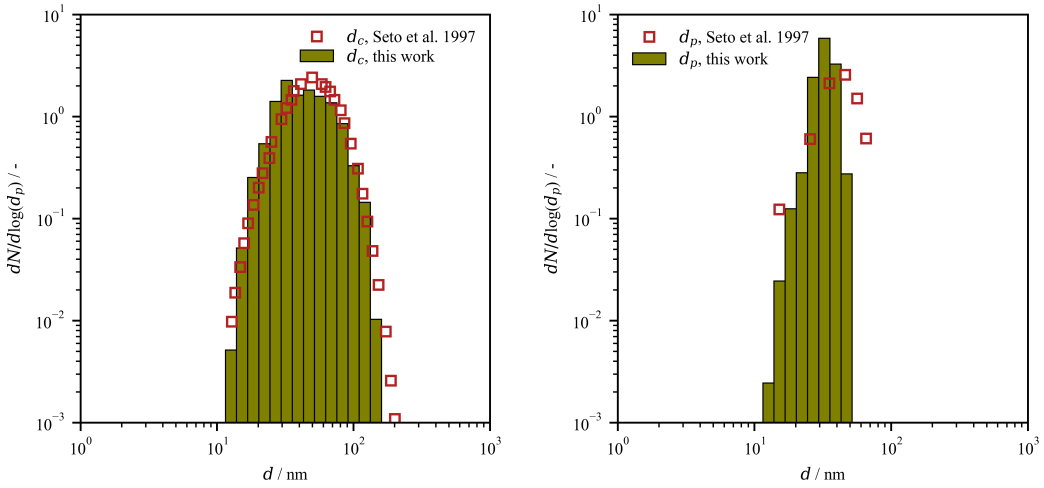

Fig.: 3.13 Particle size distributions of the collision diameter d_c (left) and the primary particle diameter d_p (right) in comparison with the experimental data by Seto et al. [198].

predicts results of comparable accuracy. In addition, artificially reconstructed 3D-particle models of randomly chosen aggregates of the simulation results are presented in Fig. 3.15. The 3D-particle models serve for as visual comparison with the TEM images shown in the work of Onischuk et al. [157]. The 3D reconstruction was performed balistically without considering the fractal dimension. In a first step, a volume was randomly filled with all primary particles of an aggregate, while in a second step they were randomly connected according to their connectivity within the stochastic simulation. The penetration depth of the primary particles within the 3D reconstruction is calculated according to their sintering progress.

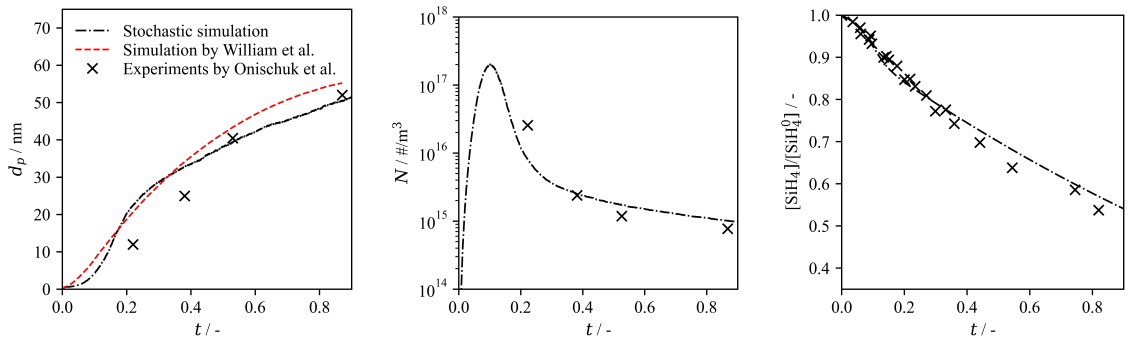

Fig.: 3.14 Comparison of the stochastic simulation with experimentally obtained data from Onischuk et al. [156]. From left to right: the primary particle dimaeter d_p, the aggregate number concentration N, and the monosilane concentration normalized by the initial value $[SiH_4]/[SiH_4^0]$. Data for the primary particle diameter d_p (left) is additionally compared with the results of a stochastic simulation as presented by Menz and Kraft [146].

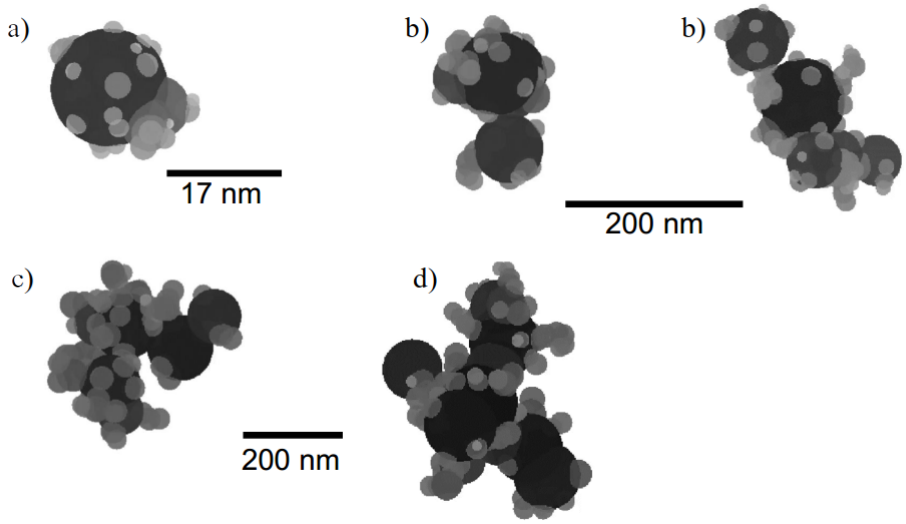

Fig.: 3.15 Artificially reconstructed 3D-particle models of randomly chosen aggregates of the simulation results for test case introduced by Onischuk et al. [157]. Aggregate data is taken from four different simulation times: a) $t = 0.22$ s, b) $t = 0.38$ s, c) $t = 0.53$ s, d) $t = 0.87$ s and can be compared to TEM images shown in the work of Onischuk et al. [157]. Smaller primary particles are brighter and have lower alpha values.

As mentioned earlier, the stochastic simulation can be performed either in a reactor simulation, directly coupled with finite rate chemistry, or as a post-processing tool, coupled via trajectories that are extracted during a CFD simulations. For the generation of particle trajectories using OpenFOAM-based solvers, a new tracking algorithm has been developed

that provides all the necessary data to use the described method as a post-processing tool for larger three-dimensional simulations. In order to guarantee an efficient workflow in a parallel environment, the trajectories are tracked on each MPI rank separately and written only once, as soon as the tracer particle has left the global domain. For the reconstruction of the global trajectory, tracers are equipped with a unique trajectory tag, which identifies the trajectory fragments on all processes (see 3.16).

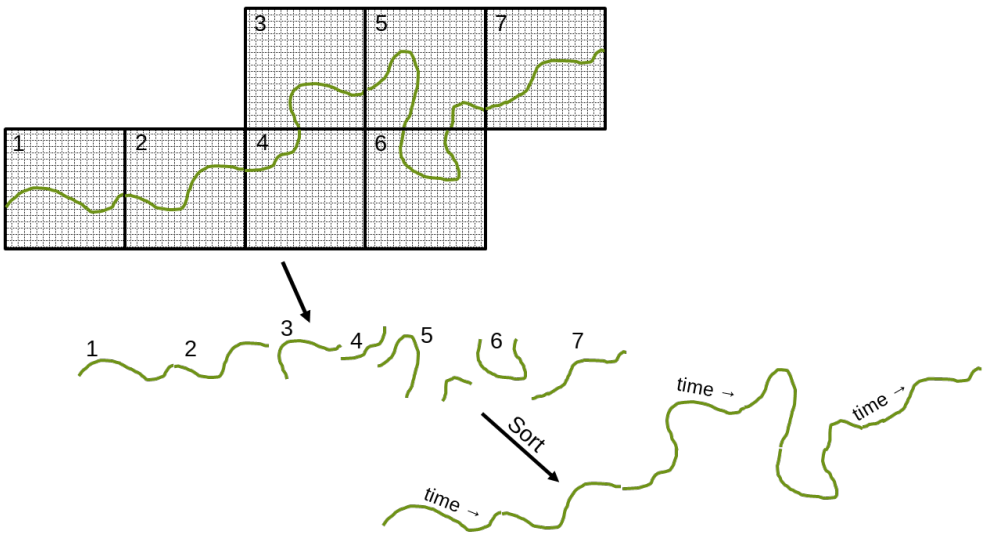

Fig.: 3.16 Sketch of the tracking algorithm used to extract particle trajectories from parallel OpenFOAM 3D simulations. For the reconstruction of the global trajectory, tracers are reconstructed and sorted chronologically.

4 Multiscale Simulation of the Formation of Platinum-Particles on Alumina Nanoparticles in a Spray Flame Experiment

P. Wollny, S. Angel, H. Wiggers, A.M. Kempf, I. Wlokas

P. Wollny developed and implemented the heterogeneous particle models, the tabulated nucleation approach, the post-processing algorithms, ran all the simulations, wrote the paper, including all figures and tables, excluding the experimental part. S. Angel ran the experiments and contributed the data and the chapter and pictures about the experiment. The authors H. Wiggers, A.M. Kempf and I. Wlokas contributed feedback, corrections and proof-reading.

This paper was published in Fluids, 5, 4, 201, Copyright ©MDPI (2020) [249] and is reprinted with permission from MDPI.

4.1 Abstract

Platinum decorated alumina particles have the potential of being a highly (cost-) effective catalyst. The particles are synthesized from platinum(II) acetylacetonate dissolved in a mixture of isopropanol and acetic acid with dispersed alumina carriers. The process is simulated by means of large eddy simulation with reaction kinetics and aerosol dynamics modeling. A two mixture fraction approach for tabulated chemistry with a thickened flame model is used to consider the complex reaction kinetics of the solvent spray combustion. Diffusion is described followings Ficks law with a unity Lewis number for the gas phase species, whereas the particle diffusion coefficients are calculated according to the kinetic theory. An extended model for aerosol dynamics, capable of predicting deposition rate and surface particle growth, is derived from the classical sectional technique. The simulations are compared and validated with product particle characteristics obtained from the experimental observations. Distributions for different locations within the simulation domain show the evolution of particle sizes deposited on the alumina particle surface, and transmission electron microscopy (TEM) images of the composite particles are shown in comparison to

3D particles ballistically reconstructed from simulation data. The ratio of deposited platinum on the alumina carrier particles and the mean diameters of the deposited particles are in good agreement with the experimental observation. Overall, the new method has demonstrated to be suitable for simulating the particle decoration process.

4.2 Introduction

Platinum powders play an integral role as catalyst for processes in the automotive, chemical and pharmaceutical industry. The efficiency of the catalyst is directly related to the free surface area. Composite nanoparticles are suitable to reduce the amount of platinum mass required to achieve a large surface area and provide a stable support structure at the same time. The production of composite nanomaterials puts high demands on the flexibility and reliability of the synthesis, and the flame spray pyrolysis [132] has shown to be a very good option for such a process. The SpraySyn burner is used in the present study [98, 195], which allows mixing priorly generated (and possibly pre-processed) carrier particles into the precursor solvent, which reduces the process complexity by removing the step of carrier particle formation. The simulation of the entire synthesis requires the properly coupled numerical solution of a series of processes taking place at different scales: spray evaporation and combustion, convective transport, combustion and decomposition of the particle precursor, particle formation and growth. The modeling and simulation challenge is obvious and Buesser and Gröhn [15] pointed out, that the coupling between processes taking place at very different scales remains a challenge. The present work is devoted to an attempt of a numerical simulation that covers the scales from the operating synthesis device, down to the decoration of carrier particles with freshly formed nanoparticles. As these simulations require a large portfolio of models and solution methods, the following review is compact and limited to methods relevant for this work.

In the past, the flame spray pyrolysis was simulated using RANS (Reynolds-averaged Navier-Stokes), for example by Noriler et al. [155], Weise et al. [238] and Gröhn et al. [67]. The quality of the simulations usually suffered form a large uncertainty in the boundary conditions and the closure approaches between the turbulence, the reaction kinetics and the particle dynamics. To obtain spray and droplet boundary conditions, Weise et al. [238] conducted a direct simulation of the primary spray breakup prior to the main simulations. To compensate for the uncertainties in the breakup mechanism, they investigated the sensitivity of the simulation to this boundary condition. All these simulation approaches [155, 238, 67] used global reaction kinetics schemes for the combustion of the solvent and of the nanoparticle precursor. The particle dynamics were described using the monodisperse

This chapter was previously published [249] and is reprinted with permission of the journal.

moment model introduced by Kruis et al. [113]. The results of these simulations appear to be in line with the experimental observation, but the prediction quality is difficult to assess. The over-simplification of the reaction kinetics, particle growth and formation physics, and their interaction with turbulent mixing may lead to compensating errors. In turn, large eddy simulation (LES) promises to provide a higher level of fidelity for the coupling of reaction kinetics and particle dynamics in the presence of turbulent mixing. Rittler et al. [186] showed an LES with tabulated chemistry approach, coupled with the monodisperse moment method model to predict the spray-flame synthesis of silica nanoparticles. This approach was also used for the assessment of the newly developed SpraySyn Burner [195]. Until now, these remained the only LES of the flame spray pyrolysis process. Very recently, Abdelsamie et al. [1] presented a direct numerical simulation (DNS) of the SpraySyn burner, but without modeling the particle dynamics. It should however be stressed that even with LES, closure modeling of nanoparticle synthesis is in its early development, and that more sophisticated models will be needed in the future. The present work is an attempt to demonstrate what can be achieved today, but is also meant to inspire future work and to improve the many closure models involved.

The mechanisms controlling particle evolution are a complex interplay of thermodynamic, chemical and mixing phenomena in time and space [226, 228]. Only few analytical solutions for generic configurations of the initial and boundary conditions and reduced sets of particle properties exist [53]. The population balance equation (PBE) describing the dynamics of particle evolution is usually solved numerically, considering sets of constraining assumptions [184, 180]. Among the large variety of solution methods, the sectional model is highly attractive for coupling with computational fluid dynamics (CFD), despite the unfavorable algorithmic complexity if more than a single particle property is considered. The fundamental idea of the sectional approach [54] is to distribute the particle size spectrum into fixed, discrete sections. Because of its rather simple implementation, the standard sectional model is prominent for being an extension for CFD calculations, as resolved polydispersity is vital for modeling real flame synthesis processes and computational costs are moderate. The model has been applied to non-reactive direct numerical simulations (DNS) and large eddy simulations have been performed by Garrick et al. [52] and Loeffler [129]. Later, the sectional model was extensively utilized in the simulation of soot-PSD in turbulent and laminar flames [12, 126, 187, 192].

The present paper describes the simulation of platinum particle synthesis and their subsequent deposition on alumina carrier particles; it is structured as follows: The next section presents the experiment, the synthesis setup and the employed characterization methods followed by the the models and numerical methods as a central topic of this work.

This chapter was previously published [249] and is reprinted with permission of the journal.

The results, experiment and simulation of the synthesis process are discussed in the fourth section, while the details on verification and validation of the proposed simulation strategy are discussed in the appendix.

4.3 Experimental

A solution with a concentration of 8 mM Platinum(II)acetylacetonate ($Pt(acac)_2$, 98% purity, Acros Organics) in 50%-vol acetic acid (99.8% purity, for analysis, Acros Organics) and 50%-vol isopropanol (VWR Chemicals), was prepared. Aluminum oxide nanoparticles (3%-weight, Al_2O_3 NanoGrain Umicore) were dispersed in the solution using an ultrasonic homogenizer (UP200S, Hielscher). The mixture was burnt in an enclosed spray-flame reactor (described in other publications [73, 72]) by supplying the prepared dispersion to a two-fluid external-mixing atomizing nozzle at a flow rate of 2 mL/min, using a high precision syringe pump (neMESYS, Cetoni GmbH). Using a flow rate of 6 slm (standard liters per minute) of oxygen (O_2, Air Liquide, technical) as atomizing gas, a fine spray of the supplied dispersion was formed. This spray is ignited by a premixed pilot flame of 2 slm methane (CH_4, Air Liquide, N25, 99.5% purity) and 4 slm oxygen (O_2, Air Liquide, technical). The pilot flame is stabilized on a sintered bronze plate and is surrounded by a sheath-gas flow of air (approx. 0.63 m/s at 25°C), which also shields the flame from the walls of the reactor. Above the reaction zone, a quenching gas flow is supplied (80 slm, air) in order to freeze the aerosoldynamics, and to control the temperature before the collection of the particles in the filter of the system. The morphology, particle size, and composition of the synthesized materials were studied by transmission electron microscopy (TEM-EDX; JEOL JEM- 2200FS). Figure 4.1 shows an example TEM-EDX image of a platinum-decorated alumina particle created in the described synthesis process.

4.4 Modeling

The large eddy simulation (LES) of the reactive flow field uses an extended premixed flamelet generated manifolds approach (PFGM) [224, 167]. A single-step global reaction is introduced for the decomposition of $Pt(acac)_2$, based on observations reported in literature [220, 21, 151]. The tabulated chemistry is applied for the combustion of $Pt(acac)_2$ dissolved in a mixture of isopropanol and acetic acid. The sectional model is extended in order to account for interactions between the small sized (0.34-20.0 nm) platinum and the much larger (400 nm in average) alumina nanoparticles. Therefore, a second particle ensemble is introduced representing the particles deposited on the alumina particle surface (in the following referred

This chapter was previously published [249] and is reprinted with permission of the journal.

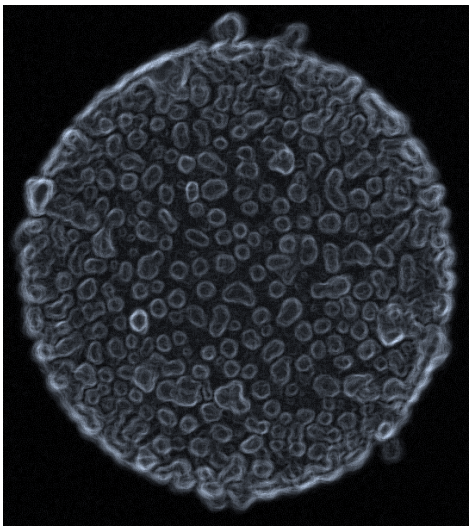

Fig.: 4.1 TEM-EDX of decorated alumina particle produced by flame spray synthesis (isopropanol and toluene). Small platinum particles are deposited on the large, spherical alumina carrier particle.

to as carrier). As shown by Simonsen et al. [205], the deposited particle matter tends to reduce its free surface area due to surface coagulation. Thus, a two-dimensional coagulation model, based on the theory for free molecular collision, is derived to describe the particle motion on the carrier's surface and which is in close agreement with the theory by Peev [163]. The goal is predicting tendencies for deposition rates and structure sizes of the deposited material in a real flame, without claiming predictions to come close to the accuracy reached by detailed molecular dynamics simulations.

4.4.1 Reaction Kinetics and Turbulence Chemistry Interaction

The role of the solvent is to stabilize the carrier particles in the liquid and to provide, through combustion, the controlled amount of energy to decompose the nanoparticle precursor into gas phase molecules. The mixture of 50%-vol isopropanol (C_3H_8O) and acetic acid (CH_3COOH) enabled stable dispersions, but is unusual for general combustion purposes. In order to describe the combustion kinetics of this mixture the "Primary Reference Fuels (PRF) + PAH" mechanism for high and low temperatures [164, 36] was used, which includes 300 species and 11790 reactions. The mechanism was extended by a single global reaction for the decomposition of $Pt(acac)_2$ into platinum and volatiles at 155°C, based on the observations, which were found in the work of Utrianen et al. [220].

$$Pt(acac)_2 \rightarrow Pt + 2\,CH_2CHO + 2\,HCCO + 2\,CH_3$$

This chapter was previously published [249] and is reprinted with permission of the journal.

Due to the lack of data for the kinetics of the $Pt(acac)_2$ decomposition, the reaction rate expression was adjusted to the reported decomposition temperature and to remain within the kinetic collision limit, leading to :

$$k = 1.8 \cdot 10^6 \mathrm{T}^{0.5} \exp(-7500\,\mathrm{K/T})$$

Platinum is a strong catalyst and may interact with the flame chemistry creating various ephemeral platinum intermediates [14]. This interaction is neglected in the current model due to lacking data for an implementation into the reaction mechanism. Moreover, platinum is known for its very high chemical stability justifying our assumption of pure platinum clusters as product from a flame synthesis. The reaction mechanism of the solvent mixture is complex and intractable in LES with a finite rate model (at least without extreme mechanism reduction). Instead, the premixed flamelet generated manifold approach (PFGM), as introduced by van Oijen et al. [224, 225], has been applied by using a pre-generated table of one-dimensional, steady, premixed flame solutions [166, 168]. Due to the presence of two fuel streams (pilot flame and spray), the PFGM approach had to be extended by an additional fuel mixture fraction (f_2). Consequently, the dimensionality of the chemistry database is increased from two to three. The progress variable Y_p is represented by a weighted linear combination of product- and fuel/precursor species consumption.

$$Y_p = \sum \alpha_i Y_i + \sum \beta_i (Y_{f,i} - Y_i) \tag{4.1}$$

Here, the first and the second term on the right hand side (rhs) represent the product and fuel species contribution with their respective weighting factors α and β, while $Y_{f,i}$ denotes the mass fraction of the given fuel composition. We considered a progress variable combination of CO, CO_2, H_2 and Pt (with $\alpha = 1, 2, 20, 200$, respectively) together with consumption variables CH_4, isopropanol and acetic acid ($\beta = 1$ for each) to be suitable for the given case. The weighting is important, if species with different molar masses or concentrations contribute considerably to the progress variable. Due to the variable bounds of Y_p, the more convenient scaled progress variable c is used for tabulation [224].

$$c = \left. \frac{Y_p}{Y_{p,max}} \right|_{f_1, f_2} \tag{4.2}$$

The scaled progress variable given by eq. (4.2) offers always a convenient range between 0 and 1 due to the division by the maximum value of the progress variable value $Y_{p,max}$ and corresponds to a given set of f_1 and f_2. Figure 4.2 shows the data obtained by this procedure for 4 different quantities and conditioned for $f_2 = 0.15$. Considering a constant

This chapter was previously published [249] and is reprinted with permission of the journal.

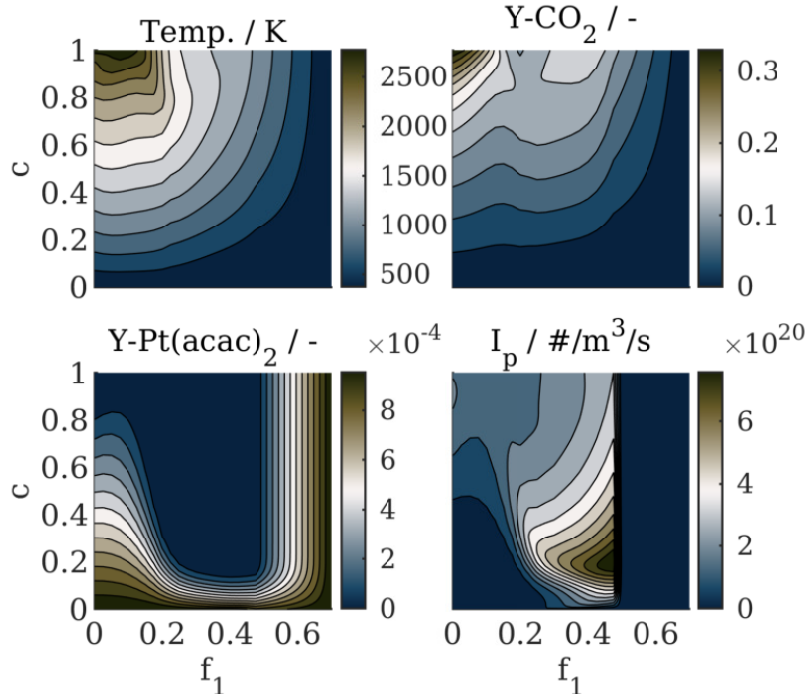

Fig.: 4.2 Snippet of the thermochemical data stored in the PFGM table for the given case at $f_2 = 0.15$. From left to right and top to bottom: temperature, mass fractions of CO, CO_2, O_2, $Pt(acac)_2$ and the nanoparticle inception source term

Lewis number of unity for the turbulent flow field, the conservation equations for the Favre averaged mixture fractions $\widetilde{f_i}$ can be given as follows:

$$\frac{\partial \overline{\rho}\widetilde{f_i}}{\partial t} + \nabla \cdot \widetilde{\mathbf{u}}\overline{\rho}\widetilde{f_i} = \nabla \cdot \left(\left[F_D \Xi_\Delta \frac{\lambda}{c_p} + (1-\Omega)\frac{\mu_t}{Sc_t} \right] \nabla \widetilde{f_i} \right) + \Gamma_{f,i} \tag{4.3}$$

The quantities $\overline{\rho}$ and $\widetilde{\mathbf{u}}$ denote the filtered spatially averaged density and the Favre averaged velocity vector [172]. The variables λ, c_p, μ_t and Sc_t represent the thermal conductivity, the isobaric heat capacity, the subgrid viscosity obtained by the sigma model [154] and the turbulent Schmidt number ($Sc_t = 0.7$) of the gas mixture. The last term of eq. (4.3) adds mass fluxes due to spray evaporation:

$$\Gamma_{f,i} = \left[\frac{d\overline{\rho}_i}{dt} \right]_{evap} \tag{4.4}$$

The variable $\overline{\rho}_i$ denotes the averaged mass per volume of fuel i added to the gas phase. The evaporation source only contributes to the second mixture fraction, such that the first evaporation source vanishes, $\Gamma_{f,1} = 0$. The influence of turbulence on chemical sources is

This chapter was previously published [249] and is reprinted with permission of the journal.

modeled by the artificial flame thickening approach (ATF, [17, 119]) in combination with the sigma model [154] for modeling of the subgrid fluxes. Here, the thickening factor F_D is calculated based on the normalized progress variable c:

$$F_D(c^*, f_i) = \frac{(dc/dx)|_{c=c^*}}{(d\widetilde{c}/dx)|_{\widetilde{c}=c^*}} \tag{4.5}$$

The denominator $(d\widetilde{c}/dx)|_{\widetilde{c}=c^*}$ is computed by Gaussian filtering of the c-profile [179] at c^* with a filter width of the LES cell size Δ. Subsequently, the flame sensor Ω is obtained by normalizing the thickening factor:

$$\Omega = \frac{F_D - 1}{F_{D,max} - 1} \tag{4.6}$$

The variable $F_{D,max}$ denotes the maximum thickening factor of the laminar flame. The sub filter wrinkling factor Ξ_Δ is computed following Charlette et al. [20] and Wang et al. [234]. The progress variable equation is given below:

$$\frac{\partial \overline{\rho}\widetilde{Y_P}}{\partial t} + \nabla \cdot \widetilde{\mathbf{u}}\overline{\rho}\widetilde{Y_P} = \nabla \cdot \left(\left[F_D \Xi_\Delta \frac{\lambda}{c_p} + (1-\Omega) \frac{\mu_t}{Sc_t} \right] \nabla \widetilde{Y_P} \right) + \Gamma_{Y_P} \tag{4.7}$$

The term Γ_{Y_P} in eq. (4.7) is the sum of chemical reaction $\dot{\omega}_P$ and the evaporating fresh fuel (second term) given by:

$$\Gamma_{Y_P} = \frac{\Xi_\Delta}{F_D} \dot{\omega}_P - \left[\frac{d\overline{\rho}}{dt} \right]_{evap} \tag{4.8}$$

The spray droplets are transported as Lagrangian particles and the model of droplet evaporation follows the implementation presented by Rittler et al. [186, 185]. The conservation equation for the nucleated mass is then derived consistently with the progress variable Y_p, eq. (4.7) and results in:

$$\frac{\partial \overline{\rho}\widetilde{Y_I}}{\partial t} + \nabla \cdot \widetilde{\mathbf{u}}\overline{\rho}\widetilde{Y_I} = \nabla \cdot \left(\left[F_D \Xi_\Delta \frac{\lambda}{c_p} + (1-\Omega) \frac{\mu_t}{Sc_t} \right] \nabla \widetilde{Y_I} \right) + \frac{d\overline{\rho}_I}{dt} \tag{4.9}$$

The last term of eq. (4.9) is the averaged mass source given for a certain combustion state. Due to the fact that the gas composition is shifted by spray evaporation and nucleating species are formed unevenly over the combustion progress, using a tabulated source term would lead to drastic errors in predicting the nucleating mass for the dispersed phases. Instead, it is

This chapter was previously published [249] and is reprinted with permission of the journal.

obtained by tracking the change of the incepted particle mass Φ_p per time step.

$$\frac{d\overline{\rho}_I}{dt} = \frac{\Xi_\Delta}{F_D}\dot{\omega}_I\bigg|_{x_i,t} \approx \frac{1}{\Delta t}\Delta\Phi_p(c, f_i) \tag{4.10}$$

The incepted particle mass Φ_p is tabulated and represents the produced nucleating matter per volume for a given condition (f_i, c). It is obtained using the flamelet data:

$$\Phi_p(c, f_i) = \int_0^{x(c,f_i)} \frac{\dot{\omega}_I}{u\rho} dx\, \rho(c, f_i) \tag{4.11}$$

The quantity $\dot{\omega}_I$ represents the chemical net production rate of the incepted species, x the axial position and ρ the gas density, respectively. It should be mentioned that the ATF approach is implicitly included in the change of integral nucleated mass $\Delta\Phi_p(c, f_i)$ and therefore not applied in the last term of eq. (4.10).

4.4.2 Modeling Nanoparticle Dynamics

The transport of nanoparticles within the CFD context is given by applying the Reynolds transport theorem on the PBE. In the case of LES coupled with the sectional model [54], this leads to an additional conservation equation for the filtered spacial averaged number concentration $\overline{N}_k$ of every considered section (see. Loeffler et al. [129]) given by:

$$\frac{\partial\overline{N}_k}{\partial t} + \nabla\cdot\widetilde{\boldsymbol{u}}\overline{N}_k = \nabla\cdot\left(\left[F_D\Xi_\Delta D_{N_k} + (1-\Omega)\frac{\nu_t}{Sc_t}\right]\nabla\overline{N}_k\right) + \frac{d\overline{N}_k}{dt} \tag{4.12}$$

In this work, a second set of particles in the gas phase (alumina carrier particles of constant size), as well as the PBE of the particles deposited on the carrier particle surface must be considered. Therefore, conservation equations for the carrier particle number concentration C, eq. (4.13), and for the deposited particle number concentrations Q_k, eq. (4.14), are derived by the same principle, with special attention to the diffusion term in eq. (4.14), which has to be adapted for the deposited particles, by Ficks' law [8].

$$\frac{\partial\overline{C}}{\partial t} + \nabla\cdot\widetilde{\boldsymbol{u}}\overline{C} = \nabla\cdot\left(\left[F_D\Xi_\Delta D_C + (1-\Omega)\frac{\nu_t}{Sc_t}\right]\nabla\overline{C}\right) + \frac{d\overline{C}}{dt} \tag{4.13}$$

$$\frac{\partial\overline{Q}_k}{\partial t} + \nabla\cdot\widetilde{\boldsymbol{u}}\overline{Q}_k = \nabla\cdot\left(\left[F_D\Xi_\Delta D_C + (1-\Omega)\frac{\nu_t}{Sc_t}\right]\nabla\overline{Q}_k\right) + \frac{d\overline{Q}_k}{dt} \tag{4.14}$$

This chapter was previously published [249] and is reprinted with permission of the journal.

For equations (4.12) to (4.14), the kinematic subgrid viscosity is given by $\nu_t = \mu_t/\rho$, whereas the particle diffusion coefficient for each section D_i and for the carrier particle D_C are computed as proposed by Friedlander [48]. The last terms on the rhs of equations (4.12) to (4.14) contain the changes by particle dynamics, i.e. coagulation between all particle classes and inception rates and will be explained in the following. Figure 4.3 sketches the general modeling strategy, where equally sized carrier particles suspended within the spray droplet are assumed to be released when the droplet collapses. The platinum precursor evaporates together with the fuel as a perfect mixture, whereas nucleation and coalescence take place within the gas phase until condensation on the carrier surface. Particle growth on the carrier surface is modeled kinetically, based on the coverage of deposited particle size classes. Collisions between particle pairs i, j within the gas phase (i.e. for platinum particles)

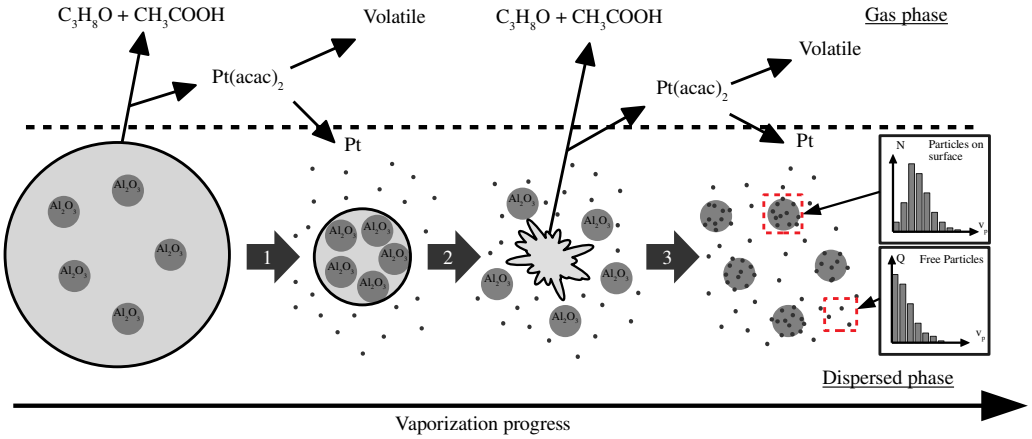

Fig.: 4.3 Processes description in 3 steps; FLTR: 1 – droplet evaporation/shrinking, 2 – droplet collapsing and carrier particle release, 3 – platinum particle growth in gas phase and on carrier surface, gas phase particle deposition.

are described by the harmonic mean, eq. (4.15), of the collision frequencies $\beta^f_{i,j}$ for the free molecular regime, eq. (4.16) and $\beta^c_{i,j}$ for the continuum regime, eq. (4.17) [175, 95].

$$\beta^*_{ij} = \frac{\beta^c_{ij}\beta^f_{ij}}{\beta^c_{ij} + \beta^f_{ij}} \tag{4.15}$$

In the free molecular regime, the collision frequency is:

$$\beta^f_{ij} = 2.2\left(\frac{\pi k_b T}{2}\right)^{1/2}\left[\frac{1}{m_i} + \frac{1}{m_j}\right]^{1/2}\left(d_{c,i} + d_{c,j}\right)^2 \tag{4.16}$$

This chapter was previously published [249] and is reprinted with permission of the journal.

The particle mass is denoted by m_i, while the foregoing multiplicator 2.2 is the van der Waals enhancement factor originally defined for soot particles [74], but successfully applied for other material systems [146, 199]. The variables k_b, T and $d_{c,i}$ stand for the Boltzmann constant, the gas phase temperature and the collision diameters of the particles [190]. In the continuum regime, the collision frequency is given as a function of the Cunningham slip correction factor C_i [232]:

$$\beta_{ij}^{c} = \frac{2k_bT}{3\mu}\left[\frac{C_i}{d_{c,i}} + \frac{C_j}{d_{c,j}}\right]\left(d_{c,i} + d_{c,j}\right) \tag{4.17}$$

Since particles in the present case are mainly of round shape, the collision diameter is equal to that of a spherical particle $d_{c,i} = d_i$. The particle size discretization (see [54]) is kept equal for the particles dispersed in the gas phase as well as for the particles deposited on the carrier surface using 17 grid points. The section sizing follows the logarithmic rule $v_i = v_0\gamma^{i-1}$ with the volume of the platinum monomers v_0, the volume v_i of particles corresponding to section i and the growth factor $\gamma = 2.0$ used to control the spacing between the sections. Changes for the dispersed platinum phase N_k due to particle dynamics on mesoscopic scale are considered by the contributions:

$$\frac{dN_k}{dt} = \left[\frac{dN_k}{dt}\right]_{c,N} - \left[\frac{dN_k}{dt}\right]_{c,C} + \left[\frac{dN_k}{dt}\right]_{I} \tag{4.18}$$

The first term on the rhs denotes the change by collision with other platinum particles within the dispersed phase N_k:

$$\left[\frac{dN_k}{dt}\right]_{c,N} = \frac{1}{2}\sum_{i,j=1}^{k}\chi_{ijk}\beta_{ij}^{*}N_iN_j - \sum_{i=1}^{n}\beta_{ik}^{*}N_iN_k \tag{4.19}$$

The size splitting operator χ_{ijk} interpolates coagulation contributions of particle combinations, which fall in between the defined sections, while n indicates the number of sections chosen for the representation of the PSD [173, 209]. Gas particle deposition onto the carrier surface is represented by the second term in equation (4.18) and modeled as collision process following eq. (4.20), with C indicating the carrier particle number concentration.

$$\left[\frac{dN_k}{dt}\right]_{c,C} = \beta_{i,C}^{*}N_iC \tag{4.20}$$

Particle inception (third term in eq. (4.18)) only affects the first (monomer) section N_1 and is calculated by:

$$\left[\frac{dN_k}{dt}\right]_{I} = \frac{d\overline{\rho}_I}{dt}\frac{N_A}{\rho_{Pt}}\delta_{d_1}(d_k) \tag{4.21}$$

This chapter was previously published [249] and is reprinted with permission of the journal.

Here, $d\overline{\rho}_I/dt$ is given by eq. (4.10), N_A is the Avogadro constant, ρ_{Pt} the density of platinum and δ_{d_1} the Dirac measure.

Deposited particle dynamics, which take place on the carrier particle surface, are realized by the contributions of on surface coagulation (first term, rhs) and particle deposition on the free carrier surface (second term, rhs).

$$\frac{dQ_k}{dt} = \left[\frac{dQ_k}{dt}\right]_c + \left[\frac{dQ_k}{dt}\right]_D \tag{4.22}$$

The approach for calculating the surface coagulation rate is derived from the free molecular collision kernel (eq. 4.16), assuming a rectangular path way as projection of the typical cylindrical path way on the carrier particle surface:

$$\beta_{ij}^{Q} = \alpha_c \frac{q_i q_j}{a_{car}^2} \left(\frac{2k_b T}{\pi}\right)^{1/2} \left[\frac{1}{m_i} + \frac{1}{m_j}\right]^{1/2} \left(d_{s,i} + d_{s,j}\right) \tag{4.23}$$

Here, $q_i = Q_i/C$ denotes the deposited particle number of section i per carrier particle, whereas a_{car} is the carrier particle surface area. The model constant $\alpha_c = 6.0{\cdot}10^{-6}$ decreases the rate of coagulation to a level suitable for surface reactions. This concept is comparable to the van der Waals enhancement factor [74] in case of free molecular collision, but accounts for the reduced particle motion by sticking. The first term of equation (4.22), the surface coagulation, has additionally to account for collisions, which occur during the deposition process, i.e. platinum particle from the dispersed phase do not hit the free carrier surface, but other, already deposited, platinum particles. With all contributions included, it is calculated as:

$$\left[\frac{dQ_k}{dt}\right]_c = \sum_{i,j=1}^{k} \left(\chi_{ijk} \left[\xi_i \left[\frac{dN_k}{dt}\right]_{c,C} + \beta_{ij}^{Q}\right]\right) - \sum_{i=1}^{n} \left(\xi_k \left[\frac{dN_k}{dt}\right]_{c,C} + \beta_{ik}^{Q}\right) \tag{4.24}$$

The deposition on the free carrier particle surface (second term eq. 4.22) is given by:

$$\left[\frac{dQ_k}{dt}\right]_D = (1 - \xi_t) \left[\frac{dN_k}{dt}\right]_{c,C} \tag{4.25}$$

The growth of deposited particle concentration Q_k is a function of the surface coverage $\xi_i = c_{s,i}/a_{car}$ and the total surface coverage $\xi_t = \sum \xi_i \leq 1$, whereas $c_{s,i} = x_{s,i} q_i$ is the surface area, which is covered by particles of section i. The simplified single particle projection area is given by $x_{s,i} = \pi/4 d_i^2$.

Collision among carrier particles is rarely observed within the experiments, therefore it is

This chapter was previously published [249] and is reprinted with permission of the journal.

neglected in the modeling. Thus, the only contribution to the source term (eq. 4.13, last term rhs) is the alumina particle inception during the spray droplet collapse (see figure 4.3). It is divided between the closest cells within the Eularian field according to trilinear weighting by the droplets position relative to the grid points. For a single collapsing spray droplet, the carrier particle source term is calculated by:

$$\frac{dC}{dt} = \frac{1}{\Delta t \Delta v} \frac{\mathcal{Y}_C}{m_C} \mathcal{M}_S^0 \tag{4.26}$$

Since spray droplets shrink during the evaporation process, $\mathcal{M}_S^0$ represents the initialized droplet mass at the beginning of its life time, wheres $\mathcal{Y}_C = 0.03$ denotes the mass fraction of the carrier particle matter suspended in the spray liquid and Δv is the constant cell volume of the discretized domain. The mass of a carrier particle individual m_C is calculated by assuming a spherical shape and a given diameter c_C. In order to reduce the complexity it is held constant. Two simulations using different carrier particle sizes (d_C = 150 nm and the d_C = 400 nm) are performed and compared to investigate the impact of different carrier particle sizes d_C. A meaningful variable for quantifying the efficiency of the deposition process is the particle loading η_m:

$$\eta_m = \frac{\sum q_i m_i}{m_c} \tag{4.27}$$

It represents the ratio of the deposited mass loaded on a single carrier particle to its own mass m_C.

The simulation strategy and it's implementation was verified by generic one-dimensional test-setups. For details on this procedure we refer to the supplementary material of this work (Appendix A).

4.5 Simulation results

4.5.1 Numerical Setup

Two simulations were performed using the in-house code PsiPhi. The code is optimized for large eddy simulations and has been proven to perform well in massively parallel CFD calculations [177, 179, 185]. The code is based on a Cartesian, equidistant grid throughout the whole domain, leading to a very good performance for highly resolved LES [99] with high accuracy and superior stability for high order schemes compared to codes based on unstructured grids [177, 176]. PsiPhi allows the use of finite rate chemistry as well as of tabulated chemistry within the context of PFGM [224, 167], whereby the later is used in the extended form as described earlier in this work. For the present simulations, a cuboid of 50 ×

50×210 mm was chosen as computational domain, resolved by 33.6 million cells at a grid size of $\Delta = 0.25$ mm, which captures the artificially thickened flame front [179]. An explicit three step Runge-Kutta scheme was used for time integration, while spatial derivatives for the momentum equations were approximated by a second order central differencing scheme. Spatial derivatives of the convective fluxes of the remaining scalars were calculated by TVD-scheme applying the non-linear CHARM limiter [255].

4.5.2 Results

Figure 4.4 shows the instantaneous fields for the cases with carrier particle sizes of $d_C = 150$ nm and the $d_C = 400$ nm. An overlapping area with high values of N_t and q_t can be found after first carrier particles C are formed. Those areas indicate a high deposition rate, leading to a rapid decrease of dispersed particles (N_t), which become deposited particles and therefore increase q_t. A higher number of total deposited particles per carrier particle q_t is observed

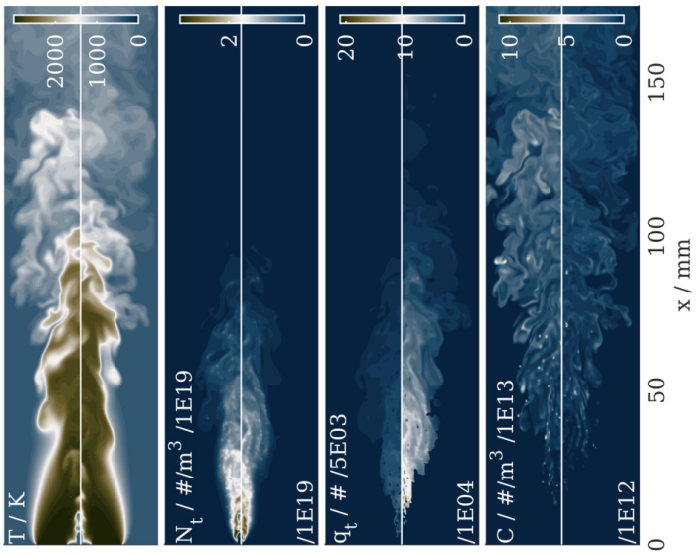

Fig.: 4.4 Contour plots along x-y plane; from left to right: Temperature T, total gas phase particle number concentration N_t, total deposited particle number q_t, carrier particle concentration C. Images are split in two parts: the left part corresponds to to the simulation with smaller carrier particles ($d_C = 150$ nm) and the right part to the simulation with larger carrier particles ($d_C = 400$ nm) respectively.

for the large carrier particles ($d_C = 400$ nm). This is for two reasons, first: since the total mass of the carrier material is held constant, the carrier particle concentration drops for larger sized carrier particles and therefore, more platinum matter may deposit on a single carrier.

This chapter was previously published [249] and is reprinted with permission of the journal.

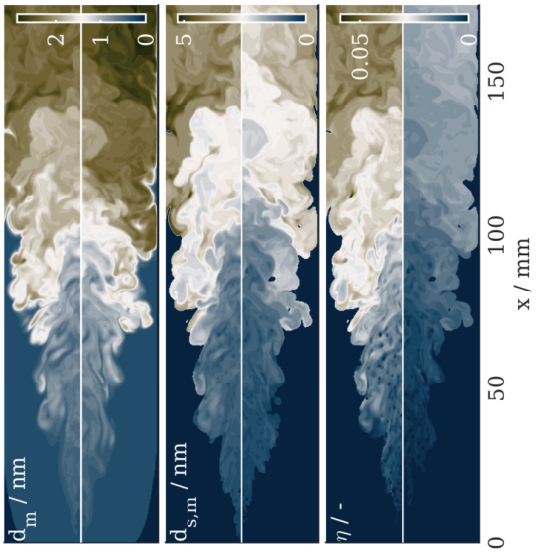

Fig.: 4.5 Contour plots along x-y plane; From left to right: Mean gas particle diameter d_a, mean deposited particle diameter $d_{s,a}$, carrier particle load η_m. Images are split in two parts: the upper part corresponds to to the simulation with smaller carrier (d_C = 150 nm) and the lower part to the simulation with larger carrier (d_C = 400 nm) respectively.

Second: due to the wider surface of larger sized carrier particles, on-surface deposition rates decrease for the same amount of deposited particles compared to smaller carrier particles.

Fields for mean dispersed and deposited platinum particle diameters d_a and $d_{s,a}$, as well as for the particle load η_m are shown in fig. 4.5. In general, both particle sizes d_a and $d_{s,a}$ exhibit a similar behavior for both carrier sizes and spatial deviations might result from turbulent fluctuations. Larger carrier particles with almost 10 times more captured particles show lower particle loading due to their significantly larger mass (19 times the mass of the smaller carrier particles).

Further investigations are made regarding temporal averaged free and deposited mean particle sizes ($\bar{d}_m$ and $\bar{d}_{s,m}$) in comparison to the normalized total number concentrations of free particles $\bar{N}_t^* = \bar{N}_t / \bar{N}_{t,max}$ and the normalized total number of deposited particles per carrier particle $\bar{q}_t^* = \bar{q}_t / \bar{q}_{t,max}$. The line data shown in fig. 4.6 is volume averaged along the y-z-plane (see eq. 4.28) for Δx being the grid size.

$$\phi^a(x,t) = \frac{1}{V_s} \int_{\Delta x,y,z} \phi(x,y,z,t) dy dz dx \tag{4.28}$$

Here, $V_s = \int_{\Delta x,y,z} dV$ denotes the volume of the slice used for averaging. It can be seen that free platinum particles are generally smaller sized in comparison to those found on the

This chapter was previously published [249] and is reprinted with permission of the journal.

carrier particle surface. Nevertheless, the mean diameters show a similar behavior between all cases, while the scattering of the instantaneous quantity is comparable for the different carrier sizes (top vs bottom). Comparison of the normalized total number concentrations of free ($\bar{N}_t^{a*}$) and deposited particles ($\bar{q}_t^{a*}$) shows almost identical slopes for the different carrier sizes. Comparing the dispersed particle number concentrations $\bar{N}_t^{a*}$ and the deposited particle numbers $\bar{q}_t^{a*}$, a correlation between both can be found: the dispersed particle number concentrations $\bar{N}_t^{a*}$ rise, until the rates for deposition dominate. Once this stage is reached, the deposited particle numbers $\bar{q}_t^{a*}$ increases, while $\bar{N}_t^{a*}$ falls off drastically. This strong decrease takes place within the zone of particle inception and is therefore an evidence for high deposition rates. The range, in which inception takes place can be estimated by the appearance of monomers (i.e. up to 100 mm above the burner). A further comparison without normalization is given by fig. 4.7. It becomes obvious that changing the carrier

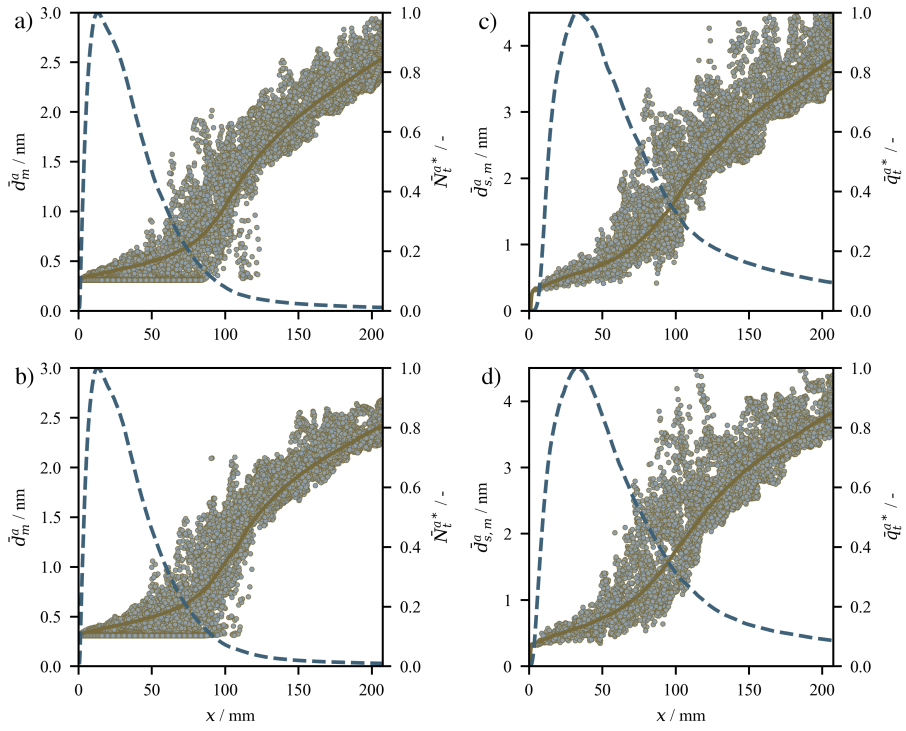

Fig.: 4.6 Profiles along the centerline of time averaged free particle mean diameter $\bar{d}_m^a$ and normalized time averaged total dispersed particle number concentration $\bar{N}_t^{a*}$ for the cases a) $d_C = 400\,\text{nm}$ and b) $d_C = 150\,\text{nm}$.
Profiles along the centerline of time averaged deposited particle mean diameter $\bar{d}_{s,m}^a$ and normalized temporal averaged total deposited particle number per carrier $\bar{q}_t^{a*}$ for the cases c) $d_C = 400\,\text{nm}$ and d) $d_C = 150\,\text{nm}$ (see text for quantity definition).
Dots represent the instantaneous values of d_m and $d_{s,m}$.

This chapter was previously published [249] and is reprinted with permission of the journal.

particle diameter in the investigated range does not affect the free particle deposition rate, as the total free particle concentrations $\bar{N}_t^a$ are identical (overlap). The different number of captured surface particles per carrier particle $\bar{q}_t^{a*}$ for different carrier particle sizes becomes now apparent, underlining the observation that a larger carrier particle captures more surface particles on average and even they occur in a smaller number, the deposition rate seems to be comparable. This is not obvious, since the coagulation kernel defined by a complex interplay of particle number concentrations, inertia and particle sizes, embedded in a complex environment. Plots for the time averaged total surface coverage $\bar{\xi}_t^a$ show that the variable stagnates after a maximum is reached. This happens, even the particle load $\bar{\eta}^a$ is increasing and therefore, deposition is still ongoing. This behavior can be explained by the accelerated on-surface coagulation process, combining more, single particles together to form bigger structures while reducing their surface area and therefore the covered surface of the carrier particle $\bar{\xi}_t^a$.

Figures 4.8 and 4.9 illustrate gas phase and deposited particle distributions averaged over time for different axial and radial locations. Although bigger carrier particles capture more platinum particles, the shapes of the PSDs appear very similar for dispersed and deposited platinum particles at all locations.

In both cases, particles size slightly increases in axial and radial direction, since the residence time increases, while particle concentration decreases (see 4.4). Nevertheless, time averaged PSDs do not show the real instantaneous size distribution. It is possible that very different PSDs alternate strongly in time and create a very different picture of the size distribution. High RMS values, as shown in areas closer towards the burner in figures 4.10 and 4.11, indicate this behavior. Accounting for this effect is of special importance for the given case, as a few PSDs of deposited material on single carrier particles are compared and different trajectories have a strong impact. Therefore, when comparing with experimental PSDs obtained by TEM counts of deposited particles, a comparison of instantaneous, time correlated values might give further insights. Thus, instantaneous PSDs for three different locations, as well as a contour of the particle loading η_m, at an axial height of x =200 mm are shown in fig. 4.10 and fig. 4.11 for both carrier sizes Due to the high inertia of the carrier particles, a filamentation can be observed. Thus, probe locations are chosen for areas with low-, intermediate-, and high mass load η_m, respectively. In all cases, a mode of smaller particles (2-4 nm) can be observed for all locations, whereas the PSDs gets broader with higher carrier load η_m and smaller carrier particle sizes.

Figure 4.12 shows that the calculated particle load η_m incorporate well with those from the experiment, following a negative trend towards increasing carrier particle diameter d_C. In comparison with the experimentally measured distributions, shown in fig. 4.13, the simulated

This chapter was previously published [249] and is reprinted with permission of the journal.

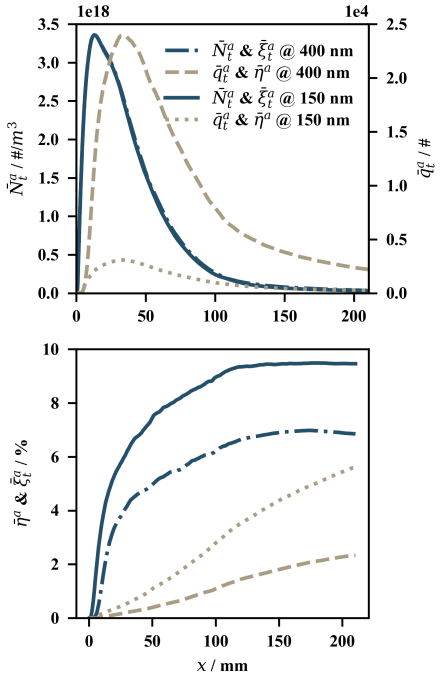

Fig.: 4.7 Time averaged quantities of different carrier particle size in comparison. Top: free particle number concentration $\bar{N}_t^a$ and number per carrier $\bar{q}_t^{a*}$. Bottom: total surface coverage $\bar{\xi}_t^a$ and carrier loading $\bar{\eta}^a$.

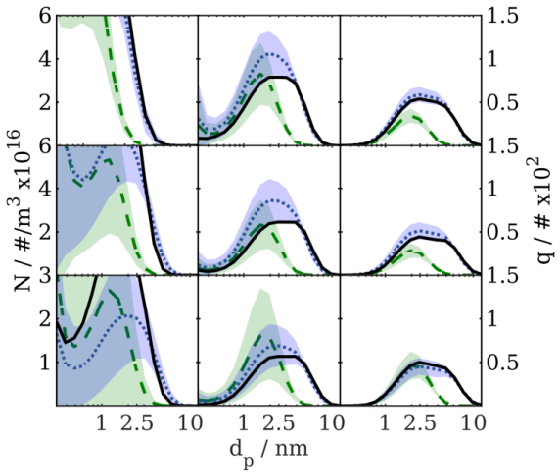

Fig.: 4.8 Averaged PSDs of platinum particles for d_C = 150 nm in gas phase N (green) and on carrier surface q (blue). Dashed lines indicating the RMS of flow field fluctuations. Black lines show the instantaneous PSDs of q. Left-to-Right: different distances from burner $x = 80, 125, 170$ mm; Top-to-Bottom: different radial positions from axis $r = 0, 10, 15$ mm.

This chapter was previously published [249] and is reprinted with permission of the journal.

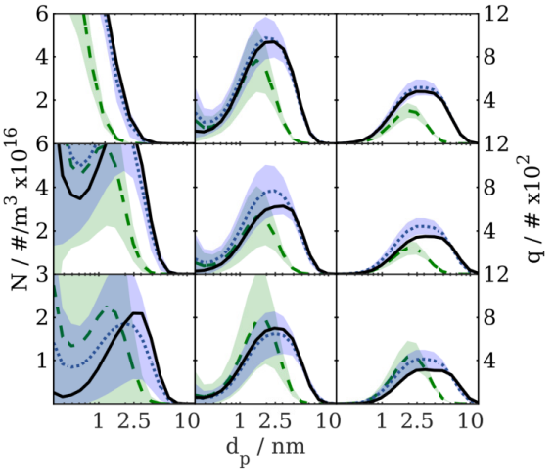

Fig.: 4.9 Averaged PSDs of platinum particles d_C = 400 nm in gas phase (green) and on carrier surface (blue) with dashed lines indicating the RMS of flow field fluctuations. Black lines show the instantaneous PSDs of q. Left-to-Right: different distances from burner $x = 80, 125, 170$ mm; Top-to-Bottom: different radial positions from axis $r = 0, 10, 15$ mm.

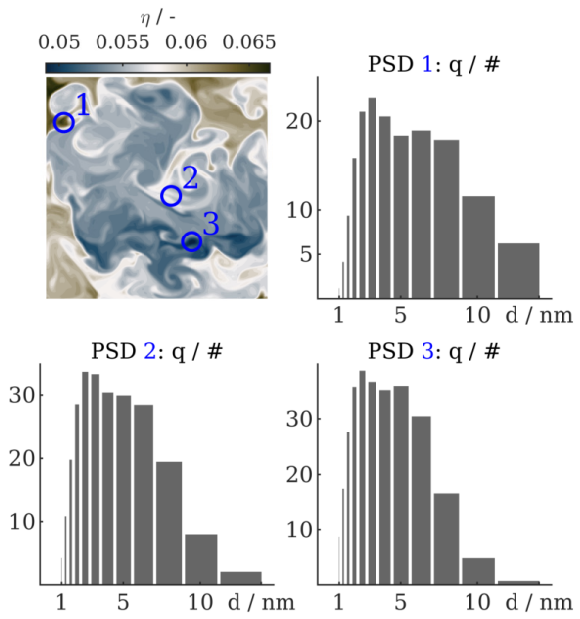

Fig.: 4.10 Instantaneous PSDs of deposited platinum material for the case d_C = 150 nm. PSDs obtained at 3 locations at an axial height of x =200 mm. The contour plot visualizes the 3 locations taken for the PSDs within the particle mass load field η_m.

This chapter was previously published [249] and is reprinted with permission of the journal.

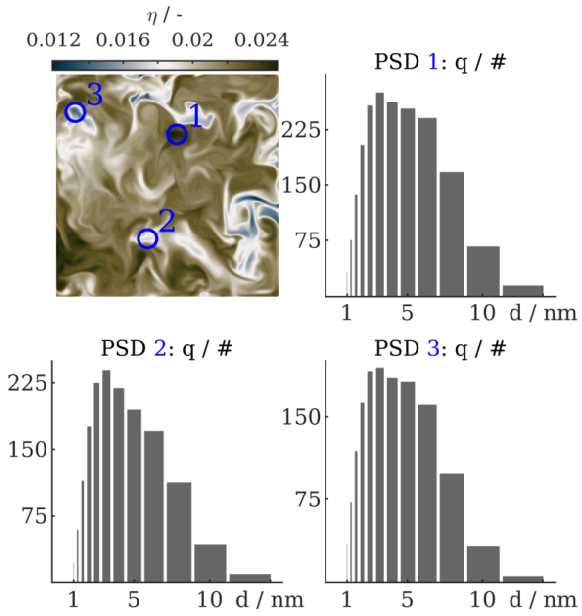

Fig.: 4.11 Instantaneous PSDs of deposited platinum material for the case d_C = 400 nm. PSDs obtained at 3 locations at an axial height of x =200 mm. The contour plot visualizes the 3 locations taken for the PSDs within the particle mass load field η_m.

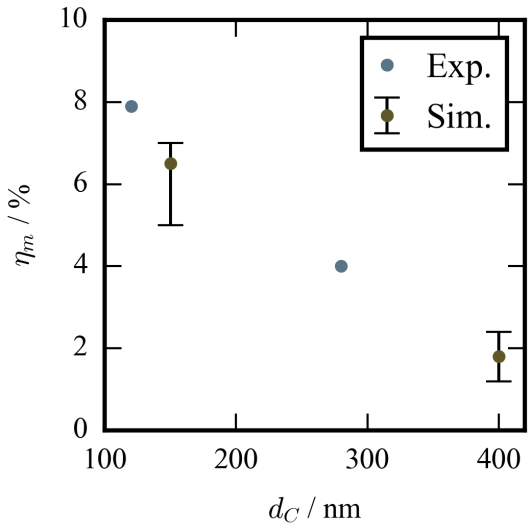

Fig.: 4.12 Particle load η_m of platinum particles deployed on alumina carrier particle surface obtained by experiments and simulations. Values of calculated particle load η_m correspond to location 1 from fig. 4.10 and location 2 of fig. 4.11 respectively. Error bars represent the range of computed η_m at the location x = 200 mm above the burner.

This chapter was previously published [249] and is reprinted with permission of the journal.

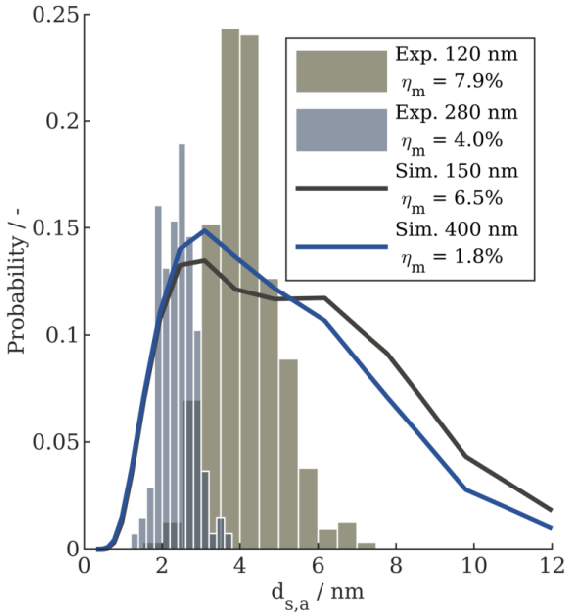

Fig.: 4.13 Measured and calculated PSDs of platinum particles deployed on alumina carrier particle surface. Calculated distributions correspond to PSD 1 from fig. 4.10 and PSD 2 of fig. 4.11 respectively.

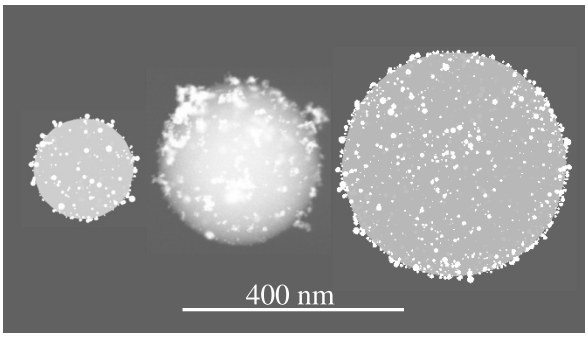

Fig.: 4.14 Artificial TEM representation of two calculated particles (left: d_C = 150 nm, right: d_C = 400 nm). TEM particle (center: d_C = 280 nm) is source for distribution given in figure 4.13.

This chapter was previously published [249] and is reprinted with permission of the journal.

PSDs agree in the area of smaller particles and the location of the highest particle counts. Mean diameters found by the experiments, given with 4.12 and 2.40 nm for the carrier particles of 120 and 280 nm, are within the range of those predicted by the simulations (3.75 and 4.18 nm for carriers of 150 and 400 nm). In both cases, distributions predicted by the simple surface coagulation model are a lot broader than given by the experiment though. The good good agreement with the experimental observations concerning the particle loading η_m gives rise to the assumption that deposition rates are predicted correctly. It is therefore likely that this behavior is in a large part explained by a too high value for the surface coagulation constant. The value was fitted in a one dimensional configuration using a constant mixture and might be corrected by a more appropriate procedure in future work. Nevertheless, stressing the overall complexity of the global process, the remaining uncertainties of all sub models, the sensitivity of the investigated quantities, as well as the limited options for experimental validation, we consider the results as in surprisingly good agreement. Studies without surface coagulation model led to a sensible different distribution with a very dominant peak at sizes around the monomer diameter and therefore, were far off the values shown by the experiment. Finally, figure 4.14, illustrates three dimensional representations of the simulation results previously shown in figure 4.13. The volumetric models are obtained by ballistic reconstruction i.e. spherical particle models are constructed according to the calculated PSDs and randomly "shot" on the carrier particle surface, whereby particle-particle collisions are considered as well. Here, a d_C = 150 nm and a d_C = 400 nm composite nanoparticles are shown together with a real TEM picture of a composite particle, giving a TEM-like visual impression of the simulated data.

4.6 Conclusions

Spray flame synthesis of composite nanoparticles (Pt/Al_2O_3) has been investigated by experiment and numerical modeling in the scope of LES with a solvent of isopropanol and acetic acid. Simulations were performed using premixed flamelet generated manifolds (PFGM) for tabulated chemistry with artificially thickened flame approach (ATF) for the three-dimensional model of the synthesis setup. The simulation strategy was verified in generic one-dimensional simulations (Appendix A). Aerosol dynamics have been taken into account by a sectional model, extended for surface deposition of platinum onto the alumina carrier surface, as well as for on-surface coagulation. The three dimensional simulations performed for different constant carrier particle sizes (150 and 400 nm) show good agreement with experimental observations regarding deposition rates and mean particle diameter. High deposition rates are found directly downstream of the flame, but the deployment of platinum

This chapter was previously published [249] and is reprinted with permission of the journal.

particles continues further downstream. Particle size distributions (PSD) of deposited platinum matter are predicted with a large deviation in width towards bigger particle sizes. Due to the good agreement of the deposited particle mass, it is likely that the surface coagulation constant has to be refitted in order to avoid too high surface coagulation rates. Investigations should be made in order to elaborate the validity of the definition of the surface collision constant and my replace it by a more general expression, or a function which decreases with higher inertia and size of deposited particles. Experiments with a larger database of particle and thermochemical data are mandatory for the development of more accurate numerical models and closures, as needed for the interaction of turbulence and coagulation processes. Simplified experiments with less complex chemistry would allow the use of finite rate chemistry and avoid the inaccuracies from using tabulated chemistry approaches and evaporation of spray mixtures.

4.7 Acknowledgements

The authors acknowledge the financial support by the European Commission in the Horizon 2020 framework (project Nanodome, reference: 646121). Further, we would like to thank the Center for Computational Sciences and Simulation (CCSS) for provision of computational resources.

This chapter was previously published [249] and is reprinted with permission of the journal.

Appendix A – Verification of model implementation

The verification of the model setup and the implementation of the numerical methods was performed in one-dimensional, generic test cases. Three simulations have been performed applying two different codes: Cantera and the in-house code PsiPhi, the latter described in section 4. Cantera is widely known and utilized in the chemical kinetics community for simulation of one-dimensional laminar flame configurations with finite rate chemistry and adaptive grid refinement. For the comparison between both codes, a laminar freely propagating flame configuration with stoichiometric air to fuel ratio has been chosen. The fuel (solvent-spray and pilot) and precursor ratio is kept the same as in the experiments and the liquid fuel is assumed to be completely evaporated. The particle model is implemented and conducted in PsiPhi only. Alumina carrier particles are injected at a distance of about 15 mm behind the flame front in order to account for the delayed release from the encapsulating droplet in case of a spray injection. The alumina carrier particle inception considers the mass flow given by the experiments at a fixed diameter of d_C = 150 nm. Two of three simulations are performed using PsiPhi, where the first simulation resolves the flame front with a grid size of $\Delta = 15.625\,\mu$m. The second PsiPhi calculation uses a grid size of $\Delta = 0.25$ mm and resolves the flame front by ATF on a width of 8 cells. This corresponds to the setup used for further 3D calculations of the complete synthesis flame configuration. The Navier-Stokes equations were solved in the low-Mach number formulation applying a fractional step pressure-velocity coupling, while an explicit three step Runge-Kutta scheme was used for time integration. Spatial derivatives for momentum equations were approximated by a second order central differencing scheme, while for the convective fluxes of all remaining scalars a TVD-scheme was used applying the non-linear CHARM limiter [255].

Verification Results

Figure 4.15 shows the results of all three simulations in terms of spatial temperature and species mass fraction profiles. While the finite rate chemistry solution performed using Cantera is considered as the "reference solution", it is evaluated, how accurate the different settings are in direct comparison. Within the shown window of 1.5 cm around the flame front, no deviation between the Cantera and the resolved PsiPhi solution can be observed, testifying the applied tabulated chemistry method combined with the defined progress variable being able to reconstruct the flames structure in the given configuration. The coarser PsiPhi simulation with ATF approach exhibits a stretched flame front in comparison to the resolving simulations, while conserving a similar slope. This effect is due to the ATF and allows the flame front being resolved on coarser grids, avoiding artifacts and larger errors for flame speed

This chapter was previously published [249] and is reprinted with permission of the journal.

and progress. Nevertheless, it is obvious that further simulations would benefit from a finer spatial resolution, but keeping in mind the dimensions of the real-world flame, the authors consider this setting as the best trade-off between computational expenses and accuracy. Further investigations are made for the developed sectional particle deposition model in order

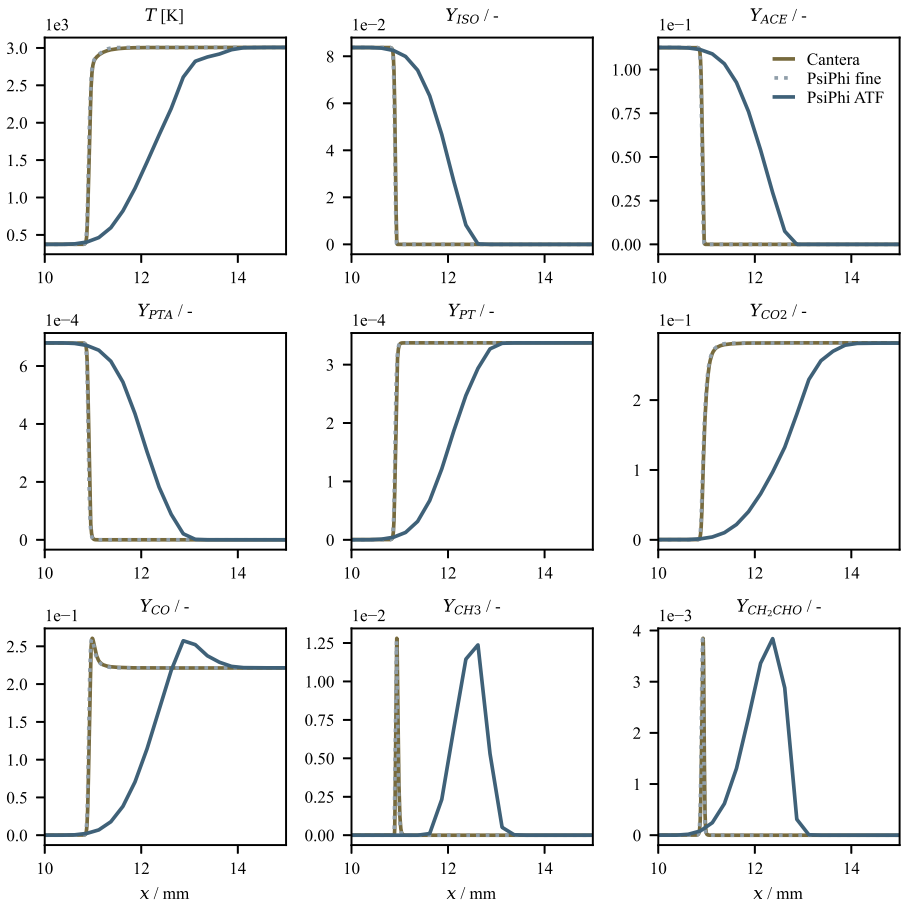

Fig.: 4.15 Comparison of thermochemical states obtained by different one-dimensional simulations using finite rate chemistry (Cantera) and tabulated chemistry (PsiPhi) with direct resolved flame front and flame front resolved by applying ATF.

to verify the model behavior within the simplified one-dimensional environment. Figure 4.16 shows the direct comparison of the evolution process of free and deposited particle distributions, as well as the total carrier coverage ξ_t and loading η. It can be observed that after a strong growth in number and size close to the reaction zone, the number concentration of free particles N is remarkably reduced after carrier particle being released. As the quadratic dependency of the deposition process indicates, free particle numbers decrease in sections with high number concentrations and vice versa. The consequence for the surface particle distributions is a drastic increase of particle numbers in the corresponding sections within

This chapter was previously published [249] and is reprinted with permission of the journal.

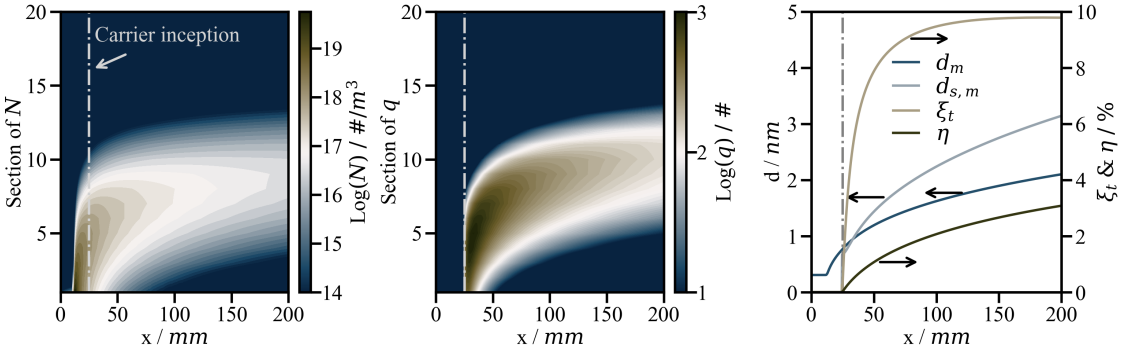

Fig.: 4.16 Contours and line plots of different quantities over axial distance x, the location of carrier particle injection (x = 25 mm) is indicated by a gray dotted line. From left to right: contour of free particle N size distribution over x; contour of deposited particle q size distribution over x; line plots of mean free and deposited particle diameters d_m and $d_{s,m}$, as well as the total surface coverage ξ_t and the carrier particle load η along the x-direction

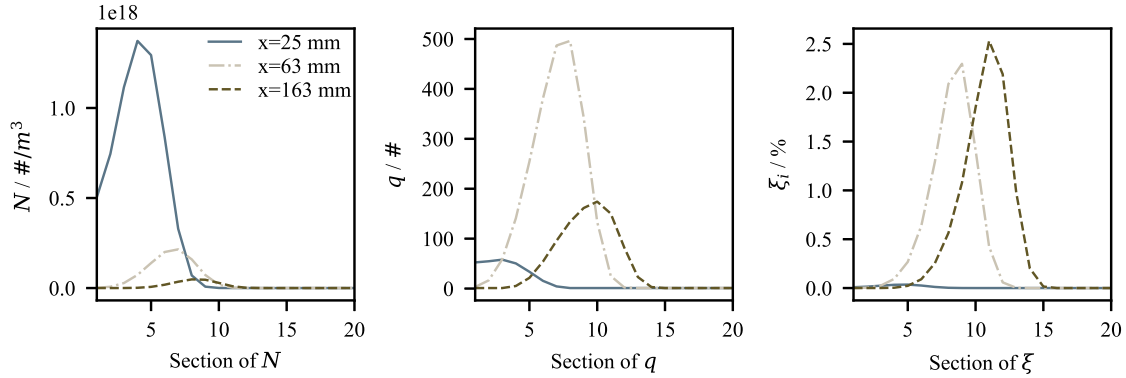

Fig.: 4.17 From left to right: Distributions of free particle sizes N, deposited particle sizes q and particle coverage ξ for all sections at different axial distance x = 25, 63 and 163 mm.

the zones of intermediate and small sized particles right after the carrier particle release. Due to the surface coagulation model, coagulation of platinum particles continues on the carrier particle surface and the PSD of deposited particles q is shifted towards larger particle sizes downstream. Interestingly, after the deposition process is initialized, particles on the carrier surface grow faster that the remaining free particles within the gas phase. The increasing surface particle coagulation rate is additionally a reason for the stagnating total surface coverage ξ_t at simultaneously increasing carrier particle loading η_m. At a distance of $x \approx 150$ mm, the surface particle coagulation rate outnumbers the deposition rate in such a way that the particle coverage starts decreasing. Figure 4.17 visualizes this process by showing distributions of the free gas particles N_i, deposited particles q_i and the carrier

This chapter was previously published [249] and is reprinted with permission of the journal.

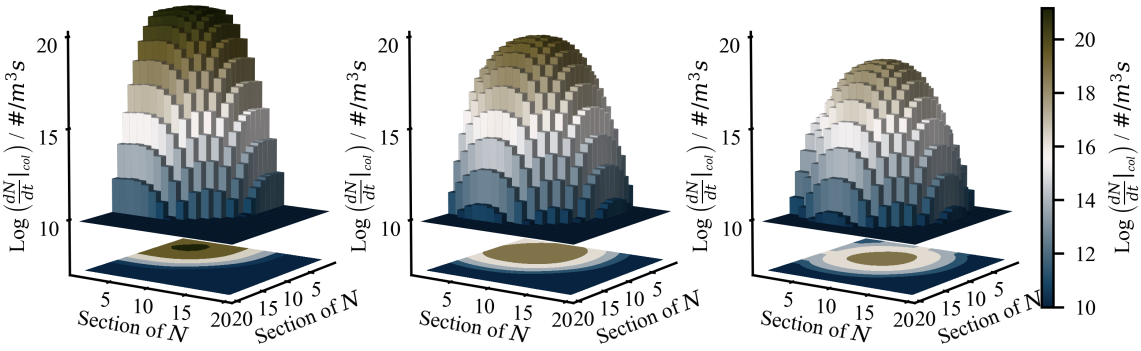

Fig.: 4.18 Representation of the symmetric free particle coagulation rate matrix at different axial distance (FLTR) x = 25, 63 and 163 mm.

coverage ξ_i for section index i at three different positions (x = 25, 63, 163 mm), respectively. It becomes obvious that the main deposition process takes place directly after the carrier particle inception at x = 25 mm, transferring a large number of free gas phase platinum particles N to the carrier surface distributions q between position x = 25 mm and x = 63 mm. Accordingly, the hampered growing of free gas phase particle sizes is attributed to the fact that the number concentration N gets thinned out due to the deposition process. Figure 4.18 illustrates this behavior by visualizing the trend of the free platinum particle coagulation rate tensor $[dN_{ij}/dt]_{c,N}$ for the same positions as used for prior investigations (i.e. x = 25, 63, 163 mm). As expected, drop of the coagulation rate after the particle release (between x = 25 and 63 mm) is considerably larger than the following step, as the linear trend is shown on a logarithmic scale. Due to the growth of the remaining free platinum particles within the gas phase, the coagulation maximum moves along the symmetric tensors' main diagonal, towards larger particle sizes in flow direction. In order to investigate the behavior of the deposition process of free platinum particles to the carrier surface, the total deposition rate $[dN_k/dt]_{c,C}$ (Eq. (4.20)) is split into its contribution for different sections according to the equation given below.

$$\left.\frac{dQ_{ij}}{dt}\right|_{dep} = \xi_j \left[\frac{dN_i}{dt}\right]_{c,C} + (1-\xi_t)E_j \left[\frac{dN_i}{dt}\right]_{c,C} \delta_{ij}, \tag{4.29}$$

where E_j is j-th component of the first order unit matrix and δ_{ij} is the Kronecker delta. Rates corresponding to the contributions from Eq. (4.29) are indicated in Fig. 4.19. In contrast to the free particle coagulation rate, the matrix resulting from the deposition rate is not symmetric. It can be observed that the distribution in N direction (x-axis) very much equals the free molecular particle coagulation rate (Fig. 4.18) though. In Q direction (y-axis), the distribution is generated by the coverage ξ_i, which moves to a higher maxima according to

This chapter was previously published [249] and is reprinted with permission of the journal.

the on-surface coagulation. With respect to the similarity to the distributions given by Fig. 4.17 (right), the distribution in Q direction can be well explained. The comb along the main diagonal represents the deposition rate of particles which either directly contact the surface, or collide with a deposited platinum particle of the same size. Further, every value off the diagonal corresponds to a collision of a free gas particle N_i with a particle attached to the carrier surface Q_j. For better understanding, Fig. 4.20 shows the deposition rates on the main diagonal, given by the equation below

$$\left.\frac{dQ_{ij}}{dt}\right|_{dep}^{d} = \left.\frac{dQ_{ij}}{dt}\right|_{dep} \delta_{ij}, \tag{4.30}$$

for illustration of the contributions of the direct deposition on the carrier surface and collision with particles covering the carrier. The evolution of the overall three-dimensional distribution is an example for the whole deposition process and in line with observations made before (Fig. 4.16 - 4.18). Explained at the example of Fig. 4.19 and Fig. 4.20, the process can be described from left to right (in flow direction): (I) The free particles, which were generated in and after the flame front, strongly deposit on the almost empty surface. Therefore, rates off the main diagonal are very low, with high values for small N and Q. (II) A major amount of particles was already deposited and the surface is covered by platinum particles by more than 4% (see Fig. 4.17). Direct deposition on the carrier surface is still dominant, but collision with deposited platinum material is more relevant. Particles deposited on the carrier have a larger average size in comparison to free gas particles due to on-surface coagulation. (III) Particle deposition rate decreases further, especially in the region of smaller particle sections. The importance of free particle and deposited particle interactions increases for larger particle sections, as particle growth on the carrier surface increases the coverage of particles in that size range. Summarizing, free particle coagulation and on-surface coagulation can be understood as individual processes, connected by the deposition procedure. Deposition is in first place driven by free particle and carrier particle concentrations and therefore dominant in regions, in which carrier particles are incepted to existing platinum particles. More sophisticated tests must be performed to justify further adaption of the on-surface coagulation constant α_c.

This chapter was previously published [249] and is reprinted with permission of the journal.

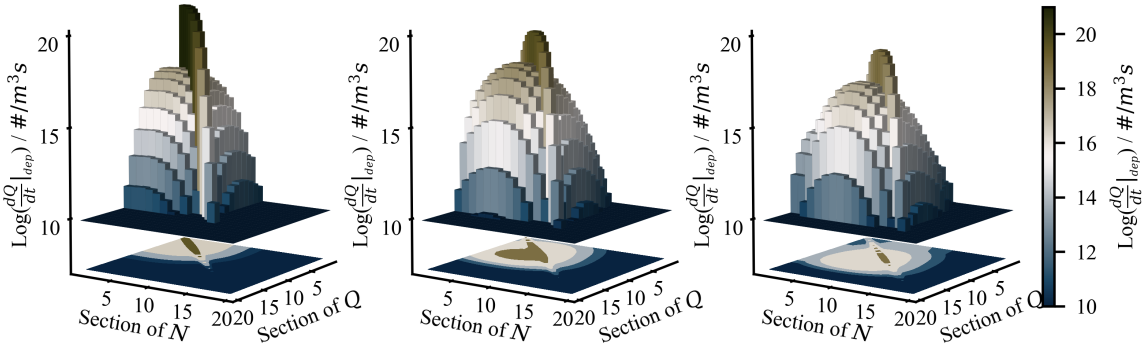

Fig.: 4.19 Representation of the non symmetric particle deposition rate matrix at different axial distance (FLTR) x = 25, 63 and 163 mm.

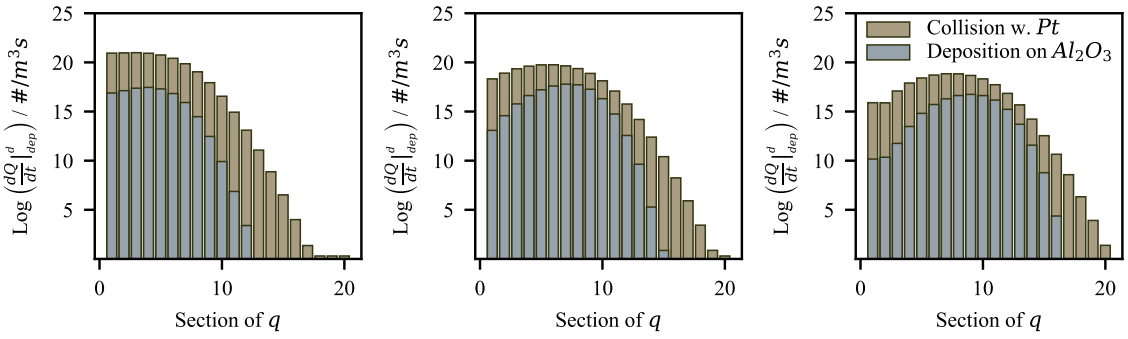

Fig.: 4.20 Particle deposition rate contributions of the main diagonal of the particle deposition rate matrix given by Eq. 4.30 at different axial distance (FLTR) x = 25, 63 and 163 mm.

This chapter was previously published [249] and is reprinted with permission of the journal.

5 The role of phase transition by nucleation, condensation, and evaporation for the synthesis of silicon nanoparticles in a microwave plasma reactor — Simulation and experiment

P. Wollny, J. Menser, L. Engelmann, J. Sellmann, C. Schulz, H. Wiggers, A. Kempf, I. Wlokas

P. Wollny developed and implemented all models, ran all the simulations, wrote the paper, including all figures and tables, excluding the experimental part. J. Menser ran the experiments and contributed with the data, the chapter and pictures about the experiment. The authors L. Engelmann, J. Sellmann, C. Schulz, H. Wiggers, A.M. Kempf and I. Wlokas contributed feedback, corrections and proof-reading.

5.1 Abstract

A novel particle model is presented to simulate the synthesis of silicon nanoparticles from monosilane in a laboratory sized microwave plasma reactor.The simulations contribute essentially to the understanding of the particle formation process and the spatial and size distribution of particles observed in the experiment. The model approach features phase transition and explains the observed, tube-shaped particle formation zones by a competing nucleation, condensation, and evaporation process coupled with complex transport phenomena. The simulation results are in excellent agreement with experimental data from Rayleigh scattering and line-of-sight optical absorption with onion-peeling reconstruction (LOSA) measurements of the particle front, as well as with multiline SiO laser-induced fluorescence (LIF) temperature measurements. Particle size distributions determined from transmission electron microscopy (TEM) on thermophoretically sampled particles are in good agreement with the simulation results. Average diameters of 25.8 nm calculated in the simulation compare well to 27.6 nm measured in the experiment. It was found that thermophoresis has a crucial impact on particle trajectories, as it extends the particle residence time within the

reactor by about 20 % and provides the determining force for particles to escape zones of high temperature in which particles evaporate otherwise.
The sectional model features two-way coupled phase transition formulations for the condensing matter, which is formed through the decomposition of monosilane diluted in argon / hydrogen mixtures. The process is investigated by the combination of two simulations with different grid resolutions, which show differences for the high Schmidt number particle phase only. The simulations feature a global monosilane decomposition reaction, while the microwave plasma source is simplified by a local heat source.

5.2 Introduction

Gas-phase synthesis is one of the most prominent methods of industrial nanoparticle production, not only, because of the varity of involved control parameters (i.e., pressure, temperature, residence time, etc.), which open a large optimization space for the product quality and design, but also because of its versatility regarding the materials system: The product material can be changed by using different precursors – or even by mixing with other substances. The gas-phase process is continuous and scalable. All gas-phase particle-synthesis processes need a heat source to thermally decompose the precursor and restructure the atoms and molecules to particle nuclei. The process can be driven either by external heating from walls, by exothermic chemical reactions (flame) or by plasma. External heating is limited by heat conduction and convection in the process gas and therefore, does not enable steep temperature gradients. Flames provide steep temperature gradients but the process is limited to oxide particles. Plasmas provide both: Fast heating, fast reactions, and a nearly unrestricted choice of process gases. Among the plasma based synthesis processes, the microwave-plasma has the advantage of high ionization rate facilitating fast precursor decomposition but at – compared to arc discharge plasma – moderate gas temperatures. The microwave-plasma process was used quite early for the generation of thin layers, e.g., by Kobashi et al. for diamond films [104], or powders, e.g. by Takagi et al. for Si particles [215]. For details on the history of the microwave-plasma nanoparticle synthesis we refer to the reviews by Szabo and Schlabach [214] and by Kortshagen et al. [111]. The laboratory size reactor investigated in this work was introduced by Knipping et al. [103] for synthesis of high purity silicon nanoparticles. Technical modifications were introduced to improve the diagnostic accessibility of the reactor and the fluid mechanical stability of the flow, based on the tangential injection of the swirl gas [165].
Recent publications were devoted to optical diagnostics and the investigation of the aerosol dynamics and transport within the reactor [127, 128, 4, 142]. By line-of-sight attenuation,

This chapter was previously published [250] and is reprinted with permission of the journal.

Rayleigh scattering, and spatially resolved laser-induced incandescence, it was shown that most of the particles are located in an approximately one to two millimeter thin layer at the circumference of the glowing particle stream. The fact, that three independent measurements performed by different experimenters yield nearly the exact radial particle distribution, show that this behavior is not a measurement artifact but a characteristic of the particular microwave-plasma reactor design. Perhaps it is the complexity of the microwave-plasma as a heat source which so far discouraged the investigation of the process by simulations. However, the plasma can be modeled in a simplified way as a distributed heat source and as the gas temperature usually does not exceed 3000 K, kinetic gas theory-based models for transport properties were sufficient to describe the transport and thermodynamic properties of the gas-phase in the manner of temperature depending polynomials and NASA polynomials [28]. The disadvantage of such a simplistic model is the enforced steady state of the plasma and a more or less assumed power distribution within the heating zone. Ionization of the gas is totally neglected and the decomposition kinetics of the precursors are assumed to be fast. Using such a model, Giesen et al. [57] investigated the formation and transport of Si nanoparticles. Giglmaier et al. [58] used a similar approach for the particle growth in a similar reactor with a down-stream heating zone and other works were devoted to the fluid dynamical optimization of such a reactor [165, 153, 114]. Nevertheless, the section of the process that is accessible for optical diagnostics, is located down-stream of the plasma and is neither affected by the plasma itself or by the unknown reaction kinetics.

The fast precursor decomposition on the one hand and the moderate temperature on the other create a spatially narrow zone of particle monomer formation, where the conditions for nucleation are quickly achieved. The simulations by Giesen et al. [57] and by Giglmaier et al. [58] neglected the condensation processes and showed a quite homogeneous distribution of the particle volume fraction. This contradicts the recent observation of a formed thin and tube-shaped particle front [127, 128, 4, 142]. Therefore, detailed modeling of the nucleation and the particle dynamics could provide additional insight by predicting particle formation in regions with suitable conditions, which are not too hot for particle existence.

For synthesis at lower operating temperatures (< 950 K), very different particle formation mechanisms where observed by Ho et al. [79], Frenklach et al. [47], and Onischuk et al. [156, 157] for the formation of amorphous silicon particles from monosilane. Particle clusters are formed after the partial dehydrogenation due to collisions of different silylene intermediates and grow by surface reactions with silanes and collision with silylenes. For the same material systems, the particle forming mechanism changes completely, if the process environment reaches higher temperatures, as featured by plasma reactors.

Models for thermal plasma synthesis processes with temperatures of 10,000 K and more

This chapter was previously published [250] and is reprinted with permission of the journal.

have been developed applied in the frame of computational fluid dynamics (CFD) by many authors in the last decades. Shigeta and Watanabe [202, 203] introduced a successful model strategy for thermal plasma processes using metal powder precursors. In those processes, precursor material has been fed into the plasma in the form of metal particles that evaporate and form new, mixed particles within a so called co-condensation process. The evaporated mass is captured by a separate monomer conservation equation that serves as source for the condensation process. The general dynamics equation (GDE) is implemented based on a discrete sectional approach, which supports homogeneous and heterogeneous nucleation following the idea of Prakash et al. [173]. The latter supports an implementation of surface growth and evaporation without the rather complex and numerically pricey approach of moving sections [209]. This simplification comes, however, at the cost of artificial diffusion in the particle size space, as particles are limited to be shifted between static sections as they change in size.

Recently, Shigeta et al. [204] have applied their plasma model to investigate the effect of quenching on thermal plasma synthesis and found out that rapid cooling of supersaturated gas forces higher nucleation rates and decreased the surface growth in the next step. The resulting product nano-powder therefore showed on average smaller particles with larger specific surface area compared to the non-quenched product. These observations support the findings of Mendoza et al. [139], who followed a similar modeling strategy applying the moment method introduced by Kazakov and Frenklach [95] for solving the GDE in the context of silica nanoparticle synthesis. Evaporation of the precursor powder was realized by evaporation due to thermal heating of the carrier gas. Efforts to numerically study and optimize the silicon nanoparticle synthesis processes within thermal plasma reactors have also been made by Colombo, Ghedini, and others [29] by following the same model philosophy coupled with a plasma thermo-fluid-dynamic model, while the GDE is modeled by a rather simple presumed PSD moment method. As previously mentioned, the process temperatures in microwave plasmas are low compared to those in thermal plasma processes. Following Giesen et al. [**?**], the presented model simplifies the plasma source as a homogeneous heat source, but features nucleation as suggested by Girschik and Chiu [59], as well as a formulation for condensation and evaporation depending on the saturation rate. The phase-transition model is embedded in a discrete sectional description of the PSD based on the strategy suggested by Prakash et al. [173] and applied by Shigeta and Watanabe [202, 203]. As we promote a stronger relation between the carrier gas phase and the dispersed phase, we drop the monomer conservation equation and therefore, the idea of the GDE being a one way linked "top on model". Instead, the proposed model applies a direct coupling between the GDE and the governing equations of the gas phase as used in some zero-dimensional multivariate population balance models

This chapter was previously published [250] and is reprinted with permission of the journal.

(mpbm) [146]. Mass fluxes from species therefore have a direct impact on the chemical equilibrium, the gas composition, the density, and other related factors. Moreover, initially formed particles can evaporate again to attend in further nucleation reactions as observed by Lalanne et al. [115].
Applying this novel CFD simulation approach, we are able to predict the characteristic tubular particle front (see Fig. 5.1) as observed in the investigated microwave plasma reactor. Optical measurements confirm the position, size, and intensity of the simulated particle formation. The particle-size distribution derived by TEM measurements is in good agreement with the simulations and new insight of the overall process could be gained.

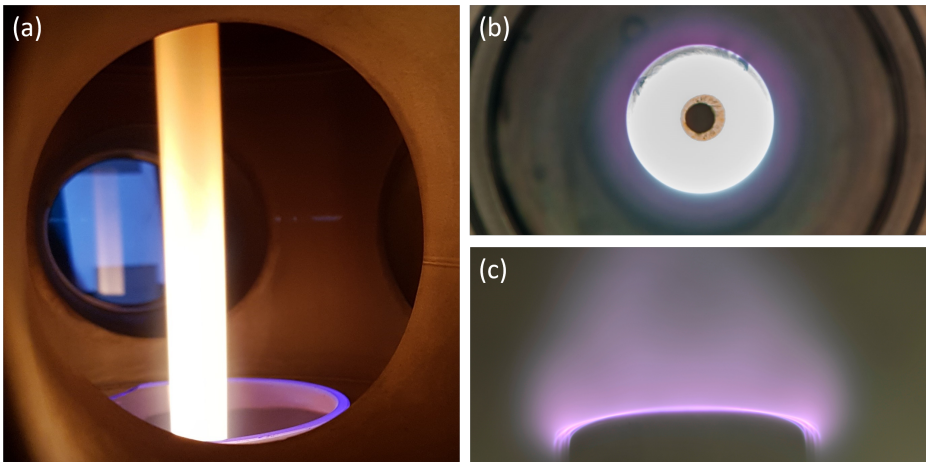

Fig.: 5.1 (a) View into the reactor during silicon nanoparticle synthesis with the conditions described in this publication. (b) Top view onto the plasma provides a view onto the hollow structure. (c) Side view of the H_2/Ar plasma showing that the plasma attaches to the nozzle. Due to the electric field enhancement at small radii, the glow is increased near edges.

Our literature review left us with a few open questions concerning the effect of the grid size on the particle field and the impact of thermophoresis. We therefore investigated the grid dependence and the effect of thermophoresis.
In this work, we present a detailed three-dimensional simulation for the transport and particle dynamics of silicon nanoparticle from monosilane pyrolysis in a fully coupled simulation. We demonstrate that the nucleation and evaporation phenomena are vital for the understanding of the experimental observations. Section 2 briefly describes the experimental setup, the diagnostic methods and the observations that motivated this work. Section 3 explains the modeling approach and gives a brief review of the methods employed in this work. The results are presented and discussed in section 4, followed by the conclusions. In addition, a

This chapter was previously published [250] and is reprinted with permission of the journal.

generic, zero-dimensional test case is shown in the appendix to explain the model concept and provide a simple benchmark for implementations of the presented model.

5.3 Microwave plasma: Experiment

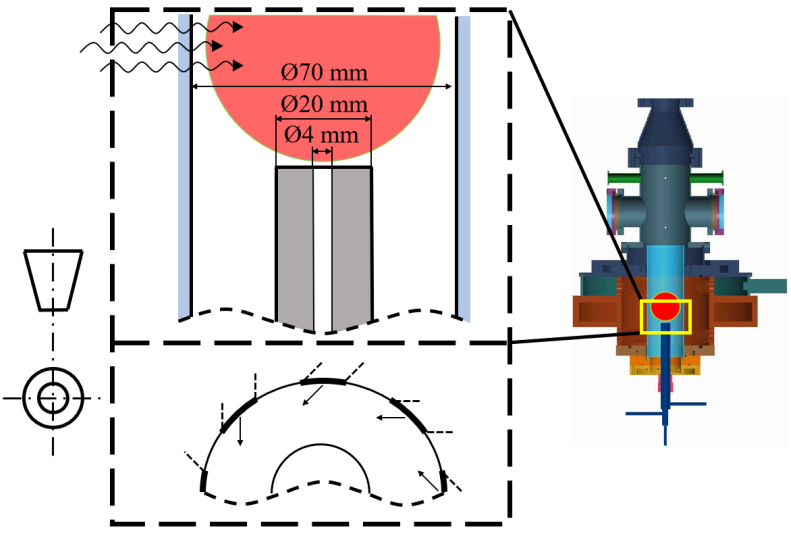

Fig.: 5.2 The experimental setup of the microwave reactor for the production of Si nanoparticles. Nozzle and swirler are sketched on the left; the plasma zone is marked by the red spherical area.

The silicon nanoparticles are synthesized using a microwave plasma reactor. The reactor was object of previous studies with focus on the measurement techniques [140, 141]. The particles are generated by the plasma process at 10 kPa absolute pressure, where the precursor gas mixture (0.2 slm H_2, Ar 2 slm, 0.03 slm SiH_4) is injected into the plasma zone through a nozzle of 4 mm diameter. To confine the precursor gas and minimize particle deposition on the quartz inliner as a result of thermophoresis a co-annular swirl flow of Ar/H_2 with 6.6/0.5 slm is used. The swirl-generating nozzle (located below the inliner) was optimized by Petermann et al. [165] and corresponds to the setup featuring eight tangential tubes (T08). A microwave slot antenna with 800 W incoupled power is located above the center nozzle and abruptly heats and thus decomposes the gas. The detailed description of the plasma reactor can be found in [140, 141].
All measurements have been performed at approximately 400 mm above the nozzle. Therefore, a cross-piece with nitrogen-purged quartz windows was mounted at this position. Due to the mechanical construction of the plasma resonator, it was not possible to achieve a shorter distance to the nozzle exit. It has long been speculated that the particle stream is

This chapter was previously published [250] and is reprinted with permission of the journal.

hollow. This assumption was supported by an observation through an additional viewport that enables optical access from the top onto the nozzle. The structure of the nanoparticle torch was measured using Rayleigh scattering. The second harmonic of a Nd:YAG laser (QuantaRay Lab 170; pulse length of: 8 ns) was formed into a 60-mm high light sheet with a thickness of approximately 0.5 mm. The light sheet was adjusted to pass through the center of the nanoparticle stream. Perpendicular to the light sheet, an iCCD camera (LaVision Imager ProX) equipped with a narrowband 532-nm band rejection filter recorded the elastic scattering signal. The intensifier gate length was set to 100 ns to suppress the thermal radiation of the nanoparticle stream on the images. The entire system operates at 10 Hz and 1000 pictures have been taken in one go (a video is available as supplemental material).

In Fig. 5.3, two instantaneous images (c) and (d) and the average (b) over the whole dataset is shown. A line-integrated incandescence image (a) is shown for comparison. The incandescence image and the averaged Rayleigh scattering signal show a smooth structure with straight lines at the edges. The two example instantaneous images are more structured. The edges are slightly winkled attributed to Helmholtz instabilities.

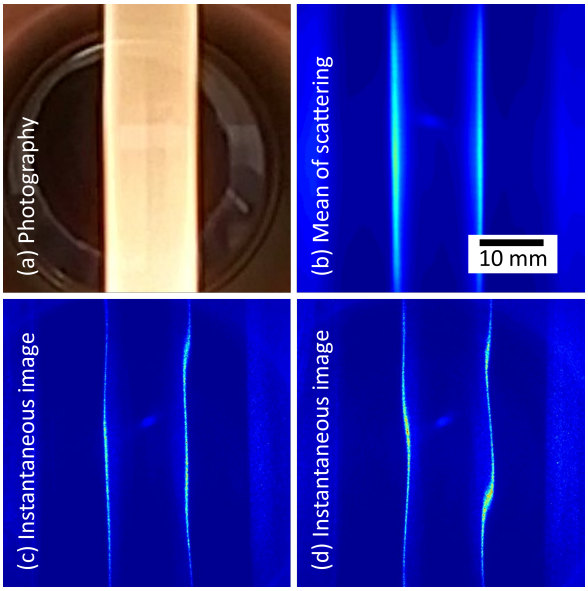

Fig.: 5.3 (a) Line-of-sight averaged incandescence signal recorded with a consumer camera. (b) Time-averaged images of elastic scattering showing the general structure of the particle torch. (c) and (d) show examples of instantaneous Rayleigh scattering.

Sequences of single-shot measurements shows that the particle torch is not fully stable, but oscillates around the centerline shifting the position by approximately 1–3 mm to each side with a frequency between 1 and 10 Hz. This behavior is not captured in the simulation, as no

This chapter was previously published [250] and is reprinted with permission of the journal.

data about the energy distribution within the plasma torch is available. Thus, the simulation approximates the microwave plasma by a spherical, stationary, and homogeneous heat source without perturbations, which results in a steady flow field. Due to the slow and laminar characteristics of the oscillations that do not intercept the particle front, we consider their impact as insignificant.

Particle diameters within the observation zone have been measured by *ex-situ* TEM micrographs an by *in-situ* time-resolved laser-induced incandescence measurements (TiRe-LII). The samples were taken by thermophoretic sampling on a TEM grid that was exposed to the particle-laden stream with exposure times between 20 and 50 ms [122]. The grids have been analyzed with a high-resolution TEM (JEOL 2200FS) and the visualized nanoparticles are counted and sized by hand (see Fig. 5.15). The obtained particle-size distribution has a mean particle size of 27 nm with fitted log-normal width of approximately 1.35 geometrical standard deviations.

The average gas-phase temperature was determined from the rotational temperature of SiO by multi-line laser-induced fluorescence (LIF) [24]. The high-purity argon gas used, contains 2 to 5 ppm oxygen, which is sufficient to form small concentrations of SiO that can be exploited for LIF imaging. A dye-laser system (Sirah Cobra stretch pumped with a Quanta Ray LAB 170) was used to scan the SiO A–X(2,0) band at around 225 nm, where nine rotational transitions are present. Using our in-house multiline fitting routine, we determined two-dimensional time-averaged temperature distributions, shown in Fig. 5.11.

5.4 Modeling framework

5.4.1 Fluid dynamics model

In the given case, the fluid phase consists of the described bath gas and precursor (monosilane), which is injected into the plasma through the central inlet nozzle. Additionally to the conventional Navier-Stokes equations, which are exhaustively discussed in the field of CFD (Ref. [171] for more information), conservation equations for the partial densities $\rho Y_\kappa = \rho_\kappa$ (Y denotes the mass fraction) attending gaseous species κ, are added. Applying the Fick law for diffusion of a unity Lewis number, together with a chemical net production rate $\dot{\omega}_\kappa$ for the precursor decomposition, the coupled system of equations can be given as:

$$\frac{\partial \rho Y_\kappa}{\partial t} + \nabla \cdot (\boldsymbol{u} \rho Y_\kappa) = \nabla \cdot \left(\frac{k}{c_p} \nabla Y_\kappa \right) + \dot{\omega}_\kappa + \Gamma_\mathrm{p} \delta_\mathrm{Si}(\kappa). \tag{5.1}$$

This chapter was previously published [250] and is reprinted with permission of the journal.

Here, ρ is the gas density, where k and c_p are the thermal conductivity and the isobaric heat capacity. The term Γ_t, is the phase transition sink/source, which considers the mass transfer by homogeneous $\Gamma_\mathcal{I}$ and heterogeneous $\Gamma_\mathcal{S}$ condensation. Both are explained in the next section. The Dirac measure $\delta_\mathrm{Si}(\kappa)$ is employed in order to apply the mass transition only to the condensating substance of atomic silicon:

$$\Gamma_\mathrm{t} = \sum_{\alpha=\mathcal{I},\mathcal{S}} \Gamma_\alpha \tag{5.2}$$

The decomposition reaction for monosilane is modeled as suggested by Woiki et al. [247] for a the global reactions step $SiH_4 \rightarrow 2H_2$+Si. The first order rate constant is hereby determined as a function of the temperature T:

$$k = 2\times 10^8 \exp(-14140\,\mathrm{K}/T)\left[s^{-1}\right] \tag{5.3}$$

Attention must be payed to the energy equation that is defined by the sum of the chemical and internal energy and described as e_s and conserved by the following equation:

$$\begin{aligned} &\frac{\partial \rho(e_\mathrm{s}+K)}{\partial t} + \nabla\cdot(\boldsymbol{u}\rho(e_\mathrm{s}+K)) + \nabla\cdot(\boldsymbol{u}p) = \\ &\nabla\cdot\left(\frac{k}{c_p}\nabla e_\mathrm{s}\right) + \rho\boldsymbol{g}\cdot\boldsymbol{u} + \Gamma_\mathrm{t} h_\mathrm{s}^\mathrm{Si} + \rho S_\mathrm{p}. \end{aligned} \tag{5.4}$$

With the knowledge about the kinetic energy $K = |\boldsymbol{u}|^2/2$, e_s can be computed as part of our system of partial differential equations. The additional variables $\boldsymbol{g}$, h_s^Si and S_p denote the gravitational vector, the specific sensible enthalpy of silicon vapor and the thermal heat source for the plasma torch. The latter is given by eq. (5.5) with the volume of the spherical source V_p and the plasma power of the setup P_p together with the efficiency of the plasma η_p to generate heat within the reactor. We found that a value of $\eta_\mathrm{p} \approx 0.5$ gives a close match with the experimental measured temperature:

$$S_\mathrm{p} = \frac{P_\mathrm{p}}{V_\mathrm{p}}\eta_\mathrm{p}. \tag{5.5}$$

5.4.2 Dispersed phase model

Transported particle dynamics equation

Homogeneous and heterogeneous condensation, as well as evaporation processes strongly depend on the gas-phase conditions as well as the particle characteristics, i.e., surface area a,

This chapter was previously published [250] and is reprinted with permission of the journal.

particle diameter d_p, and more. In this particular case, the high temperature throughout the reactor and the resulting fast sintering rates allow for the assumption of spherically shaped particles over the occurring size spectrum. The univariate approach, is strongly size and shape dependent and as result, particle dynamics equations (PDE) become a function of the particle volume v only. Functions $f(v)$ that depend on the local particle-size distribution (PSD) $n(v)$, hence become one-dimensionally dependent as well:

$$\Phi(v) = \int_0^\infty f(v)n(v)dv. \tag{5.6}$$

Examples for particle-size dependent functions $f(v)$ are condensation, evaporation, and surface reaction processes – to name a few. A conservation law for the PDE transported by convection and diffusion can therefore be derived by applying the Reynolds transport theorem and accounting for diffusive fluxes for a one dimensional PSD, only.

$$\frac{\partial n(v)}{\partial t} + \nabla \cdot \boldsymbol{u}_\mathrm{t} n(v) = \nabla \cdot j(v) + \Gamma(v) \tag{5.7}$$

In eq. (5.7), $\boldsymbol{u}_\mathrm{t}$ denotes the total velocity as sum of the gas phase velocity $\boldsymbol{u}$ and the thermophoretic velocity $\mathcal{T}$ – given by the Waldmann equation [**?**]. The diffusive fluxes are denoted by $j(v)$, while $\Gamma(v)$ is the sum of all relevant mesoscopic sources, which will be segregated and discussed respectively. The limited complexity of a one dimensional particle-size distribution enables to apply a more sophisticated closure for the representation of the PSD and thus, the discrete sectional model is considered as a good trade-off between computational costs and accuracy [54]. The accurate size depended equation (5.8) can therefore be approximated by a sufficient number of Dirac peaks n in v space at discrete grid points v_k. It follows:

$$\begin{aligned}\Phi(v) &= \int_0^\infty f(v)n(v)dv \approx \sum_{k=1}^{n} \int_0^\infty f(v)n(v)\delta\left(v_\mathrm{k} - v\right)dv \\ &= \sum_{k=1}^{n} f(v_\mathrm{k})q_\mathrm{k}.\end{aligned} \tag{5.8}$$

With the particle number per unit mass q_k at grid point v_k being known, equation (5.8) can be approximated by the very simple relation in the above equation. In the context of this work, this is a vital feature, since particle evaporation at the same thermochemical conditions strongly vary over the particle size spectrum.

This chapter was previously published [250] and is reprinted with permission of the journal.

A set of governing equations (5.9) can then be derived for a series of $k = 1 \ldots n$ coupled equations representing the PDE in time and space. Those equations include the non-size-dependent particle inception source $\mathcal{I}_\mathrm{k}$, as well as size dependent contributions for the particle coagulation C_k and the condensation / evaporation at the particle surface $\mathcal{S}_\mathrm{k}$:

$$\frac{\partial \rho q_\mathrm{k}}{\partial t} + \nabla \cdot (\boldsymbol{u}_\mathrm{t} \rho q_\mathrm{k}) = \nabla \cdot j_\mathrm{m} + \mathcal{I}_\mathrm{k} + \rho \mathcal{S}_\mathrm{k} + \rho^2 C_\mathrm{k} \tag{5.9}$$

In the frame of a laminar flow, the system of equations (5.9) is closed and the diffusive flux j_m for each grid point v_k in v-space can be calculated by:

$$j_\mathrm{m} = \rho D_\mathrm{k} \nabla q_\mathrm{k}. \tag{5.10}$$

The particle diffusion coefficient D_k is:

$$D_\mathrm{k} = \frac{k_\mathrm{B} T}{3\pi\mu d_\mathrm{k}} \zeta(Kn). \tag{5.11}$$

The equation depends on the gas phase temperature T and viscosity μ, as well as on the particle diameter d_k, while k_B is the Boltzmann constant and $\zeta(Kn)$ denotes the transition correction – free molecular to continuum regime – as function of the Knudsen number Kn:

$$\zeta(Kn) = \frac{5 + 4Kn + 6Kn^2 + 18Kn^3}{5 - Kn + (8+\pi)Kn^2} \tag{5.12}$$

Nucleation

Within the plasma environment, monosilane decays rapidly into hydrogen and atomic silicon at hight temperatures. The latter forms clusters outside the hot plasma torch up to a critical size d_k at which it condensates in form of nano-sized droplets, which in the liquid state have metallic properties. The model framework captures this phenomena by the inception source $\mathcal{I}$, which computes the rate of nucleation droplets depending on the thermochemical gas state and material properties. Because of its performance with condensing metals [56, 159], the self consistent classical nucleation theory of Girshick and Chiu [59] is applied in this work and given by equation (5.17). Note that this equation depends on the dimensionless surface tension Θ, which is denoted by equation (5.14):

$$\mathcal{I}^* = v_\mathrm{m} \left(\frac{2\sigma}{\pi m_\mathrm{m}} \right)^{1/2} \frac{n_\mathrm{s}^2}{\rho} S \exp\left(\Theta - \frac{4\Theta^3}{27(\ln S)^2} \right) \tag{5.13}$$

This chapter was previously published [250] and is reprinted with permission of the journal.

$$\Theta = \frac{\sigma s_\mathrm{m}}{k_\mathrm{B} T} \tag{5.14}$$

Here, n_s is the saturation monomer concentration, while v_m and s_m are the volume and the surface area of the condensating monomer. The molecular mass of a monomer is denoted by m_m, whereas $S = p_\mathrm{m}/p_\mathrm{s}$ is the saturation ratio with p_m being the partial pressure of the condensating matter and p_s denoting the vapor pressure. The latter was calculated by Körmer et al. [109] using an Antoine-fit (eq. 5.15). Even though the fit was given for a confidence interval of $T < 1650$ K, a new fit of the source data [64] ($1550 < T < 2500$ K) did result in similar values.

$$p_\mathrm{s} = 10^{(7.5341 - 23399/T)} 101325 \text{ [Pa]} \tag{5.15}$$

The surface tension σ is given by a linear regression fitted to experimental data from Mezey and Giber [149, 109].

$$\sigma = 1152.0 \left[\frac{\mathrm{kN}}{\mathrm{m}}\right] - 0.1574/T \left[\frac{\mathrm{kNK}}{\mathrm{m}}\right] \tag{5.16}$$

For one location in the state space, a unique critical particle size v_c is defined by the thermochemical state of the gas phase. A Dirac measure is therefore introduced, which connects the critical particle volume v_c with the next larger section γ ($v_\gamma > v_\mathrm{c} > v_{\gamma-1}$).

$$\mathit{I}_\mathrm{k} = \mathit{I}^* \frac{v_\mathrm{c}}{v_\mathrm{k}} \delta_\gamma(k) \tag{5.17}$$

For the sake of mass conservation, the nucleation rate I^* needs to be scaled in the upper equation. All other inception sources ($k \neq \gamma$) are zero. Applying the logarithmic grid spacing $v_\mathrm{i} = v_1 g_\mathrm{f}^{i-1}$ for the particle sizes v_i within section i, matching sections for nucleation can be computed with:

$$\gamma = \left\lceil \frac{\log(v_\mathrm{c}/v_1)}{\log(g_\mathrm{f})} \right\rceil. \tag{5.18}$$

Since atomic silicon is defined as a gaseous species, the first section has a particle size of $v_1 = 2v_\mathrm{m}$, while our growth factor g_f is chosen as 2. The nucleating droplet is of spherical shape and its critical diameter d_c is calculated by the Kelvin relation, which predicts the critical nuclei size for gas to particle conversion

$$d_\mathrm{c} = \frac{4\sigma V_\mathrm{m}}{R_\mathrm{u} T \, ln(S)}. \tag{5.19}$$

The variables V_m and R_u are the molar volume of the particle substance and the universal gas constant. The corresponding mass sink due to phase transition by nucleation is obtained by

This chapter was previously published [250] and is reprinted with permission of the journal.

the conservation of nucleated atoms

$$\Gamma_{\mathcal{I}} = -\frac{\mathcal{I}^* n_\mathrm{c}}{N_A} W_\mathrm{I} \tag{5.20}$$

Here, N_A is the Avogadro constant, W_I the molar weight of the nucleating species and $n_\mathrm{c} = v_\mathrm{c}/v_\mathrm{m}$ is the number of monomers within one nucleus

Condensation and evaporation

The monomer flux towards and from the surface of existing particles, i.e., heterogeneous condensation and evaporation, strongly depends on the existing PSD, as each particle surface contributes with a different flux per particle. The monomer fluxes are therefore computed for the section k according to their size d_k [237], respectively:

$$\mathcal{S}_\mathrm{k}^{(*)} = (n_\mathrm{m} - n_\mathrm{k}^*) q_\mathrm{k} \left(\frac{R_\mathrm{u} T \pi}{2 W_\mathrm{I}} \right)^{\frac{1}{2}} d_\mathrm{c}^2 \, \xi(\mathrm{Kn}) \tag{5.21}$$

Here, $\xi(\mathrm{Kn})$ is the Fuchs-Sutugin correction factor [237], while the variable n_k^* denotes the curvature corrected saturation monomer concentration given by:

$$n_\mathrm{k}^* = n_\mathrm{s} \exp\left(\frac{4 \sigma V_\mathrm{m}}{d_\mathrm{p} R_\mathrm{u} T} \right). \tag{5.22}$$

Note that equation (5.21) only predicts the monomer fluxes $\mathcal{S}^{(*)}$ per section k, the effect on those have to be modeled in a further step. As stated by Prakash et al. [173], the monomer flux has to be reformulated into the number of particles migrating from one section k into the neighboring section. The particle source for each section is therefore composed of contributions from both neighbors. Depending on the situation (condensation or evaporation) particles in section k will either grow, or shrink and therefore the positive part $\mathcal{S}_\mathrm{k}^{(+)}$ of the source therm $\mathcal{S}_\mathrm{k}$ arises from the smaller section $k-1$ (condensation) or from the larger section $k+1$ (evaporation). For the negative contribution $\mathcal{S}_\mathrm{k}^{(-)}$ the relation to condensation and evaporation is the opposite:

$$\mathcal{S}_\mathrm{m}^{(+)} = f^+ \left(\mathcal{S}_\mathrm{m-1}^{(*)} \right) \frac{v_\mathrm{m}}{v_\mathrm{m} - v_\mathrm{m-1}} - f^- \left(\mathcal{S}_\mathrm{k+1}^{(*)} \right) \frac{v_\mathrm{m}}{v_\mathrm{k+1} - v_\mathrm{k}} \tag{5.23}$$

$$\mathcal{S}_\mathrm{m}^{(-)} = f^- \left(\mathcal{S}_\mathrm{k}^{(*)} \right) \frac{v_\mathrm{m}}{v_\mathrm{m} - v_\mathrm{m-1}} - f^+ \left(\mathcal{S}_\mathrm{m}^{(*)} \right) \frac{v_\mathrm{m}}{v_\mathrm{k+1} - v_\mathrm{m}} \tag{5.24}$$

This chapter was previously published [250] and is reprinted with permission of the journal.

The filter functions $f^+\left(\mathcal{S}_\mathrm{k}^{(*)}\right)$ and $f^-\left(\mathcal{S}_\mathrm{m}^{(*)}\right)$ only forward the values of $\mathcal{S}_\mathrm{k}^{(*)}$ with the respective sign – positive or negative – or sets it equal zero. Both parts $\mathcal{S}_\mathrm{m}^{(+)}$ and $\mathcal{S}_\mathrm{m}^{(-)}$ make the total surface source $\mathcal{S}_\mathrm{k}$ for each section k, respectively:

$$\mathcal{S}_\mathrm{k} = \mathcal{S}_\mathrm{m}^{(+)} + \mathcal{S}_\mathrm{m}^{(-)} \tag{5.25}$$

The mass flux per volume from or towards the gas phase is obtained by the sum of all volume fluxes within the PSD multiplied with the density of the particle material ρ_p:

$$\Gamma_\mathcal{S} = -\rho_\mathrm{p} \sum_{k=1}^{n} \mathcal{S}_\mathrm{k}^{(*)} v_\mathrm{k}. \tag{5.26}$$

Coagulation

Particle collision is a function of quadratic complexity regarding the total number of sections and is computed by equation (5.27):

$$C_\mathrm{k} = \frac{1}{2} \sum_{i,j=1}^{k} \chi_\mathrm{ijk} \beta_\mathrm{ij}^* q_\mathrm{i} q_\mathrm{j} - \sum_{i=i}^{n} \beta_\mathrm{ik}^* q_\mathrm{i} q_\mathrm{k}. \tag{5.27}$$

Since the size of coagulated particles likely fall between the defined sections, an interpolation procedure is mandatory for conserving the particle masses. This is considered by the pre-computed splitting factor χ_ijk, as applied in the work of Spicer et al. [209]. The collision frequency β_ij^* is calculated using the harmonic mean intruduced by Pratsinis [175] and further investigated by Kazakov and Frenklach [95]:

$$\beta_\mathrm{ij}^* = \frac{\beta_\mathrm{ij}^c \beta_\mathrm{ij}^f}{\beta_\mathrm{ij}^c + \beta_\mathrm{ij}^f} \tag{5.28}$$

The free molecular β_ij^f and continuum collision frequencies β_ij^c are given by the equations (5.29) and (5.30), respectively.

$$\beta_\mathrm{ij}^f = 2.2 \left(\frac{\pi k_b T}{2}\right)^{1/2} \left[\frac{1}{m_\mathrm{i}} + \frac{1}{m_\mathrm{j}}\right]^{1/2} \left(d_\mathrm{i} + d_\mathrm{j}\right)^2 \tag{5.29}$$

The variables $m_{\mathrm{i/j}}$ are the particle masses of the corresponding sections i and j, while the pre-factor of 2.2 represents the van der Waals enhancement factor. This factor was originally introduced for soot particles [74], but successfully applied also in combination with other

This chapter was previously published [250] and is reprinted with permission of the journal.

materials systems [146, 199]. With increasing particle size, particles tend to slip instead of collide and stick. This fact is considered in equation (5.30) by the Cunningham slip correction factor $C_{i/j}$ as given by Wang et al. [232]:

$$\beta_{ij}^{c} = \frac{2k_bT}{3\eta}\left[\frac{C_i}{d_i} + \frac{C_j}{d_j}\right](d_i + d_j) \tag{5.30}$$

5.4.3 Numerical setup

The calculations were performed utilizing an in-house solver based on the open source finite volume library OpenFOAM [239], where a standard "seulex" ordinary differential equation (ODE) solver is utilized to solve the finite rate chemistry equations. The in-house solver features all models mentioned in this chapter and applies the pressure-velocity-density coupling [43] to respect compressibility in the frame of a pressure based solver design.
The physical 3D domain is resolved using an unstructured grid with high orthogonality and a refined cylindrical zone within a radius of 0.5 cm from the central axis of the geometry. The mesh consists of 99 % hexagonal cells as well as polyhedral cells close to geometry features (edges, holes, etc.) and in the transition region around the refinement region.
In order to quantify the effect of the mesh resolution on the simulation results, two different mesh sizes were utilized featuring 3.5 and 26 million computation cells at a resolution of 0.2 and 0.1 mm within the refinement zone. Here, the chemical reaction as well as the nucleation and coagulation around the main jet take place and a high grid quality is mandatory. The volume of the plasma torch is modeled as a strong local heat source within a spherical volume (r = 35 mm). Buoyancy effects are considered by volume forces in the momentum conservation as well as by hydrostatic pressure. The PSD of the particle phase is discretized by 30 sections with a growing factor g_f of 2, whereby the first particle section v_1 consists of two monomers v_m.
The following setup is chosen for the boundary conditions: The temperature of the reactor outer wall is set to a profile along the reactors main axis, which represents a Dirichlet condition. The profile was generated by a preceding simulation with the plasma as heat source, but without the disperse phase and without chemical kinetics for the sake of efficiency. The simulation featured conjugate heat transfer to predict the heat flux through the quartz inliner and yields the inner surface temperature as function of the axial distance (Fig. 5.4). All swirl inlets have a Dirichlet boundary condition for the magnitude velocity (see experiment) and for the temperature (297.15 K). The center jet has a Dirichlet temperature (297.15 K), velocity profile and composition setting (see experiment). The outlet has a fixed pressure non-reflective boundary condition. Not mentioned boundaries and quantities have zero-

This chapter was previously published [250] and is reprinted with permission of the journal.

gradient conditions. The spatial derivatives of the momentum equation are approximated by a second-order central differencing scheme and by total variation diminishing (TVD) schemes [222] for energy and species equation. Spatial derivatives for the number concentration of the dispersed phase are computed applying the MUSCL scheme [223]. Time derivatives are discretized using the Crank-Nicolson scheme [30].

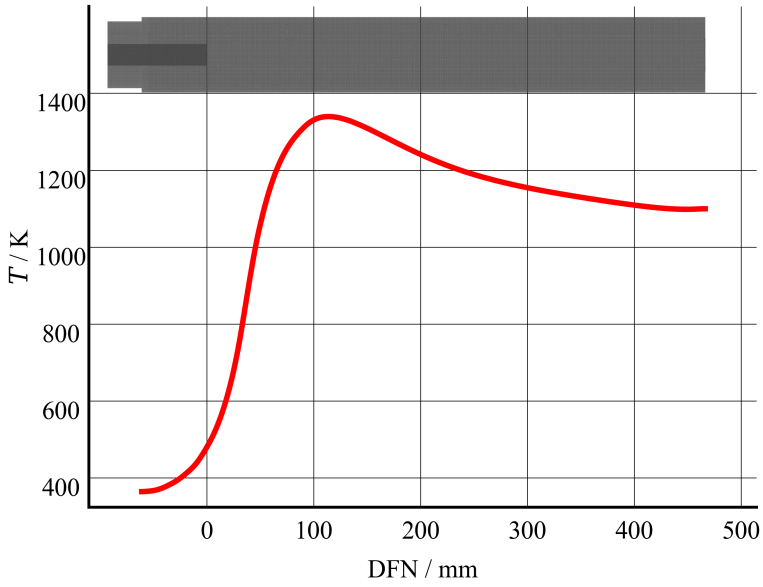

Fig.: 5.4 Red line shows the temperature boundary condition over the distance from the central nozzle (DFN) obtained from a conjugate heat transfer simulation. The simulation domain is employed as visual support (gray structure).

5.5 Results

The simulations of the microwave-plasma reactor were performed on two different grid resolutions to study grid dependence and give an idea of the resolution requirements for the simulation of the dispersed phase, which is characterized by high Schmidt numbers. For the sake of clarity, this chapter is split into three parts: 1) investigation of the pattern of the flow field (i.e., velocities), 2) study of the thermochemical and dispersed phase model predictions, 3) investigation of tracer particle histories difference of gas and particle trajectories (thermophoretic drift).

This chapter was previously published [250] and is reprinted with permission of the journal.

5.5.1 Flow field pattern

The inner jet is stabalized by a supporting outer swirl flow that is generated by eight tangentially aligned ducts at the bottom of the reactor.

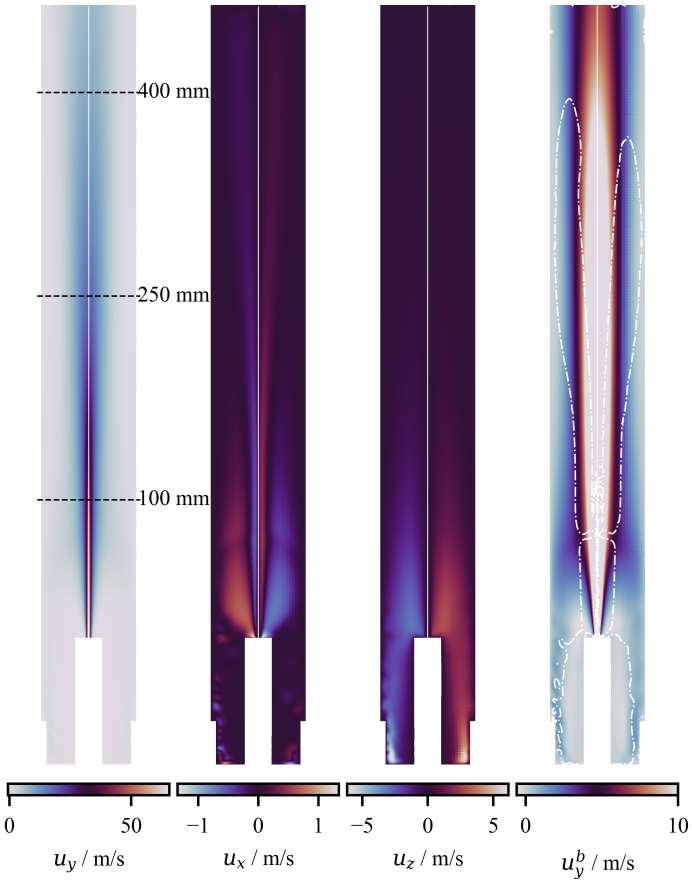

Fig.: 5.5 Cross-sectional planes normal to the z-axis of the computational domain. From left to right: Axial velocity u_y, radial velocity u_x, plane normal velocity u_z and radial velocity bounded to a maximum value of 10 m/s u_y^b. Dashed lines in the right plot indicate a Q-criterion of 0 1/s^2, marks in the left plot show the following cross-section positions. Each plot shows the results of the fine and coarse simulation on the left and right side of the center axes, respectively.

As intended by Petermann et al. [165], the swirl prevents the core jet from deflection and yields a smooth and centered reaction path within the reactor that does not interfer with the reactor walls. This is confirmed by both simulations, as shown by Fig. 5.5.
The flow field is stabilized in a way that both the fine and coarse resolved simulations predict steady flow fields – perturbations within the plasma torch are neglected (see experimental section). Both simulations agree on the jet length and predict the decay of the core region

around 250 mm. The simulations generally agree well regarding the velocity predictions in all directions. Differences towards stronger irregularities for radial and face normal velocities (u_x and u_y) below the core nozzle orifice indicate a better conservation of the individual co-flow jets in case of the higher-resolved simulation. To determine the recirculation and swirl zones within the reactor, the plot of the axial velocity field was clipped to 10 m/s and is shown together with the zero contour line for the Q-criterion (Fig. 5.6, right), where we define the border of a vortex. Two regions can be detected: The first region starts at the inlet of the co-flow gases (bottom) and maintains an inner, recirculating vortex core. This core breaks down at DFN = 75 mm and forms the second swirling region, which is stabilized by an outer recirculation zone. The swirl in this region loses momentum and widens around DFN = 160 mm for both simulations. The end of the second swirl zone – indicated by the Q-criterion – is predicted to be at DFN = 390 mm for the higher-resolved simulation and DFN = 370 mm in case of the coarse simulation. Cutting planes normal to the geometry axis (y-direction) are shown in Fig. 5.6 and illustrate the same quantities (columns) at three different DFN (rows). The graphics support the discussed findings and show the decrease of the swirl momentum with increasing DFN. It can also be seen that the y- and z-velocities are superpositions of an expansion close to the core of the jet and the outer swirl. The latter becomes less dominant with increasing DFN. In Fig. 5.7, radial profiles of all velocity u and thermophoretic velocity components $\mathcal{T}$ are compared for the three DFN indicated in Figs. 5.5 and 5.6. The inaccuracy for the circumferential velocity u_z at DFN = 100 mm (coarse mesh), is explained by the interference with the transition the zone for the mesh refinement, which is located in this area ($r \approx 15-20$ mm). The fine grid has a similar transition zone in the same area, but the simulation appears to be not effected in this area. A reason could be the generally finer resolution that may also lead to a better mesh quality within the refinement zone. Overall, both simulations – fine and coarse – predict the velocity field in a very similar way and the coarse grid can be considered as almost equally accurate. The same applied to the thermophoretic velocities $\mathcal{T}$ except for the x-direction. The profile sampled along the z-axis, $\mathcal{T}_x$ is supposed to be zero due to the axial symmetry of this case. However, since the mesh is of cubic nature, symmetry is not guaranteed at every point in the computational domain and thus, inaccuracies occur especially at smaller radii, i.e., at low r/Δ ratios. Nevertheless, the values of $\mathcal{T}_x$ are small in comparison to those of the axial and radial directions ($\mathcal{T}_y$ and $\mathcal{T}_z$) and converge towards zero for larger radii for the fine-grid case. Comparing the gas-phase velocity in radial direction u_z with the radial thermophoretic velocity $\mathcal{T}_z$, shows that thermophoresis has a strong effect on particle transport. The radial thermophoretic velocity acts in the opposite direction to the radial gas-phase velocity and decreases the expansion of the inner particle matter towards outer radii by about 50 % ($r < 10$

This chapter was previously published [250] and is reprinted with permission of the journal.

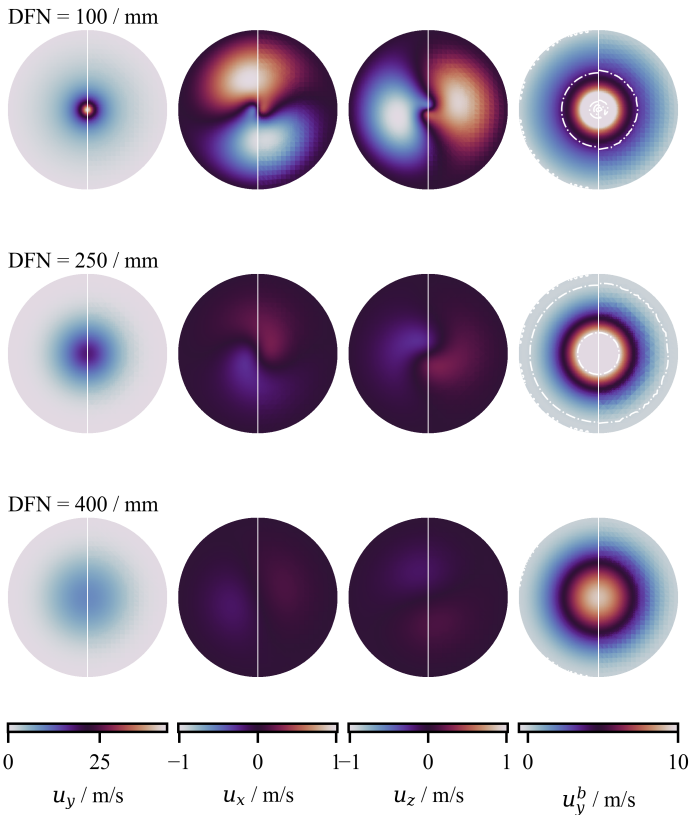

Fig.: 5.6 Cross-sectional planes (normal to y-axis) within three positions of the computational domain (DFN = y = 100, 250, 400 mm). From left to right: axial velocity u_y, radial velocity u_x, plane normal velocity u_z and radial velocity bounded to a maximum value of 10 m/s u_y^b. Dashed lines on the right plot indicate a Q-criterion of 0 1/s^2. Each plot shows the results of the fine and coarse simulation on the left and right side of the center axes, respectively.

mm). This goes into reverse for larger radii ($r > 15$ mm), where the thermophoretic velocity forces particles towards the cooler reactor wall while the dominating gas-phase transport is directed towards the symmetry axis.

5.5.2 Thermochemical and dispersed phase predictions

The temperature field strongly depends on the residence time of the gas within the plasma zone and therefore on the previously discussed velocity field. Figure 5.8 therefore shows cross-sectional planes (normal to the z-axis) for the temperature T, the particle volume concentration V_p, the averaged particle diameter d_p, the atomic silicon mole fraction x_Si and the phase transition mass flux due to surface growth / evaporation $\Gamma_\mathcal{S}$. The planes show results from the simulations, whereby each plane is cut in a left hand side and a right hand side showing the results of the fine simulation (left) and the coarse simulation (right). The

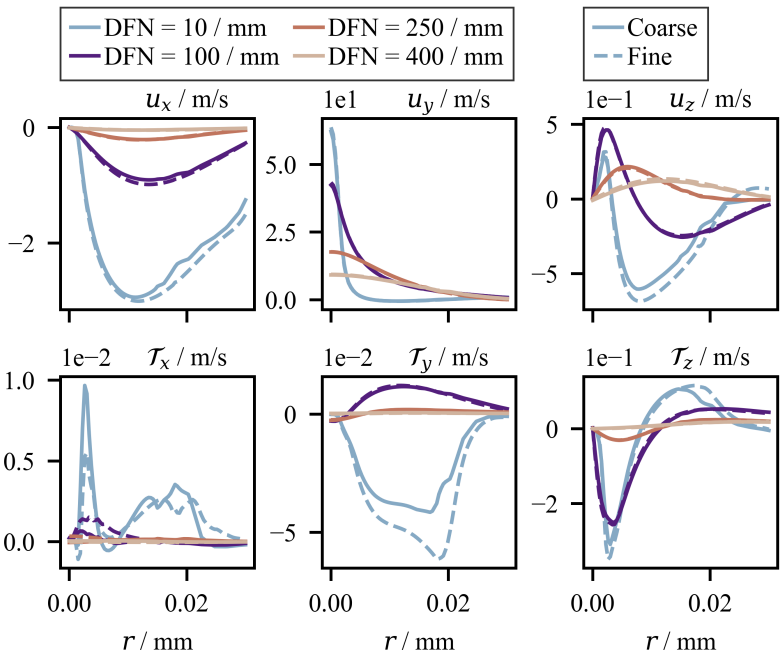

Fig.: 5.7 Radial profiles along z-axis for fine (dashed lines) and coarse (solid lines) simulation for different distances from the nozzle (10, 100, 250, 400 mm). Top row – from left to right: axial velocity u_y, radial velocity u_x, plane normal velocity u_z; bottom row – left to right: axial thermophoretic velocity $\mathcal{T}_y$, radial thermophoretic velocity $\mathcal{T}_x$, plane normal thermophoretic velocity $\mathcal{T}_z$.

center line (white) separates both solutions. While the temperature field looks qualitatively identical, deviations are noticeable for the remaining quantities that are directly affected by the dispersed phase. Even the velocity fields are almost identical for both cases (see previous chapters), the particle volume concentration V_p of the coarse case is less concentrated and blurred when compared with the fine result. This is attributed to the grid resolution: The fine grid resolves the smaller scales occurring within the dispersed phase clearly and decreases the numerical dissipation, which has a noticeable effect on the dispersed phase. The latter is characterized by high Schmidt numbers and therefore tends to conserve existing filaments of particle-containing gas – especially for larger particles. It is therefore a consequence that the field of the average particle size d_p shows sharper gradients with more compact, large particle layers for the fine-grid case. A second layer of larger average particle size is formed close to the wall, within the recirculation zone (Fig. 5.5, right), indicating a weaker secondary condensation zone in that area. The third structure of noticeable increased particle sizes (arrow shaped, between DFN 0 and 230 mm) is located in an area of too extreme conditions for particle existence and is attributed to the numerical procedure, i.e. the threshold of minimum 10 #/m^3 particles in each section. The field data of the silicon atom mole fraction

This chapter was previously published [250] and is reprinted with permission of the journal.

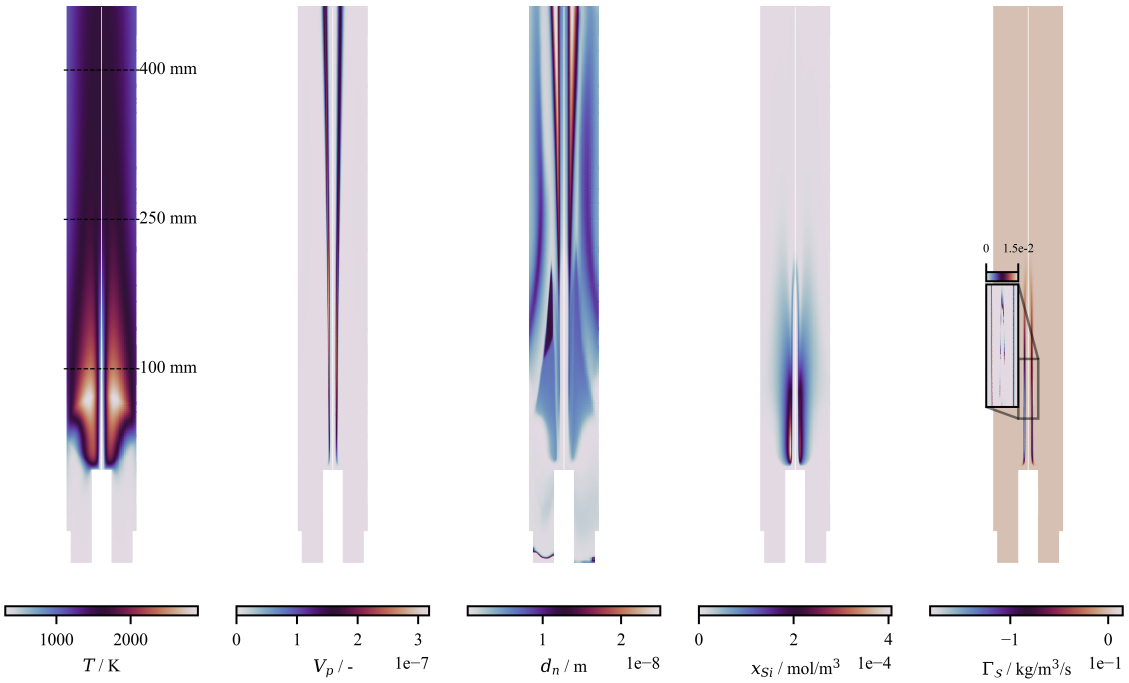

Fig.: 5.8 Cross-sectional planes normal to z-axis of computational domain. From left to right: Temperature T, particle volume concentration V_p, average particle size d_n, atomic silicon mole fraction x_Si and heterogeneous condensation/evaporation mass flux $\Gamma_\mathcal{S}$. The enlarged inset in the right plot is limited to positive values of $\Gamma_\mathcal{S}$ (evaporation). Each sub plot shows the results of the fine and coarse simulation on the left and right side of the center axes, respectively. Marks in the left plot show the cross-section positions of the following figure.

x_Si shows the presence of atomic silicon along the border of the high momentum inner jet, where high temperature gradients are present. The latter – plus the formed particle front – justifies the main zone of heterogeneous condensation $\Gamma_\mathcal{S}$ in that area (Fig. 5.8, right). Since the rate of evaporation is about hundred times smaller than the condensation peak value an enlarged area with only positive values has been added – it must be stressed that negative values indicate the transfer of matter from the gas to the dispersed phase and vice versa. Even though, the evaporation rates are comparable small, the area in which evaporation takes place forms a secondary region of atomic silicon apart from the centered jet (see x_Si), which is source for the mentioned, secondary condensation zone, close to the reactor walls.
Figure 5.9 shows the same quantities for cross sections at different DFN positions (indicated by Fig. 5.8, left) for the fine and coarse simulation (left and right part of respecting cutting plane). Generally, the mentioned observations can be justified: The temperature fields in both simulations are in good agreement, the thin particle front and condensation areas are better conserved by the finer resolution. Moreover, it can be seen that the secondary zone of

This chapter was previously published [250] and is reprinted with permission of the journal.

atomic silicon x_{Si} is located in the hotter regions of the reactor and therefore is present further downstream, where the main condensation zone has already finished (DFN > 250 mm). A

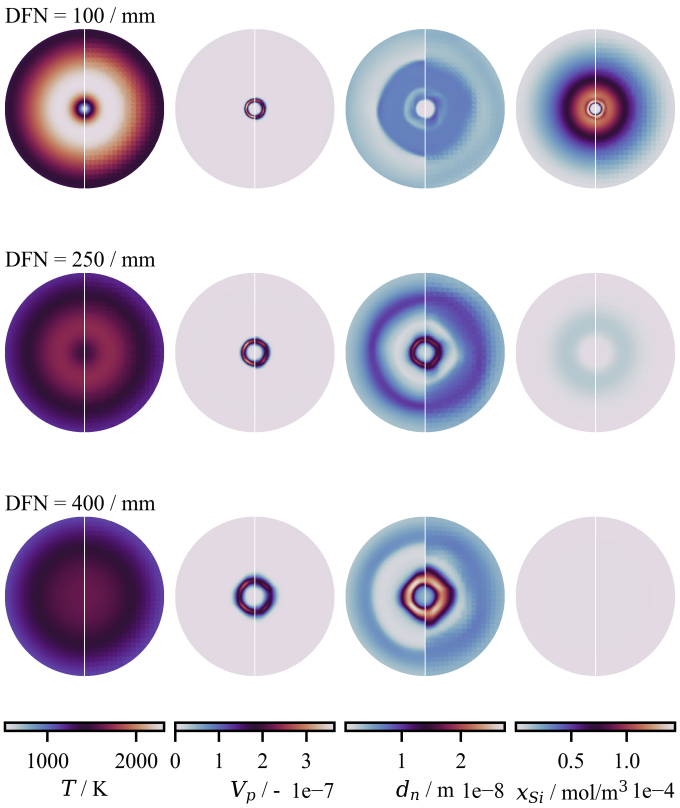

Fig.: 5.9 Cross-sectional planes (normal to y-axis) within three positions of the computational domain (DFN = y = 100, 250, 400 mm DFN). From left to right: temperature T, particle volume concentration V_{p}, average particle size d_{n} and atomic silicon mole fraction x_{Si}. Each plot shows the results of the fine and coarse simulation on the left and right side of the center axes, respectively.

deeper insight is provided by the line plots in Fig. 5.10, which were sampled along the z-axis for different DFN (Fig. 5.8) plus an early stage at DFN = 10 mm. Despite of the already discussed quantities, the total particle number concentration N_{t}, the rate of homogeneous and heterogeneous condensation sources $\Gamma_{\mathcal{I}}$ and $\Gamma_{\mathcal{S}}$, as well as the number concentration of some sections $Q_{\mathrm{i}} = q_{\mathrm{i}}\rho\,;\, i = 1, 7, 13, 19, 25$ are shown.

This chapter was previously published [250] and is reprinted with permission of the journal.

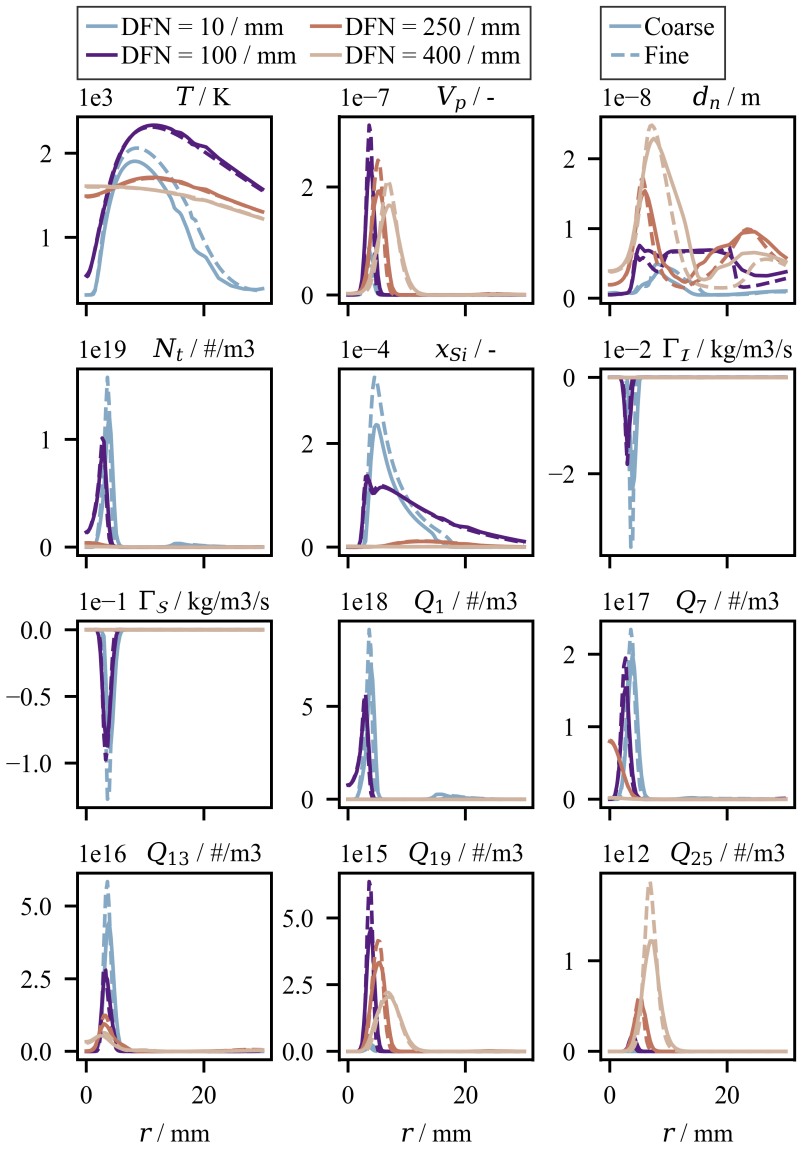

Fig.: 5.10 Radial profiles along z-axis for fine (dashed lines) and coarse (solid lines) simulation for different DFN (10, 100, 250, 400 mm). First row (top) – from left to right: Temperature T, particle volume concentration V_p, average particle diameter d_n; second row: total particle concentration N_t, atomic silicon mole fraction x_Si, homogeneous condensation mass flux Γ_I; third row: heterogeneous condensation/evaporation mass flux Γ_S, number concentration section 1 Q_1, number concentration section 7 Q_7; fourth row: number concentration section 13 Q_{13}, number concentration section 19 Q_{19}, number concentration section 25 Q_{25}.

First observations to be mentioned though, are the overall higher and more narrow distributions for both the particle concentrations and the condensation in case of the finer grid. Even though, the location and the shape of the local distributions are in good agreement, the

finer resolution allows sharper local gradients and therefore more narrow, higher rates for all sources (Γ_I, Γ_S). Additionally, the finer-grid cases suffers less from numerical diffusion and thus is superior in conserving finer structures with high Schmidt numbers. Increasing particle volume concentrations V_p (Fig. 5.10, DFN < 250 mm) at high total number concentrations N_t give evidence of ongoing nucleation as well as surface condensation. This is also justified by both condensation rates Γ_I and Γ_S. As a result, the high number concentration within the first section Q_1 and is considerable high until DFN < 250 mm. The spatial distribution of the atomic silicon x_Si splits into two modes at DFN = 100 mm, where the first mode (left, narrow) represents the main condensation zone. The second mode (right, wide) is explained by atomic silicon being captured in evaporation zones, which are too hot for condensation. Atomic silicon is transported towards outer radii (DFN = 250 mm) until it vanishes in colder zones, in which pre-existing particles recirculate close to the reactor wall. It is obvious that discrepancies between the fine and coarse simulation lead to higher number concentrations of higher sections ($i \geq 13$), which is a logical consequence of of the quadratic nature of the underlying collision physics. Figure 5.11 shows the comparison of the measured and calculated particle loading in the gas phase at DFN = 400 mm, as well as a temperature comparison between the LIF data and the finely resolved simulation. In order to compare the measured intensities ($I_\mathrm{Rayleigh} \propto d^3$) and the predicted volume fractions V_p, the data was transformed to yield the probability density functions (PDFs). It can be seen that the location and width of the measured and calculated particle fronts are in excellent agreement, while the peak of the different experimental techniques and calculations vary. Why the Rayleigh scattering measurements yield a narrower confinement of the particles cannot be explained with certainty. One possible explanation could be that the larger particles contribute the most to the scattering signal. Those particles have lower diffusion velocities and are therefore concentrated in a thin layer. However, the simulated data falls in between of the range of measured values (min: LOSA, max: Rayleigh scattering), whereby the data of the coarse resolution simulation agrees well with the lower end of the experimental data (LOSA measurement), while the result of the finer resolved simulation falls exactly in between of both measured distributions. Both results are in the range of the experimental obtained data and therefore predict the observed tubular particle front accurately, emphasizing the correctness of the coupled particle model.

The LIF temperature measurement is based on an early development stage of the transition energy model of SiO. The model has been developed for a H^2/O^2 flame with a low precursor concentration. Here, the conditions are different and it must be questioned if the rotational degree of freedom is the most important one in the context of this reactions. Thus, the agreement between the simulation at DFN = 400 mm and the measurement is promising,

This chapter was previously published [250] and is reprinted with permission of the journal.

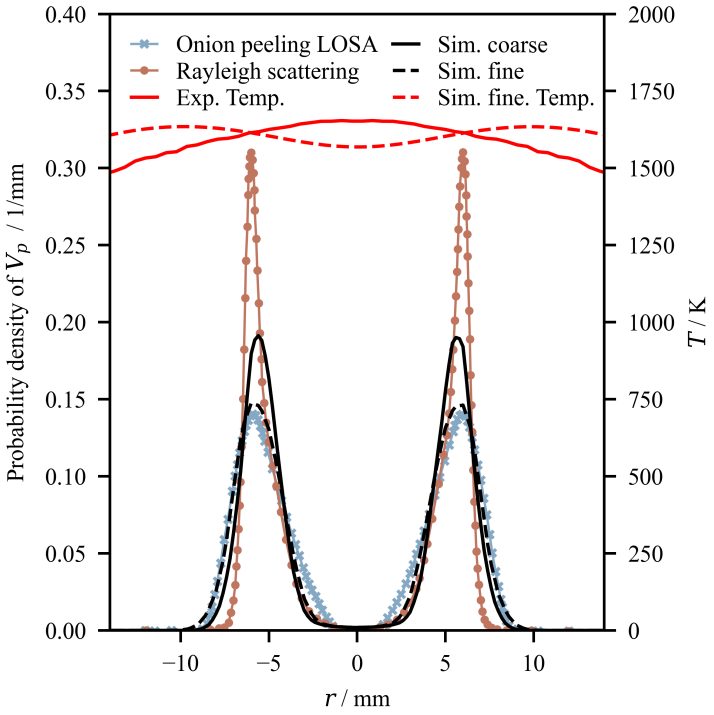

Fig.: 5.11 Left y-axis: Comparison between Rayleigh scattering and LOSA measurements and results obtained from simulations on course and fine grid at DFN = 400 mm. Right y-axis: Comparison of temperature measured by LIF and extracted from fine simulation data at 400 mm.

because both the peak value and the flattening of the temperature towards outer diameters match very well. Another reason for the differences could be the assumption of the simulation that all rotational degrees of freedom are in equilibrium. The positions of peak particle concentration in the simulation and the measurement differ by up to 7 mm, which can be attributed to the time-varying position in the experiment due to minor flow instabilities. Figure. 5.12 sketches the particle formation processes within the reactor. The sketch shows the formation of the tube like particle front at the edge of the central jet as well as the secondary condensation layer close to the colder reactor walls. The latter is mostly heterogeneous condensation on particles that are caught within the recirculation zone.

5.5.3 Tracer volume time histories

After it has been shown that the flow fields of the coarse- and fine-grid simulations are in good agreement, we will now focus on the results of the fine-grid simulation case. The differences in predictions of the particle phase because of the refined grid resolution has

This chapter was previously published [250] and is reprinted with permission of the journal.

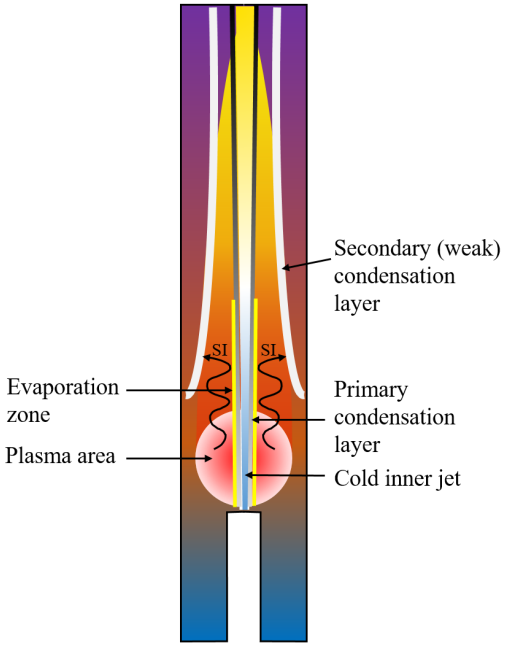

Fig.: 5.12 Sketch of the particle formation processes within the reactor showing the plasma zone and the two condensation layers.

been covered in the last section, where it has been found that the fine grid provide a better resolution of the particle front. With the investigation of trajectories, we will aim at gaining a more detailed understanding of the synthesis process. In the simulation, 1000 tracer particles were seeded randomly within a spherical plane of 10 mm diameter (equally distributed). This number of particles was chosen, as the resulting distributions statistically converges at this point. The plane, where the particles are introduced is normal to the geometry axis, which traverses the center of the plane at DFN = 1 mm. Generally, the particle velocity u_t must be used to obtain particle trajectories, including all contributions (i.e., acceleration, settling, magnetic fields, etc.). On the time scales resolved for CFD simulation, nanoparticles can be assumed to be in equilibrium with the gas-phase velocity, as acceleration takes place on a significantly smaller time scale (nanoseconds), while the settling velocity is many orders of magnitude slower than the convection velocity.

This chapter was previously published [250] and is reprinted with permission of the journal.

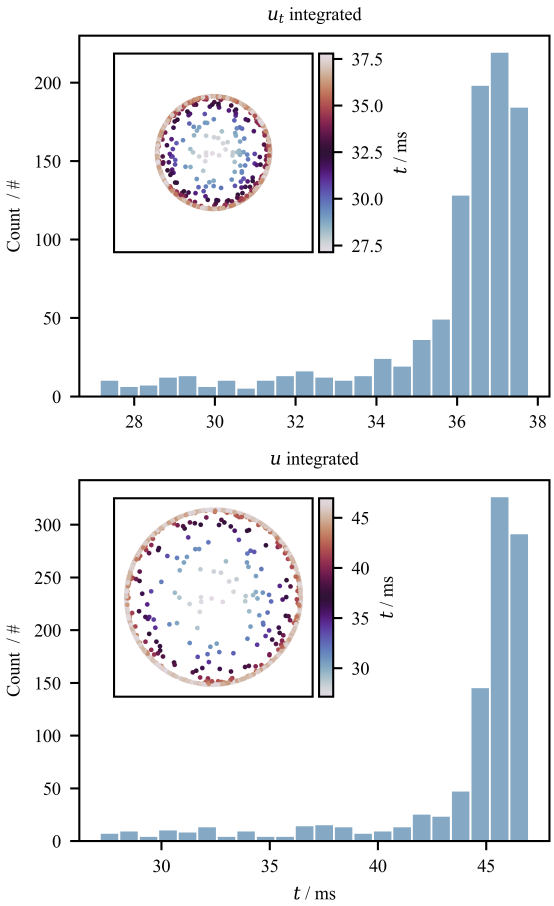

Fig.: 5.13 Distributions of the residence time within the reactor of tracer particles within the computational domain using the total particle velocity $u_t = \mathcal{T} + u$ (top) and the gas velocity u only (bottom). The boxes within the plots show the particles positions at the end of the domain (x-z-plane) and are color-coded by the residence time. The boxes are equally sized in all directions ($\Delta x = \Delta z = 24$ mm) and centrally located within the domains cross-section.

Nevertheless, in reacting flows, strongly directed steep temperature gradients occur and thermophoretic drift can become important. The impact of thermophoresis – compared to pure gas phase convection – on the particle trajectory will therefore be included in the analysis. Figure 5.13 shows the residence time distributions for the particle trajectories from the particle seeding plane until the outlet of the simulation domain, which is located at DFN = 450 mm. The trajectories are calculated with (top) and without (bottom) thermophoresis. The majority of the tracers show a residence time in the reactor of 35 to 37.5 ms, if thermophoresis is considered. Without thermophoresis, the residence times within the reactor increase to 44 to 48 ms.

The reason for this behavior can be found in the structure formed by the tracer particles at

This chapter was previously published [250] and is reprinted with permission of the journal.

the same DFN. Both ensembles (with and without thermophoresis) form a narrow concentric structure around the geometry axis, which is more compact, if thermophoresis is considered. This a consequence of the thermophoretic velocity counteracting the gas-phase velocity in radial direction (Fig. 5.7) and decreasing the radial expansion of the structure. Since the velocity decelerates towards larger radii, particles without thermophoretic velocity are predicted to stay approximately 20 % longer within the reactor when the peak values of the residence times are compared. Not considering thermophoresis will therefore impact the simulation, not only because of deviating residence times, but also because of different particles trajectories, which probably affect the thermochemical time history of the synthesis process. Figure 5.14 shows the temperature T, the particle volume concentration V_p, the average particle diameter d_n and the atomic silicon mass fraction Si not only for the tracer time history obtained by integrating u_t (top), but also u (bottom). Each line represents one trajectory and is plotted with an low opacity value to better identify, where the trajectories condense and build a more likely time history. Since particles are seeded within a radius of 5 mm, they start at different temperature conditions and converge towards a more narrow distribution of about 300 K from 2 ms on. At around 10 ms, the heating rate decreases and the distrubution narrows to around 10 K after a maximum of around 1600 K. After the maximum has been reached, the temperature decreases slowly. Trajectories without thermophoresis show a considerable difference, since they are not forced back by temperature gradients, regions of almost 2000 K are reached. The temperature distribution widens in this region but according to the densely packed main slope, the majority of the trajectories traverses the maximum temperature in case of no thermophoresis. This would be a serious issue in simulations like the presented one, since it can be assumed that it leads to largely overpredicted evaporation of the initially formed particles. As Fig. 5.8 (right) shows, this is already the case, as particle evaporation takes place at the outer (limiting) radius of the tubular particle front, which is predicted too wide without considering thermophoresis (Fig. 5.13). Thermophoresis can therefore be seen as a mechanism for particles to escape regions of strong evaporation and thus as evaporation inhibitor.

That thermophoresis can strongly affect evaporation, can be also observed in Fig. 5.14, where the trajectories for the particle volume concentration V_p and the average diameter d_n are shown. Contemplating the trajectories with thermophoresis (top), it can be seen that the rise of the average particle size d_n is delayed in comparison to the total particle volume V_p. Reason is the initial nucleation, in which small nuclei are seeded. After sufficient particle surface area is provided, heterogeneous condensation dominates and d_n rapidly grows in size. In case of the particle volume concentration V_p, the ensemble of particle histories unfold after reaching a local maximum (around 10 ms). This is caused by higher temperature gradients

This chapter was previously published [250] and is reprinted with permission of the journal.

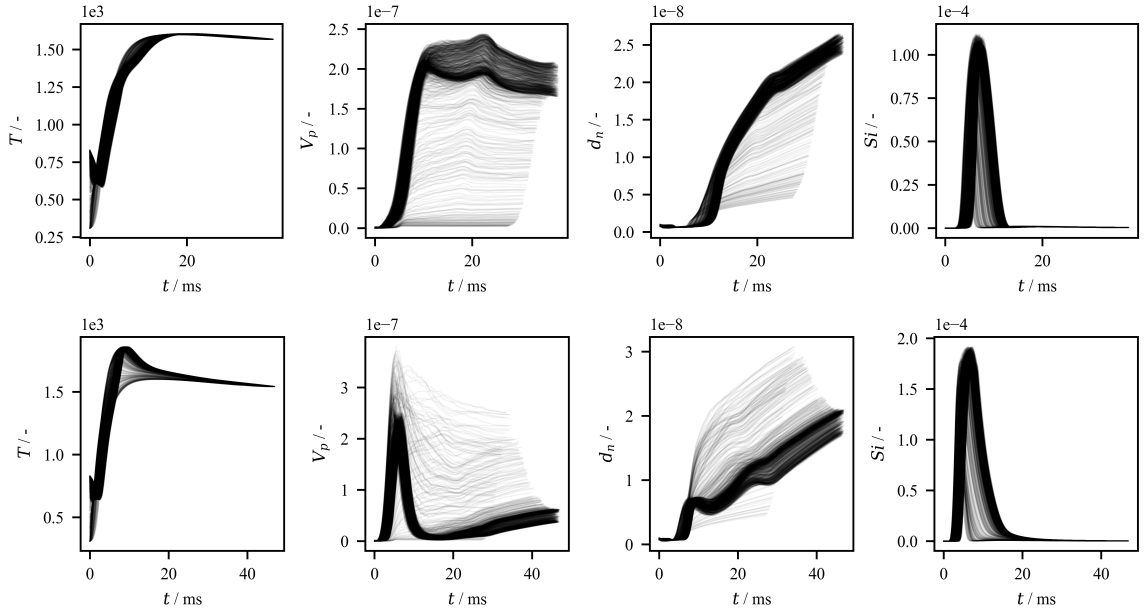

Fig.: 5.14 Comparison between trajectories of tracer particles integrated using the total particle velocity $u_t = \mathcal{T} + u$ (top) and the gas velocity u only (bottom). Variables from left to right: Temperature T, particle volume fraction V_p, averaged particle diameter d_n, and silicon mole fraction x_{Si}.

separating the particles as well as starting evaporation and thus due to the loss of particle matter (smaller V_p). After the point of maximum temperature has been passed ($t \approx 19$ ms), all silicon matter instantly condenses, increasing the particle inertia and lowering the coagulation rate as visible in the growth rate of d_n after 20 ms. On the other hand, the tracer particles in absence of thermophoresis (Fig. 5.14, bottom) show a strong loss in particle matter (see V_p) and size d_n after a certain temperature has been reached. Only some trajectories result in a higher volume concentration V_p as predicted by the thermophoretic trajectories (top).
The average particle diameter d_n shows more comparable sizes, even the single trajectories (gray, detached from main slope) are located at the opposite site, towards larger sizes. Those single, fine, trajectories that unfold from the main (intensely colored) path belong to less likely tracer histories, which again remain inside the jet, apart from the main tubular particle front.
The comparison of both kinds of trajectories regarding the atomic silicon mass fraction (Fig. 5.14, right) verifies this situation, as the tracers particles without thermophoresis drift experience almost twice the silicon atom concentration compared to those that include thermophoresis. The higher level of atomic silicon concentration also remains longer inside the gas phase, until the tracer particles escape the high-temperature zone (bottom, left).

This chapter was previously published [250] and is reprinted with permission of the journal.

The investigations on both trajectories (with an without thermophoresis) have been made using the same simulation data, in which the particles have been transported considering the thermophoretic drift velocity (eq. (5.9)). The particle data (V_p and d_n) therefore should not be confused as simulation result, of a full simulation without thermophoresis.

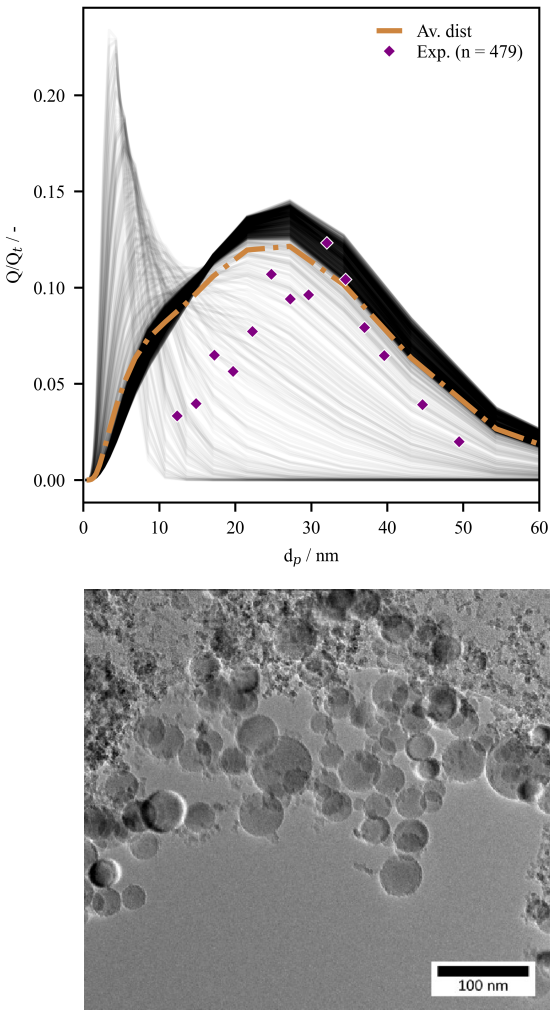

Fig.: 5.15 Top: Comparison between experimentally obtained particle-size distribution (PSD) (manual TEM count) and the PSDs from simulated streamlines at the same height above the nozzle. The particle number is normalized by the total number / number concentrations of the PSD (n = 479 in case of the experiment). Bottom: TEM image of product particles used for generating the experimental PSD. Experimental particles and simulation particle data are obtained at DFN = 400 mm.

However, as particle nucleation and evaporation does have a minor effect on the momentum field, the overpredicted expansion of the tubular particle front, in absence of thermophoresis (Fig. 5.13) remain. Thus, similar effects as shown can be expected from a full simulation

This chapter was previously published [250] and is reprinted with permission of the journal.

without thermophoresis for all investigated quantities.
Figure 5.15 shows a comparison of the experimental product particles with simulation predictions at the end of the domain. The experimental particles are obtained by TEM grid probing, while their resulting particle-size distributions (top) are generated by manual postprocessing of the TEM images (bottom). For the simulation data, the distribution at the probing location (DFN = 400 mm) of every 1000 trajectories (considering thermophoresis) are plotted with low opacity, similar as in Fig. 5.14 (darker areas mean higher probability). In addition, the PSD has been averaged based on the particles number (brown dash-dotted line). The experimental particle-size distribution is based on the analysis of 479 individual particles. Despite this small number, the comparison to the simulation results show a reasonably good agreement. All particle-size distributions have been normalized by the total number of particles n or the total number concentration N_t, respectively. It is surprising that the computed particle-size distributions of single trajectories (thin gray lines) show a distribution of smaller particles around 5 nm, which represent the late nucleation mode of less likely, fast transported tracer particles that remain close to the center of the jet. This can be correlated to the less prominent section of low particle volume fraction V_p and small averaged particle diameter d_n of Fig. 5.14 (top) and – for practical reasons – is not visible in the measured particle-size distribution. The TEM image (Fig. 5.15, bottom), however, shows a larger group of small, chained particles within the mentioned size range and testifies the presents of this nucleation mode in the real synthesis process. Discarding particle sizes in that region (below 10 nm), the average diameter d_n of the simulation and the experiment compare well with 25.8 nm and 27.6 nm, respectively.

5.6 Conclusion

A silicon nanoparticle synthesis process within a lab-scale microwave plasma reactor has been simulated by applying a new approach for modeling the general dynamics equation within an Eulerian framework. The model features two-way coupling by phase transitions between gas and dispersed phase due to homogeneous and heterogeneous condensation, as well as evaporation and a sectional particle-size distribution. The energy fed by the plasma into the gas flow has been represented as a spherical homogeneous heat source with the net power of the plasma. The monosilane precursor decay was modeled by a one-step reaction mechanism. Two simulations with different grid resolutions have been performed and compared with the experimental data to identify possible grid-resolution dependencies. Both simulations show very similar results regarding the flow field and thermophoretic velocities, as well as temperatures, but differences in the prediction of the dispersed quantities. The finer resolved

This chapter was previously published [250] and is reprinted with permission of the journal.

simulation shows a narrower and better defined condensation layer and particle front with higher condensation and nucleation rates and higher particle number concentrations. Both simulations predict all main process features (i.e., recirculation zones, condensation and evaporation layers, particle sizes) well. Due to the sophisticated condensation modeling, the tubular particle front, which is observed in the experiments can be reproduced by the simulations. Rayleigh images identified an outer, weaker particle zone apart from the main particle front, which the simulation found to be attributed to the diffusion of atomic silicon and the evaporation and re-condensation of particle matter at the edge of the particle front. Additional investigations were made using 1000 tracer particles transported with and without thermophoresis. It has been found that thermophoresis has a crucial effect on the particle trajectories and therefore, the predicted therochemical time histories. When thermophoresis is neglected, the expansion of the tubular particle front towards larger radii was overpredicted by more than 30 %, directing the particle trajectories through an area of high temperatures and extensive evaporation. In our case, thermophoresis may therefore also be understood as evaporation inhibitor and is important especially in simulations, in which high temperature gradients are present. In addition, good agreement was achieved by using tracer particles to compare the product particle-size distributions between simulation and experiments.
Additional investigations should be made that consider particles to not be in thermodynamic equilibrium with the gas phase and gas and particle temperatures deviate for freshly nucleated particles at low pressure, since this effect could influence the evaporation process. The present model features a sectional representation of the particle-size distribution and is therefore computational more expensive in comparison to most moments methods. The sectional representation is mandatory because of the strong dependence of the evaporation rate on the particle sizes – small particles are more prone to evaporate and vanish. A suitable model for the description of particle shrinking and vanishing could lower the computational effort fur such simulations. The presented work helps in verifying such a model and determine possible model constants.

5.7 Acknowledgments

The authors gratefully acknowledge the financial support from the German research Foundation within the research unit FOR2284 "Model-based scalable gas-phase synthesis of complex nanoparticles" (DFG, grant number KE-1751-11 and 262219004) and the support through the Gauss Centre for Supercomputing e.V. (www.gauss-centre.eu) by funding this project (grant DUE-HAWK2021) by providing computing time on the GCS Supercomputer HAWK at Hoechstleistungsrechenzentrum Stuttgart (www.hlrs.de).

This chapter was previously published [250] and is reprinted with permission of the journal.

5.8 Appendix A – Model benchmark

In order to provide a benchmark for model implementations and to demonstrate the principle model concept, a simple, generic test case has been developed. The test case shows the phase transition and the effect on the particle dynamics in a trivial way: A perfectly stirred, isobaric reactor (at 10 kPa) is exposed to a temperature change from 2200 to 500 K in a given time t_c followed by a change from 500 to 3000 K in the same time frame $t_\mathrm{h} = t_\mathrm{c} = t_\mathrm{c/h}$. With the consecutive cooling and heating phases, the total simulation time is $t_\mathrm{tot} = 2t_\mathrm{c/h}$. The initial gas composition is given by $y_\mathrm{Ar} = 0.999$ and $y_\mathrm{Si} = 0.001$ and no chemical kinetics mechanism is used. All other quantities can be found in section 5.4. Three simulations were performed featuring different cooling/heating rates with $t_\mathrm{c/h}$ = 10, 100, 1000 ms (t_tot = 20, 200, 2000 ms).

All simulations show the transition from gas to particle phase by nucleation and condensation as well as the transition from particle to gas phase by evaporation. Since we assume a closed system without any chemical reactions, the species mass is conserved. Any discrepancy in mass concentration can be associated with issues in model implementation. Figure 5.16 shows the time history of the gaseous silicon mass concentration $\rho_\mathrm{Si} = y_\mathrm{Si}\rho$ as well as the total particle mass concentration $m_\mathrm{p} = \rho_\mathrm{p}\sum(Q_\mathrm{i}v_\mathrm{i})$ and the conserved sum of both. It can be observed that the nucleation/condensation processes starts shifting the silicon mass into the particle phase at a similar temperature in all cases. The same applies to the following evaporation process. As higher cooling rates are supposed to increase the nucleation rate (see [204, 139]) Fig. 5.17 compares the total number concentrations and the absolute homogeneous condensation mass flux $|\Gamma_I|$ of all benchmarks by employing the normalized time $\theta = t/t_\mathrm{tot}$ and testifies this statement: the total number concentration N_t as well as the homogeneous condensation mass flux $|\Gamma_I|$ differ by more than two orders of magnitude between each change in cooling rate ($\Delta T/\Delta t$ = -1700, -17000, -170000 K/s for cases 1-3), which gives evidence of a quadratic dependence.

This chapter was previously published [250] and is reprinted with permission of the journal.

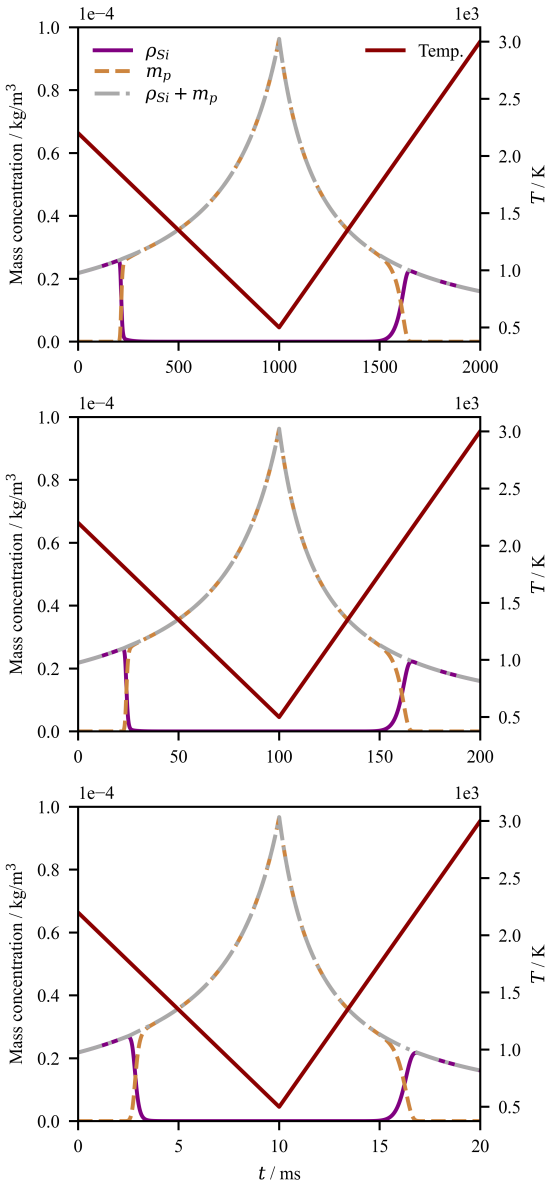

Fig.: 5.16 Mass concentrations of gaseous and dispersed silicon matter (ρ_{Si} and m_{p}; left y-axis) for different cooling and heating periods $t_{\mathrm{c/h}}$ of (from top to bottom) 1000, 100, and 10 ms. Starting, as well as target cooling and heating temperatures are constant (2200, 500, 3000 K) for all cases.

Since also the coagulation rate follows a quadratic dependence, based on the number concentration, the particle number density is decreased by coagulation faster for the higher cooling rates. Note that the plots are shown in normalized time space θ and the real difference between each step is therefore more sensible as it appears here.

This chapter was previously published [250] and is reprinted with permission of the journal.

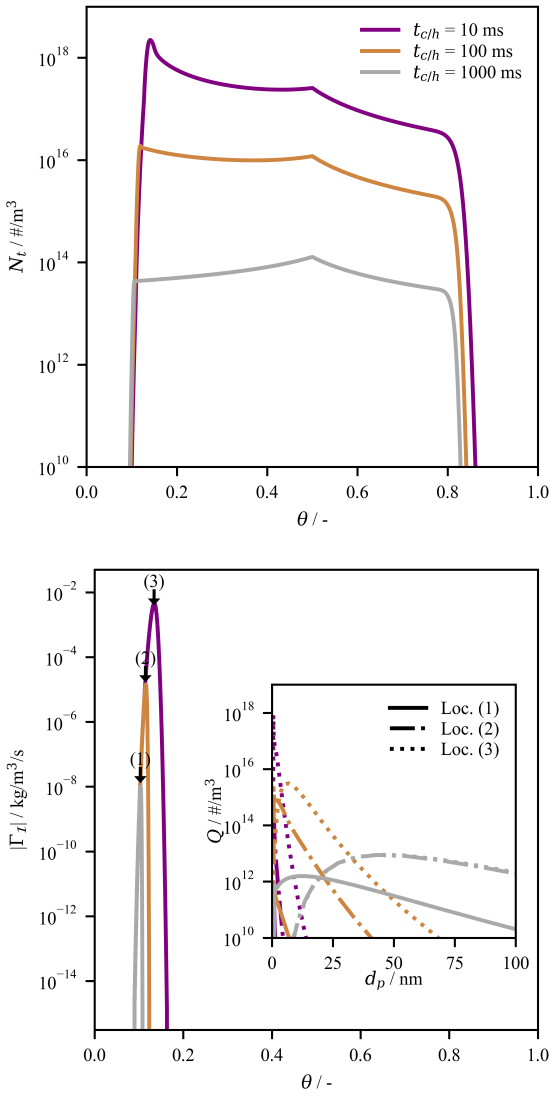

Fig.: 5.17 Total number concentrations N_t (top figure) and absolute homogeneous condensation mass flux $|\Gamma_\mathcal{I}|$ (bottom figure) for all cases ($t_\mathrm{c/h}$ = 10, 100, 1000 ms) plotted over the normalized time θ. Bottom figure additionally shows the PSD for all cases at two positions (1) and (2) during nucleation.

The illustrated particle size spectra at three normalized times θ (Fig. 5.17, bottom) are located at the maximum of the respective nucleation rate and show that the mentioned behavior has a crucial impact on the early formed particle sizes, i.e. lower cooling rates yield fewer and larger (less mobile) particles. Although, it can be seen that each PSD of the corresponding cooling rate owns a small sized nucleation mode ($d_\mathrm{p} < 5$ nm), the PSD width becomes wider with lower cooling rates.

This chapter was previously published [250] and is reprinted with permission of the journal.

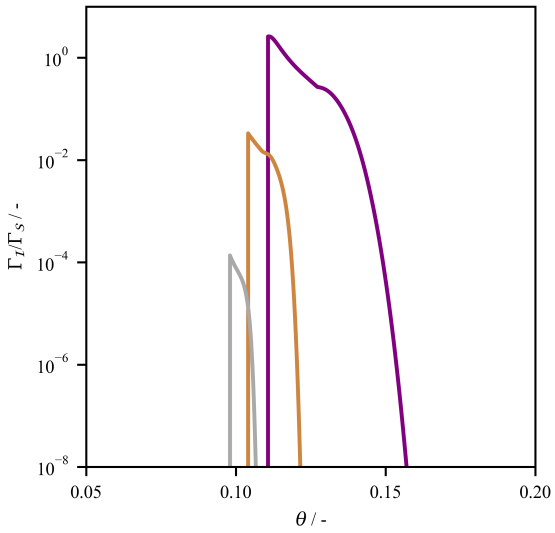

Fig.: 5.18 Ratios of homogeneous to heterogeneous condensation mass flux $\Gamma_{\mathcal{I}}/\Gamma_{\mathcal{S}}$ for all cases ($t_{\mathrm{c/h}} = 10, 100, 1000$ ms) plotted over the normalized time θ.

The reason for this behavior can be explained by the fact that the ratio of homogeneous to heterogeneous condensation rate drastically increases with higher cooling rates, as it is shown in Fig. 5.18. With other words, condensing matter prefers to deposit on existing nuclei earlier at moderate cooling rates, while more nuclei are built spontaneously as cooling rates become stronger. The fast growth of particles at lower cooling rates does not only quickly increase the particle size, but also demobilizes existing particles at a fast rate. This is illustrated in Fig. 5.19 (top) by the history of the number averaged particle diameter d_{p} as well as by two PSDs, taken after the condensation phase (1) and before the evaporation takes place (2). Even though the particle sizes are smaller with lower cooling rates, the growth by coagulation is obviously faster and the higher particle number and lower inertia overweight the shorter simulation time. At later stages of the experiment ($\theta > 0.7$) particle sizes drop due to the impact of beginning evaporation. The evaporation (positive values) and condensation (negative values) processes can be located by observing the history of the heterogeneous condensation mass flux $\Gamma_{\mathcal{S}}$, which is shown Fig. 5.19 (bottom). The chosen times for the PSDs (1), (2), and (3) are positioned before, within and at the end of the evaporation phase. Thus, the given PSDs (Fig. 5.19, bottom, inner plot) show the effect of evaporation with different heating rates on all given size spectra. All PSDs experience a shift towards lower diameter and number concentrations, which is in line with the decreasing average particle diameter d_{p}. Due to curvature effects, smaller particles tend to evaporate faster (see eq. (5.22)) and therefore, smaller particles run into to numerical limit first (here 10 particles for each section), which makes the average particle size artificially rise d_{p} as a mathematical

This chapter was previously published [250] and is reprinted with permission of the journal.

artifact. As a pure post processing quantity, the average particle size s_p does not affect the simulation in any way.

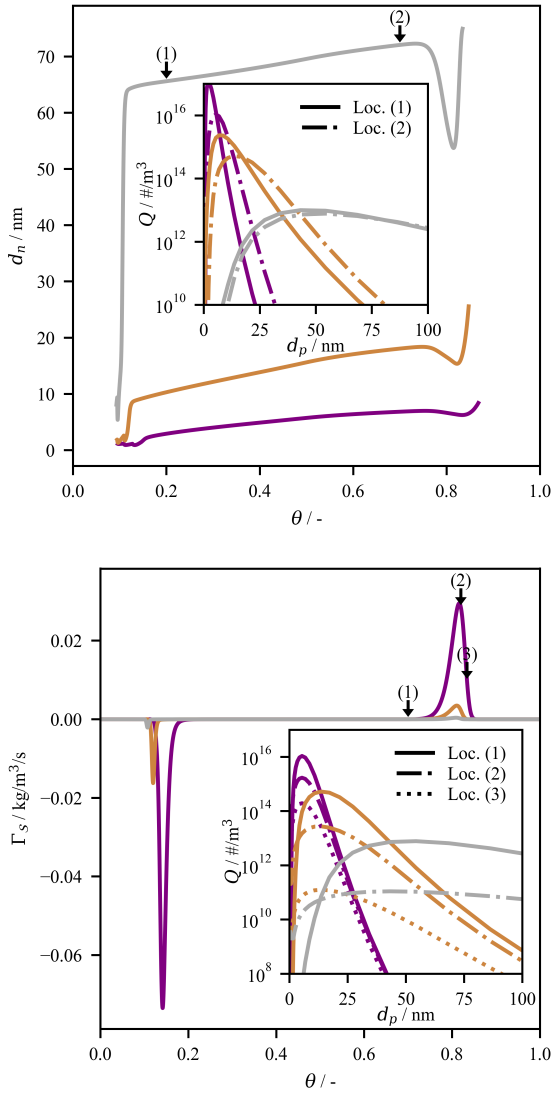

Fig.: 5.19 Number-averaged particle size d_n (top figure) and heterogeneous condensation mass flux Γ_S (bottom figure) for all cases ($t_\mathrm{c/h} = 10, 100, 1000$ ms) plotted over the normalized time θ. Figures additionally show particle-size distributions for all cases at two positions (1) and (2). The positions are in the zone between condensation and evaporation (top figure) and before and within the evaporation zone (bottom figure).

This chapter was previously published [250] and is reprinted with permission of the journal.

6 The role of phase transition by inception and surface reactions for the synthesis of silicon nanoparticles in a hot-wall reactor – simulation and experiment

P. Wollny, L. Engelmann, M. Loewenich, I. Rahinov, H. Wiggers, C. Schulz, A. Kempf, I. Wlokas

P. Wollny developed and implemented all models, ran all the simulations, wrote the paper, including all figures and tables, excluding the experimental part. L. Engelmann supported with conceptional work, post processing, and proof reading. M. Loewenich ran the experiments and contributed with the data, and the chapter about the experimental setup. The authors C. Schulz, H. Wiggers, A.M. Kempf and I. Wlokas contributed feedback, corrections and proof-reading.
This paper is a preprint version of a manuscript accepted for publication at the Chemical Engineering Journal, Elsevier (2022).

6.1 Abstract

A novel Eulerian particle model tailored for the application in computational fluid dynamics (CFD) is presented. The model is based on a bivariate moment method and features a full coupling with the gas-phase by kinetic formulations for inception, and activated and non-activated surface reactions. A new formulation for the particle composition accounts for the volatile content and its emission. The model is applied in the context of silicon nanopowder synthesis from monosilane, where a validation is performed with a well-established hot-wall reactor experiment from the literature. It is characterized by high precursor concentrations at moderate heating temperature of 853 K. Further, a new experiment was conducted for the comparison with the new model approach in a three-dimensional, transient simulation. The semi-industrial hot wall reactor features an unsteady complex flow field with buoyancy driven recirculation. The simulations enable new insights into the unsteady flow, mixing

and nanoparticle formation process and contribute to their understanding. For the validation, residence-time dependent data for the precursor concentration, the primary particle size, and the particle number concentration are compared with results of the simulation at different stages. A comparison with the results of stochastic methods serves as further benchmark for the presented model. An excellent agreement with the experimental data is obtained, if essential growth mechanisms are considered. For the semi-industrial hot-wall reactor experiment, the BET surface and particle diameter, as well and the precursor consumption, are compared to the results of the new model and to a description with inception, coagulation, and sintering only. Due to the absence of crucial activated and non-activated surface reactions, the latter model predicts values that deviate more than one order of magnitude from the experimental data, while the new model shows an overall good agreement.

6.2 Introduction

Synthesis of nanoparticles from the gas-phase in a flow reactor is a path for production of materials in a continuous process at large scale ranging from metals of high purity or with well-defined dopant concentrations, up to mixed, metastable oxides or composite particles [210, 125, 106, 97]. The energy for the particle precursor conversion is typically fed by a flame, or a plasma, or even simpler, by convection from a hot wall in a tubular reactor. The synthesis in a flow reactor follows a quite complex path of reaction kinetics, transport and aerosol dynamics in coupled interaction and simulations are imperative for understanding and successful process scaling.

Gas-phase synthetized silicon nanoparticles have received large interest in the past decades for a growing number of applications, ranging from simple interest in pure solar or electronic grade Si [241] to more specific applications like thermoelectric devices [165, 193, 100] or battery materials [158], where the nanostructure of the materials play an essential role [131]. The dominating synthesis path of pure or composite silicon nanoparticles (Si NPs) involves the thermal decomposition of a gaseous Si precursor, typically trichlorosilane ($HSiCl_3$) or monosilane (SiH_4), in a flow reactor. A common setup of such flow reactor is a wallheated tube, like used in numerous lab-, pilot-, and production-scale devices for synthesis of gas-phase borne (nano)powders [69]. The advantages of the hot-wall reactor are simplicity, robustness and at the same time great flexibility in adjusting the bath gas composition and the heating scheme of the process. Prominent examples for production scale processes (besides of Si NPs) are high purity iron and nickel from iron pentacarbonyl [92] and nickel tetracarbonyl [93] respectively. Especially, when the particle properties such as crystallinity and morphology are important, the advantages of the hot-wall reactor become obvious due

to the flexibility in adjusting the bath-gas, temperature and residence time. Just to mention few early reports focusing on Si NPs, Xiao et al. synthesized Si(N, C) powders from a silane aerosol [253], while an economic, safe and technically feasible synthesis path was introduced by Wiggers et al. for solar grade silicon nanoparticles from silane [241]. The setup introduced by Wiggers et al. was later on used to produce a large variety of nanostructured Si materials and Si based composite materials [158, 253] including materials that feature gradients of $Si-N$ [253] and $Si-C$ [158]. An overview of these and similar processes can be found in the reports by Körmer et al. [110, 108] and Hülser et al. [83].

The variety of Si and Si-based NPs from the hot-wall reactor implicates a complex physical process. The modeling of the gas-phase synthesis process requires to couple the reaction kinetics of precursor pyrolysis and the particle dynamics with the convective transport within the reactors, which determines the history of the particles. The simplest transport models presume a plug flow and therefore a one-dimensional residence time history based on the mass flow rate and the heating profile. This assumption is easily violated [124], which makes a tight coupling of computational fluid dynamics (CFD) with the reacting flow and with the population balance equation (PBE) model necessary. There exist many reports on CFD of hot-wall synthesis reactors, however, most of them concentrate on the flow and temperature field, omitting the close coupling to a particle dynamics model. The same applies for the modeling of particles dynamics, where usually a plug flow assumption is made. The following short review focusses on works devoted to synthesis of Si NPs from SiH_4. Talukdar and Swihart employed three different methods: The classical method of moments, the quadrature method of moments, and the sectional method in order to investigate the dynamics of Si nanoparticle growth [216]. Woo et al. investigated the Si NP formation by surface reactions, coagulation and transport, coupled to detailed gas-phase reaction kinetics computation using the method of moments [251]. While both used the plug-flow assumption to describe the connective transport, Woo et al. employed CFD in order to reconstruct the residence-temperature history in the process. Dang and Swihart introduced a two-dimensional model using the method of lines in order to solve the steady-state two-dimensional flow field [32]. Later, Menz and Kraft investigated Si NP formation and growth from silane pyrolysis considering detailed reaction kinetics, a stochastic PBE model and plug-flow conditions, reported in a series of papers [148, 146, 147]. Due to the universality of the employed solution methods, few reports on numerical investigations of comparable systems need to be mentioned as well. First simulations (with coupling to CFD) of a wallheated aerosol flow reactor were presented by Schild et al. for titania flame synthesis from $TiCl_4$ [194]. Schild et al. implemented the monodisperse model by Kruis et al. [113] using the solver interface of a commercial CFD code. Akroyd et al. presented a CFD-population-balance coupling based

on the method of moments with interpolative closure and detailed reaction kinetics treatment, also implemented into a commercial CFD code [3]. Gröhn et al. investigated spray-flame synthesis of zirconia [66] and Weise et al. investigated the same process for titania [238], both using the monodisperse model for particle dynamics but with different treatment of the reaction kinetics. Dasgupta et al. reported coupled CFD-PBE simulations with the hybrid method of moments [33]. Recent reports, some of them driven by the SpraySyn initiative [195], demonstrate the feasibility of coupling the sectional model of the PBE with CFD of the flame spray pyrolysis (FSP) process, but usually at very high computational costs and/or strong simplification in modeling the particle morphology [249, 196, 186]. Also recently, Wollny et al. presented coupled CFD-PBE simulations of Si NP synthesis using a sectional model which considers the phase transitions of condensation/evaporation and the interaction with molecular and thermophoretic drift, causing an intriguing number density field pattern [250]. In this work, we present the numerical investigation of a pilot-scale Si NP synthesis reactor. The flow inside the wall-heated tubular reactor is laminar but strongly transient due to the buoyancy induced by density gradients that result from heating and mixing. As the mixing by convection and diffusion is vital for the mass and heat transfer and consequently for the particle formation itself, the modeling requires a tight coupling of the flow-field solution, the gas-phase reaction kinetics and the particle dynamics. The PBE model introduced in this report is the model philosophy as shown by stochastic approaches which are directly coupled with chemical kinetics [146, 200]: A mathematical description of the dispersed phase [113] is coupled with the gas-phase by expressions that are crucial for the formation and growth of the particles. The presented model was developed for the use where no condensation into the liquid phase occurs, but chemical kinetics lead to the formation of particulate clusters. This is the case for some metal oxides formed by flame synthesis [196], but mainly for synthesis processes at moderate temperatures, at which particles are synthesized in hot wall reactors or other flow reactors. The particle formation and growth processes differ significantly from those in liquid phases, as kinetic processes are responsible for particle formation and growth. Reactions at the surface of existing particles with metallic gas species are therefore likely. As particles are formed from intermediate species, volatile components can be incorporated into the particle which are released depending on the particle temperature and composition.

6.3 Experimental

6.3.1 Hot-wall reactor

The synthesis conducted in a resistively heated hot-wall reactor, has been described in detail before [241, 158, 253]. The reactor is used to produce powder by the thermal decomposition

of monosilane (SiH_4, UHP, Air Liquide). As shown by the sketch schematics of the vertical hot-wall reactor in Fig. 6.1, a quartz inliner with inner diameter $d_{\mathrm{I}} = 112$ mm and the length of 2400 mm is used as reaction tube. The SiH_4 precursor was fed in from the top through a concentrical water-cooled (80°C) nozzle (Fig. 6.1) with the inner and outer diameters $d_{n1} = 21.1$ mm and $d_{\mathrm{n2}} = 55$ mm, respectively, and 200 mm immersed in the 1000 mm long heating zone. The target temperature is set to 715°C for all heating zones, while the pressure is kept at 1000 mbar. The heating zone is followed by an actively cooled zone, which continues to the bottom of the reactor. The resulting temperature profiles at the inliner and the outer nozzle wall were measured by thermocouples which were attached to the respective walls. Fig. 6.1 shows the sketch of the reactor alongside the wall-temperature profile. The powder is separated from the gas by a porous metal filter and collected after the experiment has been conducted, the powder production rate is ~ 100 g/h. Gas flows, delivered by mass-flow controllers, are 3slm of SiH_4 though the central nozzle and 97 slm of argon as sheath gas resulting in comparable velocities at the end of the nozzle and a plug flow residence time of about 1.6 s. An overview of the hot wall reactor operating parameters, the measured BET (Brunauer Emmet Teller) - specific surface area and primary particle sizes of the silicon product nanopowder collected at the end of the process are given in Table 6.2.

Pressure / mbar	1000
Silane / slm	3
Argon / slm	97
Precursor consumption / %	59
BET surface / m^2/g	20.7
BET size / nm	123.9

Table 6.1 Hot-wall reactor operating parameters, precursor consumption, measured BET surface area, and BET particle sizes of the resulting nanopowder.

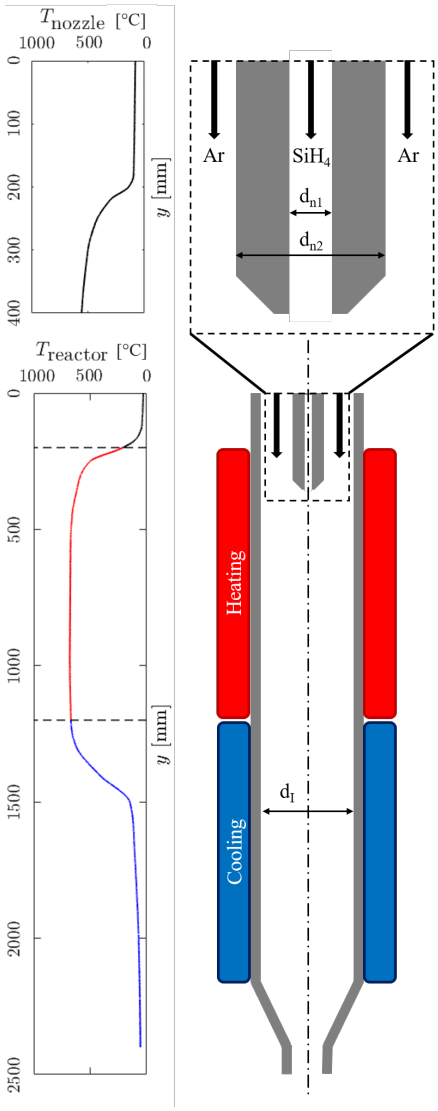

Fig.: 6.1 Sketch of the hot-wall reactor geometry together with the temperature profiles used as boundary conditions on the inside of the reactor wall. *Note that the figure has been squeezed in vertical direction for a better graphical representation.*

6.3.2 Measurements

The SiH_4 mass fraction consumption was monitored by a quadrupole mass spectrometer (QMS, GAM-200, Inficon) to quantify the precursor consumption. For that reason, a small fraction of the off-gas was continuously extracted from the reactor outlet through a capillary into a probe volume set at 500 mbar and analyzed with respect to concentrations of selected molecular weights. Temperature measurements on the inner surface of the inliner were conducted by attaching type-K thermocouples. The specific surface area of the powder was

measured by nitrogen adsorption (BET method, Quantachrome, Nova2000) and averaged over the time of the experiment. An equivalent particle diameter depends on the silicon density ρ_{Si} and the experimentally obtained specific surface area, SSA, and is calculated by the following equation under the assumption of monodisperse spherical particles: The SiH_4 mass fraction consumption was monitored by a quadrupole mass spectrometer (QMS, GAM-200, Inficon) to quantify the precursor consumption. For that reason, a small fraction of the off-gas was continuously extracted from the reactor outlet through a capillary into a probe volume set at 500 mbar and analyzed with respect to concentrations of selected molecular weights. Temperature measurements on the inner surface of the inliner were conducted by attaching type-K thermocouples. The specific surface area of the powder was measured by nitrogen adsorption (BET method, Quantachrome, Nova2000) and averaged over the time of the experiment. The equivalent particle diameter d_{BET} depends on the silicon density ρ_{Si} and the experimentally obtained specific surface area, SSA, and is calculated by the following equation under the assumption of monodisperse spherical particles:

$$d_{\mathrm{BET}} = \frac{6}{\rho_{\mathrm{Si}}\,\mathrm{SSA}}. \tag{6.1}$$

6.4 Modeling framework

6.4.1 Gas-phase model

The gas-phase consists of a mixture of all species included in the chemical mechanism described by Ho et al. [79]. The mechanism consists of eight species and ten reactions and includes important conversion reactions between silanes $\left(\mathrm{Si_xH_y}\right)$, silene ($H_2SiSiH_2$), and silyenes ($SiH_2, H_3SiSiH$). Conservation equations are solved for species, the mass, the momentum (three components), and the sensible enthalpy in a compressible framework. The conservation equations in the context of CFD are extensively discussed in the literature [171]. In the following, we describe the treatment of the source terms in the conservation equations for the species. Applying the Fick law for diffusion of a unity Lewis number, the system of equations for the partial densities $\rho Y_\beta = \rho_\beta$ (where Y is the mass fraction) conservation is given by:

$$\frac{\partial \rho Y_\beta}{\partial t} + \nabla \cdot \left(\boldsymbol{u}\rho Y_\beta\right) = \nabla \cdot \left(\frac{k}{c_p}\nabla Y_\beta\right) + \dot{\omega}_\beta + \Gamma_\beta^{\mathrm{P}}. \tag{6.2}$$

Here, the variables $\boldsymbol{u}, k$, and c_p denote the gas velocity, the thermal conductivity, and the isobaric heat capacity, respectively. The chemical net production rate of a species β is given by $\dot{\omega}_\beta$, while the source/sink due to phase transition between the gas and particle phase is

given by $\Gamma^{\mathrm{P}}_{\beta}$. It is the interface to the gas-phase of our new model and represented by the sum of all molecular fluxes of processes involved in the phase transition:

$$\Gamma^{\mathrm{P}}_{\beta} = \frac{W_{\beta}}{N_{\mathrm{A}}} \left(\Gamma^{\mathrm{I}}_{\beta} + \Gamma^{\mathrm{G}}_{\beta} + \Gamma^{\mathrm{VR}}_{\zeta} \delta_{\zeta}(\beta) \right). \tag{6.3}$$

The source term Γ superscripts I, G, and VR denote inception, growth, and volatile release. The variable W_{β} is the molar weight of species β, while N_{A} denotes the Avogadro constant. To consider that the inception source $\Gamma^{\mathrm{I}}_{\beta}$ for a species β can be a result of collisions with the same or with different species, the process is formulated with the help of the Dirac measure $\delta_{\alpha}(\beta)$ which is 0 if $\beta \neq \alpha$ and 1 otherwise. With x and y being the list of collision partners, the species inception source is given by:

$$\Gamma^{\mathrm{I}}_{\beta} = -\sum_{x,y} \left(\Gamma^{\mathrm{I}}_{xy} \delta_{x}(\beta) + \Gamma^{\mathrm{I}}_{xy} \delta_{y}(\beta) \right)_{\beta}. \tag{6.4}$$

The particle growth $\Gamma^{\mathrm{G}}_{\beta}$ term is of linear complexity and was derived as:

$$\Gamma^{\mathrm{G}}_{\beta} = -\left(\sum_{C} \Gamma^{\mathrm{N}}_{C} \delta_{\mathrm{C}}(\beta) + \sum_{S} \Gamma^{\mathrm{A}}_{S} \delta_{\mathrm{S}}(\beta) \right)_{\beta}. \tag{6.5}$$

Here, Γ^{A}_{S} and Γ^{N}_{C} are the activated and non-activated surface reaction rates of species C and S, respectively. Similar dependencies are used to derive the volatile contribution $\Gamma^{\mathrm{VR}}_{\zeta}$ given by Eq. (6.6). It summarizes all contributions (i.e., volatile release processes) as source for the volatile species ζ.

$$\Gamma^{\mathrm{VR}}_{\zeta} = -\frac{1}{\nu_{\zeta}} \left(\sum_{\mathrm{C}} \Gamma^{\mathrm{N}}_{C} \left(\nu_{C} - \mathrm{v}^{\mathrm{N}}_{C} \right) + \sum_{\mathrm{S}} \Gamma^{\mathrm{A}}_{S} \left(\nu_{S} - \mathrm{v}^{\mathrm{A}}_{S} \right) + \Gamma^{\mathrm{VR}} \right) \tag{6.6}$$

The activated and non-activated reacting molecules may also lose volatile content during the deposition on the particle surface, thus, the contribution of volatiles re-entering the gas-phase must be taken into account. The difference of the deposited volumes $\nu_{C/S}$ before and after activated $\mathrm{v}^{\mathrm{A}}_{S}$, or non-activated surface reaction $\mathrm{v}^{\mathrm{N}}_{C}$ therefore equals the detached volume that re-enters the gas-phase. Additionally, volatiles are released due to internal particle reactions that are accounted by the source term Γ^{VR}.

Note, that a reaction mechanism may contain a variety of species, while the number of collision partners relevant to particle-gas matter exchange can be small in comparison. Therefore, we avoid summing up all species β, and use instead defined lists x, y, or C and S of collision partners to reduce the numerical overhead.

Other gas-phase conservation equations can be extended by the sum of the transition source terms $\Gamma^{\mathrm{P}}_{\beta}$ of all species.

$$\Gamma^{\mathrm{P}} = \sum_{\beta} \Gamma^{\mathrm{P}}_{\beta} \tag{6.7}$$

The source term can then be applied for the mass conservation, the pressure correction, and the momentum conservation $\left(\Gamma^{\mathrm{P}}_{\boldsymbol{u}} = \Gamma^{\mathrm{P}}\boldsymbol{u}\right)$. An exception is the source term for the energy equation Γ^{PE}, for which all sources need to be summed up together with the respective specific enthalpy of the corresponding species β :

$$\Gamma^{\mathrm{PE}} = \sum_{\beta} \Gamma^{\mathrm{P}}_{\beta} h^{\mathrm{S}}_{\beta}. \tag{6.8}$$

6.5 Dispersed phase model: method of moments

The set of conservation equations used for the basic monodisperse model which accounts for the particle number concentration N, the particle surface area concentration A, and the particle volume concentration V is extended by the new Eq. (6.12). It describes the conservation of the volatile volume fraction ζ within the particle phase. The set of four equations is given by:

$$\frac{\partial N}{\partial t} + \nabla \cdot \boldsymbol{u}_t N = \nabla \cdot (j_N) + \Gamma^{\mathrm{I}}_n + \Gamma^{\mathrm{CO}}, \tag{6.9}$$

$$\frac{\partial A}{\partial t} + \nabla \cdot \boldsymbol{u}_t A = \nabla \cdot (\boldsymbol{j}_A) + \Gamma^{\mathrm{I}}_a + \frac{2}{d_p}\left(S_r \Gamma^{\mathrm{G}} + 2\Gamma^{\mathrm{VR}}\right) + \Gamma^{\mathrm{S}}, \tag{6.10}$$

$$\frac{\partial V}{\partial t} + \nabla \cdot \boldsymbol{u}_t V = \nabla \cdot (j_V) + \Gamma^{\mathrm{I}}_v + \Gamma^{\mathrm{G}} + \Gamma^{\mathrm{VR}}, \tag{6.11}$$

$$\frac{\partial (V\zeta)}{\partial t} + \nabla \cdot \boldsymbol{u}_t (V\zeta) = \nabla \cdot \left(\boldsymbol{j}_{V\zeta}\right) + \Gamma^{\mathrm{I}}_{\zeta} + \Gamma^{\mathrm{G}}_{\zeta} + \Gamma^{\mathrm{VR}}. \tag{6.12}$$

Eq. (6.10) includes the model constant S_r that accounts for surface rounding effects which occur during extensive surface growth, when the original shape of connected primary particles gets covered by layers of deposited material [146, 200]. The first terms on the right-hand sides of all equations denote the changes due to diffusive fluxes $j_N, j_A, j_V, j_{V\zeta}$ of the particle phase and are calculated by the Fick law. The total velocity is the sum of the gas-phase velocity and the thermophoretic velocity $\boldsymbol{u}_t = \boldsymbol{u} + \boldsymbol{\xi}$. The thermophoretic velocity is calculated as suggested by Waldmann [48]. To obtain the primary particle number and size from the moments N, A, V, it is necessary to assume that all primary particles of an agglomerate are in point contact. The primary particle diameter is then calculated as the ratio of the volume V

and the surface A concentrations:

$$d_\mathrm{p} = \frac{6V}{A}. \tag{6.13}$$

The number of primary particles can then be obtained by:

$$n_\mathrm{p} = \frac{6V}{\pi N d_\mathrm{p}^3}. \tag{6.14}$$

With the knowledge of both, the primary particle size d_p and primary particle number within an agglomerate n_p, the collision diameter can be derived [194]:

$$d_\mathrm{c} = d_\mathrm{p} n_\mathrm{p}^{\frac{1}{D_\mathrm{f}}}. \tag{6.15}$$

In this model, the asymmetrically evolving fractal dimension D_f is defined as a pre-defined model constant, depending on the material system and the synthesis conditions. In this work, only cases are investigated, in which silicon is synthesized and therefore a dimensional fraction of $D_\mathrm{f} = 1.6$ is applied [146].

It should be emphasized that the present approach is based on a monodispersed model that provides the simplicity to enable a bivariate description of the particle phase. As shown in Section 6.6, the good agreement with a wide variety of experimental observables as well as with results from our stochastic code with thousands of individual particles underlines the applicability of a monodispersed model particle representation as well as the importance of surface reactions. Note, that a directly computed particle distribution, such as in the case of the sectional model, would come with the bottleneck of presently unmanageable computational costs for CFD-application (see Section 6.7), if the dimensionality of the particle size distribution is increased. Furthermore, surface growth would add additional artificial broadening in the size space, in this case, if fixed section sizes are used. A method of moments approach with presumed size distribution would require a two-dimensional distribution in volume and surface space which comes with new uncertainties, assumptions and costs. We note, in passing, that a model that could, in principle, match our requirements at computationally manageable costs, is the EQMOM model by Wright et al. [252]. However, the mathematical context of such an approach is rather complex and would probably mask the clarity of the introduced role of surface reactions which is the primary focus of the current work.

6.5.1 Particle inception

The net inception source term for quantity $\alpha = n, a, v, \zeta$ is the sum of all particle forming combinations of species x and y:

$$\Gamma_{\alpha}^{\mathrm{I}} = \sum \sum \Gamma_{xy}^{\mathrm{I}} \gamma. \tag{6.16}$$

Where γ substitutes the different variables $1, a_{xy}, v_{xy}$, or $a_{xy}\zeta_{xy}$ for the cases of α being n, a, v, ζ, respectively. The inception source term Γ_{xy}^{I} for a combination of two species $x$and y is calculated by collision process. It is given by:

$$\Gamma_{xy}^{I} = \frac{1}{2} n_x n_y \beta^*(x, y). \tag{6.17}$$

The number concentrations of the gas species x and y are given by n_x and n_y, while the harmonic mean collision kernel β^* is explained in section 6.5.4.

6.5.2 Particle growth

The source term Γ^{G}, responsible for particle growth, is calculated by the contributions of two growth mechanisms: activated and nonactivated surface reactions – denoted by the superscripts A and N. Following the mechanism of Ho et al. [79], we classify barrierless particle-gas encounters with intermediate gas-phase species as nonactivated reaction, while deposition of stable silanes involving a considerable activation barrier is considered as activated surface reaction. The surface flux of molecules of species i by non-activated reactions can be calculated via the expression:

$$\Gamma_{i}^{\mathrm{N}} = N d_{\mathrm{c}}^{2} n_i \left(\frac{\pi R_u T}{2 W_i} \right)^{\frac{1}{2}} f(Kn). \tag{6.18}$$

The gas-phase molecule number concentration is denoted by n_i, while the free molecular-to-continuum transition correction $f(Kn)$ is described by the Fuchs-Sutugin correction factor [237] as a function of the Knudsen number Kn. The remaining variables R_{u}, W_i, and T are the universal gas constant, the molar mass of species i, and the gas-phase temperature. Particle growth by activated surface reactions is considered by a modified Arrhenius like equation. We extended the classical formulation by the surface of the collision equivalent sphere $\left(d_c^2 \pi\right)$ and the slip correction given in Eq. (6.18) to account for the changing probability of molecules

to get in contact with the particle surface. For species i, this equation is defined as:

$$\Gamma_i^{\mathrm{A}} = a_i \frac{N}{N_{\mathrm{A}}} d_c^2 \pi n_i \exp\left(-\frac{E_i}{R_{\mathrm{u}} T}\right) f(Kn). \tag{6.19}$$

Following the common practice with Arrhenius expressions, particle surface reactions are fitted with the help of a pre-exponential factor a_i and an activation energy E_i. The net source term by particle growth Γ^{G} is given by the sum of the contributions of activated and non-activated surface reactions:

$$\Gamma^{\mathrm{G}} = \sum \Gamma_i^{\mathrm{N}} \mathrm{v}_i^{\mathrm{N}} + \sum \Gamma_i^{\mathrm{A}} \mathrm{v}_i^{\mathrm{A}}. \tag{6.20}$$

Where $\mathrm{v}_i^{\mathrm{N}}$ and $\mathrm{v}_i^{\mathrm{N}}$ are the volumes of the deposited molecule material of species i. It is common for a surface reaction that some volatile atoms of the deposited material re-enter the gas-phase, making the deposited volumes $\mathrm{v}_i^{\mathrm{N}}$ and $\mathrm{v}_i^{\mathrm{A}}$ smaller than that of the original gas species v_i. An example is the surface reaction of disilane Si_2H_6, in which four hydrogen atoms are released in the process:

$$\mathrm{Si_2H_6(g)} + \mathrm{Si_nH_m(b)} \rightarrow \mathrm{Si_{n+2}H_{m+2}(b)} + 2\mathrm{H_2(g)}. \tag{6.21}$$

Here, “b” and “g” in the parentheses denote the molecule as bulk material (particle), or as gas molecule that arises from, or re-enters the gas-phase, respectively.
The model of particle inception (Section 6.5.1), growth – described in this section, and volatile release (Section 6.5.3) does not include an additional (particle-related) energy conservation framework as we assume thermal equilibrium between the particles and the gas phase.
Furthermore, since the nanoparticles within this study are not reaching the liquid phase at any stage in the process for the hot wall reactor temperatures considered in the current work, the heat exchange due to liquid-solid phase transition is not required. However, if this model is implemented for applications with higher process temperature, those energy exchanges might become important and should be considered.

6.5.3 Volatile release

The net source term for the volatile volume by particle growth $\Gamma_\zeta^{\mathrm{G}}$ given by Eq. (6.11) is calculated by multiplying the deposited volumes with their volatile volume fractions $\zeta_i^{\mathrm{N}} = \left(v_i - v_i^N\right)/v_i$ and $\zeta_i^{\mathrm{S}} = \left(v_i - v_i^S\right)/v_i$, respectively.

$$\Gamma_\zeta^{\mathrm{G}} = \sum \Gamma_i^{\mathrm{N}} \mathrm{v}_i \zeta_i^{\mathrm{N}} + \sum \Gamma_i^{\mathrm{A}} \mathrm{v}_i \zeta_i^{\mathrm{A}} \tag{6.22}$$

Inter-particle reactions which lead to the release of volatile atoms are again calculated by an Arrhenius like expression with the pre-exponential factor a_ζ and the activation energy E_ζ. It is given by:

$$\Gamma^{\mathrm{VR}} = -a_\zeta N\theta \exp\left(-\frac{E_\zeta}{R_\mathrm{u}T}\right) v_\zeta. \tag{6.23}$$

The variable θ is the ratio of volatile atoms per metal atoms within the particle which can be derived from ζ by following equation:

$$\theta = \frac{\zeta}{1-\zeta}\frac{W_\mathrm{met}}{W_\mathrm{vol}}\frac{\rho_\mathrm{vol}}{\rho_\mathrm{met}} \tag{6.24}$$

Here, the densities ρ and molar masses W for the metal and volatile content are subscripted by "met" and "vol", respectively. In the present context of silicon nanoparticles synthesized from SiH_4, θ is defined as the ratio of hydrogen atoms to silicon atoms contained within a particle $\theta = \frac{\mathrm{H}}{\mathrm{Si}}$.

6.5.4 Coagulation

The non-linear problem of particle coagulation is strongly simplified using a monodisperse model formulation, as it reduces the dependence to one particle size d_c:

$$\Gamma^{\mathrm{CO}} = -\frac{1}{2}N^2\beta^*. \tag{6.25}$$

The collision frequency is obtained by the harmonic mean transition kernel as suggested by Pratsinis [175]:

$$\beta^* = \frac{\beta^\mathrm{C}\beta^\mathrm{f}}{\beta^\mathrm{C}+\beta^\mathrm{f}}. \tag{6.26}$$

The harmonic mean transition kernel approximates the interpolation kernel introduced by Fuchs [51] very accurately [95] at a lower mathematical and algorithmic complexity. The two contributions within the harmonic mean are the collision kernels for the free molecular β^f and the continuum β^c regimes [48]. The free molecular regime frequency – simplified for the monodisperse case – is given by:

$$\beta^\mathrm{f} = \left(\frac{16k_\mathrm{B}T}{m_\mathrm{a}}\right)^{\frac{1}{2}} d_\mathrm{c}^2. \tag{6.27}$$

Where k_B is the Boltzmann constant and m_a is the mass of an aggregate. With the same simplifications as applied for the free molecular collision frequency, the continuum collision

frequency can be calculated by:

$$\beta^{c} = \frac{8 k_b T}{3\eta} C. \tag{6.28}$$

Here, the variable η is the dynamic viscosity, while the factor C denotes the Cunningham slip correction factor $C = 1 + 1.257Kn$ [232].

6.5.5 Sintering

The sintering process is described in terms of a characteristic sintering time τ and the difference of particle surface area concentration A to the surface concentration of spherical shaped particles, A_S, containing the same volume. This linear model shown in Eq. 6.12 corresponds to experimental and numerical investigations reported in literature [45, 50] after the faster "sintering-neck-forming" initialization time has elapsed.

$$\Gamma^{S} = \frac{1}{\tau}(A - A_S). \tag{6.29}$$

The surface concentration of spherical particles with equivalent mass can be calculated by:

$$A_S = \pi d_v^2 N. \tag{6.30}$$

Where $d_v = \left(\frac{V6}{N\pi}\right)^{\frac{1}{3}}$ is the spherical diameter of an aggregate.

6.6 Validation – time depending reactor benchmark

We validate the introduced model by a comparison with experimental data from Onischuk et al. [156, 157]. Because of the similarity of the operating conditions to the following comparison with own experimental data (Section 6.3) and the variety of available particle and gasphase data at different residence times, this case delivers an optimal benchmark for the desired model. In comparison to the work of Menz and Kraft [146], we prepare the model to fit not only the particle sizes, but also their number concentrations and precursor concentrations for this specific case. As the kinetics for the decomposition of the precursor are expected to strongly change with increasing temperature, fitting a broad range of conditions would lead to further generalization at the cost of accuracy. Nevertheless, the mechanism for the decomposition of SiH_4 introduced by Ho et al. [79] was developed for a broader range of conditions at moderate temperatures, to match particle and gas conditions - independent of the case by Onischuk et al. [156]. It is therefore considered as best choice for creating a generalized model in the range of conditions which yield low temperature synthesized

silicon nanomaterial. The synthesis experiments were conducted using a hot-wall reactor at a pressure of 39mbar, at a temperature of 853 K, and with a high precursor concentration of $x_{\mathrm{siH4}} = 5\%$. The gas-phase reaction mechanism suggested by Ho et al. [79] was used for SiH_4 decomposition in the gas-phase. The non-activated surface reactions (with SiH_2, H_2SiSiH_2, H_3SiSiH), the activated surface reactions (with SiH_4, Si_2H_6, and Si_3H_8), as well as the values for the model parameters a_ζ and E_ζ in Eq. (6.23) were adopted from Menz and Kraft [146]. As the surface reaction pre-factors of Eq. (6.18) are unknown for the present parametrization of Arrhenius-like expression, they were fitted according to the available data. The surface rounding factor has been kept constant with a value of $S_\mathrm{r} = 1.9$. Two combinations of nucleating species were used with $x = (H_2SiSiH_2, H_3SiSiH)$ and $y = (H_3SiSiH)$ (Eq. 6.17). The simulations were performed in an isobaric 0D reactor setup at a run time of 0.9 s. Time histories of the computational results were compared with the available data of the experiment. Fig. 6.2 (left) shows the comparison between the primary particle diameter d_p from the experiments by Onischuk et al. [157], from the stochastic simulation results by Menz and Kraft [146], and from the simulation with the introduced model for five cases with different combinations (see Fig. 6.2) of the surface reaction pre-factors a_i. Results are also given for a stochastic simulation performed using our in-house code with the same non-activated and activated surface reactions, sintering and coagulation. Further, one simulation without any surface growth, similar to the standard monodisperse model introduced by Kruis et al. [113] is shown for comparison. On the right-hand side of Fig. 6.2, the collision diameters resulting from the mentioned simulations are visualized. It can be seen that the new model together with the applied reaction mechanism captures the primary particle diameter d_p observed by Onischuk et al. [156] comparably well to the more complex and computationally demanding stochastic approach by Menz and Kraft [146]. The stochastic simulation performed with our in-house code shows that the surface reactions are not fitted to generate matching results with the presented model only, as similar predictions are obtained for the different models. The predictions without surface growth models which are state of the art for CFD simulations - predict unrealistically small primary particle sizes d_p and collision diameters d_c underlining the demand of growth mechanisms with phase coupling to be included in the model framework. Note, that tweaking the sinter parameters may help to increase the primary particle diameter d_p, but for the wrong physical reasons, since extensive sintering cannot be expected at low temperatures and with amorphous material.

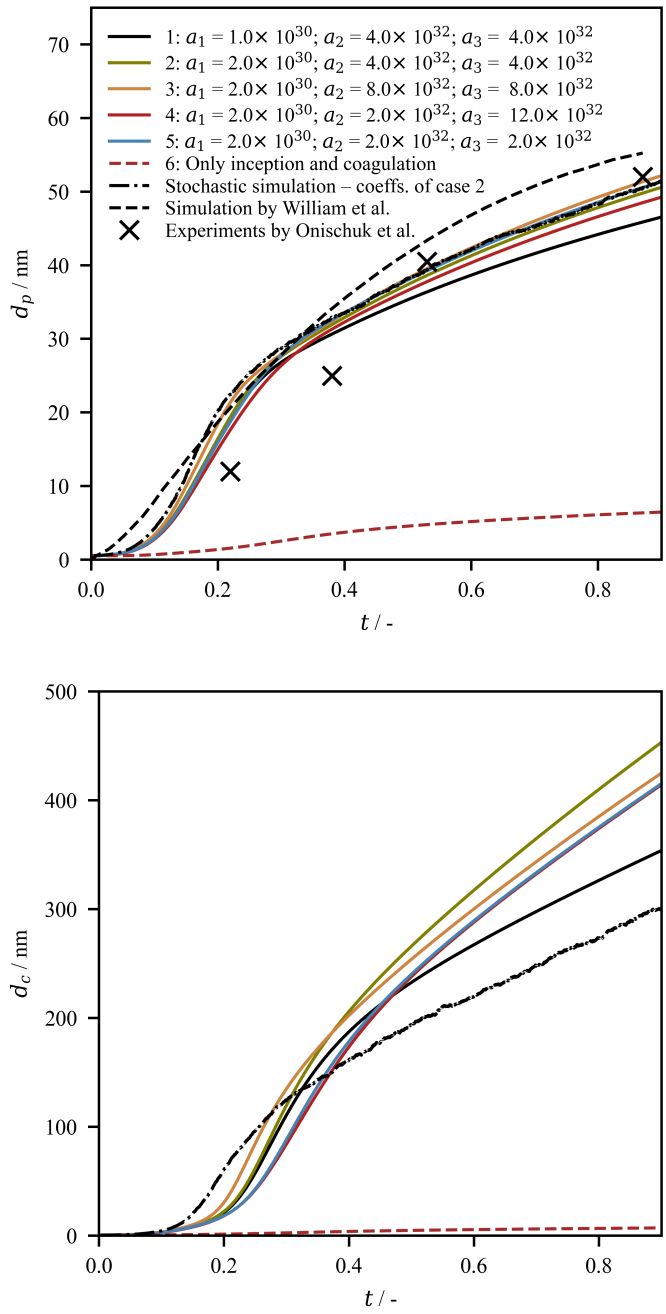

Fig.: 6.2 Top: Primary particle diameter d_p of the parameter study calculated by the introduced mode in comparison with experiments by Onischuk et al. [156] and with a statistical simulation performed by Menz and Kraft [146]. Bottom: Collision diameter d_c of the parameter study calculated by the introduced model.

	Reaction	1	2	3	4	5
a_1	$SiH_4(g) + Si_nH_m(b) \rightarrow Si_{n+1}H_{m+2}(b) + {}_1H_2(g)$	1.0×10^{30}	2.0×10^{30}	2.0×10^{30}	2.0×10^{30}	2.0×10^{30}
a_2	$Si_2H_6(g) + Si_nH_m(b) \rightarrow Si_{n+1}H_{m+2}(b) + {}_2H_2(g)$	4.0×10^{32}	4.0×10^{32}	8.0×10^{32}	2.0×10^{32}	2.0×10^{32}
a_3	$Si_3H_8(g) + Si_nH_m(b) \rightarrow Si_{n+1}H_{m+2}(b) + {}_3H_2(g)$	4.0×10^{32}	4.0×10^{32}	8.0×10^{32}	1.2×10^{33}	2.0×10^{32}

Table 6.2 Set of fitted parameter for the surface reaction pre-factors a_1, a_2, a_3 as plotted in Fig. 6.2 and Fig. 6.3 in comparison with the experimental data given by Onischuk et al. [156]. Set 2 was used for simulations of the semi-industrial hot-wall reactor

Fig. 6.3 shows the silane concentrations (left) and particle number concentrations (right) in comparison with the experimentally obtained data [156]. The silane concentrations are given as the ratio of the current concentration $[SiH_4]$ normalized by the initial value $\left[SiH_4^0\right]$. The simulations compare well with the measured data and the statistical simulations in both cases - for the normalized silane concentrations $[SiH_4] / \left[SiH_4^0\right]$ and for the particle number concentrations N. The new model shows an overall excellent agreement with the experimental data and proves that the model concept of coupling gas-phase and particle kinetics is not only possible for detailed stochastic simulation approaches, but also for more computationally affordable methods. Figs. 6.2 and 6.3 provide, in fact, a measure of sensitivity of the observables such as primary/collision particle diameters as well as gas phase precursor composition and number density at late and early stages of the synthesis process to the rate constants of activated surface reactions (Table 2). It is apparent that the suggested surface reaction constants (within a factor of ~ 2) capture all the experimental observations by Onischuk et al. [156] well. Moreover, the strongly deviating predictions given without phase transition models for particle growth, show the need for including such sub-processes for similar cases. As stated before, tweaking the sintering parameters lead to increase of the primary particle size, but will not change precursor composition which is decomposed due to the presence of Si-containing intermediates until it reaches the equilibrium state. In case of considered surface growth, those intermediates are removed from the gas-phase by phase transfer processes. This fact further underlines the need of phase coupling in the modeling approach, as remaining gas species change the gas-phase kinetics as well as the equilibrium.

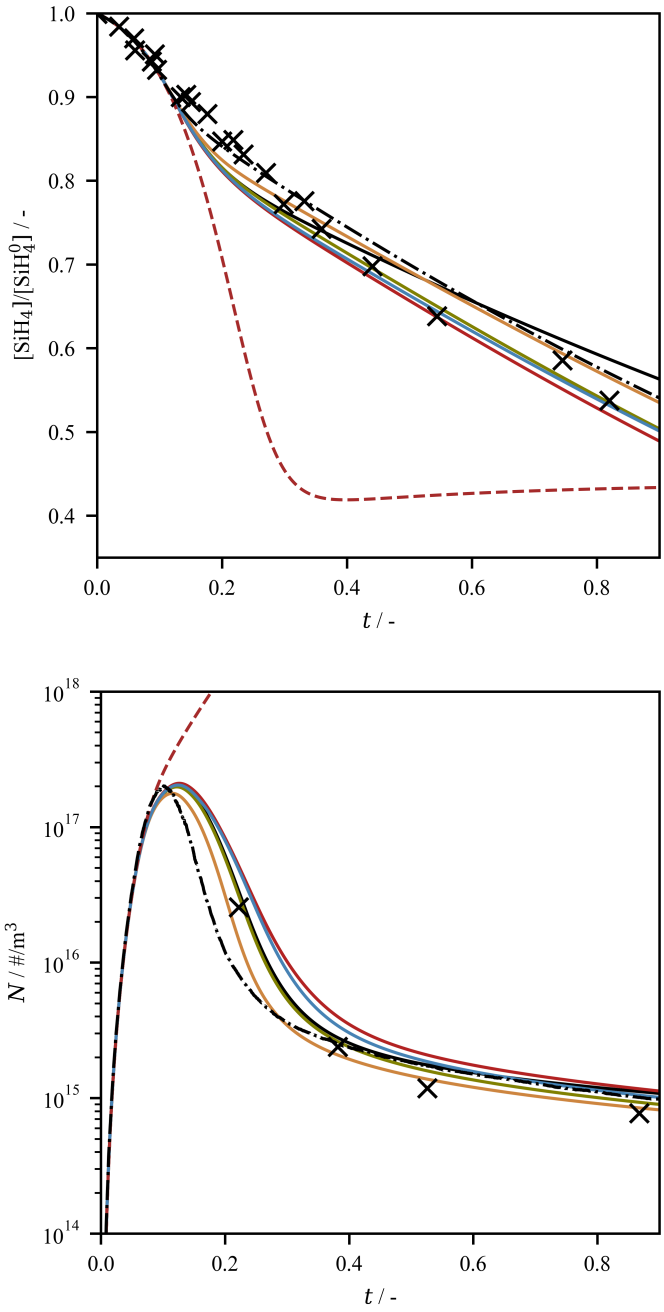

Fig.: 6.3 Top to bottom: concentration ratio of monosilane $[SiH_4]/[SiH_4^0]$ and particle number concentration N of the parameter study calculated by the introduced mode in comparison with experiments by Onischuk et al. [156].

6.7 Simulation: Hot-wall reactor

6.7.1 Simulation setup

In the next step, the new model was applied in the CFD of significantly more complex reactor: A semi-industrial hot wall reactor. The simulation has been performed using the open-source CFD library OpenFOAM [239] as foundation for the developed solver. The solver applies the pressure-velocity-density coupling [43] to consider the effect of changes in the density field. Buoyancy effects are taken into account by the impact of the hydrostatic pressure and source terms for the gravitational force within the momentum conservation. Due to the strong coupling between the surface reactions and the gas and particle phase, solving the system of Eqs. (6.9)-(6.12) explicitly with time steps sizes used in CFD simulations is possible only at low precursor concentrations. Then, the time scales for nucleation and growth must be large enough to justify a direct solution method. For practical situations, such as here, where precursor concentrations are above some hundred ppm at atmospheric pressure, the source terms must be calculated by a separate implicit ODE solver and coupled with the CFD solver by an operator splitting method. This has been done for the implementation of the introduced method into the OpenFOAM framework. The software library used for this work and for the previous work [250] will be made available online as an extension for the OpenFOAM CFD framework. The computational grid consists of about 6 million cells, nearly 99% of which are of hexahedral structure, while the rest are tetrahedral. A boundary layer at the reactor wall has been added in order to capture the temperature gradient and possible thin layers of particle formation. The first layer thickness is 0.3 mm, while the growth factor in wall normal direction is 1.15. The temporal derivatives are discretized using the Crank-Nicolson scheme, while spatial derivatives have been approximated by the central differencing scheme (CDS) for the momentum fields and by the total variation diminishing (TVD) schemes for the remaining transported scalars. The TVD limiter functions were van Leer [223] for the scalars of the particle phase and Sweby [213] for the remaining scalars. The simulations ran until a real time of 30 s was reached to guarantee that initialized values do not vitiate the results. The computational expenses amounted to 225,000 CPUh for each simulation. All boundary conditions other than zero gradient or non-slip conditions at walls are listed in Table 6.3.

Reactor wall	T: profile from Fig. 6.1
Outer nozzle wall	T: profile from Fig. 6.1
Central jet inlet	u_x: mass flux (table 6.2) SiH_4: mass fraction 1.0 T = 353.15 K
Annular gap inlet	u_x: mass flux (table 6.2) Ar: mass fraction 1.0 T = 303.15 K
Outlet	p = 1 bar

Table 6.3 Boundary conditions for the simulation. Remaining boundary conditions are zero gradient or non-slip conditions for the momentum equations at walls.

6.7.2 Results

Fig. 6.4 shows cross-sectional planes (z-normal) of the instantaneous flow field quantities predicted by the simulation. Presented are the axial velocity U_a, the temperature T, the mean thermophoretic velocity U_t and the SiH_4 mass fraction y_{SiH4}. The velocity field reveals two strong recirculation zones caused by heating (0.5 – 1.5 m) and cooling (from 1.5 m) at the walls of the reactor. Due to the upward directed flow at the heated reactor walls, a cold funnel flow is formed close to the symmetry axis of the reactor which eventually heats up at x = 1.4 m and decays at around x = 1.7 m. The reversed flow pattern occurs in the cooling zone: The flow close to the cooled walls is downward directed, while the upward directed recirculation occurs closer to the central axis of the reactor. It can be seen that the mean thermophoretic velocity develops as a direct consequence of the temperature gradients and is therefore present at the heated wall and in mixing areas. It has to be mentioned that thermophoretic velocities smaller than the threshold of 10^{-4} m/s are close to the heated reactor wall, as the precursor quickly decays in that area. With a calculated SiH_4 consumption of around 50%, the simulation compares well to the measured value of 59%. It needs to be taken into account that no intermediate Si species are measured and Si subspecies as well as larger silanes could be present within the gas-phase which are not part of the presented reaction mechanism.

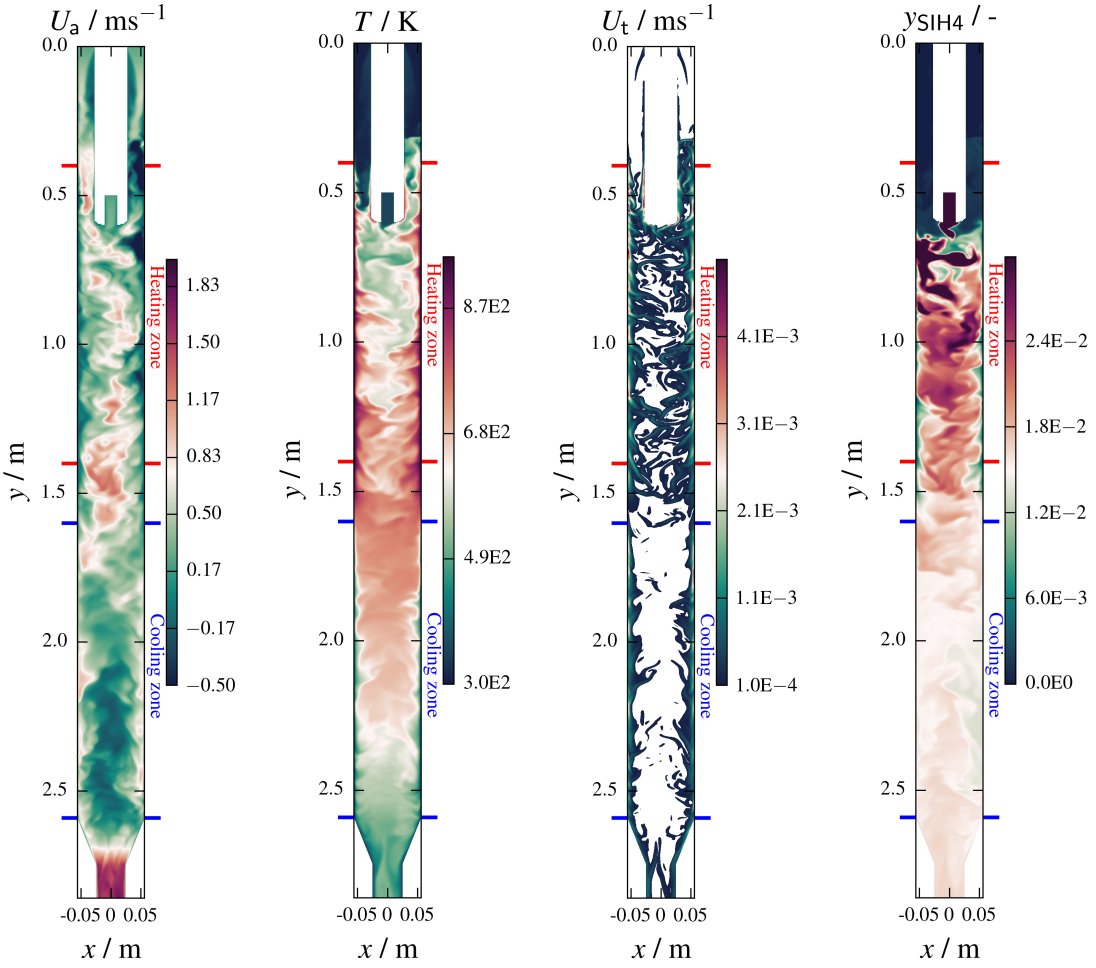

Fig.: 6.4 Cross-sectional planes (z-normal) for different quantities of the instantaneous flow field predicted by the simulation. From left to right: axial velocity U_a, temperature T, mean thermophoretic velocity U_t, and monosilane mass fraction SiH_4. *Note that the figures have been squeezed by a factor of 2 in vertical direction to improve the graphical representation.*

The same cross-sectional plane is given for the illustration of the particle phase in Fig. 6.5 , where the primary particle diameter d_p, the collision diameter d_c, the primary particle number per aggregate n_p, the particle number concentration N, and the ratio of H to Si atoms θ within the particles are shown. The primary particle diameter d_p grows rapidly close to the reactor walls, at locations where a combination of high temperatures and high precursor concentrations appear. The growth further downstream is predicted to slow down and reaches its maximum within the second recirculation zone inside the cooling area.

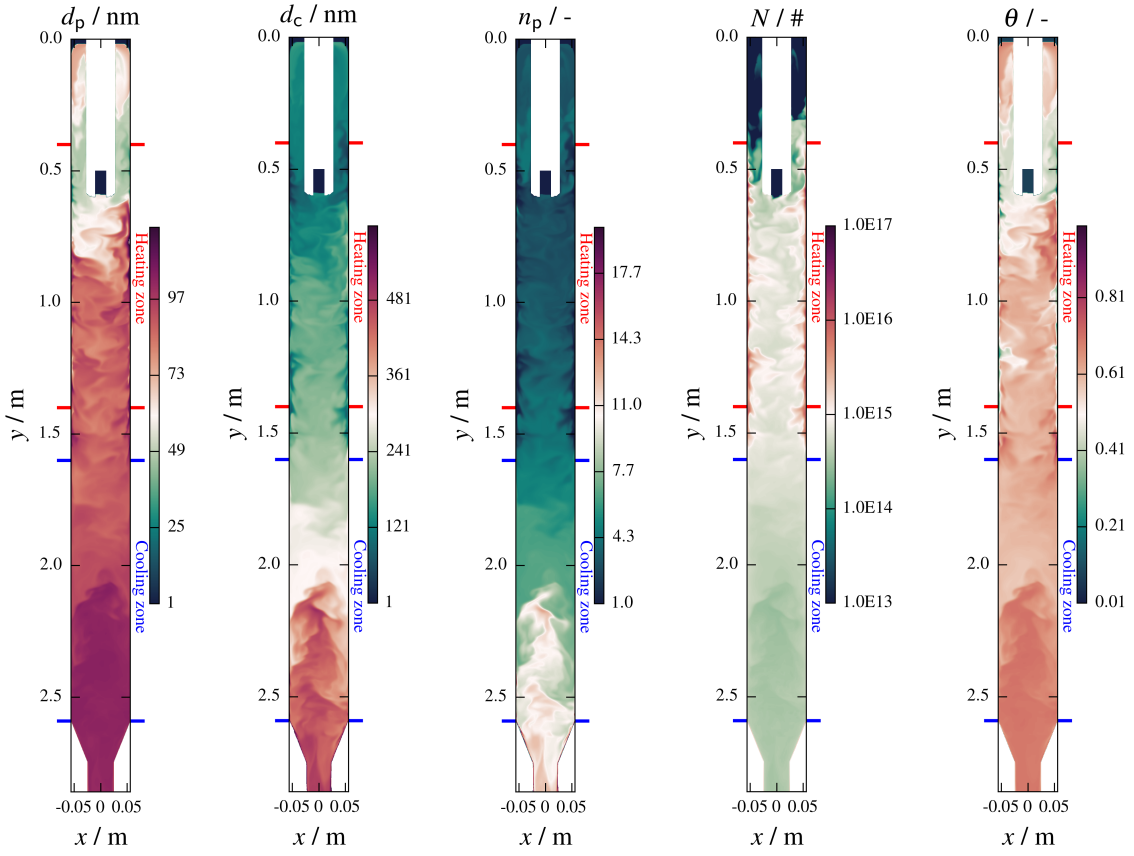

Fig.: 6.5 Cross-sectional planes (z-normal) for different quantities of the instantaneous particle field predicted by the simulation. From left to right: primary particle diameter d_p, collision diameter d_c, primary particle number per aggregate n_p, particle number concentration N, and ratio of H to Si atoms within the particle θ. *Note that the figures have been squeezed by a factor of 2 in vertical direction to improve the graphical representation.*

The same applies for the prediction of the collision diameter d_c, with the exception that it becomes smaller in the hot zones close to the reactor walls. The reason are the strong nucleation and surface growth which lead to a high number of freshly nucleated particles which decreases the average particle diameter. The number of primary particles per aggregate n_p follows directly the evolution of the collision diameter d_c, since the latter is a direct consequence of the increasing aggregate size by clustering. The particle number concentration N shows a strong increase at the hot reactor walls and high temperature zones, where the precursor is decomposed. The particle number concentration is decreasing in the mixing areas due to dilution and coagulation. The evolution of θ, i.e., the ratio of H to Si atoms within the particle, follows the evolution of the particle number concentration N and the silicon mass fraction y_{SiH4}, since freshly formed particles have a high H-to-Si ratio.
It is, however, overpredicted by the model, as the H to Si ratio θ of the product particles

in experiment has been measured to be 0.1. It provides motivation to investigate and refit the activation energy E_ζ or the pre-exponential factor α_ζ of Eq. (6.23) for volatile release reactions within a less complex numerical experiment in a future work. The calculation is validated against the experiments by a comparison of the BET diameter d_{BET}, BET surface A_{BET} and the measured consumption of silane. The BET diameter d_{BET}, BET surface A_{BET} are shown in Fig. 6.6 as line plots along the central axis of the reactor (y coordinate) as comparison between the simulation with surface growth and a simulation without surface growth (only inception, coagulation, and sintering). It can be seen that the particle formation/reaction area is located mainly within the heating zone, if surface growth is considered, while a steady phase is reached afterwards. It can be concluded that ongoing coagulation in the phase of steady BET sizes mainly lead to soft bonds between particles, as the surface area remains almost constant. In case of missing surface growth mechanisms, the BET surface A_{BET} steadily increases downstream by the constant inception of fresh particles which leads to large values compared to when surface growth is applied. The opposite applies for the BET diameter d_{BET} : After a certain size is reached at the top of the reactor, no further growth can be observed. This leads to particles that are more than one order of magnitude smaller than predicted with surface growth.

Due to the limited accessibility of the reactor, comparisons could be made for the product particles only, which have been collected in a filter below the reactor. For that reason, the comparison in Fig. 6.6 is limited to the values given at the end of the simulation domain, while the values are given in Table 6.4 for comparison together with the precursor consumption. The experiments and simulation results compare well, especially given the high complexity of the synthesis process, if surface growth is considered. In comparison with predicted values by the simulation without surface growth, which is state-of-the-art in CFD simulation, the results of the introduced framework show a major improvement, as the absence of surface growth mechanisms predict values which deviate more one order of magnitude from those observed by the experiments.

	Experiment	With surface growth	Without surface growth
A_{BET} / $\mathrm{m^2/g}$	20.7	25.1	217.6
d_{BET} / nm	123.9	102.8	11.8
SiH_4 consumption / %	59	50	72

Table 6.4 Comparison of experimentally obtained and simulated product particles characteristics and precursor consumption at the end of the reactor.

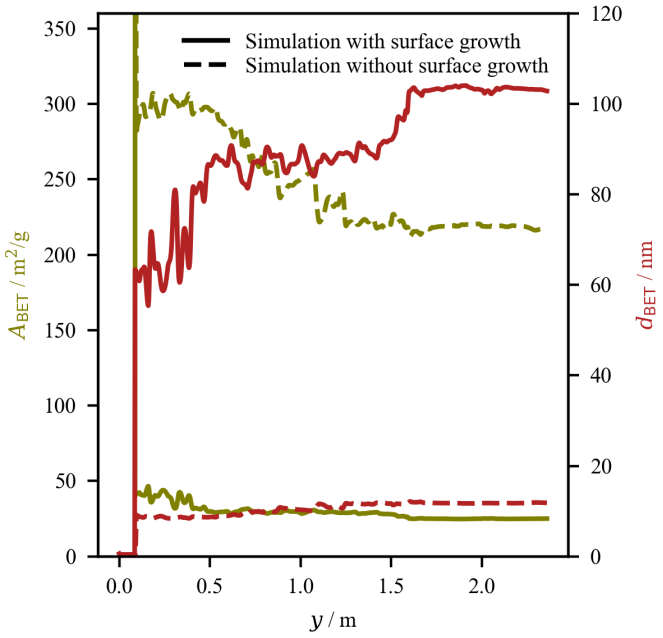

Fig.: 6.6 Line plots of the BET diameter and BET surface along the central axis of the reactor (y coordinate). Comparison of simulations with surface growth (bolt lines) with simulation without surface growth (dashed lines).

6.8 Conclusions

A model for predicting the particle dynamics for the synthesis process of nanoparticles from the gas-phase was built on the foundation of the bivariate monodisperse formulation by Kruis et al. [113]. The novel model features a direct coupling of the gas- and particle-phase by a series of inception, activated and non-activated surface reaction processes, which describe the particle formation and growth within the particle phase. All interfaces for the integration of the processes have been developed within this work, while the surface reaction formulation has been extended to consider the collision probability and be consistent to the formulation of the non-activated reaction. Further, the particle characteristics described by the general method of moments has been extended by the description of the hydrogen content captured and released by the particles. The model has been validated for the case of low temperature synthesis of silicon nanoparticles from monosilane, SiH_4, by a hot-wall reactor for two different setups. The first validation case has been adopted from the experiments of Onischuk et al. [156, 157], where available experimental data has been compared with a zero-dimensional reactor simulation with the same conditions.

Measured particle sizes and number concentrations, as well as concentrations of non-

decomposed precursor have been compared for different residence times from the experiment. In the case of the classical model (no surface reactions), far too small particle sizes and too fast precursor decomposition are predicted. The new model with activated and non-activated surface reaction shows an excellent agreement with all compared quantities (i.e., precursor concentration, primary particle size, and particle number concentration).
A semi-industrial hot-wall reactor with large buoyancy-driven recirculation zones has been conducted for the comparison with three-dimensional, transient simulations featuring the classical and the new particle model, respectively. Comparison with the BET diameter and the BET surface of the product particles, as well as the comparison of the precursor consumption are shown for both cases. The simulation results of the classical approach (no surface reactions) deviate about one order of magnitude from the measured data. In comparison, the results of the new model show a very good agreement with the experimental data due to the coupling by a series activated and non-activated surface reactions which are essential for particle growth.
The hydrogen release from the particles, however, is underpredicted, as indicated by the high H:Si ratio calculated by the model. This is due to the reaction parameters adopted from the literature and should be corrected in future work by fitting experimental data in relatively simple experiments. The massive error induced by skipping the important surface growth mechanism in case of the classical modeling approach could be eliminated with the novel model introduced in this work. It clearly indicates that phase transition modeling together with a sophisticated coupling approach is of key importance for the modeling of synthesis processes like in the presented cases, where particles are formed and grow due to a chain of kinetics reactions. Further, it is having been shown that detailed transport phenomena have to be considered by three-dimensional, transient simulation for fluid dynamically complex systems. Only then, the crucial thermochemical time history of synthesized particles can be predicted correctly in order to improve investigated reactor and particle designs.

6.9 Appendix

Here, additional information about the used reaction mechanisms are provided for the gas-phase reactions (see Table 6.5) and the activated and non-activated surface reactions as well for the hydrogen release (see Table 6.6).

Reaction	α_i	E_i	Comment	Ref.
$SiH_4 + p(Si_n, H_m)$ $\rightarrow p(Si_{n+1}, H_{m+2}) + H_2$	2.00×10^{32}	37.5	Eq. (19) modified, parameters α_i refitted in this work.	[146, 79]
$Si_2H_6 + p(Si_n, H_m)$ $\rightarrow p(Si_{n+2}, H_{m+2}) + 2H_2$	4.00×10^{34}	37.5	–	[146, 79]
$Si_3H_8 + p(Si_n, H_m)$ $\rightarrow p(Si_{n+3}, H_{m+2}) + 3H_2$	4.00×10^{34}	37.5	-	[146, 79]
$SiH_2 + p(Si_n, H_m)$ $\rightarrow p(Si_{n+1}, H_{m+2})$			Non-activated surface reaction according to Eq. (18).	[146, 79]
$H_3SiSiH + p(Si_n, H_m)$ $\rightarrow p(Si_{n+2}, H_{m+4})$			-	[146, 79]
$H_2SiSiH_2 + p(Si_n, H_m)$ $\rightarrow p(Si_{n+2}, H_{m+4})$			-	[146, 79]
$p(Si_n, H_m)$ $\rightarrow p(Si_n\ H_{m-2}) + H_2$	1.20×10^{19}	47.0	Hydrogen release according to Eq. (23).	[146, 79]

Table 6.5 Activated and non-activated surface reactions and hydrogen release reactions. Reactions are introduced by Ho et al. [79], modified by Menz and Kraft [146]. Activated reaction equation was modified (see Eq. (6.19)) and reaction pre-factors α_i were refitted in this work. The parameters are given in cm, s, kcal, K, mol.

Reaction	A	β	E_a	α	T1	T2	T3	Ref.
$SiH_4(+M) \leftrightarrow SiH_2 + H_2(+M)$	3.12×10^{09}	1.70	54.71					[79]
Low-pressure Troe parameters	5.21×10^{29}	-3.54	57.55	-0.4984	209.4	2760.0	888.3	[79]
$Si_2H_6(+M) \leftrightarrow SiH_4 + SiH_2(+M)$	1.81×10^{10}	1.70	50.203					[79]
Low-pressure Troe parameters	5.09×10^{53}	-10.37	56.034	4.375×10^{-5}	2726.0	438.2	438.5	[79]
$Si_2H_6(+M) \leftrightarrow H_2 + H_3SiSiH(+M)$	9.09×10^{09}	1.80	54.197					[79]
Low-pressure Troe parameters	1.94×10^{44}	-7.77	59.023	-0.1224	2400.0	11.39	793.3	[79]
$Si_3H_8(+M) \leftrightarrow SiH_2 + Si_2H_6(+M)$	6.97×10^{12}	1.00	50.850					[79]
Low-pressure Troe parameters	1.73×10^{69}	-15.07	60.491	-4.375×10^{-5}	2412.0	128.30	442.0	[79]
$Si_3H_8(+M) \leftrightarrow SiH_4 + H_3SiSiH(+M)$	3.73×10^{12}	1.00	50.850					[79]
Low-pressure Troe parameters	4.36×10^{76}	-17.26	59.303	0.4157	3102.0	9.72	365.3	[79]
$H_3SiSiH(+M) \leftrightarrow H_2SiSiH_2(+M)$	2.54×10^{13}	-0.20	5.381					[79]
Low-pressure Troe parameters	1.10×10^{33}	-5.76	9.152	-0.4202	214.5	103.0	136.3	[79]
$H_3SiSiH + H_2 \leftrightarrow SiH_2 + SiH_4$	9.41×10^{13}	0.00	4.0923					[79]
Reverse reaction parameters	9.43×10^{10}	1.10	5.7903					[79]
$H_3SiSiH + SiH_4 \leftrightarrow Si_2H_6 + SiH_2$	1.73×10^{14}	0.40	8.8987					[79]
Reverse reaction parameters	2.65×10^{15}	0.10	8.4734					[79]

Table 6.6 Gas phase reaction mechanism as adopted from Ho et al. [79]. The parameters are given in cm, s, kcal, K, mol.

6.10 Acknowledgments

The authors gratefully acknowledge financial support from Federal Ministry of Economic Affairs and Energy, Germany (Funding code 03EI3027A) and the support through the Gauss Centre for Supercomputing e.V. (www.gauss-centre.eu) by funding this project (grant DUE-HAWK2021) by providing computing time on the GCS Supercomputer HAWK at Hoechstleistungsrechenzentrum Stuttgart (www.hlrs.de). IR acknowledges the support of the Israel Science Foundation, ISF (grant No. 2187/19) and Mercator Fellowship (374957702) within the German Research Foundation, (DFG)- funded research group FOR 2284.

7 Summary

Five new particle dynamic models have been developed including different approaches for extended phase coupling controlled by particle formation and growth processes [249]. Three of the introduced models have been published in peer reviewed journals, while the other two are also presented in the thesis but so far unpublished.

The first in the series of the published models is an approach for simulating heterogeneous particle systems [249]. It was developed and tested in a case, where spray flame synthesized Pt-particles decorated priorly generated Al_2O_3-carrier-particles. To achieve a multi class model for particles in the gas phase and particles on the carrier particle surface, the sectional model had to be extensively extended [249]. In fact, the model consists of two interacting sectional size distributions whose transition is calculated by deposition rates and collision probabilities. A simple model for particle coagulation on the carrier surface is introduced to capture the particle growth after their deposition. The SpraySyn burner setup [195] was used for the experiments, where Al_2O_3 carrier particles were suspended in a solution of acetic acid, isopropanol, and Platinum(II)acetylacetonate. The applied two mixture fraction FGM approach was extended by a new tabulated nucleation source term which has been derived by transforming the flamelet solution into time space. The simulation results are compared with experimentally obtained carrier-particle loadings (ratio of deposited platinum mass to carrier particle mass) of single product particles, where the good results verify the validity of the developed deposition model. Measured particle distributions of deposited Pt-particles on carrier-particles show a good agreement of the average particle size, while artificially reconstructed 3D TEM images offer a good visual comparison with the real TEM images from the experiment. The discussed publication [249] presents the first coupled CFD/particle dynamics simulation of a spray flame synthesized heterogeneous particle system and delivers promising results and a basis for future investigations of this delicate process.

A further model developed within this work focuses on the synthesis by condensation of metallic vapor from the gas phase. The employed sectional approach therefore includes a direct coupling with the gas phase by homogeneous and heterogeneous condensation and evaporation [250]. It applies the nucleation model by Girshick and Chiu [59] together with suitable data for the vapor pressure and the surface tension for the silicon material system. The condensation/evaporation term was extended by a curvature correction considering the higher stability of larger particles. The model was applied in the frame of a microwave plasma synthesis process [140], where the plasma source was approximated by a homogeneous heat

source assuming that particle nucleation takes place outside the active plasma torch, where suitable conditions for the nucleation of the vapor exist. The saturation rate, the driving force for particle formation and growth, tends to exponentially increase within a thin layer (nucleation burst) [159] which makes an investigation of the numerical grid dependency mandatory. Those studies show similar results for the fine and coarse grid resolutions regarding all gas phase properties, but noticeable differences for the particle phase as an effect of the high inertia. The simulations show an excellent agreement with the experimental data: Due to the extended phase-transition modeling, the tubular particle front around the central jet – which is observed in the experiments – could be reproduced by simulations for the first time. The secondary condensation zone that was observed in the experiments close to the reactor walls, has been captured and could be explained by the simulations. The atomic silicon is conserved at gas conditions which are too hot for condensation until it diffuses towards the colder recirculation zone close to the reactor walls, where it tends to condensate on existing particles.

Further studies were conducted using a thousand tracer particles which were calculated with and without thermophoresis. It has been proven that thermophoresis has a crucial effect on the particle trajectories, as the residence times differ by 20% and the time histories for the gas and particle states are significantly different. It was found that thermophoresis forces particles in a direction away from high temperature zones and therefore prevents particles from being evaporated.

Due to the high computational costs of applying the sectional model in CFD simulations together with its' limitations regarding the predictions of particle morphologies, a monodisperse approach was extended by formulations for nucleation and condensation/evaporation. Since an implementation of evaporation into the moment method is problematic, a novel approach was developed which features a fitted complementary error function as transition parameter. It splits the evaporation contributions into parts which decrease the particle diameter and remove existing particles in dependency of the number of metallic atoms within a primary particle. The model has proven to deliver good accuracy, as it performs well in comparison with a computationally more expensive sectional approach [250] and allows predictions of the particle morphology due to its' bivariate definition. The model is so far unpublished but presented in section 3.7 of this thesis.

This model is only valid if particles are formed from vapor due to homogeneous or heterogeneous condensation. The following model was therefore developed for the use where no condensation into the liquid phase occurs, but chemical kinetics lead to the formation of particulate clusters. It combines the model philosophy of sophisticated stochastic models which are coupled with chemical kinetics of the gas phase [146, 199] with an affordable

monodisperse description of the dispersed phase [113] extended by a further moment which is responsible for tracking the particle composition. The latter addition is important since reactions at the surface of existing particles are often dominant and volatile components can be incorporated into the particle and re-enter the gas phase depending on the temperature and composition of the particle. Two low temperature synthesis processes of silicon nanoparticles within hot wall reactors were simulated and validated against experiments. The first case is adopted from the experiments described by Onischuk et al. [156] and validated by zero-dimensional isobaric reactor simulations. It is shown that the model is able to predict the synthesis process in close agreement with the measurements and with comparable accuracy as stochastic approaches. In the second case, a semi-industrial hot wall reactor experiment was conducted for the validation with the product material. The experiment features a complex, buoyancy driven flow for which three-dimensional and instantaneous CFD simulations serve as foundation for the applied particle model that is solved by an additional ODE-solver. It is the first simulation attempt for the mentioned reactor setup that features aerodynamics, chemistry, and particle dynamics in a fully coupled model framework. The experiments are compared with two simulations which feature either only particle inception, coagulation, and sintering – like the state of the art in CFD simulations –, or the full developed model including sticking- and surface reactions. It is shown that all compared quantities are in good agreement with the experiments only in case of the full model. The absence of important particle growth formulations predict values for the BET-surface and -diameter which deviate about one order of magnitude from those given by the experiment. Following, it can be concluded that surface chemistry plays a crucial role in the investigated cases and must be considered to make reliable predictions about the process and the particle design.
The digital clone probability weighted Monte-Carlo method, introduced and validated in section 3.8 has been developed by the author together with the new in-house simulation software "ant" (another nanoparticle tool). It is capable of performing stochastic simulations with hundreds of thousands individual digital particle representations. The model can be used for zero-dimensional analysis of reactive gas synthesis, similarly as shown in the works by Shekar et al. [199] and Menz et al. [146]. Moreover, the model can be used with sampled thermochemical time histories from CFD calculations which serve as dynamic boundary conditions defining the gas phase state. The model has shown to deliver excellent predictions of particle size distributions in cases where more complex particle morphologies are assumed and is applied as verification for simplified models as shown in chapter 6.

8 Conclusions

The presented population balance models (PBM) were developed with the primary objective of incorporating significant multiscale physics while maintaining limited algorithmic complexity. This approach allows for effective phase-coupling with Computational Fluid Dynamics (CFD) simulations, enabling a comprehensive and accurate representation of gas-to-particle transition phenomena across different scales. It has been demonstrated that appropriate formulations for particle formation and particle growth are crucial for accurately predicting the synthesis process in many industrially relevant applications. The examples presented in this work clearly demonstrate that it is feasible to implement these processes in CFD simulations at a level that enables sophisticated multiscale modeling. Moreover, the results indicate a significant improvement in particle model predictions for all studied cases. It can be shown that neglecting growth mechanisms in processes with high precursor content can result in the prediction of non-physical particle structures and incorrect gas phase compositions. When dealing with condensing vapors, additional issues arise. Presented studies [250] demonstrate that in zones with high temperature gradients, a thin particle front is formed due to nucleation burst, which is then followed by intense particle growth. This particular process feature can be accurately predicted only when both homogeneous and heterogeneous condensation mechanisms are taken into account. Furthermore, a good spatial accuracy is achieved only by additional consideration of thermophoresis in cases of intense temperature gradients as present in plasma and hot wall reactors. It is shown that thermophoresis is crucial at high local process temperatures as particles escape zones where they would be otherwise vaporized.

On the other hand, rather simple approaches such as the monodisperse representation of the particle phase give good results compared to more complex approaches such as the sectional model, if adequate phase transition modeling is applied.

Issues with current and frequently employed methods for the aforementioned model extensions are emphasized. Models such as low-order moment methods and discrete methods can suffer from significant limitations in certain cases. For example, the monodisperse model [113] does not approximate the particle size spectrum but assumes a single size for all particles at one location in physical space. It therefore ignores the strong size dependency of the growth, coagulation, and diffusion functions. Consequently, larger inaccuracies have been detected in case of higher ratios of particle growth to nucleation rates and thus for broader particle size spectra (see section 3.7). The sectional model, on the other hand,

reaches a bottleneck of unmanageable computational complexity, when the dimensionality of the particle size distribution is expanded to allow for bi- or multivariarity. Therefore, the heterogeneous model presented (see chapter 4) can only be applied to systems where two interconnected univariate size distributions adequately describe the particle characteristics. Multicomponent aggregates with complex structure and primary particles of mixed size are multivariate problems and therefore cannot be realized applying classical discrete approaches – at least in the context of CFD. Hence, more attention should be paid to other approaches that offer a better trade-off between accuracy and computational effort while maintaining good future-proofing.

Promising approaches are bi- and multivariate models based on the QMOM approach which can be extended to include closures for particle formation and growth in a gas-phase coupled framework. Although the underlying theory is more challenging compared to most classical approaches, the algorithmic complexity to find the necessary quadratic abscissas and their weights does not increase exponentially with the dimensionality of the particle size distribution. This fact opens new opportunities for future models, especially in the area of mixed material systems for heterogeneous particle designs. Another promising approach to deal with the high computational complexity of approximating the multidimensional particle size distribution is the application of artificial intelligence, i.e, machine learning algorithms. In particular, methods that learn directly from a given set of equations, as in the case of physically informed neural networks (PINNs), can potentially cover a wide range of conditions and promise a good generalization of the approximated distributions. The success by using this framework to simulate entire, complex reactor synthesis processes and include process-dependent gas-to-particle closures has already been discussed by other groups and led to cooperative works as well as to new research projects.

A Additional Publications

This chapter gives a brief overview of the author's contributions to other published works. Presented are the paper abstracts of publications which are relevant to the topic of the present work together with a description about which parts the author of this thesis contributed.
For other publications by P. Wollny, which focus on combustion modeling, the interested reader is referred to [248, 68, 41, 137].

A.1 Absolute concentration imaging using self-calibrating laser-induced fluorescence: application to atomic iron in a nanoparticle flame-synthesis reactor

M.R. Lalanne, A. Pilipodi-Best, O. Blumer, P. Wollny, M. Nanjaiah, I. Wlokas, S. Cheskis, I. Rahinov

P. Wollny contributed models, codes and simulation of nucleation rates for the different investigated conditions, post-processing and plots, discussion, corrections and proof-reading.
This paper was published in Applied Physics B, 127(9), 1–14, Copyright ©Springer (2021) [115], the abstract is reprinted with permission from Springer.

Abstract

Quantitative, spatially-resolved measurements of intermediates in flame synthesis reactors are required for the validation of precursor decomposition and oxidation mechanisms, preceding the nanoparticle formation. In this work we demonstrate how the laser-induced fluorescence (LIF) can be used in a self-calibrating fashion to image absolute concentrations of the strong absorber, such as atomic iron generated during the thermal decomposition of iron pentacarbonyl precursor in the preheat zone of synthesis flame. Flame symmetry facilitates deduction of the absolute concentrations. A comparison of LIF fluorescence patterns on both sides of axisymmetric flow configuration cancels out symmetric factors such as fluorescence quantum yield, fluorescence trapping and optical aberrations. This approach, utilizing one laser beam and one spectral transition provides a refinement of previous methods that have used either two spectral transitions or two collinear laser beams in counter-propagating geometry. Its spectral resolution and the detection sensitivity of que are not compromised when the spectral width of the laser exceeds that of the absorber. The measured Fe-atom concentration field is qualitatively consistent with the predictions of nucleation theory approach and suggest that flame synthesis model should be expanded beyond the formation of small incipient iron clusters to several nm-sized iron particles.

A.2 LES of nanoparticle synthesis in the spraysyn burner: A comparison against experiments

J. Sellmann, P. Wollny, S.-J. Baik, S. Suleiman, F. Schneider, C. Schulz, H. Wiggers, I. Wlokas, A.M. Kempf

P. Wollny contributed models and codes for the chemistry tabulation, particle nucleation, harmonic mean coagulation, generated chemistry/nucleation tables for the use in the simulation, discussion and support for the implementation of the intermittency model, corrections and proof-reading.
This paper was published in Powder Technology, 404, 117466, Copyright ©Elsevier (2022) [196], the abstract is reprinted with permission from Elsevier.

Abstract

The synthesis of iron oxide nanoparticles from iron nitrate in the SpraySyn spray flame reactor was investigated by experiment and simulation. The focus was on the spray and flame structure, the particle growth by nucleation and coagulation, and the unresolved effects and their impact on the dispersed phase. The reacting flow was modeled in large eddy simulations with the premixed flamelet generated manifolds technique, including modifications for aerosol nucleation. Particle dynamics were described with a sectional model and a subgrid scale coagulation kernel. The particle size distributions at different distances from the burner surface were obtained using a particle mass spectrometer. The experiments and simulations are in good agreement for the flame centreline velocity and both size distribution and mean size of the particles (for particles larger 1 nm – the approximate detection limit of the experiment). Furthermore, simulations enabled to interpret the temporal evolution of the particle size distribution.

A.3 Determining the Sintering Kinetics of Fe and FexOy-Nanoparticles in a Well-defined Model Flow Reactor

T. Rosenberger, I. Skenderović, J. Sellmann, P. Wollny, A. Levish, I. Wlokas, A. Kempf, M. Winterer, F.E. Kruis

P. Wollny contributed codes for the particle tracking with diffusive drifts and thermophoresis, simulations for extracting particle time histories, which were used to calculate the presented sinter mechanics, support for post-processing, discussion, corrections and proof-reading.
This paper was published in Aerosol Science and Technology, 1–18, Copyright ©Taylor & Francis (2022) [189], the abstract is reprinted with permission from Taylor & Francis.

Abstract

A model flow reactor provides a narrow particle temperature-residence time distribution with well-defined conditions and is mandatory to measure changes of the particle structure precisely. The experimental data of iron and iron oxide agglomerates are used to determine the sintering kinetics considering the temperature-time history of the particles. Thousand particle trajectories are tracked in a validated CFD model at three different furnace temperatures each. Strongly agglomerated particles with a small primary particle size (~4 nm) are synthesized by spark discharge and are size-selected (25 - 250 nm) before sintering. The structure development is measured simultaneously with different online instrumentations and the structure calculated by means of structure models. A simple sintering model, based on the reduction of surface energy, is numerically quantified with the experimental results. The surface of the particles is strongly dependent on the primary particle size and the agglomerate structure. The chemical phase is analyzed using the offline techniques XANES, XRD, and EELS. It is observed that the addition of hydrogen led to a reduction of iron oxide to iron nanoparticles and to changes of the sintering kinetics. The sintering exponent $m = 1$ was found to be optimal. For Fe, an activation energy E_a of 59.15 kJ/mol and a pre-exponential factor A_s of 1.57 10^4 s/m were found, for Fe_3O_4 an activation energy E_a of 55.22 kJ/mol and a pre-exponential factor A_s of 2.54 10^4 s/m.

A.4 Early particle formation and evolution in iron-doped flames

M.R. Lalanne, P. Wollny, M. Nanjaiah, J. Menser, C. Schulz, H. Wiggers, S. Cheskis, I. Wlokas, I. Rahinov

P. Wollny contributed with models, codes and simulation of particle nucleation/evaporation for the different investigated conditions within the flame and for generic test cases, post-processing and plots, discussion, corrections and proof-reading.
This paper was published in Combustion and Flame, 244, 112251, Copyright ©Elsevier (2022) [116], the abstract is reprinted with permission from Elsevier.

Abstract

In flame synthesis of nanoparticles, the temperature history experienced by the nascent particle aerosol defines the morphology, composition, and crystallinity of the resulting nanomaterial. Commonly, flame-synthesis processes are modeled with an isothermal approximation assuming that the particle temperature replicates that of the surrounding gas phase, avoiding inclusion of an additional internal coordinate in the population balance model, and thus reducing the computational cost. This simplification neglects the influence of matter- and energy-exchange as well as thermochemistry between the particle and reactive gas phase, impacting the particle temperature. In this work, we investigate the temperature history of the particles in incipient formation stages and their evolution in iron-doped flames, prototypical for many other transition-metal (oxide) synthesis systems. The temperature and relative volume-fraction distributions of early particles forming in H2/O2/Ar flames doped with iron pentacarbonyl were determined for the first time, based on spectrally and spatially resolved flame emission measurements and pyrometric analysis of the continuum emission emanating from the nascent particle aerosol. The nascent particle temperature was found to be several hundred degrees above the gas-phase temperature for all physically reasonable assumptions concerning particle composition and emission efficiency. Early particles volume fraction rises sharply shortly after the decomposition of iron pentacarbonyl and decreases steeply in the flame front, in excellent agreement with previous particle-mass spectrometry/quartz-crystal microbalance measurements. By modeling the evaporation process of isothermal iron particles, we show that vanishing of particles in the flame front cannot be explained by evaporation of particles that are in thermal equilibrium with the gas phase. A single-particle Monte-Carlo simulation based on a simple model comprising Fe-monomer condensation, concurrent with oxidation, reduction, etching, and evaporation occurring at the particle

surface, captures both the flame structure with respect to early particle formation and their excess temperature compared to the gas phase.

A.5 Spatially resolved measurement of the distribution of solid and liquid Si nanoparticles in plasma synthesis through line-of-sight extinction spectroscopy

G. Liu, P. Wollny, J. Menser, T. Dreier, T. Enders, I. Wlokas, K. J. Daun, C. Schulz

P. Wollny was throughout involved in the development process of this work, he contributed the presented simulation data, post-processing, discussion, corrections and proof-reading.
This abstract is a preprint version of a manuscript submitted to Optics Express (2022).

Abstract

In many high-temperature gas-phase nanoparticle synthesis processes, freshly nucleated particles are liquid and solidify during growth and cooling. This study presents an approach to determine the location of the liquid-to-solid phase transition and the volume fraction and number density of particles of both phases within a gas phase reactor. Spectrally-resolved line-of-sight attenuation (LOSA) measurements are applied to a silicon nanoparticle aerosol generated from monosilane in a microwave plasma reactor. A phantom-based analysis using direct numerical simulation (DNS) data indicates that the contributions from the two particle phases can be decoupled under practical conditions, even with noisy data. The approach was applied to analyze spatially and spectrally resolved LOSA measurements from the hot gas flow downstream of the plasma zone where both solid and liquid silicon particles coexist. Extinction spectra were recorded along a line perpendicular to the flow direction by a spectrometer with an electron-multiplying charge-coupled device (EMCCD) camera, and two-dimensional projections were deconvolved to obtain radial extinction coefficient distributions of solid and liquid particles across the cross-section of the flow. Particle number densities of both particle phases were retrieved simultaneously based on the size-dependent extinction cross-sections of the nanoparticles. The particle-size distribution was determined via thermophoretic sampling at the same location with subsequent transmission electron microscopy (TEM) analysis. The particle temperature distribution was determined from the particle's thermal radiation based on line-of-sight emission (LOSE) measurements. The approach for phase-selective data analysis can be transferred to other materials aerosol systems as long as significant differences exist in extinction spectra for the related different particle classes.

References

[1] A. Abdelsamie, C. Chi, M. Nanjaiah, I. Skenderović, S. Suleiman, and D. Thévenin. Direct numerical simulation of turbulent spray combustion in the spraysyn burner: Impact of injector geometry. *Flow Turbul. Combust.*, pages 1–17, 2020.

[2] A. Aiello, J. R. Morey, K. J. Livi, H. C. DeLong, H. ElBidweihy, P. C. Trulove, and D. P. Durkin. Lignocellulose-stabilized iron-palladium nanomagnetic biocomposites. *Journal of Magnetism and Magnetic Materials*, 497:165964, 2020.

[3] J. Akroyd, A. J. Smith, R. Shirley, L. R. McGlashan, and M. Kraft. A coupled cfd-population balance approach for nanoparticle synthesis in turbulent reacting flows. *Chemical Engineering Science*, 66(17):3792–3805, 2011.

[4] M. Asif, J. Menser, T. Endres, T. Dreier, K. Daun, and C. Schulz. Phase-sensitive detection of gas-borne si nanoparticles via line-of-sight uv/vis attenuation. *Optics Express*, 29(14):21795–21809, 2021.

[5] J. Barrett and J. Jheeta. Improving the accuracy of the moments method for solving the aerosol general dynamic equation. *Journal of Aerosol Science*, 27(8):1135–1142, 1996.

[6] E. Bekyarova, M. Davis, T. Burch, M. Itkis, B. Zhao, S. Sunshine, and R. Haddon. Chemically functionalized single-walled carbon nanotubes as ammonia sensors. *The Journal of Physical Chemistry B*, 108(51):19717–19720, 2004.

[7] M. Benelmekki. *Designing hybrid nanoparticles*. Morgan & Claypool Publishers San Rafael, CA, 2015.

[8] H. C. Berg. *Random walks in biology*. Princeton University Press, 1993.

[9] B. R. Bird. *Transport Phenomena*. John Wiley & Sons, 2002.

[10] F. Bisetti, A. Attili, and H. Pitsch. Advancing predictive models for particulate formation in turbulent flames via massively parallel direct numerical simulations. *Philosophical Transactions of the Royal Society A: Mathematical, Physical and Engineering Sciences*, 372(2022):20130324, Aug. 2014. doi: 10.1098/rsta.2013.0324. URL https://doi.org/10.1098/rsta.2013.0324.

[11] P. Biswas and C.-Y. Wu. Nanoparticles and the environment. *Journal of the air & waste management association*, 55(6):708–746, 2005.

[12] T. Blacha, M. Di Domenico, P. Gerlinger, and M. Aigner. Soot predictions in premixed and non-premixed laminar flames using a sectional approach for pahs and soot. *Combust. Flame*, 159(1):181–193, 2012.

[13] M. Boger, D. Veynante, H. Boughanem, and A. Trouvé. Direct numerical simulation analysis of flame surface density concept for large eddy simulation of turbulent premixed combustion. *Symp. (Int.) Combust.*, 27(1):917–925, 1998.

[14] M. Brönstrup, D. Schröder, I. Kretzschmar, H. Schwarz, and J. N. Harvey. Platinum dioxide cation: Easy to generate experimentally but difficult to describe theoretically. *J. Am. Chem. Soc.*, 123(1):142–147, Jan. 2001. ISSN 0002-7863.

[15] B. Buesser and A. J. Groehn. Multiscale aspects of modeling gas-phase nanoparticle synthesis. *Chem. Eng. Technol.*, 35(7):1133–1143, 2012.

[16] U. Burke, K. P. Somers, P. O'Toole, C. M. Zinner, N. Marquet, G. Bourque, E. L. Petersen, W. K. Metcalfe, Z. Serinyel, and H. J. Curran. An ignition delay and kinetic modeling study of methane, dimethyl ether, and their mixtures at high pressures. *Combustion and Flame*, 162(2):315–330, 2015. ISSN 0010-2180. URL http://www.sciencedirect.com/science/article/pii/S001021801400251X.

[17] T. Butler and P. O'rourke. A numerical method for two dimensional unsteady reacting flows. *Symp. (Int.) Combust.*, 16(1):1503–1515, 1977.

[18] O. Calin. *An informal introduction to stochastic calculus with applications*. World Scientific, 2015.

[19] L. S. Caretto, A. D. Gosman, S. V. Patankar, and D. B. Spalding. Two calculation procedures for steady, three-dimensional flows with recirculation. In *Proceedings of the Third International Conference on Numerical Methods in Fluid Mechanics*, pages 60–68, Berlin, Heidelberg, 1973. Springer Berlin Heidelberg.

[20] F. Charlette, C. Meneveau, and D. Veynante. A power-law flame wrinkling model for les of premixed turbulent combustion part i- non-dynamic formulation and initial tests. *Combust. Flame*, 131:159–180, 2002.

[21] J. C. Chaston. Reactions of oxygen with the platinum metals. *Platinum Met. Rev.*, 9 (2):51–56, 1965.

[22] J. H. Chen. Petascale direct numerical simulation of turbulent combustion – fundamental insights towards predictive models. *Proceedings of the Combustion Institute*, 33(1): 99–123, Jan. 2011. ISSN 1540-7489. URL http://www.sciencedirect.com/science/article/pii/S1540748910003962.

[23] J. H. Chen, A. Choudhary, B. de Supinski, M. DeVries, E. R. Hawkes, S. Klasky, W. K. Liao, K. L. Ma, J. Mellor-Crummey, N. Podhorszki, R. Sankaran, S. Shende, and C. S. Yoo. Terascale direct numerical simulations of turbulent combustion using s3d. *Computational Science & Discovery*, 2(1):015001, Jan. 2009. ISSN 1749-4699. URL http://dx.doi.org/10.1088/1749-4699/2/1/015001.

[24] R. S. Chrystie, O. M. Feroughi, T. Dreier, and C. Schulz. Sio multi-line laser-induced fluorescence for quantitative temperature imaging in flame-synthesis of nanoparticles. *Applied Physics B*, 123(4):1–12, 2017.

[25] W. Coblenz, J. Dynys, R. Cannon, and R. Coble. Initial stage solid state sintering models. a critical analysis and assessment. *Sintering Processes. Materials Science Research*, 13:141–157, 1980.

[26] W. S. Coblenz. The physics and chemistry of the sintering of silicon. *Journal of Materials Science*, 25(6):2754–2764, 1990.

[27] M. Colombo, S. Carregal-Romero, M. F. Casula, L. Gutiérrez, M. P. Morales, I. B. Böhm, J. T. Heverhagen, D. Prosperi, and W. J. Parak. Biological applications of magnetic nanoparticles. *Chemical Society Reviews*, 41(11):4306–4334, 2012.

[28] V. Colombo, E. Ghedini, and P. Sanibondi. Thermodynamic and transport properties in non-equilibrium argon, oxygen and nitrogen thermal plasmas. *Progress in Nuclear Energy*, 50(8):921–933, 2008.

[29] V. Colombo, E. Ghedini, M. Gherardi, and P. Sanibondi. Modelling for the optimization of the reaction chamber in silicon nanoparticle synthesis by a radio-frequency induction thermal plasma. *Plasma Sources Science and Technology*, 21(5):055007, 2012.

[30] J. Crank and P. Nicolson. A practical method for numerical evaluation of solutions of partial differential equations of the heat-conduction type. In *Mathematical Proceedings of the Cambridge Philosophical Society*, volume 43, pages 50–67. Cambridge University Press, 1947.

[31] E. L. Cussler. *Diffusion: mass transfer in fluid systems*. Cambridge university press, 2009.

[32] H. Dang and M. T. Swihart. Computational modeling of silicon nanoparticle synthesis: I. a general two-dimensional model. *Aerosol Science and Technology*, 43(3):250–263, 2009.

[33] D. Dasgupta, P. Pal, R. Torelli, S. Som, N. Paulson, J. Libera, and M. Stan. Computational fluid dynamics modeling and analysis of silica nanoparticle synthesis in a flame spray pyrolysis reactor. *Combustion and Flame*, 236:111789, 2022.

[34] M. De, P. S. Ghosh, and V. M. Rotello. Applications of nanoparticles in biology. *Advanced Materials*, 20(22):4225–4241, 2008.

[35] M. J. De Witt, D. J. Dooling, and L. J. Broadbelt. Computer generation of reaction mechanisms using quantitative rate information Application to long-chain hydrocarbon pyrolysis. *Ind. Eng. Chem. Res.*, 39(7):2228–2237, 2000. doi: 10.1021/ie990608k.

[36] M. R. Djokic, K. M. Van Geem, C. Cavallotti, A. Frassoldati, E. Ranzi, and G. B. Marin. An experimental and kinetic modeling study of cyclopentadiene pyrolysis: First growth of polycyclic aromatic hydrocarbons. *Combust. Flame*, 161(11):2739–2751, 2014.

[37] R. Dobbins and G. Mulholland. Interpretation of optical measurements of flame generated particles. *Combustion Science and Technology*, 40(5-6):175–191, 1984.

[38] E. C. Dreaden, A. M. Alkilany, X. Huang, C. J. Murphy, and M. A. El-Sayed. The golden age: gold nanoparticles for biomedicine. *Chemical Society Reviews*, 41(7): 2740–2779, 2012.

[39] M. Düsing, A. M. Kempf, F. Flemming, A. Sadiki, and J. Janicka. Combustion les for premixed and diffusion flames. *Prog. Comp. Fluid Dyn.*, 5:363–374, 2005.

[40] A. Eibeck and W. Wagner. An efficient stochastic algorithm for studying coagulation dynamics and gelation phenomena. *SIAM Journal on Scientific Computing*, 22(3): 802–821, 2000.

[41] L. Engelmann, J. Laichter, P. Wollny, M. Klein, S. A. Kaiser, and A. M. Kempf. Cyclic variations in the flame propagation in an spark-ignited engine: Multi cycle large eddy simulation supported by imaging diagnostics. *Flow, Turbulence and Combustion*, pages 1–14, 2022.

[42] A. Favre. Statistical equations of turbulent gases. *Problems of hydrodynamics and continuum mechanics*, pages 231–266, 1969.

[43] J. H. Ferziger and M. Peric. *Computational methods for fluid dynamics*. Springer Science & Business Media, 2012.

[44] I. Freestone, N. Meeks, M. Sax, and C. Higgitt. The lycurgus cup—a roman nanotechnology. *Gold bulletin*, 40(4):270–277, 2007.

[45] J. Frenkel. Viscous flow of crystalline bodies under the action of surface tension. *J. phys.*, 9:385, 1945.

[46] M. Frenklach and S. J. Harris. Aerosol dynamics modeling using the method of moments. *Journal of colloid and interface science*, 118(1):252–261, 1987.

[47] M. Frenklach, L. Ting, H. Wang, and M. J. Rabinowitz. Silicon particle formation in pyrolysis of silane and disilane. *Israel Journal of Chemistry*, 36(3):293–303, 1996.

[48] S. Friedlander. *Smoke, dust and haze: Fundamentals of aerosol behavior*. 1977.

[49] S. Friedlander and C. Wang. The self-preserving particle size distribution for coagulation by brownian motion. *Journal of Colloid and interface Science*, 22(2):126–132, 1966.

[50] S. K. Friedlander and M. K. Wu. Linear rate law for the decay of the excess surface area of a coalescing solid particle. *Physical Review B*, 49(5):3622, 1994.

[51] N. A. Fuchs, R. Daisley, M. Fuchs, C. Davies, and M. Straumanis. The mechanics of aerosols. *Physics Today*, 18(4):73, 1965.

[52] S. Garrick, M. Zachariah, and K. Lehtinen. Modeling and simulation of nanoparticle coagulation in high reynolds number incompressible flows. *Proceeding of the National Conference of the Combustion Institute*, 2527, 2001.

[53] F. Gelbard and J. H. Seinfeld. The general dynamic equation for aerosols. theory and application to aerosol formation and growth. *J. Colloid Interface Sci.*, 68(2):363–382, Feb. 1979. ISSN 0021-9797.

[54] F. Gelbard, Y. Tambour, and J. H. Seinfeld. Sectional representations for simulating aerosol dynamics. *J. Colloid Interface Sci.*, 76(2):541–556, Aug. 1980. ISSN 0021-9797.

[55] M. Germano, U. Piomelli, P. Moin, and W. H. Cabot. A dynamic subgrid-scale eddy viscosity model. *Physics of Fluids A: Fluid Dynamics*, 3(7):1760–1765, 1991. ISSN 0899-8213. doi: 10.1063/1.857955. URL https://doi.org/10.1063/1.857955.

[56] A. Giesen, A. Kowalik, and P. Roth. Iron-atom condensation interpreted by a kinetic model and a nucleation model approach. *Phase Transitions*, 77(1-2):115–129, 2004.

[57] B. Giesen, H. Wiggers, A. Kowalik, et al. Formation of si-nanoparticles in a microwave reactor: Comparison between experiments and modelling. *Journal of Nanoparticle Research*, 7(1):29–41, 2005.

[58] M. Giglmaier, J. Quaatz, J. Matheis, and N. Adams. Numerical analysis of particle growth in a microwave driven plasma reactor and comparison to experimental data. *AIChE Journal*, 34:11, 2011.

[59] S. L. Girshick and C.-P. Chiu. Kinetic nucleation theory: A new expression for the rate of homogeneous nucleation from an ideal supersaturated vapor. *The journal of chemical physics*, 93(2):1273–1277, 1990.

[60] M. Goodson and M. Kraft. An efficient stochastic algorithm for simulating nanoparticle dynamics. *Journal of Computational Physics*, 183(1):210–232, 2002.

[61] D. G. Goodwin. An open-source, extensible software suite for cvd process simulation. *Chemical vapor deposition XVI and EUROCVD*, 14(40):2003–08, 2003.

[62] E. Goudeli, M. L. Eggersdorfer, and S. E. Pratsinis. Coagulation–agglomeration of fractal-like particles: Structure and self-preserving size distribution. *Langmuir*, 31(4): 1320–1327, 2015.

[63] E. Goudeli, M. L. Eggersdorfer, and S. E. Pratsinis. Coagulation of agglomerates consisting of polydisperse primary particles. *Langmuir*, 32(36):9276–9285, 2016.

[64] D. Gray, B. Billings, and D. Bleil. *American Institute of Physics Handbook*. A McGraw-Hill classic handbook reissue. McGraw-Hill, 1972. ISBN 9780070014855.

[65] C. J. Greenshields. *OpenFOAM programmers guide*. URL http://foam.sourceforge.net/docs/Guides-a4/OpenFOAMUserGuide-A4.pdf.

[66] A. J. Gröhn, S. E. Pratsinis, and K. Wegner. Fluid-particle dynamics during combustion spray aerosol synthesis of zro2. *Chemical Engineering Journal*, 191:491–502, 2012.

[67] A. J. Gröhn, S. E. Pratsinis, A. Sánchez-Ferrer, R. Mezzenga, and K. Wegner. Scale-up of nanoparticle synthesis by flame spray pyrolysis: the high-temperature particle residence time. *Ind. Eng. Chem. Res.*, 53(26):10734–10742, 2014.

[68] P. Gruhlke, H. Janbazi, P. Wollny, I. Wlokas, C. Beck, B. Janus, and A. Kempf. Large-eddy simulation of a lifted high-pressure jet-flame with direct chemistry. *Combustion Science and Technology*, pages 1–25, 2021.

[69] A. Gutsch, M. Krämer, G. Michael, H. Mühlenweg, M. Pridöhl, and G. Zimmermann. Gas-phase production of nanoparticles. *KONA Powder and Particle Journal*, 20:24–37, 2002.

[70] O. L. Gülder. Turbulent premixed flame propagation models for different combustion regimes. *Symp. (Int.) Combust.*, 23(1):743 – 750, 1991. ISSN 0082-0784. doi: https://doi.org/10.1016/S0082-0784(06)80325-5. Twenty-Third Symposium (International) on Combustion.

[71] M. J. Hajipour, K. M. Fromm, A. A. Ashkarran, D. J. de Aberasturi, I. R. de Larramendi, T. Rojo, V. Serpooshan, W. J. Parak, and M. Mahmoudi. Antibacterial properties of nanoparticles. *Trends in biotechnology*, 30(10):499–511, 2012.

[72] N. A. Hamid, S. Wennig, S. Hardt, A. Heinzel, C. Schulz, and H. Wiggers. High-capacity cathodes for lithium-ion batteries from nanostructured lifepo4 synthesized by highly-flexible and scalable flame spray pyrolysis. *J. Power Sources*, 216:76–83, Oct. 2012. ISSN 0378-7753.

[73] S. Hardt, I. Wlokas, C. Schulz, and H. Wiggers. Impact of ambient pressure on titania nanoparticle formation during spray-flame synthesis. *J. Nanosci. Nanotechnol.*, 15 (12):9449–9456, 2015.

[74] S. J. Harris and I. M. Kennedy. The coagulation of soot particles with van der waals forces. *Combust. Sci. Technol.*, 59(4-6):443–454, June 1988. ISSN 0010-2202.

[75] C.-H. He, J.-H. He, and H. M. Sedighi. Fangzhu: An ancient chinese nanotechnology for water collection from air: History, mathematical insight, promises, and challenges. *Mathematical Methods in the Applied Sciences*, 2020.

[76] F. J. Heiligtag and M. Niederberger. The fascinating world of nanoparticle research. *Materials today*, 16(7-8):262–271, 2013.

[77] J. Hinze. *Turbulence*. McGraw-Hill Book Co., New York, 1975.

[78] J. O. Hirschfelder, C. Curtis, and R. Bird. *Molecular Theory of Gases and Liquids*. John Wiley & Sons, New York, 1954.

[79] P. Ho, M. E. Coltrin, and W. G. Breiland. Laser-induced fluorescence measurements and kinetic analysis of si atom formation in a rotating disk chemical vapor deposition reactor. *J. Phys. Chem.*, 98(40):10138–10147, Oct. 1994. ISSN 0022-3654. doi: 10.1021/j100091a032. URL https://doi.org/10.1021/j100091a032.

[80] H. Hottel and W. Hawthorne. Diffusion in laminar flame jets. *Symposium on Combustion and Flame, and Explosion Phenomena*, 3(1):254 – 266, 1948. ISSN 1062-2896. doi: https://doi.org/10.1016/S1062-2896(49)80034-1. Third Symposium on Combustion and Flame and Explosion Phenomena.

[81] H. M. Hulburt and S. Katz. Some problems in particle technology: A statistical mechanical formulation. *Chemical engineering science*, 19(8):555–574, 1964.

[82] J. Hulla, S. Sahu, and A. Hayes. Nanotechnology: History and future. *Human & experimental toxicology*, 34(12):1318–1321, 2015.

[83] T. Hülser, S. M. Schnurre, H. Wiggers, and C. Schulz. Gas-phase synthesis of nanoscale silicon as an economical route towards sustainable energy technology. *KONA Powder and Particle Journal*, 29:191–207, 2011.

[84] K. Inagaki and H. Kobayashi. Role of various scale-similarity models in stabilized mixed subgrid-scale model. *Physics of Fluids*, 32(7):075108, 2020.

[85] R. I. Issa. Solution of the implicitly discretised fluid flow equations by operator-splitting. *Journal of Computational Physics*, 62(1):40–65, Jan. 1986. ISSN 0021-9991. URL http://www.sciencedirect.com/science/article/pii/0021999186900999.

[86] H. Jasak. *Error analysis and estimation for the finite volume method with applications to fluid flows*. PhD thesis, Imperial College of Science, Technology and Medicine, 1996.

[87] J. Jeevanandam, A. Barhoum, Y. S. Chan, A. Dufresne, and M. K. Danquah. Review on nanoparticles and nanostructured materials: history, sources, toxicity and regulations. *Beilstein journal of nanotechnology*, 9(1):1050–1074, 2018.

[88] J. I. Jeong and M. Choi. A simple bimodal model for the evolution of non-spherical particles undergoing nucleation, coagulation and coalescence. *Journal of Aerosol Science*, 34(8):965–976, 2003.

[89] D. Johnson-McDaniel, C. A. Barrett, A. Sharafi, and T. T. Salguero. Nanoscience of an ancient pigment. *Journal of the American Chemical Society*, 135(5):1677–1679, 2013.

[90] W. Jones and B. E. Launder. The prediction of laminarization with a two-equation model of turbulence. *International journal of heat and mass transfer*, 15(2):301–314, 1972.

[91] W. Jones and R. Lindstedt. Global reaction schemes for hydrocarbon combustion. *Combust. Flame*, 73(3):233–249, 1988. ISSN 0010-2180. doi: https://doi.org/10.1016/0010-2180(88)90021-1. URL http://www.sciencedirect.com/science/article/pii/0010218088900211.

[92] M. Karlsson, K. Deppert, B. Wacaser, L. Karlsson, and J.-O. Malm. Size-controlled nanoparticles by thermal cracking of iron pentacarbonyl. *Applied Physics A*, 80(7):1579–1583, 2005.

[93] E. Kauffeldt and T. Kauffeldt. Thermodynamic-controlled gas phase process for the synthesis of nickel nanoparticles of adjustable size and morphology. *Journal of Nanoparticle Research*, 8(3):477–488, 2006.

[94] F. E. Kaviyani, A. S. Naeemi, and A. Salehzadeh. Acute toxicity and effects of titanium dioxide nanoparticles (tio2 nps) on some metabolic enzymes and hematological indices of the endangered caspian trout juveniles (salmo trutta caspius kessler, 1877). *Iranian Journal of Fisheries Sciences*, 19(3):1253–1267, 2020.

[95] A. Kazakov and M. Frenklach. Dynamic modeling of soot particle coagulation and aggregation: Implementation with the method of moments and application to high-pressure laminar premixed flames. *Combust. Flame*, 114(3):484–501, Aug. 1998. ISSN 0010-2180.

[96] R. J. Kee, M. E. Coltrin, and P. Glarborg. *Chemically reacting flow: theory and practice*. John Wiley & Sons, 2005.

[97] J. Kemmler, S. Pokhrel, L. Mädler, U. Weimar, and N. Barsan. Flame spray pyrolysis for sensing at the nanoscale. *Nanotechnology*, 24(44):442001, 2013.

[98] A. M. Kempf and C. Schulz. SpraySyn Standardbrenner: Definition, Gesamtsimulation, Charakterisierung, 2017.

[99] A. M. Kempf, B. J. Geurts, and J. C. Oefelein. Error analysis of large-eddy simulation of the turbulent non-premixed sydney bluff-body flame. *Combust. Flame*, 158(12): 2408–2419, Dec. 2011. ISSN 0010-2180.

[100] V. Kessler, D. Gautam, T. Hülser, M. Spree, R. Theissmann, M. Winterer, H. Wiggers, G. Schierning, and R. Schmechel. Thermoelectric properties of nanocrystalline silicon from a scaled-up synthesis plant. *Advanced engineering materials*, 15(5):379–385, 2013.

[101] S. J. Klaine, A. A. Koelmans, N. Horne, S. Carley, R. D. Handy, L. Kapustka, B. Nowack, and F. von der Kammer. Paradigms to assess the environmental impact of manufactured nanomaterials, 2012.

[102] M. Klein, S. Ketterl, L. Engelmann, A. Kempf, and H. Kobayashi. Regularized, parameter free scale similarity type models for large eddy simulation. *International Journal of Heat and Fluid Flow*, 81:108496, 2020.

[103] J. Knipping, H. Wiggers, B. Rellinghaus, P. Roth, D. Konjhodzic, and C. Meier. Synthesis of high purity silicon nanoparticles in a low pressure microwave reactor. *Journal of nanoscience and nanotechnology*, 4(8):1039–1044, 2004.

[104] K. Kobashi, K. Nishimura, Y. Kawate, and T. Horiuchi. Synthesis of diamonds by use of microwave plasma chemical-vapor deposition: Morphology and growth of diamond films. *Physical review B*, 38(6):4067, 1988.

[105] A. Kobata, K. Kusakabe, and S. Morooka. Growth and transformation of tio2 crystallites in aerosol reactor. *AIChE journal*, 37(3):347–359, 1991.

[106] R. Koirala, S. E. Pratsinis, and A. Baiker. Synthesis of catalytic materials in flames: opportunities and challenges. *Chemical Society Reviews*, 45(11):3053–3068, 2016.

[107] A. N. Kolmogorov. The local structure of turbulence in incompressible viscous fluid for very large reynolds numbers. *Proceedings of the Royal Society of London. Series A: Mathematical and Physical Sciences*, 434(1890):9–13, 1991.

[108] R. Körmer, M. Jank, H. Ryssel, H.-J. Schmid, and W. Peukert. Aerosol synthesis of silicon nanoparticles with narrow size distribution—part 1: Experimental investigations. *Journal of Aerosol Science*, 41(11):998–1007, 2010.

[109] R. Körmer, H.-J. Schmid, and W. Peukert. Aerosol synthesis of silicon nanoparticles with narrow size distribution—part 2: Theoretical analysis of the formation mechanism. *Journal of aerosol science*, 41(11):1008–1019, 2010.

[110] R. Körmer, H.-J. Schmid, and W. Peukert. Aerosol synthesis of silicon nanoparticles with narrow size distribution—part 2: Theoretical analysis of the formation mechanism. *Journal of aerosol science*, 41(11):1008–1019, 2010.

[111] U. R. Kortshagen, R. M. Sankaran, R. N. Pereira, S. L. Girshick, J. J. Wu, and E. S. Aydil. Nonthermal plasma synthesis of nanocrystals: fundamental principles, materials, and applications. *Chemical reviews*, 116(18):11061–11127, 2016.

[112] M. Kraft. Modelling of particulate processes. *KONA Powder and Particle Journal*, 23: 18–35, 2005.

[113] F. E. Kruis, K. A. Kusters, S. E. Pratsinis, and B. Scarlett. A simple model for the evolution of the characteristics of aggregate particles undergoing coagulation and sintering. *Aerosol Sci. Technol.*, 19(4):514–526, Jan. 1993. ISSN 0278-6826.

[114] F. Kunze, S. Kuns, M. Spree, T. Hülser, C. Schulz, H. Wiggers, and S. M. Schnurre. Synthesis of silicon nanoparticles in a pilot-plant-scale microwave plasma reactor: Impact of flow rates and precursor concentration on the nanoparticle size and aggregation. *Powder Technology*, 342:880–886, 2019.

[115] M. Lalanne, A. Pilipodi-Best, O. Blumer, P. Wollny, M. Nanjaiah, I. Wlokas, S. Cheskis, and I. Rahinov. Absolute concentration imaging using self-calibrating laser-induced fluorescence: application to atomic iron in a nanoparticle flame-synthesis reactor. *Applied Physics B*, 127(9):1–14, 2021.

[116] M. R. Lalanne, P. Wollny, M. Nanjaiah, J. Menser, C. Schulz, H. Wiggers, S. Cheskis, I. Wlokas, and I. Rahinov. Early particle formation and evolution in iron-doped flames. *Combustion and Flame*, 244:112251, 2022.

[117] B. E. Launder, G. J. Reece, and W. Rodi. Progress in the development of a reynolds-stress turbulence closure. *Journal of Fluid Mechanics*, 68(3):537–566, 1975. ISSN 0022-1120. doi: 10.1017/s0022112075001814. URL https://www.cambridge.org/core/article/progress-in-the-development-of-a-reynoldsstress-turbulence-closure/796DDAC14EF54A84A36100565D3420D5.

[118] K. Lee. Change of particle size distribution during brownian coagulation. *Journal of Colloid and Interface Science*, 92(2):315–325, 1983.

[119] J. P. Legier, T. J. Poinsot, and D. Veynante. Dynamically thickened flame LES model for premixed and non-premixed turbulent combustion. *Proc. Summer Prog.*, pages 157–168, 2000.

[120] A. Leonard. Energy cascade in large-eddy simulations of turbulent fluid flows. In F. N. Frenkiel and R. E. Munn, editors, *Advances in Geophysics*, volume 18, pages 237–248. Elsevier, Jan. 1975. URL http://www.sciencedirect.com/science/article/pii/S0065268708604641.

[121] B. P. Leonard. Simple high-accuracy resolution program for convective modelling of discontinuities. *Int. J. Numer. Meth. Fluids*, 8(10):1291–1318, Oct. 1988. ISSN 0271-2091. doi: 10.1002/fld.1650081013. URL https://doi.org/10.1002/fld.1650081013.

[122] M. Leschowski, T. Dreier, and C. Schulz. An automated thermophoretic soot sampling device for laboratory-scale high-pressure flames. *Review of Scientific Instruments*, 85 (4):045103, 2014.

[123] M. Lesieur. *Turbulence in Fluids*. Springer Netherlands, 1990. ISBN 978-94-010-6726-3.

[124] O. Levenspiel. *Chemical reaction engineering*. John wiley & sons, 1998.

[125] S. Li, Y. Ren, P. Biswas, and D. T. Stephen. Flame aerosol synthesis of nanostructured materials and functional devices: Processing, modeling, and diagnostics. *Progress in Energy and Combustion Science*, 55:1–59, 2016.

[126] R. Lindstedt and B. Waldheim. Modeling of soot particle size distributions in premixed stagnation flow flames. *Proc. Combust. Inst.*, 34(1):1861–1868, 2013.

[127] G. Liu, M. Asif, J. Menser, T. Dreier, K. Mohri, C. Schulz, and T. Endres. Spatial distribution of gas-phase synthesized germanium nanoparticle volume-fraction and temperature using combined in situ line-of-sight emission and extinction spectroscopy. *Optics Express*, 29(6):8387–8406, 2021.

[128] G. Liu, M. Asif, K. Mohri, C. Schulz, T. Dreier, T. Endres, and J. Menser. In situ measurement of gas-borne silicon nanoparticle volume fraction and temperature by spatially and spectrally line-resolved attenuation and emission imaging. *Powder Technology*, 396:535–541, 2022.

[129] J. Loeffler, S. Das, and S. C. Garrick. Large eddy simulation of titanium dioxide nanoparticle formation and growth in turbulent jets. *Aerosol Sci. Technol.*, 45(5): 616–628, Mar. 2011. ISSN 0278-6826.

[130] P. Lu, S. Fang, W. Cheng, S. Huang, M. Huang, and H. Cheng. Characterization of titanium dioxide and zinc oxide nanoparticles in sunscreen powder by comparing

different measurement methods. *journal of food and drug analysis*, 26(3):1192–1200, 2018.

[131] X. Lv, W. Wei, B. Huang, and Y. Dai. Achieving high energy density for lithium-ion battery anodes by si/c nanostructure design. *Journal of Materials Chemistry A*, 7(5): 2165–2171, 2019.

[132] L. Mädler, H. K. Kammler, R. Mueller, and S. E. Pratsinis. Controlled synthesis of nanostructured particles by flame spray pyrolysis. *J. Aerosol Sci.*, 33(2):369–389, Feb. 2002. ISSN 0021-8502.

[133] F. C. Marincola, T. Ma, and A. M. Kempf. Large eddy simulations of the darmstadt turbulent stratified flame series. *Proc. Combust. Inst.*, 34(1):1307–1315, 2013.

[134] G. Martínez, M. Merinero, M. Pérez-Aranda, E. M. Pérez-Soriano, T. Ortiz, E. Villamor, B. Begines, and A. Alcudia. Environmental impact of nanoparticles' application as an emerging technology: A review. *Materials*, 14(1):166, 2020.

[135] B. J. McBride, S. Gordon, and M. A. Reno. Coefficients for calculating thermodynamic and transport properties of individual species. Technical report tm-4513, NASA, 1993.

[136] R. McGraw. Description of aerosol dynamics by the quadrature method of moments. *Aerosol Science and Technology*, 27(2):255–265, 1997.

[137] D. Meller, L. Engelmann, P. Wollny, K. Tainaka, H. Watanabe, P. Debiagi, O. T. Stein, and A. M. Kempf. Evaluation of ammonia co-firing in the criepi coal jet flame using a three mixture fraction fpv-les. *Proceedings of the Combustion Institute*, 2022.

[138] R. Meller, F. Schlegel, and M. Klein. Sub-grid scale modelling and a-posteriori tests with a morphology adaptive multifield two-fluid model considering rising gas bubbles. *Flow, Turbulence and Combustion*, 108(3):895–922, 2022.

[139] N. Y. Mendoza Gonzalez, M. El Morsli, and P. Proulx. Production of nanoparticles in thermal plasmas: a model including evaporation, nucleation, condensation, and fractal aggregation. *Journal of thermal spray technology*, 17(4):533–550, 2008.

[140] J. Menser, K. Daun, T. Dreier, and C. Schulz. Laser-induced incandescence from laser-heated silicon nanoparticles. *Applied Physics B*, 122(11):1–15, 2016.

[141] J. Menser, K. Daun, T. Dreier, and C. Schulz. Laser-induced atomic emission of silicon nanoparticles during laser-induced heating. *Applied Optics*, 56(11):E50–E57, 2017.

[142] J. Menser, K. Daun, and C. Schulz. Interrogating gas-borne nanoparticles using laser-based diagnostics and bayesian data fusion. *The Journal of Physical Chemistry C*, 125(15):8382–8390, 2021.

[143] F. R. Menter. Performance of popular turbulence model for attached and separated adverse pressure gradient flows. *AIAA Journal*, 30(8):2066–2072, Aug. 1992. ISSN 0001-1452. doi: 10.2514/3.11180. URL https://doi.org/10.2514/3.11180.

[144] F. R. Menter. Improved two-equation k-omega turbulence models for aerodynamic flows. *NASA, United States, NASA-TM-103975, A-92183, NAS 1.15:103975*, 1992.

[145] F. R. Menter. Two-equation eddy-viscosity turbulence models for engineering applications. *AIAA Journal*, 32(8):1598–1605, 1994. ISSN 0001-1452. doi: 10.2514/3.12149. URL https://doi.org/10.2514/3.12149.

[146] W. J. Menz and M. Kraft. A new model for silicon nanoparticle synthesis. *Combust. Flame*, 160(5):947–958, May 2013. ISSN 0010-2180. URL http://www.sciencedirect.com/science/article/pii/S0010218013000291.

[147] W. J. Menz, S. Shekar, G. P. Brownbridge, S. Mosbach, R. Körmer, W. Peukert, and M. Kraft. Synthesis of silicon nanoparticles with a narrow size distribution: a theoretical study. *Journal of Aerosol Science*, 44:46–61, 2012.

[148] W. J. Menz, J. Akroyd, and M. Kraft. Stochastic solution of population balance equations for reactor networks. *Journal of Computational Physics*, 256:615–629, 2014.

[149] L. Mezey and J. Giber. Calculation of surface free energies and characteristics of surface segregation of solids. *Surface Science*, 117(1-3):220–231, 1982.

[150] G. Mie. Contribution to the optics of turbid media specifically colloidal metal particles. *Ann. Phys.(Leipzig)*, 25:377, 1908.

[151] A. Mosquera, D. Horwat, L. Vazquez, A. Gutiérrez, A. Erko, A. Anders, J. Andersson, and J. L. Endrino. Thermal decomposition and fractal properties of sputter-deposited platinum oxide thin films. *J. Mater. Res.*, 27(5):829–836, 2012. ISSN 0884-2914.

[152] V. Moureau, F. B., and H. Pitsch. A level set formulation for premixed combustion les considering the turbulent flame structure. *Combust. Flame*, 156(4):801–812, 2009.

[153] A. Münzer, J. Sellmann, P. Fortugno, A. Kempf, C. Schulz, and H. Wiggers. Inline coating of silicon nanoparticles in a plasma reactor: Reactor design, simulation and experiment. *Materials Today: Proceedings*, 4:S118–S127, 2017.

[154] F. Nicoud, H. B. Toda, O. Cabrit, S. Bose, and J. Lee. Using singular values to build a subgrid-scale model for large eddy simulations. *Physics of Fluids*, 23(8):085106, 2011. ISSN 1070-6631. doi: 10.1063/1.3623274. URL https://doi.org/10.1063/1.3623274.

[155] D. Noriler, M. J. Hodapp, R. K. Decker, H. F. Meier, F. Meierhofer, and U. Fritsching. Numerical simulation of flame spray pyrolysis process for nanoparticle productions: Effects of 2d and 3d approaches. In *Fluids Engineering Division Summer Meeting*, volume 46216, page V01AT03A021. American Society of Mechanical Engineers, 2014.

[156] A. Onischuk, V. Strunin, M. Ushakova, and V. Panfilov. Studying of silane thermal decomposition mechanism. *International journal of chemical kinetics*, 30(2):99–110, 1998.

[157] A. Onischuk, A. Levykin, V. Strunin, K. Sabelfeld, and V. Panfilov. Aggregate formation under homogeneous silane thermal decomposition. *Journal of aerosol science*, 31(11):1263–1281, 2000.

[158] H. Orthner, H. Wiggers, M. Loewenich, S. Kilian, S. Bade, and J. Lyubina. Direct gas phase synthesis of amorphous si/c nanoparticles as anode material for lithium ion battery. *Journal of Alloys and Compounds*, 870:159315, 2021.

[159] S. Panda and S. E. Pratsinis. Modeling the synthesis of aluminum particles by evaporation-condensation in an aerosol flow reactor. *Nanostructured Materials*, 5 (7-8):755–767, 1995.

[160] S. Partridge, B. Kurland, C.-L. Liu, R. Ho, and A. Ruddell. Tumor-induced lymph node alterations detected by mri lymphography using gadolinium nanoparticles. *Scientific reports*, 5(1):1–14, 2015.

[161] S. Parveen, R. Misra, and S. K. Sahoo. Nanoparticles: a boon to drug delivery, therapeutics, diagnostics and imaging. *Nanomedicine: Nanotechnology, Biology and Medicine*, 8(2):147–166, 2012.

[162] R. I. Patterson, J. Singh, M. Balthasar, M. Kraft, and W. Wagner. Extending stochastic soot simulation to higher pressures. *Combustion and Flame*, 145(3):638–642, 2006.

[163] N. S. Peev. Particle collision frequency and the two-dimensional particles nucleation. *Comptes Renuds Acad. Sci.*, 66:29–34, 2013.

[164] M. Pelucchi, M. Bissoli, C. Cavallotti, A. Cuoci, T. Faravelli, A. Frassoldati, E. Ranzi, and A. Stagni. Improved kinetic model of the low-temperature oxidation of n-heptane. *Energy Fuels*, 28(11):7178–7193, 2014.

[165] N. Petermann, T. Schneider, J. Stötzel, N. Stein, C. Weise, I. Wlokas, G. Schierning, and H. Wiggers. Microwave plasma synthesis of si/ge and si/wsi2 nanoparticles for thermoelectric applications. *Journal of Physics D: Applied Physics*, 48(31):314010, 2015.

[166] N. Peters. Laminar diffusion flamelet models in non-premixed turbulent combustion. *Prog. Energy Combust. Sci.*, 10(3):319 – 339, 1984. ISSN 0360-1285. doi: https://doi.org/10.1016/0360-1285(84)90114-X.

[167] N. Peters. Laminar flamelet concepts in turbulent combustion. *Symp. (Int.) Combust.*, 21(1):1231 – 1250, 1988. ISSN 0082-0784. doi: https://doi.org/10.1016/S0082-0784(88)80355-2. Twenty-First Symposuim (International on Combustion).

[168] N. Peters. *Turbulent combustion*. Cambridge university press, 2000.

[169] T. W. Peterson, F. Gelbard, and J. H. Seinfeld. Dynamics of source-reinforced, coagulating, and condensing aerosols. *Journal of colloid and interface science*, 63(3): 426–445, 1978.

[170] H. Pitsch. A consistent level set formulation for large-eddy simulation of premixed turbulent combustion. *Combust. Flame*, 143(4):587–598, 2005.

[171] T. Poinsot and D. Veynante. *Theoretical and numerical combustion*. RT Edwards, Inc., 2005.

[172] S. B. Pope. *Turbulent flows*. IOP Publishing, 2001.

[173] A. Prakash, A. P. Bapat, and M. R. Zachariah. A simple numerical algorithm and software for solution of nucleation, surface growth, and coagulation problems. *Aerosol Sci. Tech.*, 37(11):892–898, Nov. 2003. ISSN 0278-6826.

[174] L. Prandtl. Investigations on turbulent flow. *Zeitschrift für angewandte Mathematik und Mechanik*, 1925.

[175] S. E. Pratsinis. Simultaneous nucleation, condensation, and coagulation in aerosol reactors. *J. Colloid Interface Sci.*, 124(2):416–427, Aug. 1988. ISSN 0021-9797.

[176] F. Proch and A. Kempf. Modeling heat loss effects in the large eddy simulation of a model gas turbine combustor with premixed flamelet generated manifolds. *Proc. Combust. Inst.*, 35(3):3337–3345, 2014.

[177] F. Proch and A. M. Kempf. Numerical analysis of the cambridge stratified flame series using artificial thickened flame les with tabulated premixed flame chemistry. *Combust. Flame*, 161(10):2627–2646, 2014.

[178] F. Proch, P. Domingo, L. Vervisch, and A. M. Kempf. Flame resolved simulation of a turbulent premixed bluff-body burner experiment. part i: Analysis of the reaction zone dynamics with tabulated chemistry. *Combust. Flame*, 180:321–339, 2017.

[179] F. Proch, P. Domingo, L. Vervisch, and A. M. Kempf. Flame resolved simulation of a turbulent premixed bluff-body burner experiment. part ii: A-priori and a-posteriori investigation of sub-grid scale wrinkling closures in the context of artificially thickened flame modeling. *Combust. Flame*, 180:340–350, 2017.

[180] D. Ramkrishna and M. R. Singh. Population balance modeling: current status and future prospects. *Annual review of chemical and biomolecular engineering*, 5:123–146, 2014.

[181] C. M. Rhie and W. L. Chow. Numerical study of the turbulent flow past an airfoil with trailing edge separation. *AIAA Journal*, 21(11):1525–1532, Nov. 1983. ISSN 0001-1452. doi: 10.2514/3.8284. URL https://doi.org/10.2514/3.8284.

[182] J.-W. Rhim, H.-M. Park, and C.-S. Ha. Bio-nanocomposites for food packaging applications. *Progress in polymer science*, 38(10-11):1629–1652, 2013.

[183] L. F. Richardson. *Weather prediction by numerical process*. Cambridge University Press, 2007.

[184] S. Rigopoulos. Population balance modelling of polydispersed particles in reactive flows. *Prog. Energy Combust. Sci.*, 36(4):412–443, 2010.

[185] A. Rittler, F. Proch, and A. M. Kempf. Les of the sydney piloted spray flame series with the pfgm/atf approach and different sub-filter models. *Combust. Flame*, 162(4): 1575 – 1598, 2015. ISSN 0010-2180.

[186] A. Rittler, L. Deng, I. Wlokas, and A. M. Kempf. Large eddy simulations of nanoparticle synthesis from flame spray pyrolysis. *Proc. Combust. Inst.*, 36, 2016.

[187] P. Rodrigues, B. Franzelli, R. Vicquelin, O. Gicquel, and N. Darabiha. Coupling an les approach and a soot sectional model for the study of sooting turbulent non-premixed flames. *Combustion and Flame*, 190:477–499, 2018.

[188] P. L. Roe. Modelling of discontinuous flows. *Lectures in Applied Mathematics*, 22, 1985.

[189] T. Rosenberger, I. Skenderović, J. Sellmann, P. Wollny, A. Levish, I. Wlokas, A. Kempf, M. Winterer, and F. Kruis. Determining the sintering kinetics of fe and fexoy-nanoparticles in a well-defined model flow reactor. *Aerosol Science and Technology*, (just-accepted):1–18, 2022.

[190] M. Sander, R. H. West, M. S. Celnik, and M. Kraft. A detailed model for the sintering of polydispersed nanoparticle agglomerates. *Aerosol Science and Technology*, 43(10): 978–989, 2009.

[191] D. Schaming and H. Remita. Nanotechnology: from the ancient time to nowadays. *Foundations of Chemistry*, 17(3):187–205, 2015.

[192] M. Schiener and R. Lindstedt. Transported probability density function based modelling of soot particle size distributions in non-premixed turbulent jet flames. *Proc. Combust. Inst.*, 37(1):1049–1056, 2019.

[193] G. Schierning, R. Theissmann, H. Wiggers, D. Sudfeld, A. Ebbers, D. Franke, V. Witusiewicz, and M. Apel. Microcrystalline silicon formation by silicon nanoparticles. *Journal of applied physics*, 103(8):084305, 2008.

[194] A. Schild, A. Gutsch, H. Mühlenweg, and S. Pratsinis. Simulation of nanoparticle production in premixed aerosol flow reactors by interfacing fluid mechanics and particle dynamics. *Journal of Nanoparticle Research*, 1(2):305–315, 1999.

[195] F. Schneider, S. Suleiman, J. Menser, E. Borukhovich, I. Wlokas, A. Kempf, H. Wiggers, and C. Schulz. Spraysyn–a standardized burner configuration for nanoparticle synthesis in spray flames. *Rev. Sci. Instrum.*, 90(8):085108, Aug. 2019. ISSN 0034-6748.

[196] J. Sellmann, P. Wollny, S.-J. Baik, S. Suleiman, F. Schneider, C. Schulz, H. Wiggers, I. Wlokas, and A. Kempf. Les of nanoparticle synthesis in the spraysyn burner: A comparison against experiments. *Powder Technology*, 404:117466, 2022.

[197] A. B. Sengul and E. Asmatulu. Toxicity of metal and metal oxide nanoparticles: a review. *Environmental Chemistry Letters*, 18(5):1659–1683, 2020.

[198] T. Seto, A. Hirota, T. Fujimoto, M. Shimada, and K. Okuyama. Sintering of polydisperse nanometer-sized agglomerates. *Aerosol Sci. Technol.*, 27(3):422–438, Sept. 1997. ISSN 0278-6826. doi: 10.1080/02786829708965482. URL https://doi.org/10.1080/02786829708965482.

[199] S. Shekar, M. Sander, R. C. Riehl, A. J. Smith, A. Braumann, and M. Kraft. Modelling the flame synthesis of silica nanoparticles from tetraethoxysilane. *4th International Conference on Population Balance Modeling*, 70:54–66, Mar. 2012. ISSN 0009-2509. URL http://www.sciencedirect.com/science/article/pii/S0009250911003836.

[200] S. Shekar, M. Sander, R. C. Riehl, A. J. Smith, A. Braumann, and M. Kraft. Modelling the flame synthesis of silica nanoparticles from tetraethoxysilane. *Chemical Engineering Science*, 70:54–66, 2012.

[201] J. Shi, P. W. Kantoff, R. Wooster, and O. C. Farokhzad. Cancer nanomedicine: progress, challenges and opportunities. *Nature reviews cancer*, 17(1):20–37, 2017.

[202] M. Shigeta and T. Watanabe. Numerical analysis for co-condensation processes in silicide nanoparticle synthesis using induction thermal plasmas at atmospheric pressure conditions. *Journal of materials research*, 20(10):2801–2811, 2005.

[203] M. Shigeta and T. Watanabe. Growth mechanism of silicon-based functional nanoparticles fabricated by inductively coupled thermal plasmas. *Journal of Physics D: Applied Physics*, 40(8):2407, 2007.

[204] M. Shigeta, Y. Hirayama, and E. Ghedini. Computational study of quenching effects on growth processes and size distributions of silicon nanoparticles at a thermal plasma tail. *Nanomaterials*, 11(6):1370, 2021.

[205] S. B. Simonsen, I. Chorkendorff, S. Dahl, M. Skoglundh, J. Sehested, and S. Helveg. Direct observations of oxygen-induced platinum nanoparticle ripening studied by in situ tem. *J. Am. Chem. Soc.*, 132(23):7968–7975, June 2010. ISSN 0002-7863.

[206] J. Smagorinsky. General circulation experiments with the primitive equations: I. the basic experiment. *Mon. Wea. Rev.*, 91(3):99–164, Mar. 1963. ISSN 0027-0644. doi: 10.1175/1520-0493(1963)091<0099:gcewtp>2.3.co;2. URL https://doi.org/10.1175/1520-0493(1963)091<0099:GCEWTP>2.3.CO;2.

[207] M. v. Smoluchowski. Versuch einer mathematischen theorie der koagulationskinetik kolloider lösungen. *Zeitschrift für physikalische Chemie*, 92(1):129–168, 1918.

[208] P. Spalart and S. Allmaras. A one-equation turbulence model for aerodynamic flows. In *30th aerospace sciences meeting and exhibit*, page 439, 1992.

[209] P. T. Spicer, O. Chaoul, S. Tsantilis, and S. E. Pratsinis. Titania formation by ticl4 gas phase oxidation, surface growth and coagulation. *J. Aerosol Sci.*, 33(1):17–34, Jan. 2002. ISSN 0021-8502.

[210] R. Strobel and S. E. Pratsinis. Flame aerosol synthesis of smart nanostructured materials. *Journal of Materials Chemistry*, 17(45):4743–4756, 2007.

[211] N. Sundaria, M. Singh, P. Upreti, R. P. Chauhan, J. Jaiswal, and A. Kumar. Seed priming with iron oxide nanoparticles triggers iron acquisition and biofortification in wheat (triticum aestivum l.) grains. *Journal of Plant Growth Regulation*, 38(1): 122–131, 2019.

[212] W. Sutherland. Lii. the viscosity of gases and molecular force. *The London, Edinburgh, and Dublin Philosophical Magazine and Journal of Science*, 36.223:507–531, 1893.

[213] P. Sweby. High resolution schemes using flux limiters for hyperbolic conservation laws. *SIAM J. Numer. Anal.*, 21(5):995–1011, Oct. 1984. ISSN 0036-1429. doi: 10.1137/0721062. URL https://doi.org/10.1137/0721062.

[214] D. V. Szabó and S. Schlabach. Microwave plasma synthesis of materials—from physics and chemistry to nanoparticles: A materials scientist's viewpoint. *Inorganics*, 2(3):468–507, 2014.

[215] H. Takagi, H. Ogawa, Y. Yamazaki, A. Ishizaki, and T. Nakagiri. Quantum size effects on photoluminescence in ultrafine si particles. *Applied Physics Letters*, 56(24): 2379–2380, 1990.

[216] S. S. Talukdar and M. T. Swihart. Aerosol dynamics modeling of silicon nanoparticle formation during silane pyrolysis: a comparison of three solution methods. *Journal of Aerosol Science*, 35(7):889–908, 2004.

[217] H. Tennekes and J. L. Lumley. *A first course in turbulence*. MIT press, 1972.

[218] D. Thévenin. Three-dimensional direct simulations and structure of expanding turbulent methane flames. *Proceedings of the Combustion Institute*, 30(1):629–637,

Jan. 2005. ISSN 1540-7489. URL http://www.sciencedirect.com/science/article/pii/S0082078404000906.

[219] G. D. Ulrich. Theory of particle formation and growth in oxide synthesis flames. *Combust. Sci. Technol.*, 4(1):47–57, Sept. 1971. ISSN 0010-2202. doi: 10.1080/00102207108952471. URL https://doi.org/10.1080/00102207108952471.

[220] M. Utriainen, M. Kröger-Laukkanen, L.-S. Johansson, and L. Niinistö. Studies of metallic thin film growth in an atomic layer epitaxy reactor using m(acac)2 (m=ni, cu, pt) precursors. *Appl. Surf. Sci.*, 157(3):151–158, Apr. 2000. ISSN 0169-4332.

[221] van Albada, G. D., B. van Leer, and W. W. Roberts. A comparative study of computational methods in cosmic gas dynamics. In *Upwind and High-Resolution Schemes*, pages 95–103. Springer Berlin Heidelberg, Berlin, Heidelberg, 1997. URL https://doi.org/10.1007/978-3-642-60543-7_6.

[222] B. van Leer. Towards the ultimate conservative difference scheme. ii. monotonicity and conservation combined in a second-order scheme. *Journal of Computational Physics*, 14(4):361–370, Mar. 1974. ISSN 0021-9991. URL http://www.sciencedirect.com/science/article/pii/0021999174900199.

[223] B. Van Leer. Towards the ultimate conservative difference scheme. v. a second-order sequel to godunov's method. *Journal of computational Physics*, 32(1):101–136, 1979.

[224] J. A. Van Oijen and L. P. H. De Goey. Modelling of premixed laminar flames using flamelet-generated manifolds. *Combust. Sci. Technol.*, 161(1):113–137, 2000.

[225] J. A. Van Oijen, R. J. M. Bastiaans, and L. P. H. De Goey. Low-dimensional manifolds in direct numerical simulations of premixed turbulent flames. *Proc. Combust. Inst.*, 31 (1):1377–1384, 2007.

[226] S. Vemury and S. E. Pratsinis. Self-preserving size distributions of agglomerates. *J. Aerosol Sci.*, 26(2):175–185, Mar. 1995. ISSN 0021-8502.

[227] S. Vemury and S. E. Pratsinis. Self-preserving size distributions of agglomerates. *Journal of Aerosol Science*, 26(2):175–185, 1995.

[228] S. Vemury, S. E. Pratsinis, and L. Kibbey. Electrically controlled flame synthesis of nanophase tio2, sio2, and sno2 powders. *J. Mater. Res.*, 12(4):1031–1042, 1997. ISSN 0884-2914.

[229] A. W. Vreman. An eddy-viscosity subgrid-scale model for turbulent shear flow: Algebraic theory and applications. *Physics of Fluids*, 16(10):3670–3681, 2004. ISSN 1070-6631. doi: 10.1063/1.1785131. URL https://doi.org/10.1063/1.1785131.

[230] P. Walter, E. Welcomme, P. Hallégot, N. J. Zaluzec, C. Deeb, J. Castaing, P. Veyssière, R. Bréniaux, J.-L. Lévêque, and G. Tsoucaris. Early use of pbs nanotechnology for an ancient hair dyeing formula. *Nano letters*, 6(10):2215–2219, 2006.

[231] C.-S. Wang and S. Friedlander. The self-preserving particle size distribution for coagulation by brownian motion: Ii. small particle slip correction and simultaneous shear flow. *Journal of Colloid and Interface Science*, 24(2):170–179, 1967.

[232] C. S. Wang and S. K. Friedlander. The self-preserving particle size distribution for coagulation by brownian motion: Ii. small particle slip correction and simultaneous shear flow. *J. Colloid Interface Sci.*, 24(2):170–179, June 1967. ISSN 0021-9797.

[233] F. Wang, S. Bhaduri, and T. Baum. Hot pressing of silicon. *Sintering Processes. Materials Science Research*, 13:289–294, 1980.

[234] G. Wang, M. Boileau, and D. Veynante. Implementation of a dynamic thickened flame model for large eddy simulations of turbulent premixed combustion. *Combust. Flame*, 158(11):2199 – 2213, 2011. ISSN 0010-2180.

[235] J. Warnatz and N. Peters, editors. *Numerical Methods in Laminar Flame Propagation*. Springer, 1982. ISBN 9783663140061. doi: 10.1007/978-3-663-14006-1.

[236] J. Warnatz, U. Maas, and R. Dibble. *Combustion*, volume 3. Springer, 1996.

[237] D. R. Warren and J. H. Seinfeld. Nucleation and growth of aerosol from a continuously reinforced vapor. *Aerosol science and technology*, 3(2):135–153, 1984.

[238] C. Weise, J. Menser, S. Kaiser, A. Kempf, and I. Wlokas. Numerical investigation of the process steps in a spray flame reactor for nanoparticle synthesis. *Proc. Combust. Inst.*, 35(2):2259–2266, 2015.

[239] H. G. Weller, G. Tabor, H. Jasak, and C. Fureby. A tensorial approach to computational continuum mechanics using object-oriented techniques. *Computers in Physics*, 12(6): 620–631, 1998. doi: 10.1063/1.168744.

[240] K. T. Whitby. Determination of aerosol growth rates in the atmosphere using lumped mode aerosol dynamics. *Journal of Aerosol Science*, 12(3):173–178, 1981.

[241] H. Wiggers, R. Starke, and P. Roth. Silicon particle formation by pyrolysis of silane in a hot wall gasphase reactor. *Chemical Engineering & Technology: Industrial Chemistry-Plant Equipment-Process Engineering-Biotechnology*, 24(3):261–264, 2001.

[242] D. C. Wilcox. Reassessment of the scale-determining equation for advanced turbulence models. *AIAA journal*, 26(11):1299–1310, 1988.

[243] D. C. Wilcox. Simulation of transition with a two-equation turbulence model. *AIAA journal*, 32(2):247–255, 1994.

[244] C. R. Wilke. A viscosity equation for gas mixtures. *The journal of chemical physics*, 18.4:517–519, 1950. doi: 10.1080/14786449308620508.

[245] F. A. Williams. *Combustion Theory*. Benjamin Cummings, second edition, 1985.

[246] J. H. Williamson. Low-storage runge-kutta schemes. *Journal of Computational Physics*, 35(1):48–56, 1980.

[247] D. Woiki, A. Giesen, and P. Roth. Time-resolved laser-induced incandescence for soot particle sizing during acetylene pyrolysis behind shock waves. *Proceedings of the Combustion Institute*, 28(2):2531–2537, 2000.

[248] P. Wollny, B. Rogg, and A. Kempf. Modelling heat loss effects in high temperature oxy-fuel flames with an efficient and robust non-premixed flamelet approach. *Fuel*, 216:44–52, 2018.

[249] P. Wollny, S. Angel, H. Wiggers, A. M. Kempf, and I. Wlokas. Multiscale simulation of the formation of platinum-particles on alumina nanoparticles in a spray flame experiment. *Fluids*, 5(4):201, 2020.

[250] P. Wollny, J. Menser, L. Engelmann, J. Sellmann, C. Schulz, H. Wiggers, A. Kempf, and I. Wlokas. The role of phase transition by nucleation, condensation, and evaporation for the synthesis of silicon nanoparticles in a microwave plasma reactor — simulation and experiment. *Chemical Engineering Journal*, page 139695, 2022. ISSN 1385-8947.

[251] D. Woo, J. Seo, and T. Kim. Numerical simulation of si nanoparticle formation by silane pyrolysis. *Nano*, 4(02):107–117, 2009.

[252] D. L. Wright, R. McGraw, and D. E. Rosner. Bivariate extension of the quadrature method of moments for modeling simultaneous coagulation and sintering of particle populations. *Journal of colloid and interface science*, 236(2):242–251, 2001.

[253] L. Xiao, Y. H. Sehlleier, S. Dobrowolny, H. Orthner, F. Mahlendorf, A. Heinzel, C. Schulz, and H. Wiggers. Si–cnt/rgo nanoheterostructures as high-performance lithium-ion-battery anodes. *ChemElectroChem*, 2(12):1983–1990, 2015.

[254] A. Yoshizawa. Statistical theory for compressible turbulent shear flows, with the application to subgrid modeling. *The Physics of Fluids*, 29(7):2152–2164, 1986. ISSN 0031-9171. doi: 10.1063/1.865552. URL https://aip.scitation.org/doi/abs/10.1063/1.865552.

[255] G. Zhou. *Numerical simulations of physical discontinuities in single and multi-fluid flows for arbitrary Mach numbers*. PhD thesis, 1995.

DOI: 10.17185/duepublico/78818
URN: urn:nbn:de:hbz:465-20230824-142004-8